

**Experimental and FE Investigation of Steel-Concrete  
Composite Reduced Web Section (RWS) Connections  
Subjected to Cyclic Loading**

**Fahad Falah GH A M Almutairi**

Submitted in accordance with the requirements for the degree of  
**Doctor of Philosophy**

The University of Leeds  
Faculty of Engineering  
School of Civil Engineering

**January, 2024**

The candidate confirms that the work submitted is his own, except where work which has formed part of jointly-authored publications has been included. The contribution of the candidate and the other authors to this work has been explicitly indicated below. The candidate confirms that appropriate credit has been given within the thesis where reference has been made to the work of others.

The work in Chapter 3 of the thesis has appeared in the following publications:

Almutairi, F.F., Tsavdaridis, K.D., Alonso Rodriguez, A., Asteris, P.G. and Lemonis, M.E., 2023. Hysteretic Behaviour of Composite Reduced Web Section (RWS) Connections for Seismic Applications. *Journal of Earthquake Engineering*, pp.1-36.

Almutairi, F.F. and Tsavdaridis, K.D. The effect of degree of composite action on reduced web section (RWS) connections. *The 9th European Conference on Steel and Composite Structures (EUROSTEEL 2021)*. 1-3 September, 2021, Sheffield, UK.

Almutairi, F.F. and Tsavdaridis, K.D. The effect of degree of composite action on RWS connections subject to cyclic loading. *The 10th International Conference on the Behaviour of Steel Structures in Seismic Areas (STESSA 2021)*. 25-27 May, 2022, Timisoara, Romania.

The work in Chapter 4 of the thesis has appeared in the following publications:

Almutairi, F.F., Tsavdaridis, K.D., Alonso-Rodriguez, A. and Hajirasouliha, I., 2023. Experimental investigation using demountable steel-concrete composite reduced web section (RWS) connections under cyclic loads. *Bulletin of Earthquake Engineering*, pp.1-30.

Almutairi, F.F. and Tsavdaridis, K.D. Hysteretic performance of Reduced Web Section (RWS) connections with demountable slabs and effect of composite action. *Earthquake Engineering & Dynamics for A Sustainable Future (SECED2023)*. 14-15 September, 2023, Cambridge, UK.

The work in Chapter 5 of the thesis has appeared in the following publication:

Almutairi, F.F. and Tsavdaridis, K.D. FEA validation on the degree of composite action of composite reduced web section (RWS) connections under cyclic loading. *The 10th Hellenic National Conference of Steel Structures*. 19-21 October, 2023, Athens, Greece.

All aspects of the publications above were undertaken by the candidate. However, the candidate benefited from the guidance and suggestions from the named co-authors who played the usual role of supervisor.



This copy has been supplied on the understanding that it is copyright material and that no quotation from the thesis may be published without proper acknowledgement.

The right of Fahad Falah GH A M Almutairi to be identified as Author of this work has been asserted by her in accordance with the Copyright, Designs and Patents Act 1988. © 2024 The University of Leeds and Fahad Falah GH A M Almutairi

## Dedication

*This PhD thesis is dedicated to my beloved late father, Falah Ghanim Almutairi, who supported me throughout. I miss you more than words can say.*

## Acknowledgements

First and foremost, I wish to give all the praise to Almighty Allah, our Lord, the All-Knowing, the Almighty, the Most Merciful, and the Most Compassionate, for giving me the strength and capability to accomplish this research.

I would like to express my sincere gratitude to my supervisor, Professor Konstantinos Daniel Tsavdaridis, for his excellent supervision, continuous support, patience, and approachability throughout this research. His wisdom, guidance, helpful advice, comments and suggestions during the PhD programme have helped me gain a very critical point of view on myself and my work. I could not have imagined having a better adviser or mentor for my PhD study.

I would like to express my sincere gratitude to Dr. Andrés Alonso Rodríguez for his help and insightful feedback. I would also like to thank the University of Sheffield, especially Professor Iman Hajirasouliha, Dr Maurizio Guadagnini and all the technicians in their structural laboratory for helping to accomplish the experimental phase of this research.

I would also like to thank Dr Ioannis Mitseas and Mr David Richardson for their help during the PhD programme. My special thanks to the staff of the Heavy Structures Laboratory at the University of Leeds, especially Mr Robert Clark and Mr Stephen Holmes, who were always ready to help in times of need.

I am truly indebted to SC4 Ltd. and their commercial and technical director, Shay Eddy, for their technical support and for providing test consumables.

I am forever deeply grateful to my dear family: my mother, Shaihkah Aldihani; my brothers Khaled, Ghanim, Fawaz, and Talal; my wife, Dr. Shahad Almutairi; and my sons Faisal and Abdulrahman. I would like to express my deepest gratitude to my uncle, Dr. Saud Almutairi, for his continuous support from my Bachelor's degree to My Ph.D. studies.

I would like to express my gratitude to my friends and colleagues, Dr Mohamed Shaheen, Ahmed A. Alali, Dr Abdulrahman Abbadi, Dr Mohammad S. Almutairi, and Ali Alattas, for the stimulating discussions and their gracious help with many matters.

I would like to thank my dear friends in Kuwait and the UK, Khaled F Almutairi, Eisa EJbeli, and Dr. Husain Alajmi, for their support and encouragement. Finally, I would like to thank everybody who was involved in this work and express my apology to anyone whom I have failed to mention in this acknowledgement.

## Abstract

Based on the observations from previous earthquakes, brittle failure poses a significant threat to the integrity of steel-concrete composite moment-resisting frames (MRFs). Hence, there has been successful research in developing fuse strategies that cluster deformation demand away from the column face well within the beam. However, this approach involves the extensive intervention of the column and provision of stocky supplemental plates on flanges and the web, making retrofitting of structures complex, particularly if they were not designed with full consideration of capacity design principles. An alternative approach is to use reduced web section (RWS) connections. These rely on perforations made on the beam's web rather than flange trimming or the use of supplemental plates to increase moment capacity at the column's face. In particular, it is easier to cut through webs than remove floors to intervene on beam flanges.

Limited attention has been paid to the response of RWS connections with composite slabs subjected to cyclic loads. The presence of composite action over the protected zone has raised concerns about jeopardising the concept of a strong column-weak beam and, thereby, causing an asymmetric yield moment mechanism. The former can lead to weak column (story mechanism) and large panel zone yielding, while the latter can induce excessive strain demands on the beam's bottom flange. The response mechanism of RWS connections, acting as two partial beams above and below the opening (top and bottom Tee-sections), induces four plastic hinges around the web opening (Vierendeel mechanism). This mechanism can overcome the aforementioned concerns.

The results of experimental and numerical investigations in this research, along with the compiled and extrapolated findings from the literature, were used to assess the cyclic response of RWS connections. This thesis advocates the application of RWS connections in both new seismic-resistant structures and the retrofitting of non-seismically designed structures. The research findings demonstrate the effectiveness of the capacity design concept in achieving the expected ductile response of RWS connections with overlaid slabs. The inelastic demands and slab cracking were alleviated by eliminating composite interaction over the protected zone without compromising the beam's stability. The test results suggest that RWS connections could be a viable seismic fuse solution for existing and new structures. The experimental and numerical findings established the ability of steel-concrete composite RWS connections to meet the response requirements set by ANSI/AISC 358-16, ANSI/AISC 341-16 and Eurocode 8. These include achieving an inter-storey drift larger than 4% with strength degradation of less than 20% of the beam's plastic moment capacity and cap

shear transfer to non-ductile components of the connections. This was attributed to a highly ductile Vierendeel mechanism that led to an increase in the deformability and ductility of the reduced sections as well as the connections. The analysis of the collected RWS database supports the findings of both experimental and numerical investigations in this research, in which the current design approaches of RWS connections for seismic purposes overlooked the significant effect of a capacity design to ensure a stable yield mechanism is governed.

## Table of contents

<b>Dedication.....</b>	<b>iii</b>
<b>Acknowledgements .....</b>	<b>iv</b>
<b>Abstract .....</b>	<b>v</b>
<b>Table of contents .....</b>	<b>vii</b>
<b>List of Figures .....</b>	<b>x</b>
<b>List of Tables.....</b>	<b>xvi</b>
<b>List of Notations.....</b>	<b>xvii</b>
<b>List of Abbreviations .....</b>	<b>xx</b>
<b>List of Publications.....</b>	<b>xxii</b>
<b>Chapter 1 Introduction .....</b>	<b>1</b>
1.1 Research background and motivation.....	1
1.2 Problem statement and research objectives .....	5
1.3 Methodology .....	5
1.3.1 Necessity of numerical investigations .....	5
1.3.2 Experimental investigation .....	6
1.3.3 Desk Study and Analytical work.....	6
1.4 Thesis outline.....	7
<b>Chapter 2 Literature Review.....</b>	<b>10</b>
2.1 Introduction .....	10
2.2 Structural behaviour of seismic moment connection.....	10
2.2.1 Steel connection characterisation .....	10
2.2.2 Plastic mechanism under cyclic loading.....	12
2.2.3 Research studies on prequalified seismic connections.....	17
2.3 Design criteria .....	26
2.3.1 Eurocode 8 .....	26
2.3.2 American codes .....	28
2.4 Structural behaviour and failure modes of perforated beams .....	29
2.5 Prequalified Connections: Reduced web section (RWS) connection.....	34
2.6 Summary .....	43
<b>Chapter 3 Preliminary Finite Element Analysis.....</b>	<b>45</b>
3.1 Introduction .....	45
3.2 Finite element model validation.....	46
3.2.1 Model description.....	46

3.2.2 Element type .....	47
3.2.3 Contact modelling .....	48
3.2.4 Boundary and loading conditions .....	52
3.2.5 Material model .....	53
3.2.6 Geometric nonlinearity .....	54
3.2.7 Mesh sensitivity analysis.....	55
3.3 FE models benchmarking .....	57
3.4 Parametric study .....	59
3.4.1 Model description.....	59
3.4.2 Nominal capacities of the protected zones .....	63
3.5 Parametric results .....	66
3.5.1 Effect of web opening diameter ( <i>d<sub>o</sub></i> ).....	75
3.5.2 Strength degradation .....	77
3.5.3 Failure modes and stress and strain distribution.....	77
3.5.4 Damage patterns on the slab.....	88
3.5.5 Contribution of composite action.....	90
3.6 Discussion .....	91
3.7 Summary .....	93
<b>Chapter 4 Experimental Investigation.....</b>	<b>95</b>
4.1 Introduction .....	95
4.2 Experimental work .....	96
4.2.1 Design and details of the composite connection specimens.....	96
4.2.2 Specimen preparation.....	99
4.2.3 Test setup and loading protocol.....	101
4.2.4 Instrumentation .....	105
4.2.5 Interpretation of the test results .....	107
4.2.6 Material properties .....	108
4.3 Experimental results .....	110
4.3.1 Solid connection (no web opening).....	110
4.3.2 Yielding mode .....	112
4.3.3 Hysteretic response .....	118
4.3.4 Expected vs. actual resistances.....	126
4.3.5 Strain profile across the steel beam bottom flanges .....	129
4.4 Summary .....	132
<b>Chapter 5 Parametric Assessments.....</b>	<b>133</b>
5.1 Introduction .....	133

5.2 Finite element model validation.....	134
5.2.1 Numerical modelling .....	134
5.2.2 Material model .....	137
5.2.3 FE verification .....	140
5.3 Parametric investigation.....	142
5.3.1 Parameters .....	142
5.3.2 Connection performance characteristics.....	144
5.4 Summary .....	165
<b>Chapter 6 Capacity Design Assessment .....</b>	<b>167</b>
6.1 Introduction .....	167
6.2 Deduced response parameters of the collected RWS database.....	168
6.3 Parametric numerical investigations .....	169
6.3.1 Synopsis .....	169
6.3.2 Parametric results .....	171
6.4 Capacity assessment.....	182
6.4.1 RWS database assembly.....	182
6.4.2 Observed trends in the collected RWS database .....	185
6.4.3 Detailing recommendations .....	189
6.5 Summary .....	193
<b>Chapter 7 Conclusion.....</b>	<b>194</b>
7.1 Overview.....	194
7.2 Summary of contributions .....	195
7.3 Recommendations for future research.....	198
<b>References.....</b>	<b>200</b>
<b>Appendix A: Summary of Studies on RWS connections .....</b>	<b>210</b>
<b>Appendix B: Drawings.....</b>	<b>214</b>
<b>Appendix C: Design of Extended End-Plate Connection .....</b>	<b>226</b>
<b>Appendix D: Design of RWS Connections.....</b>	<b>241</b>



## List of Figures

Figure 1.1: Beam–slab interaction: (a) sagging moments; (b) hogging moments (Gioncu and Mazzolani, 2013). .....	1
Figure 1.2: Story Mechanism (Hamburger and Malley, 2009).....	2
Figure 1.3: Asymmetrical yield moment mechanism (Sumner, 2003; Lee et al., 2016). .....	2
Figure 1.4: RWS connection (Tsavdaridis et al., 2021).....	3
Figure 1.5: Tee-sections of the perforated beam (two partial beams).....	4
Figure 1.6: High and low moment sides.....	4
Figure 1.7: Axial forces at opening.....	4
Figure 1.8: Flow diagram to illustrate the research methods. ....	9
Figure 2.1: Connection types according to their behaviour (a) pinned; (b) rigid; and (c) semi-rigid (Díaz, Martí, et al., 2011).....	11
Figure 2.2: Classification of steel connections by rotational stiffness according to Eurocode 3: Part 1-8 (CEN, 2005b).....	11
Figure 2.3: Ductile and brittle collapse (Gioncu and Mazzolani, 2013). ....	12
Figure 2.4: Plastic collapse mechanism (Gioncu, 2000). ....	13
Figure 2.5: Soft-story collapse mechanism (Lignos et al., 2013). ....	14
Figure 2.6: Plastic mechanism at the beam (Gioncu and Mazzolani, 2013).15	
Figure 2.7: Prequalified seismic connections (ANSI/AISC 358-16, 2016)....	16
Figure 2.8: Fractures of Beam-to-Column Connections (FEMA 350, 2000; FEMA 355E, 2000). ....	16
Figure 2.9: T-stub failure modes. ....	18
Figure 2.10: Four bolt extended unstiffened connection after testing (4E-1.25-1.5-24) (Sumner, 2003).....	19
Figure 2.11: Composite slab test specimen after testing and its load-displacement curve (Sumner et al., 2000a). ....	20
Figure 2.12: Yielding regions with grey highlights and capacity design requirements for the prequalified joints (Landolfo, 2022).....	21
Figure 2.13: Typical plastic zone of the composite RBS specimen tested (Chen and Chao, 2001). ....	22
Figure 2.14: Plastic hinge region after completion of testing (Kim and Lee, 2017). ....	23
Figure 2.15: Composite RBS connection, before, during and after the test (Lee et al., 2016).....	24
Figure 2.16: Symmetric boundary conditions (EISabbagh et al., 2019). ....	25
Figure 2.17: Layout of finite element model (Wang et al., 2018).....	26
Figure 2.18: Vierendeel Mechanism (Chung et al., 2001; Shaheen et al., 2018). .....	29

Figure 2.19: Manufacturing of a cellular beam (Fares et al., 2016).....	30
Figure 2.20: Laser cutting of web opening (Qiao, Guo, et al., 2022).....	30
Figure 2.21: Tee-sections of the perforated beam. ....	31
Figure 2.22: Global moment and shear forces around the web opening.....	32
Figure 2.23: Failure modes at web openings, (a) steel beam, pure bending, (b) steel beam, low moment-shear ratio, (c) composite beam with solid slab, pure bending, and (d) composite beam with solid slab, low moment-shear ratio (Darwin, 1990). ....	32
Figure 2.24: Behaviour of composite perforated beam at ultimate load (PATRICK, 2001).....	33
Figure 2.25: High and low moment sides.....	34
Figure 2.26: Plastic stress blocks in a perforated composite beam (Lawson and Hicks, 2011).....	34
Figure 2.27: RWS connection. ....	35
Figure 2.28: Main failure modes of single web opening – RWS connections. ....	35
Figure 2.29: Vierendeel mechanism (Kerdal and Nethercot, 1984; Shin et al., 2017a).....	36
Figure 2.30: Progressive collapse test results of specimen RWS (Qiao, Xie, et al., 2022).....	38
Figure 2.31: Catenary action of welded RWS connections (Lin et al., 2022). ....	39
Figure 2.32: Overall deflection of specimens (Lin et al., 2021). ....	39
Figure 2.33: Experimental and numerical Investigations into RWS connections. ....	41
Figure 2.34: Effect of the web opening size on the capacity. ....	42
Figure 2.35: Stress distribution of different RWS models.....	42
Figure 3.1: Elevation of test setup (Chaudhari, 2017; Chaudhari et al., 2019). ....	46
Figure 3.2: Displacement Control Loading Regime of ACI report T1.1-01 (ACI, 2005). ....	47
Figure 3.3: Selected element types for FE model. ....	48
Figure 3.4: Tie constraints. ....	49
Figure 3.5: Normal and tangent interactions between steel components.....	50
Figure 3.6: Frictionless contact between concrete slab and steel beam. ....	51
Figure 3.7: Embedded element technique. ....	51
Figure 3.8: Boundary condition and bolts pretensions. ....	52
Figure 3.9: Material stress–strain curve for beam, column, and connection (Díaz et al., 2018) .....	53

Figure 3.10: Schematic representation of the stress-strain curve for structural analysis - Eurocode 2 - (CEN, 2004). .....	54
Figure 3.11: Exponential tension softening (Ahmed and Tsavdaridis, 2022). .....	54
Figure 3.12: First shape of Eigenmode. ....	55
Figure 3.13: Skelton curves for all FE models in mesh sensitivity analysis. .55	
Figure 3.14: Comparison between FE models in mesh sensitivity analysis. 56	
Figure 3.15: Comparison of Hysteresis Behaviour of FE Result with the Test Results of Chaudhari (2017). ....	57
Figure 3.16: Comparison of local buckling between experimental tests (Chaudhari, 2017; Chaudhari et al., 2019) and FE model (with render the thickness of the shell elements). ....	58
Figure 3.17: Comparison of concrete cracks between experimental test (Chaudhari, 2017; Chaudhari et al., 2019) and FE model. ....	58
Figure 3.18: AISC 2016 loading protocol (ANSI/AISC 341-16, 2016). ....	60
Figure 3.19: Model with absence of composite action. ....	60
Figure 3.20: Model identifier. ....	62
Figure 3.21: Equivalent composite section for nominal moment capacity assessment, sagging moment. ....	63
Figure 3.22: Hysteretic curves of solid model and models with the diameter of the opening equal to $0.8h$ . ....	67
Figure 3.23: Hysteretic curves of solid model and models with the diameter of the opening equal to $0.65h$ ....	68
Figure 3.24: Hysteretic curves of solid model and models with the diameter of the opening equal to $0.5h$ . ....	69
Figure 3.25: PEEQ and stresses distribution in last cycle of RWS models with $d_o = 0.5h$ and $S_o$ were complied with SCI P355 guidance (no shear studs over the protected zone). ....	80
Figure 3.26: PEEQ and stresses distribution in last cycle of RWS models with $d_o = 0.5h$ and $S_o$ were complied with SCI P355 guidance (presence of shear studs over the protected zone). ....	81
Figure 3.27: PEEQ and stresses distribution in last cycle of RWS models with $d_o = 0.65h$ and $S_o$ were complied with SCI P355 guidance (no shear studs over the protected zone). ....	82
Figure 3.28: PEEQ and stresses distribution in last cycle of RWS models with $d_o = 0.65h$ and $S_o$ were complied with SCI P355 guidance (presence of shear studs over the protected zone). ....	83
Figure 3.29: PEEQ and stresses distribution in last cycle of RWS models with $d_o = 0.8h$ and $S_o$ were complied with SCI P355 guidance (no shear studs over the protected zone). ....	84

Figure 3.30: PEEQ and stresses distribution in last cycle of RWS models with $d_o = 0.8h$ and $S_o$ were complied with SCI P355 guidance (presence of shear studs over the protected zone). .....	85
Figure 3.31: Distribution of PEEQ and Von Mises stresses of composite solid model (NR-C-L) in last cycle in the hysteretic curve .....	86
Figure 3.32: Distribution of PEEQ and Von Mises stresses of composite solid model (NR-C-H) in last cycle in the hysteretic curve.....	87
Figure 3.33: Concrete slab cracking and crushing patterns for different RWS connections.....	89
Figure 3.34: Concrete slab cracking and crushing patterns for different solid webbed-beam connections. ....	90
Figure 4.1: Dimensions of test specimens (mm). ....	97
Figure 4.2: The height of the bolted shear connector above the top beam flange (mm) .....	100
Figure 4.3: Shuttering of test specimen. ....	100
Figure 4.4: Experimental test setup – side view.....	101
Figure 4.5: Experimental test setup – side view (mm) .....	102
Figure 4.6: Experimental test setup – front and top view (mm).....	103
Figure 4.7: Cyclic loading protocol. ....	104
Figure 4.8: Instrumentation layout (mm). ....	105
Figure 4.9: Elastic, elastic-plastic and plastic stress distributions in a composite section (Davison and Owens, 2012). ....	108
Figure 4.10: Coupon details. ....	108
Figure 4.11: : Stress-strain curves of steel section coupons.....	109
Figure 4.12: Moment-Rotation curve solid connection specimen.....	110
Figure 4.13: Observed crack pattern in Solid connection specimen (mm). ..	112
Figure 4.14: Disconnecting the composite slab of the solid specimen to be reused for the next test. ....	112
Figure 4.15: Distribution of strain intensity for RWS-L-retrofit connection (N.A. = Not Available due to the loss of the strain gauge during the test). ..	113
Figure 4.16: Distribution of strain intensity for RWS-L connection. ....	114
Figure 4.17: Distribution of strain intensity for RWS-H connection.....	115
Figure 4.18: High and low moment sides. ....	116
Figure 4.19: The failure modes of RWS-H connection.....	117
Figure 4.20: Hysteretic curves for RWS-L-retrofit connection. ....	118
Figure 4.21: Hysteretic curves for RWS-L connection .....	119
Figure 4.22: Hysteretic curves for RWS-H connection.....	119
Figure 4.23: Illustration of the behaviour of Tee-sections in RWS-H.....	121

Figure 4.24: Force action at web opening without composite action above the protected zone. ....	122
Figure 4.25: Force action at web opening with composite action above the protected zone. ....	122
Figure 4.26: Failure modes of RWS-L-retrofit specimen. ....	123
Figure 4.27: Observed crack pattern in RWS-L-retrofit connection specimen (mm). ....	124
Figure 4.28: The failure modes of RWS-L connection. ....	125
Figure 4.29: Strain profiles for beam bottom flange near the connections. ....	130
Figure 4.30: Strain profiles for beam bottom flange below the web openings. ....	131
Figure 5.1: Top and side views of FE model with and without slab (shell thickness is not shown). ....	134
Figure 5.2: FE model showing meshes and partitions. ....	135
Figure 5.3: Boundary and loading conditions. ....	136
Figure 5.4: Ture stress-strain curve of the beam, column and end-plate. ...	138
Figure 5.5: Ture stress-strain curve of the other steel elements. ....	139
Figure 5.6: Uniaxial stress-strain curve of concrete under compression and tension. ....	140
Figure 5.7: Compression and tensile damage curves. ....	140
Figure 5.8: Benchmarking of the FEM hysteresis cycles. ....	141
Figure 5.9: Comparison between FE models and tested specimens (shell thickness is not shown). ....	141
Figure 5.10: Failures of RWS-H. ....	142
Figure 5.11: Defining the strength and deformation parameters of IMK model. ....	146
Figure 5.12: Skeleton curves of RWS connections with diameter = 0.5, 0.55, 0.6 and 0.65 <i>h</i> . ....	148
Figure 5.13: Skeleton curves of RWS connections with diameter = 0.7, 0.72, 0.75 and 0.8 <i>h</i> . ....	149
Figure 5.14: The effect of end-distance ( <i>S<sub>o</sub></i> ) on maximum applied moments at column face ( <i>M<sub>f</sub></i> = <i>M<sub>m</sub></i> ). ....	151
Figure 5.15: Moment-rotation curves for small to medium web opening with low and high composite action. ....	153
Figure 5.16: The development of two plastic hinges in LMS. ....	154
Figure 5.17: The effect of web opening size on the pinching mechanism. .	155
Figure 5.18: The trend of the ductility vs diameter (on average). ....	157
Figure 5.19: The trend of the dissipated energy vs diameter (on average). ....	158
Figure 5.20: Contribution of composite slab to maximum strength of the connections (on average). ....	159

Figure 5.21: The change in Vierendeel ratio vs the change in diameter (on average).....	162
Figure 5.22: Comparison between two different connections with high composite action in terms of capacity ratio. ....	164
Figure 6.1: Skeleton moment-rotation curves used for the collected RWS database. ....	168
Figure 6.2: Test set-ups and FE model for tests of Chapter 4 on the left and tests of (Chaudhari et al., 2019) on the right. ....	170
Figure 6.3: Rotation ductility of single-sided connections (based on equal-strength solid webbed-beam connection). ....	173
Figure 6.4: Rotation ductility of double-sided connections (based on full-strength solid webbed-beam connection). ....	174
Figure 6.5: Illustration of the behaviour of Tee-sections. ....	175
Figure 6.6: Comparison between two different connections with high composite action in terms of capacity ratio (from Chapter 5). ....	177
Figure 6.7: Energy dissipation.....	178
Figure 6.8: Basis to calculate the equivalent viscous damping coefficient (Shaheen, 2022). ....	180
Figure 6.9: Equivalent viscous damping coefficient at 0.04 rad. ....	181
Figure 6.10: Energy dissipation and equivalent viscous damping.....	187
Figure 6.11: Ductility for RWS connections.....	188
Figure 6.12: Diameter-to-depth ratio in relation to shear studs' location. ...	190

## List of Tables

Table 2.1: Acceptance criteria from ASCE/SEI 41-17.....	29
Table 3.1: The dimensions and the detailed configuration of the connection in the parametric study. ....	60
Table 3.2: Summary of assessed specimens. ....	61
Table 3.3: Nominal moment capacities of main specimen typologies. ....	65
Table 3.4: Load capacity, initial stiffness and strength degradation of all connections.....	70
Table 3.5: Interstory drift deformation capacity of all specimens.....	72
Table 3.6: Attained moment capacities for right beam. ....	74
Table 3.7: FE results of the contribution of composite action for right beam and failure modes. ....	78
Table 4.1: Specimen test matrix.....	96
Table 4.2: Nominal capacities specimens.....	98
Table 4.3: Concrete compressive cylinder strengths .....	109
Table 4.4: Results Summary.....	111
Table 4.5: Design resistances vs. applied actions. ....	128
Table 5.1: Parameters. ....	143
Table 5.2: Statistics for different sets of diameters based on the ratio of $M_{ye}M_o, a, R_d$ .....	161
Table 6.1: Summary of validated tested specimens.....	170
Table 6.2: Summary of Selected Parameters. ....	171
Table 6.3: Summary breakdown of the collected RWS database. ....	183
Table 6.4: Breakdown of capacity design of the collected RWS database.....	184
Table 6.5: Capacity design requirements for RWS connections for retrofitting existing structures.....	190
Table 6.6: Statistical results for the collected RWS database and parametric investigations. ....	192
Table 6.7: Capacity design requirements for RWS connections for new structures. ....	192
Table A 1. Summary of Studies on RWS connections.....	211

## List of Notations

$A_{T,e,o}$	Area of the two tee-sections.
$A_g$	The gross cross-section of the steel beam without perforations.
$E_b$ or $E$	Steel beam elastic modulus.
$E_{sh}$	Strain-hardening elastic modulus.
$I_b$	Beam moment of inertia about the section's major axis.
$K_c$	Post-capping stiffness.
$K_e$	Elastic rotational stiffness.
$K_i$	Initial rotational stiffness.
$K_s$	Strain-hardening stiffness.
$L_b$	Beam length between column centerlines.
$M_{RWS,Rd}$	Moment capacity of RWS connection.
$M_{Rb}$	Design values of the bending strength of the beam connected to the joint.
$M_{Rc}$ or $M_{pl,col}$	Design values of the bending strength of the column connected to the joint.
$M_{V,Ed}$	Applied Vierendeel moment.
$M_{V,Rd}$	Vierendeel bending resistance.
$M_{bT,NV,Rd}$	Bending resistance of the bottom tee-section.
$M_{c,Rd}$	Bending resistance of the connection.
$M_f$	Maximum beam moment at column face.
$M_{j,Rd}$	The design resistance of the joint.
$M_m$	Maximum moment.
$M_{o,Rd}$	Plastic moment resistance of composite perforated beam according to SCI P355 guidance (Lawson and Hicks, 2011).
$M_{o,a,Rd}$	Plastic moment resistance of steel perforated beam according to SCI P355 guidance.
$M_o$	Maximum applied beam moment at the centre of the web opening.
$M_{pl,Rd,RWS}$	Nominal plastic strength of the connected perforated steel beam.
$M_{pl,Rd}$	Plastic moment resistance of composite solid webbed beam.
$M_{pl,a,Rd}$ or $M_{pl}$	Nominal plastic strength of the connected steel beam.
$M_{tT,NV,Rd}$	Bending resistance of the top tee-section.



$M_u$	Ultimate moment.
$M_{vc,Rd}$	Local composite Vierendeel bending resistance.
$M_{ye}$	Effective yield moment.
$R_d$	Design resistance of non-dissipative welded or bolted connections
$R_{fy}$	Plastic resistance of connected member.
$S_e$	End-distance width from the connection face to the first shear stud' centreline.
$S_{j,ini,EC3}$	Initial stiffness.
$S_o$	End-distance from column/connection face to centreline of web opening.
$V_{Ed}$	Applied shear force.
$V_{o,Rd}$	Shear resistance for perforated section
$W_{pl,y,b}$ or $Z$	Beam's plastic section modulus.
$b_e$	The effective width of the composite slab.
$b_{ep}$	End-plate width.
$b_1$	Fin-plate width.
$d_o$	Web opening diameter.
$e_x$	Distance from the upper tension row to the top of the end plate.
$e_{x1}$	Longitudinal edge distance in fin-plate.
$e_1$	Transverse edge distance in fin-plate.
$f'c$	The nominal compression resistance of concrete in the slab.
$f_{ck}$	Concrete compressive cylinder strength.
$f_t$	Tensile strength of concrete
$f_{y,b}$	Beam's yield strength.
$f_y$	Yield strength of steel.
$h_{eff}$	Effective depth between the centroid of the tees.
$h_{ep}$	End-plate height.
$h_1$	Fin-plate height.
$k_b$	Correction coefficient.
$l_e$	Equivalent rectangular opening length.
$p_x$	Distance between the tension rows.
$p_1$	Distance between the middle rows in the fin-plate.
$t_{ep}$	End-plate thickness.

$t_{s,e}$	Equivalent thickness of the slab.
$t_{w,b}$	Beam web thickness.
$t_1$	Fin-plate thickness.
$\gamma_{ov}$	Overstrength factor = 1.25
$\epsilon_y$	Yield strain.
$\epsilon_u$	Ultimate strain.
$\theta_m$	Maximum rotation.
$\theta_u$	Ultimate rotation.
$\theta_y$	Yield rotation.
$\xi_{eq}$	Equivalent viscous damping ratio.
$\mu$	Average.
$C$	The compression force in the cross-section.
$D$	Ductility ratio.
$P$	Lateral applied load.
$T$	The tension force in the cross-section.
$a$	The depth of the equivalent uniform stress field.
$e$	Edge distance.
$g$	The gap arising due to the difference between the real thickness of the steel deck and its equal-area idealisation.
$h$	Overall section height of the steel beam.
$q$	Behaviour factor.
$w$	End-plate gauge.
$\sigma$	Standard deviation.

## List of Abbreviations

<b>ACI</b>	American Concrete Institute.
<b>AISC</b>	American Institute of Steel Construction.
<b>ANSI</b>	American National Standards Institute.
<b>ATC</b>	Applied Technology Council.
<b>BEEP</b>	Bolted extended end-plate.
<b>BS</b>	British Standards.
<b>C3D8R</b>	8-node solid elements with reduced integration.
<b>CEN</b>	Comité Européen de Normalisation (European Standardisation Organisation).
<b>CUREe</b>	California Universities for Research in Earthquake Engineering.
<b>EEP</b>	Extended end-plate.
<b>EJs</b>	EQUALJOINTS and EQUALJOINTS-Plus projects
<b>EN</b>	European Norm.
<b>Exp</b>	Experimental test.
<b>FE</b>	Finite element.
<b>FEMA</b>	Federal Emergency Management Agency.
<b>HMS</b>	High moment side.
<b>IMK</b>	Ibarra–Medina–Krawinkler model.
<b>ISO</b>	International Organisation for Standardisation.
<b>LMS</b>	Low moment side.
<b>LVDT</b>	Linear variable differential transformer.
<b>MRF</b>	Moment-resisting frame.
<b>NZS</b>	Standards New Zealand.
<b>PN</b>	Pre-Northridge connection.
<b>PNA</b>	Plastic neutral axis.

<b>RBS</b>	Reduced beam section.
<b>RC</b>	Reinforced concrete.
<b>RG</b>	Rosettes.
<b>RT</b>	Angular displacement transducers.
<b>RWS</b>	Reduced web section.
<b>S4R</b>	4-node shell elements with reduced integration.
<b>SAC</b>	a joint venture of the SEAOC, the ATC, and CUREe.
<b>SCI</b>	The Steel Construction Institute.
<b>SEAOC</b>	Structural Engineers Association of California.
<b>SG</b>	Strain gauge.
<b>SN</b>	Serial number.
<b>T3D2</b>	2-node linear truss elements.
<b>TSA</b>	Tee-section approach.
<b>UB</b>	Universal Beam.
<b>UC</b>	Universal Column.
<b>VM</b>	Vierendeel mechanism.
<b>WUF-B</b>	Welded unreinforced flange bolted web connection.

## List of Publications

### Journal and conference papers based on this thesis:

- **Journal papers**

1. Almutairi, F.F., Tsavdaridis, K.D., Alonso Rodriguez, A., Asteris, P.G. and Lemonis, M.E., 2023. Hysteretic Behaviour of Composite Reduced Web Section (RWS) Connections for Seismic Applications. *Journal of Earthquake Engineering*, pp.1-36.  
DOI: <https://doi.org/10.1080/13632469.2023.2204172>
2. Almutairi, F.F., Tsavdaridis, K.D., Alonso-Rodriguez, A. and Hajirasouliha, I., 2023. Experimental investigation using demountable steel-concrete composite reduced web section (RWS) connections under cyclic loads. *Bulletin of Earthquake Engineering*, pp.1-30.  
DOI: <https://doi.org/10.1007/s10518-023-01802-y>
3. Almutairi, F.F. and Tsavdaridis, K.D., (2024) Cyclic response characteristics of composite reduced web section (RWS) connections. (under review).
4. Almutairi, F.F. and Tsavdaridis, K.D., (2024) Capacity design assessment of composite reduced web section (RWS) connections. (ready for submission).

- **Conference papers**

1. Almutairi, F.F. and Tsavdaridis, K.D. The effect of degree of composite action on reduced web section (RWS) connections. *The 9th European Conference on Steel and Composite Structures (EUROSTEEL 2021)*. 1-3 September, 2021, Sheffield, UK.  
DOI: <https://doi.org/10.1002/cepa.1369>
2. Almutairi, F.F. and Tsavdaridis, K.D. The effect of degree of composite action on RWS connections subject to cyclic loading. *The 10th International Conference on the Behaviour of Steel Structures in Seismic Areas (STESSA 2021)*. 25-27 May, 2022, Timisoara, Romania.  
DOI: [https://doi.org/10.1007/978-3-031-03811-2\\_24](https://doi.org/10.1007/978-3-031-03811-2_24)

3. Almutairi, F.F. and Tsavdaridis, K.D. Hysteretic performance of Reduced Web Section (RWS) connections with demountable slabs and effect of composite action. *Earthquake Engineering & Dynamics for A Sustainable Future (SECED2023)*. 14-15 September, 2023, Cambridge, UK.
4. Almutairi, F.F. and Tsavdaridis, K.D. FEA validation on the degree of composite action of composite reduced web section (RWS) connections under cyclic loading. *The 10th Hellenic National Conference of Steel Structures*. 19-21 October, 2023, Athens, Greece.

# Chapter 1

## Introduction

### 1.1 Research background and motivation

Recent efforts have been made to update European standards to develop seismic prequalification procedures for steel beam-to-column connections (EQUALJOINTS, 2017). Nonetheless, challenges persist regarding the presence of composite interaction over the protected zone. Current seismic design practices emphasise the importance of decoupling the slab from the beam in these zones and preventing structural continuity between the slab and the column (Sumner and Murray, 2002; CEN, 2005d; ANSI/AISC 341-16, 2016). Aiming to reduce uncertainties that could affect the capacity design hierarchy of beam-to-column connections. However, their application is challenging, especially in existing buildings where composite action is crucial for supporting gravity loads and preventing damage from sagging moments (see Figure 1.1). Furthermore, the composite slab acts as a diaphragm to distribute the seismic loads throughout the structure, contributing to the overall stability of the steel-concrete composite moment-resisting frames (MRFs).

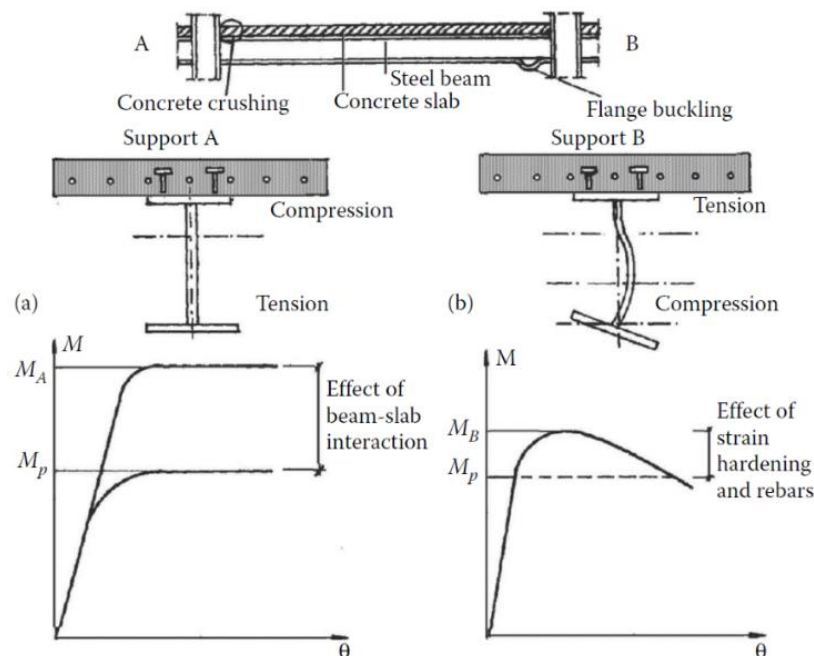


**Figure 1.1: Beam–slab interaction: (a) sagging moments; (b) hogging moments (Gioncu and Mazzolani, 2013).**

In seismic events, this mandatory composite interaction can lead to a soft story collapse mechanism (see Figure 1.2) despite adherence to capacity design principles (ANSI/AISC 341-16, 2016; Jisr, 2022). Moreover, the presence of composite action over the protected zone can cause an asymmetric yield moment mechanism (Figure 1.3), compromising the concept of strong column, strong connection and weak beam. Increased yielding moment capacity further places higher strength demands on elements outside the protected zone, causing a failure of welds and bolts in endplates and fracture at the beam bottom flange even in the well-known reduced beam section (RBS) connections (Chen and Chao, 2001; Sumner, 2003; Lee et al., 2016) As part of the strong connection-weak beam strategy, a Reduced Web Section (RWS) connection emerges as a promising solution in this context, acting as a ductile fuse and economically addressing the limitations of traditional connections.

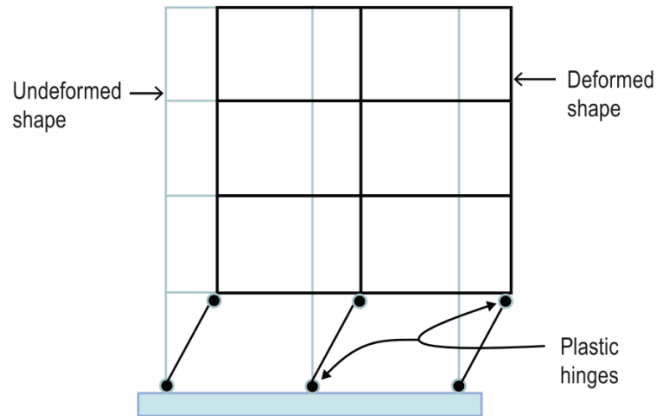


**Figure 1.2: Story Mechanism (Hamburger and Malley, 2009).**

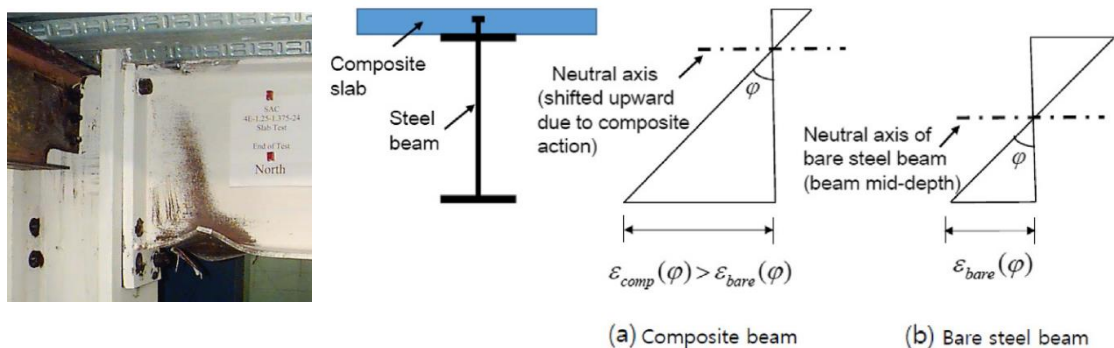


**Figure 1.3: Asymmetrical yield moment mechanism (Sumner, 2003; Lee et al., 2016).**



RWS connections have demonstrated acceptable behaviour under different types of loading with a most promising and straightforward choice that requires only one perforation within a beam web without removing the concrete slab (see Figure 1.4) (Yang et al., 2009; Tsavdaridis et al., 2014; Shin et al., 2017b; Shin et al., 2017a; Shaheen et al., 2018; Zhang et al., 2019; Erfani et al., 2020; Davarpanah et al., 2020a; Du et al., 2021; Tsavdaridis et al., 2021; Jia et al., 2021; Lin et al., 2021; Dong et al., 2021; Bi et al., 2021; Tabar et al., 2022). Thus, it could be an economic benefit in terms of both manufacture, usage, and seismic retrofit while limiting out-of-plane instability found in RBS connections and protecting non-ductile elements (Tsavdaridis et al., 2014). The concept of RWS connections as ductile fuses is derived from the development of a Vierendeel mechanism by localising the failure to the yielding and buckling of the Tee-sections within the web opening while keeping other members of MRFs in an elastic state. Optimising the size and location of the web opening is essential for triggering such a mechanism. The studies above have explored various ranges, with web opening sizes from 0.5 to 0.8 of the depth of the beam ( $h$ ) and locations from  $0.5h$  to  $1.74h$  from the column face. While there was no consensus on a single ideal configuration, a larger opening closer to the column face tends to induce the Vierendeel and strong-column weak-beam mechanisms.

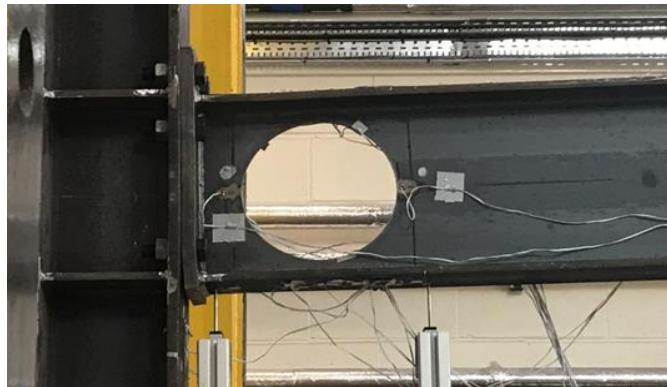


**Figure 1.4: RWS connection (Tsavdaridis et al., 2021).**

RWS connections act as two partial beams above and below the opening (i.e., top and bottom Tee-sections), as illustrated in Figure 1.5. The top Tee-section is the composite section, where the bottom one is the bare steel section. When the applied load goes upward at the high moment side (HMS), the web of the top Tee-section undergoes tension, while the flange-web of the top Tee-section exhibits compression at HMS (see Figures 1.6a and 1.7). Under the same conditions, the web of the bottom Tee-section will experience compression while

the flange-web and the bottom Tee-section will be under tension at the low moment side (LMS). Such behaviour can induce local yielding at the web of the top composite Tee-section and the flange-web of the bottom bare steel Tee-section. This early local yielding results in stretching the opening and local buckling of flanges. Both indicate the formation of the Vierendeel (ductile) mechanism, which becomes the dominant mechanism rather than simple shear failure at the web opening due to the redistribution of the global actions. Thus, the effect of the asymmetric yield mechanism is alleviated, and a seismic fuse is developed at a reduced section.

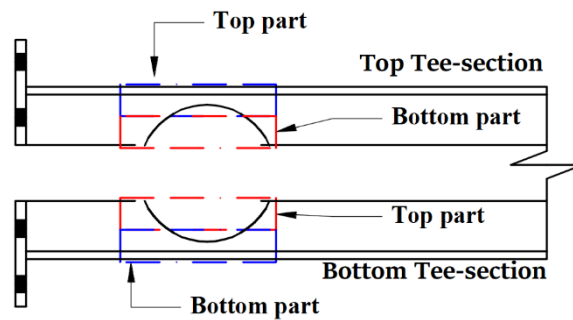
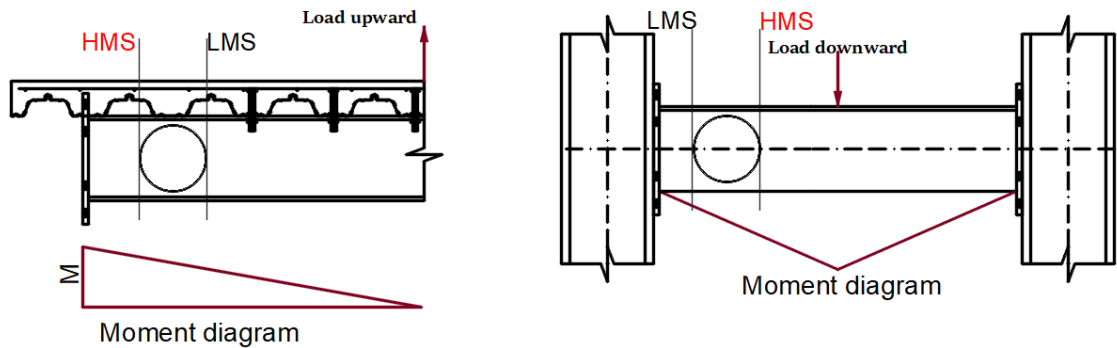


**Figure 1.5: Tee-sections of the perforated beam (two partial beams).**



**a) Cantilever configuration.**

**b) Frame configuration**

**Figure 1.6: High and low moment sides.**

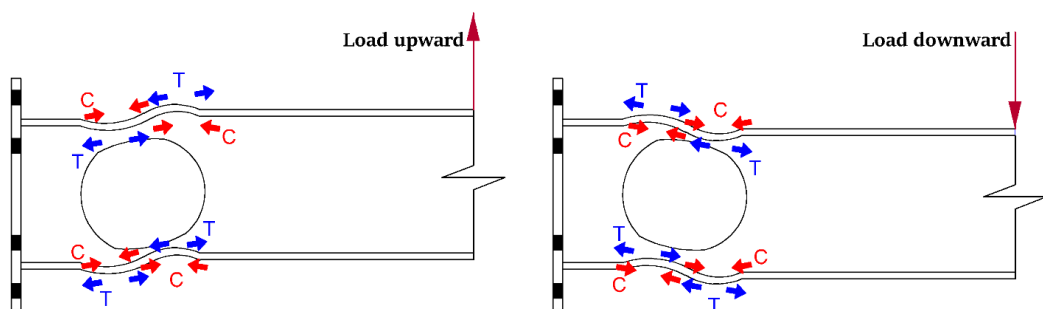


**Figure 1.7: Axial forces at opening.**

## 1.2 Problem statement and research objectives

The previous section suggests that the presence of composite interaction over the protected zone profoundly affects the overall steel MRF seismic stability due to the asymmetric yield effects. By focusing on the unique response mechanism of RWS connections, this thesis aims to advocate for utilising RWS connections as an alternative to traditional seismic fuses, often complex retrofitting strategies. The research employs a comprehensive study through the combination of experimental and numerical methods, along with the development of a database that combines empirical data from the literature and this research. This approach seeks to contribute significantly to seismic design practices by optimising RWS connections to control the extent of damage in composite steel-concrete connections. Given the above, the research objectives of this thesis are summarised as follows:

- Perform experimental tests to examine how composite action influences the cyclic behaviour of RWS connections, aiming to augment available data.
- Uncover the phenomena that govern the behaviour of composite RWS connections when subjected to cyclic actions by using adaptable but detailed finite element modelling (FEM).
- Conduct comprehensive parametric assessments to extend the observations on the experimental results.
- Compile test and FEA databases from this research and existing literature to assess the capacity design ratio effect and the applicability of SCI P355 guidance (Lawson and Hicks, 2011), thereby promoting the use of RWS connections in MRFs in seismic areas.

## 1.3 Methodology

### 1.3.1 Necessity of numerical investigations

Numerical investigations are integral to this research, serving multiple vital roles. Primarily, they provide essential preliminary insights that guide the experimental testing of RWS connections. These insights help to hypothesise and predict behaviours, which is crucial for planning practical physical experiments. Additionally, numerical analysis is invaluable for its efficiency and cost-effectiveness. It allows for the exploration and comparison of various parameters across different specimens, which would be impractical or prohibitively expensive to test physically. This aspect is particularly significant given the research's focus on a less-explored area - the interaction between RWS connections and overlying

slabs. Furthermore, a numerical investigation was employed to validate the experimental tests conducted in this research. This validation paves the way for further parametric studies exploring the influence of critical parameters governing the behaviour of RWS connections.

### **1.3.2 Experimental investigation**

Based on preliminary investigations, an experimental campaign was conducted to explore the cyclic response of composite RWS connections. This investigation fills a gap in existing research by providing empirical evidence on how the presence or absence of shear studs over the web opening, a novel aspect of this research, affects the seismic performance of these connections. The experimental results are not just a reinforcement of existing theories but a crucial step towards developing more resilient seismic designs in steel-concrete composite structures. This approach also offers practical insights for employing RWS connection designs in both new constructions and retrofitting projects, contributing to a deeper understanding in a field where such focused experimental data is currently limited.

### **1.3.3 Desk Study and Analytical work**

Over the past decade, there has been a strong push toward the development of robust guidance and numerical models and acceptance criteria for the design and promotion of the use of RWS connections in MRFs in areas predisposed to seismic events (Tsavdaridis and D'Mello, 2012; Tsavdaridis et al., 2014; Akrami and Erfani, 2015; Tsavdaridis et al., 2017; Erfani and Akrami, 2017; Erfani and Akrami, 2019; Erfani et al., 2020; Tsavdaridis et al., 2021). However, limited experimental tests on RWS connections are available to synthesise or evaluate the robustness of design guidelines and existing numerical models. Several researchers have presented different models to predict the responses of unstiffened and stiffened BEEP connections as well as RBS connections, as demonstrated by Ding and Elkady (2023). These can be categorised as analytical (e.g. the yield line method), mechanical (e.g., Eurocode 3 component method (CEN, 2005b)), or empirical (regression analysis for experimental and/or FE simulation data) (Ding and Elkady, 2023). Due to the complexity and lengthy procedures of analytical and mechanical models, empirical models are favourable among practising engineers and researchers (BCSA/SCI, 2013; D'Alessandro et al., 2018; Terracciano et al., 2018; Ding and Elkady, 2023). Thus, an empirical study was employed by developing a database on bare steel and steel-concrete composite RWS connections from the literature and this research. This database aids in verifying the assumptions and observations made during

the numerical and experimental investigations. Such a database is valuable for researchers and engineers as it allows them to refine the existing models and contribute to developing and validating design codes and standards.

## **1.4 Thesis outline**

The thesis consists of seven chapters briefly summarised in the following subsections and as illustrated in Figure 1.8:

### **Chapter 2: Literature Review**

Chapter 2 reviews the past and recent experimental and numerical investigations related to the research and the relevant design codes of practice.

### **Chapter 3: Preliminary Finite Element Analysis (FEA)**

This chapter showcases the development of numerical validated models that replicated the findings of an experimental investigation performed in beams without perforations (Chaudhari, 2017; Chaudhari et al., 2019). After its benchmarking, a numerical parametric investigation was presented to uncover the effects of interactions arising between slabs and overlaid RWS connections. Aiming to explore the untapped potential of utilising RWS-slab composite structural systems with European beam and column sections in seismic areas. The parameters included the presence and absence of composite interaction over the web opening, along with the size and location of the web opening.

### **Chapter 4: Experimental Investigation**

Chapter 4 introduces an experimental test of demountable steel-concrete composite bolted RWS connections. Aiming to verify the findings of the preliminary FEA in Chapter 3 in terms of i) the suitability of using such connections as seismic fuses for existing and new buildings and ii) the positive effect of the capacity design principle. Four composite connection specimens were subjected to sagging and hogging moments to investigate the response of RWS connections under reversible actions. A single circular opening with a diameter equal to 0.8 times the beam's depth was fabricated near the beam-column joint. Two different parameters were investigated, namely the effect of the web opening location and the presence or absence of bolted shear studs over the protected zone. The assessment of retrofitted connections was also examined by creating a web opening of the solid-webbed specimen after exposing it to cyclic actions representing moderate seismicity. This chapter presents an overview of experimental works, the design overview, test specimen details, material properties, test set-up, instrumentation and the interpretation of the test results, as well as the test observations and results.

## **Chapter 5: Parametric Assessments**

This chapter investigates the cyclic behaviour of demountable steel-concrete composite RWS connections. To enhance understanding, a high-fidelity finite element (FE) model was developed following experimental studies, focusing on parameters including the presence of composite action over the web opening, diameter, and the end-distance of the web opening. The study encompasses 285 FE models. The assessment of response characteristics of such connections follows the Ibaraa-Medina-Krawinkler (IMK) model, considering aspects such as stiffness, strength, ductility, and reinforced concrete slab contribution.

## **Chapter 6: Capacity Design Assessments**

The focus of this chapter is to compile experimental and numerical databases developed within this PhD research and existing literature for assessing the capacity design ratio on the response of the RWS connections. A gap in current design approaches demands explicitly introducing a capacity design approach when designing RWS connections. This chapter presents two main databases to identify similar trends.

The first database consists of the following:

1. The results of the parametric numerical investigation are presented in Chapter 5.
2. The benchmarked finite element (FE) models constructed and validated in Chapter 3 were utilised for further parametric investigation considering the New Zealand section profiles. The goal is to expand the database with a wider range of steel sections.

The second database was compiled and derived from experimental and numerical non-dimensionalised results in existing literature, along with results from Chapter 3.

## **Chapter 7: Conclusions**

A summary and set of conclusions drawn from the research study are presented in this chapter. Recommendations and suggestions for future work are also discussed.

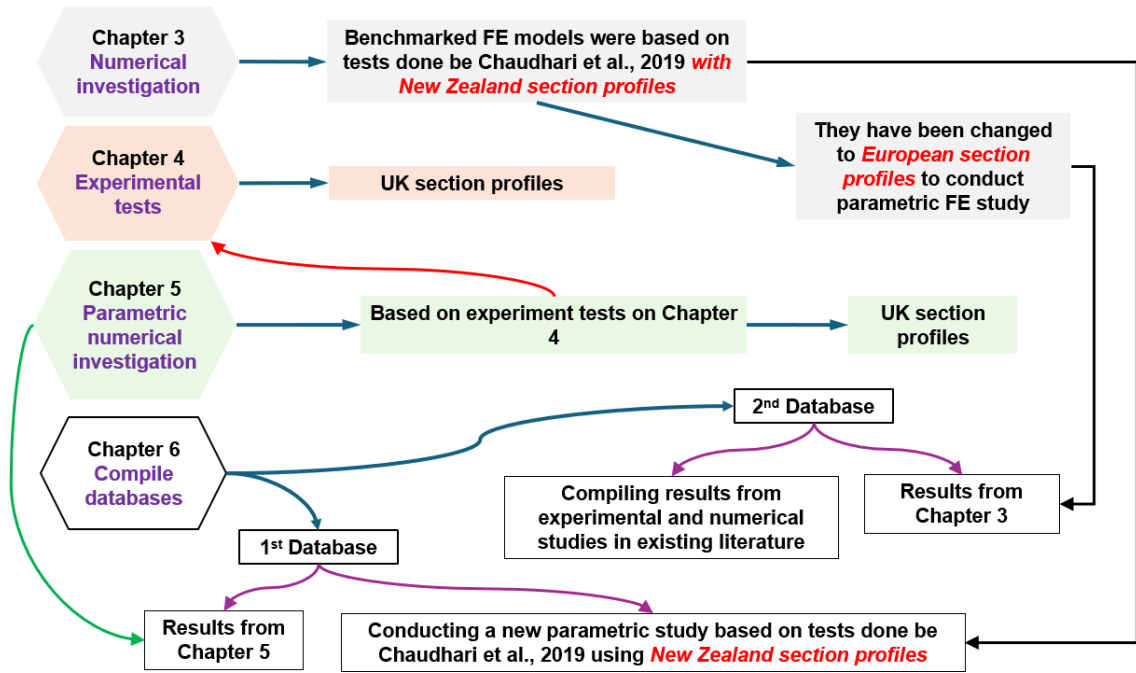


Figure 1.8: Flow diagram to illustrate the research methods.

## Chapter 2

### Literature Review

#### 2.1 Introduction

The literature review comprises five main sections: (1) structural behaviour of seismic moment connection; (2) review of prior research on seismic connections; (3) the relevant design codes of practice; (4) structural behaviours and failure modes of web opening regions; and (4) a review of reduced web section (RWS) connections. The main objective of this chapter is to identify gaps in the knowledge regarding the seismic performance of prequalified seismic-resistant and RWS connections and highlight the required research to address them.

#### 2.2 Structural behaviour of seismic moment connection

##### 2.2.1 Steel connection characterisation

A good balance between stiffness, strength, and ductility among members, as well as connections and supports of steel moment-resisting frames (MRFs), is critical when characterising a well-designed earthquake-resilient structure. Steel MRFs are highly dependent on the seismic behaviour of the beam-to-column connections. Consequently, any appropriate assessment of the MRFs' seismic performance necessitates a detailed understanding of beam-to-column connections' stiffness, strength and ductility properties. In this context, it is worth noting that, at the beam-to-column connection level, ductility is often referred to as rotational capacity.

Traditionally, steel MRF design connections are pinned or fully rigid to simplify the analysis and design processes. However, this leads to the inability to obtain a detailed understanding of the behaviour of the connection in terms of stiffness (Díaz et al., 2011; Liu et al., 2016). In practice, most connections transfer some moments and have some rotation. The term 'semi-rigid' is now frequently used to define the structural response of connections between these two extremes, as shown in Figure 2.1. According to Eurocode 3 Part 1-8, connections can be classified based on their initial rotational stiffness in relation to the elastic stiffness of the connected beam (see Figure 2.2). In unbraced frames (i.e., MRFs), a connection's stiffness is classified as semi-rigid if its initial stiffness ( $S_{j,ini,EC3}$ ) falls between  $0.5 E_b I_b / L_b$  and  $k_b E_b I_b / L_b$ . Where  $k_b$  is equal to 25 for MRFs;  $E_b$  represents the measured steel beam elastic modulus;  $I_b$  is the beam moment of inertia about the section's major axis; and  $L_b$  is the beam length between column centerlines.



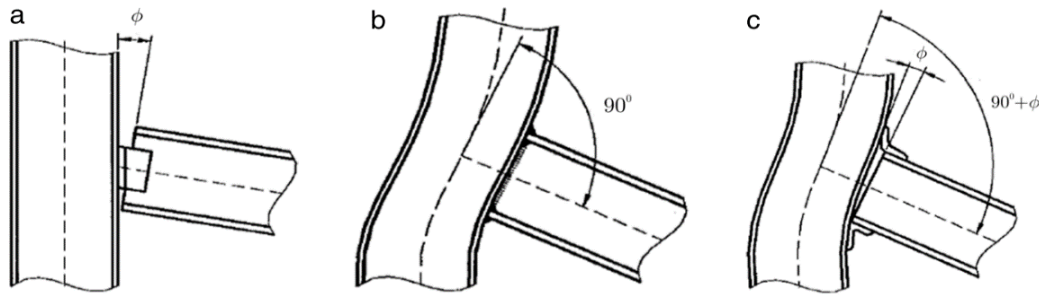


**Figure 2.1: Connection types according to their behaviour (a) pinned; (b) rigid; and (c) semi-rigid (Díaz, Martí, et al., 2011).**

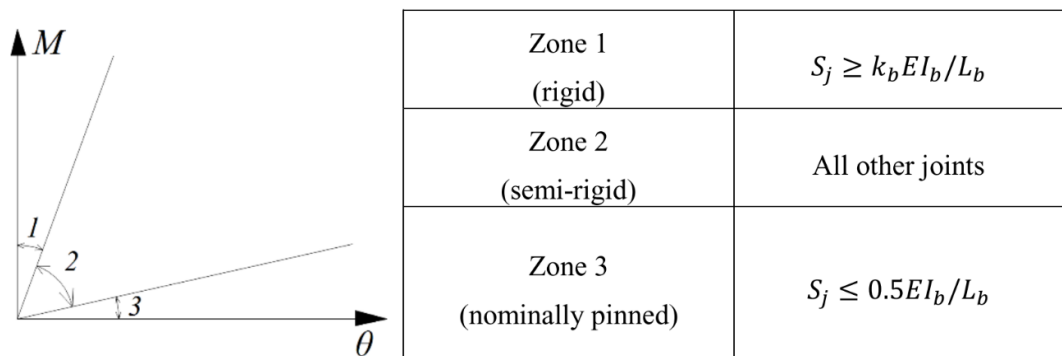


**Figure 2.2: Classification of steel connections by rotational stiffness according to Eurocode 3: Part 1-8 (CEN, 2005b).**

Regarding the strength classification, depending on the contribution of each joint component to the plastic failure mechanisms, a connection could be designed as full, equal (balanced), or partial-strength, with or without yielding of the web panel. A full-strength connection can transfer the full plastic moment of the connected beams without plastic deformations within it. In a partial-strength connection, plastic deformations occur in the connection before full plastification of the connected beam (Landolfo et al., 2010). An equal-strength falls into the category of partial-strength according to the current Eurocode 3: Part 1-8 (CEN, 2005b; D’Aniello et al., 2023). In the new generation of Eurocodes, equal-strength connections are balanced strength, where the plastic deformations in the connection (e.g., end-plate) and the beam are concurrent (D’Aniello et al., 2023).

The connection classification can also be based on ductility, a characteristic that significantly influences the seismic behaviour of the connection. In Eurocode 3: Part 1-8 (CEN, 2005b), ductility is not explicitly specified but instead defined from the geometric and mechanical properties of the connection components.

However, the approach of Eurocode 8 Part 1 (CEN, 2005d) involves ductility by giving the option to select different ductility levels for a structure by providing different ductility classes. This forms the basis for introducing ductility classes and applying behaviour factor  $q$ , as elaborated in clause 2.2.2(2). Selecting one ductility class over another directly impacts the design process. For example, a ductility class has direct consequences on the value of behaviour factor  $q$ , specific detailing and design requirements for all structural materials, and relevant types of structures as well (Landolfo et al., 2017).

### 2.2.2 Plastic mechanism under cyclic loading

The main concept of the component method coded in Eurocode 3: Part 1-8 (CEN, 2005b) is that the weakest component's behaviour governs the joint's overall behaviour. The joint components may be classified in terms of ductility, as shown in Figure 2.3. Since the main aim of seismic design is to eliminate the brittle fracture, a sufficient deformation capacity must be provided to endure the specified ground motion intensity with a low probability of collapse. Hence, a high degree of ductility is required in steel MRFs to ensure satisfactory seismic behaviour.

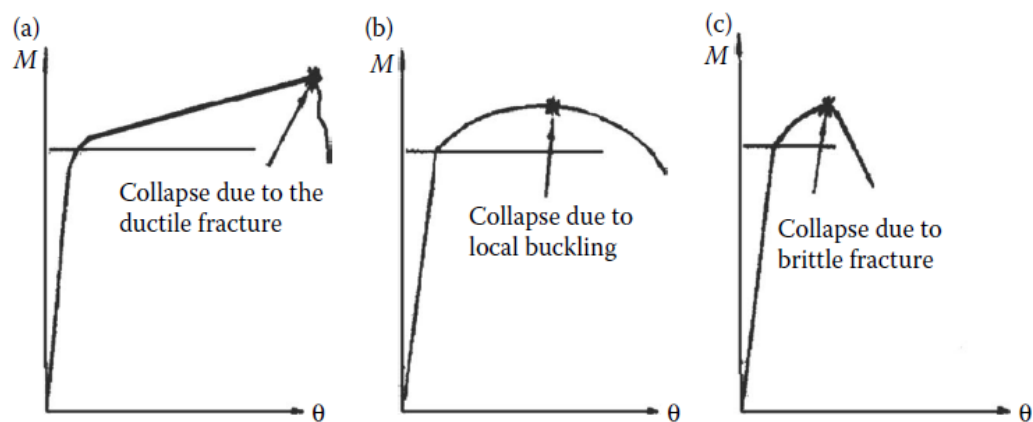


**Figure 2.3: Ductile and brittle collapse (Gioncu and Mazzolani, 2013).**

Although steel is a ductile material, that does not guarantee the ductile behaviour of the structure. This is attributed to the different plastic failure mechanisms manifesting in steel MRF systems. These mechanisms depend on the relative strengths of beams, connections (i.e. end-plates), and columns (including panel zones) framing into a joint. These components of a joint can dissipate hysteretic energy through cyclic plastic deformations, providing that fragile failure of bolts and welding is impeded (Tartaglia, D'Aniello, Rassati, et al., 2018; Mou et al., 2019; Landolfo, 2022; D'Aniello et al., 2023).

Steel MRFs derive their ductility through one or a combination of the following: plastic hinge formation in beams away from the beam-to-column connections, limited shear deformation in the panel zone or limited plastic deformation in the columns and their bases, as displayed in Figure 2.4a (Gioncu, 2000; FEMA 350, 2000). The plastic hinges are generally preferable to be formed in a beam at a distance from the column/connection face. This helps the columns and beam-to-column connections (i.e. the end-plate) to remain elastic before the formation of plastic hinges in the beams (FEMA 350, 2000) which is the strong-column-weak-beam concept. Adoption of this framework allows avoidance of the following undesirable behaviours (Hamburger and Malley, 2009), namely:

- i) storey mechanism (Figure 2.5), which leads to instability and the collapse of the whole structure; and,
- ii) high stress and strain demand on the connection, which leads to brittle damage.

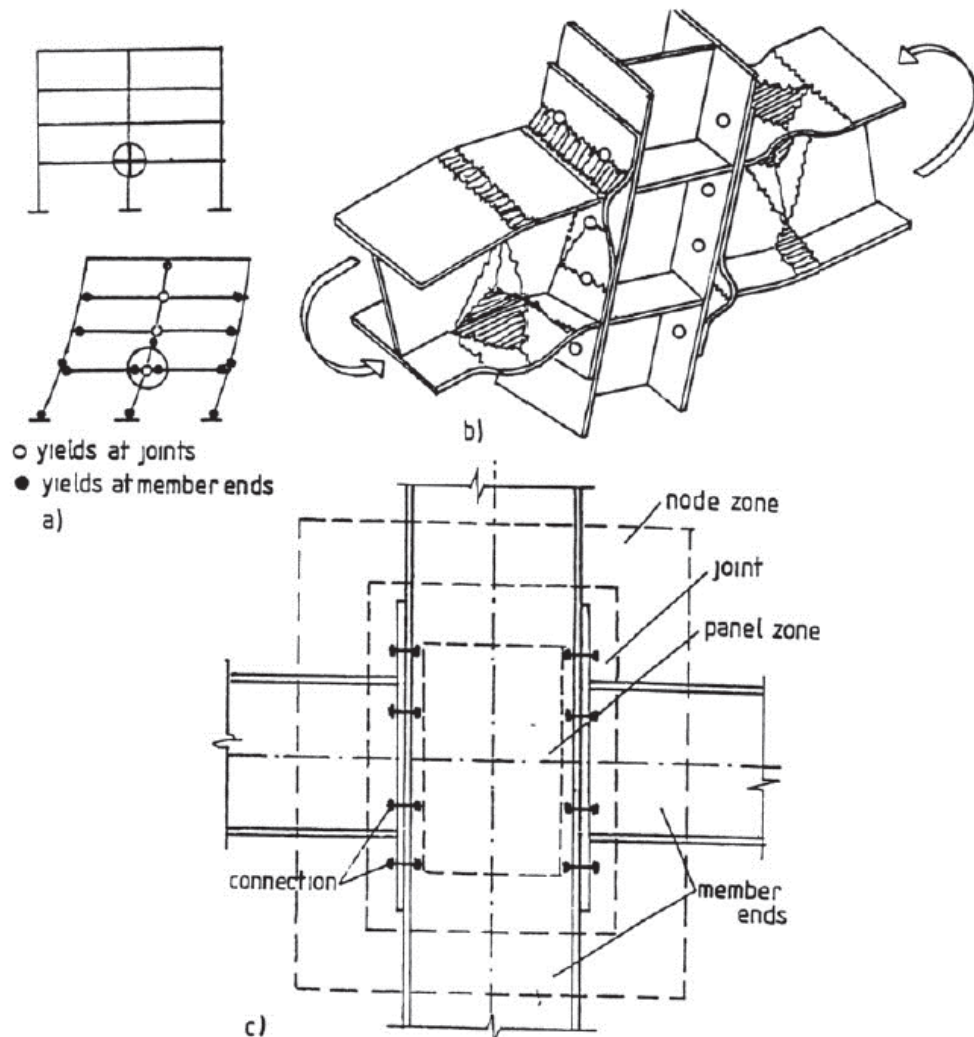


**Figure 2.4: Plastic collapse mechanism (Gioncu, 2000).**



**Figure 2.5: Soft-story collapse mechanism (Lignos et al., 2013).**

However, the beam-ends, where plastic deformations favourably form during an earthquake, are connected to the node zone, which consists of the joint components as shown in Figure 2.4c. Thus, the local plastic deformations in the MRFs could be localised not only at the member ends (i.e., beam and/or column end) but also at joints or both member ends and joints, as illustrated in Figure 2.4b (Gioncu, 2000). To this end, capacity design and ductility design employ a combination of i) components with high strength and ii) components with high plastic deformation capacity to optimise the response of the MRF. This approach involves linking a favourable failure mechanism to a responsible component to provide the needed hysteretic energy dissipation. Other elements with comparable strength are then protected to ensure elastic behaviour.

Under reversals of seismic loading, the sagging moment causes buckling of the beam's upper flange, while the hogging moment causes buckling of the beam's lower flange, as illustrated in Figure 2.6a. The buckled flanges will be straightened in subsequent cycles due to load reversal. This process will continue the same way until the applied actions cannot straighten the buckled beam flanges (Gioncu and Mazzolani, 2013). Consequently, the beam section will work with an introduced geometrical imperfection at the start of each cycle. Moreover, the accumulation of plastic deformations in the buckled flanges will make buckling and extensive deformation more likely (Gioncu and Mazzolani, 2013). Regardless of engaging strain-hardening in the steel, in Figure 2.6b, there is a net fallout in the strength and stiffness of the connected beam due to extensive local buckling.

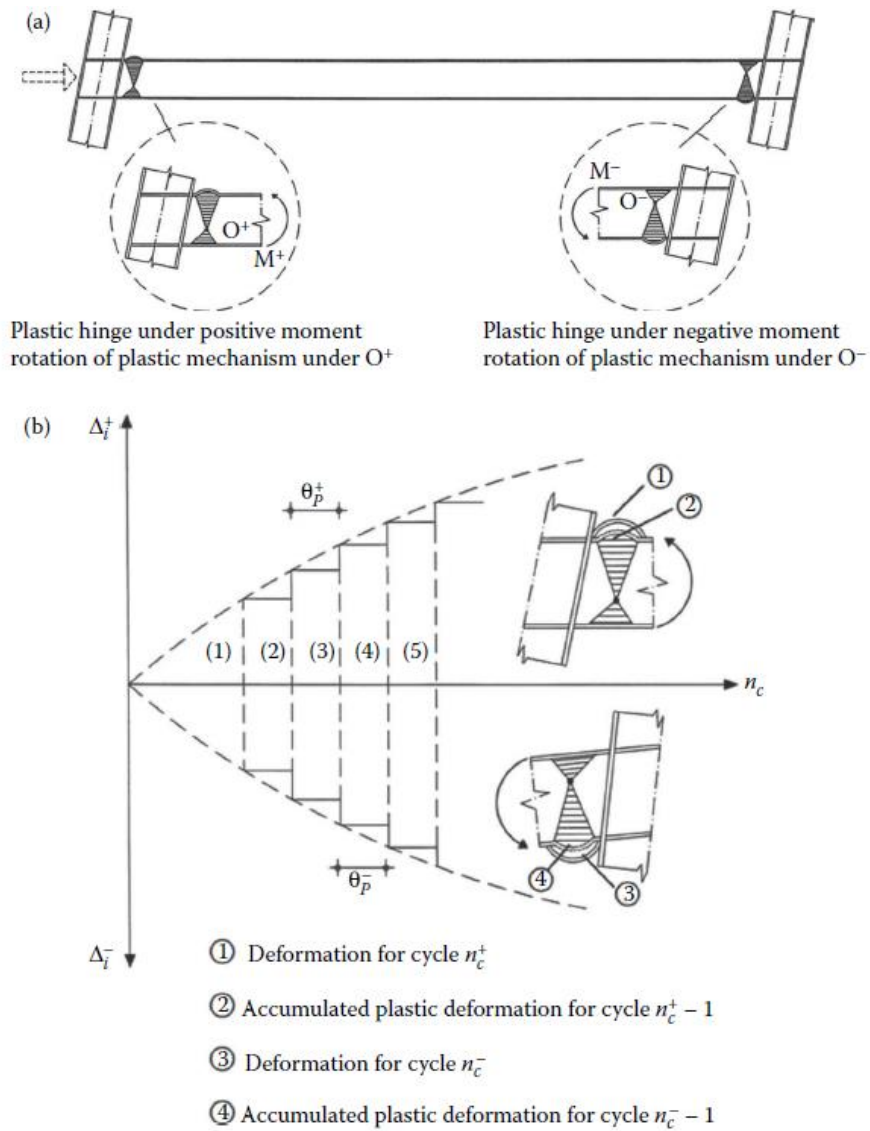


**Figure 2.6: Plastic mechanism at the beam (Gioncu and Mazzolani, 2013).**

Such behaviour is the strong-column-weak-beam concept, which is an application of the capacity design method wherein beam yielding is generally preferable to be the primary dissipative element in MRFs. It can be achieved by strengthening the connections or weakening the beam at specific locations away from the column face. Weakening the beam instead of strengthening the connections has proved to be the more cost-effective solution. The strong column-weak beam concept can be achieved by using different types of seismic connections, as shown in Figure 2.7. Amongst these are extended end-plate connections and the well-known reduced beam section (RBS) connections, which have proven their ability to enhance the seismic performance of connections while enabling the formation of plastic hinges within the beam.



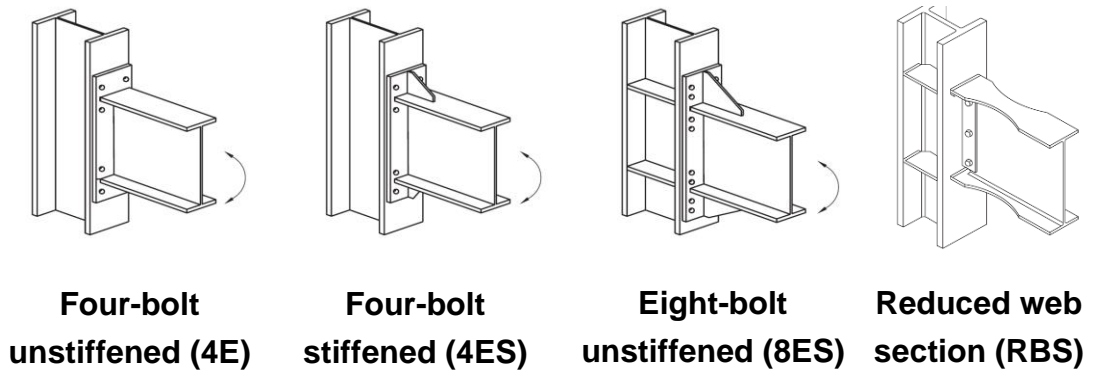


**Figure 2.7: Prequalified seismic connections (ANSI/AISC 358-16, 2016).**

Such connections were a part of the prequalification campaign after the 1994 Northridge and 1995 Kobe earthquakes. This prequalification campaign was carried out due to the challenge of the perception that the structural damage of the steel-concrete composite MRFs would be confined to protected zones, which are locations where yielding is encouraged, leading to the development of structural fuses. The damage arose in the form of brittle fractures of traditional beam-to-column, welded flange-bolted web connections in buildings with a number of floors ranging from one to twenty-six. Even this phenomenon was observed in areas that experienced only moderate ground shaking (see Figure 2.8) (FEMA 350, 2000; FEMA 355E, 2000).



**a) Fracture at fused zone.**



**b) Column flange fracture.**



**c) Fractures through column flange.**



**d) Fracture progresses into column web.**

**Figure 2.8: Fractures of Beam-to-Column Connections (FEMA 350, 2000; FEMA 355E, 2000).**

These brittle fractures in steel-concrete composite MRFs were generally due to the excessive strain demands on the bottom flange as a result of the composite slab, which might be several times larger than one fabricated with bare steel, causing a higher potential of such failure (Uang et al., 2000; Kim et al., 2004). Therefore, proper assessments should be made to avoid fragile behaviour, like the strong-beam-weak-column mechanism. This could be a dominant mechanism if the contribution of the composite slab is neglected in the design process (Roeder, 2002). Although no steel MRFs collapsed during the Northridge earthquake, expensive repair costs and time-consuming processes were incurred to fix the brittle fractures of beam-to-column connections (Bruneau et al., 2011). Consequently, a great deal of research has been undertaken to understand and enhance the seismic performance and design of steel-concrete composite MRFs since these disruptive events.

SAC Joint Venture conducted a campaign with the participation of the American Institute of Steel Construction (AISC) and other industry groups funded by the Federal Emergency Management Agency (FEMA) (ANSI/AISC 358-16, 2016). Consequently, this campaign led to improved AISC seismic provisions and the development of new seismic design criteria for beam-to-column connections that favour prequalification. Prequalification involves testing in real-scale prototypes to identify their failure mechanisms and assess their capacity to accommodate inter-story drifts without compromising the capacity to endure vertical structural demands. Now, this framework is being adopted in Europe, leading to the EQUALJOINTS and EQUALJOINTS-Plus projects. They aim to seismically prequalify a set of steel beam-to-column joints with different connections, including bolted unstiffened and stiffened extended end-plate connections (EQUALJOINTS, 2017).

### **2.2.3 Research studies on prequalified seismic connections**

Two seismic connections are mainly reviewed herein:- extended end-plate connections and steel-concrete composite RBS connections. Extended end-plate connections have been reviewed, as such connection types have been used with RWS in this thesis due to the popularity of extended end-plate connections as moment connections in Europe and seismic and wind active zones. The review of steel-concrete composite RBS connections arises because of the similarity between RWS and RBS connections in terms of the strong-column weak-beam concept (i.e., a seismic fuse). Also, other types of seismic moment connections have been reviewed to understand the impacts of the composite interactions over the plastic zone.

Generally, there are three configurations of extended end-plate moment connections in ANSI/AISC 358-16 (2016), as shown in Figure 2.7. They are shop-welded to the beam and then bolted to the column flange in situ. Several failure modes control the behaviour of this connection type, including flexural yielding of the beam section, flexural yielding of the end-plates, yielding of the column flange, tension and shear rupture of the end-plate bolts as displayed in Figure 2.9 (ANSI/AISC 358-16, 2016). Since the rotational capacity is a key factor in the ductility of structures in seismic areas, the rotational capacity of such connections is mainly controlled by the flexural yielding extended end-plate and the column flange and by elongation of the bolts (D’Aniello et al., 2017).

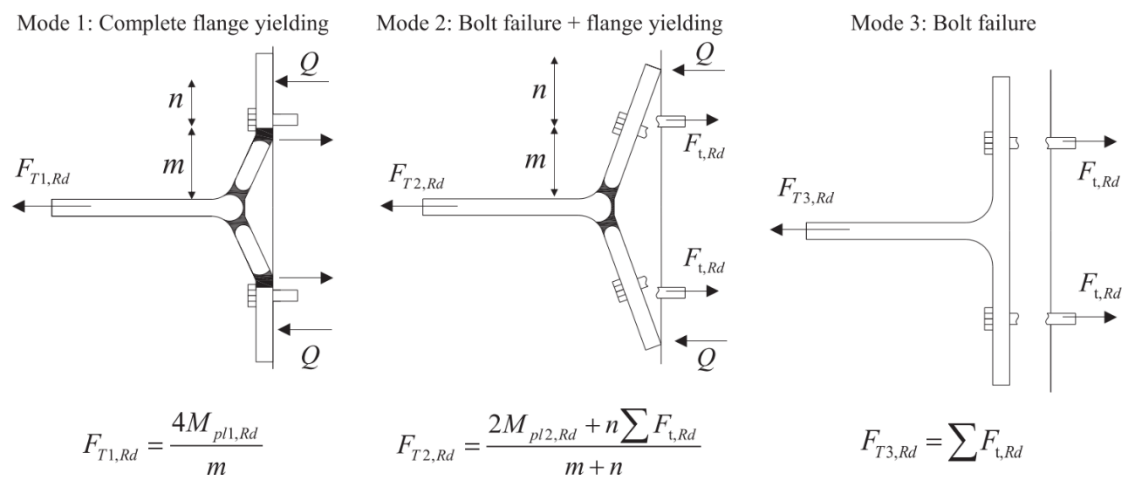


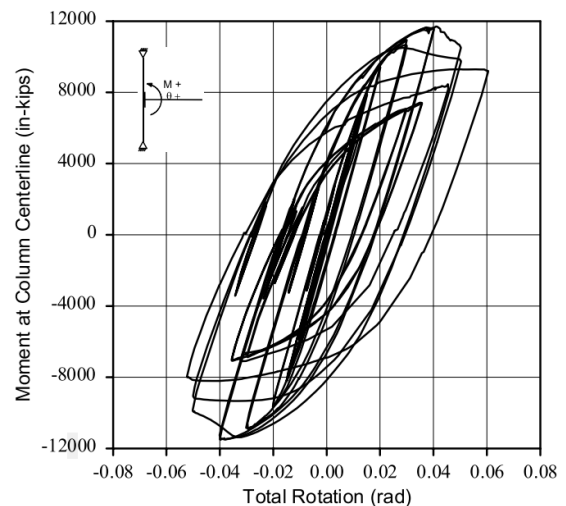
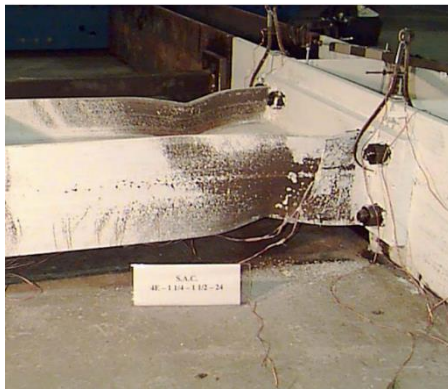
**Figure 2.9: T-stub failure modes.**

Many researchers have conducted experimental and finite element (FE) studies to investigate the behaviour of stiffened and unstiffened extended end-plate connections under monotonic and cyclic loads (Ghobarah et al., 1990; Korol et al., 1990; Bernuzzi et al., 1996; Guo et al., 2006; Augusto et al., 2017; Tartaglia, D’Aniello and Landolfo, 2018; ElSabbagh et al., 2019). All have concluded that unstiffened extended end-plate connections can exhibit satisfactory seismic performance if they are properly designed and detailed. They have found that the ductility can be enhanced by using stiffened extended end-plate connections.

Sumner et al. (2000) conducted a series of tests on the four-bolt extended unstiffened and the eight-bolt extended stiffened moment end-plate connections as a part of the SAC Steel Project. One test was an interior steel-concrete composite extended end-plate connection consisting of two main beams connected to a single column in a cruciform. Their results show that the extended end-plate connections exhibited good performance under cyclic loading in terms

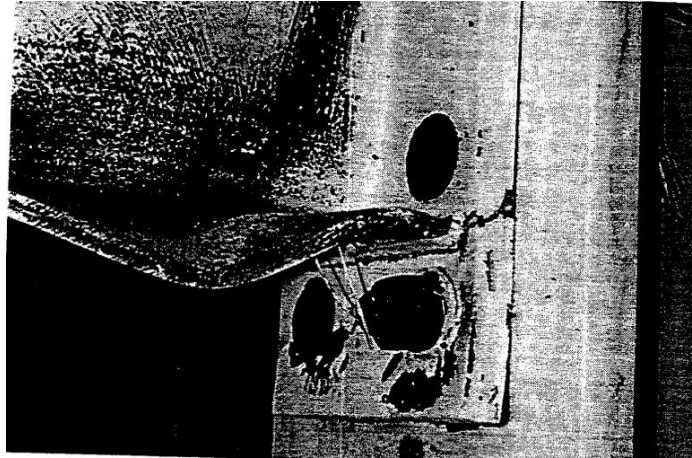


of ductility, rotation capacity and energy dissipation (see Figure 2.10). In the composite test, despite the concrete slab having positive effects in terms of providing lateral stability to the connected beam, the response was not as expected, as local buckling of the beam bottom flanges occurred. As the loading cycles continued, the composite slab maintained its contribution to the overall strength of the connection. As a result, the bottom bolts of the connection failed in tension without yielding or separation of the end-plate before failure as shown in Figure 2.11. They recommended that the composite action should be low by not placing the shear studs from the column face to 1.5 times the depth of the connected beam to reduce the cracking and crushing of the concrete slab around the column. Slab reinforcement should also be reduced in the area from the column face to twice the depth of the connecting beam. In addition, 13mm of compressible expansion joint material should be installed between the slab and the column face.



a) Moment vs. Total Rotation

**Figure 2.10: Four bolt extended unstiffened connection after testing (4E-1.25-1.5-24) (Sumner, 2003).**



(a) Connection Region



(b) View of Composite Slab Around Column

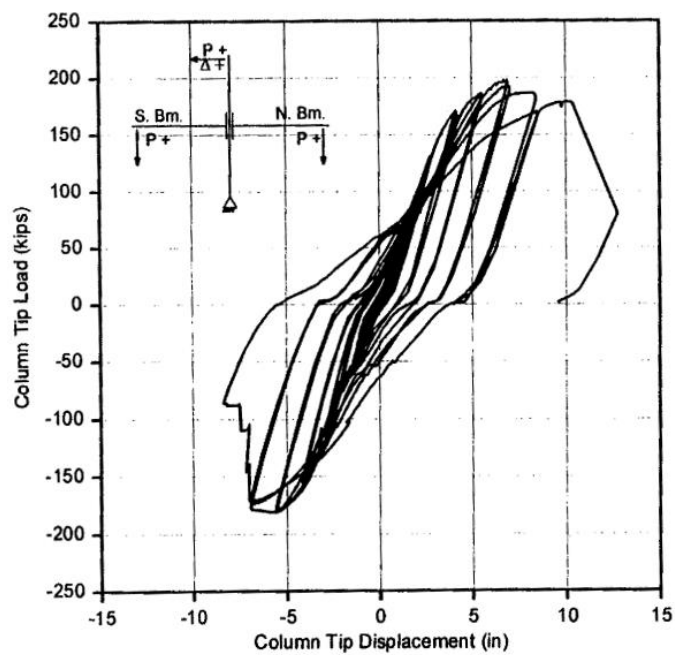


**Figure 2.11: Composite slab test specimen after testing and its load-displacement curve (Sumner et al., 2000a).**

Similar to the SAC Steel Project, an extensive research campaign of EQUALJOINTS and EQUALJOINTS-Plus, aimed to develop seismic prequalification procedures for seismic steel moment connections, currently missing in Eurocode 8 Part 1 (CEN, 2005d), was carried out in Europe (EQUALJOINTS, 2017). A set of steel beam-to-column joints that are most used in European practice, with different connection types, were included in these campaigns. These include unstiffened, haunch- and rib-stiffened bolted extended end-plate joints as well as welded RBS. Design procedures for end-plate moment connections were developed, experiment tests were conducted, and FE studies were employed to evaluate aspects of the design procedures. The findings confirmed the consistency of these joints' behaviour with the adopted capacity design criteria in terms of the locations of the expected plastic mechanisms in the joint (Figure 2.12). Moreover, the behaviour of the joints complies with both qualification criteria in North America (ANSI/AISC 358-16, 2016; ANSI/AISC 341-16, 2016) and European Eurocode 8 Part 1 (CEN, 2005d).

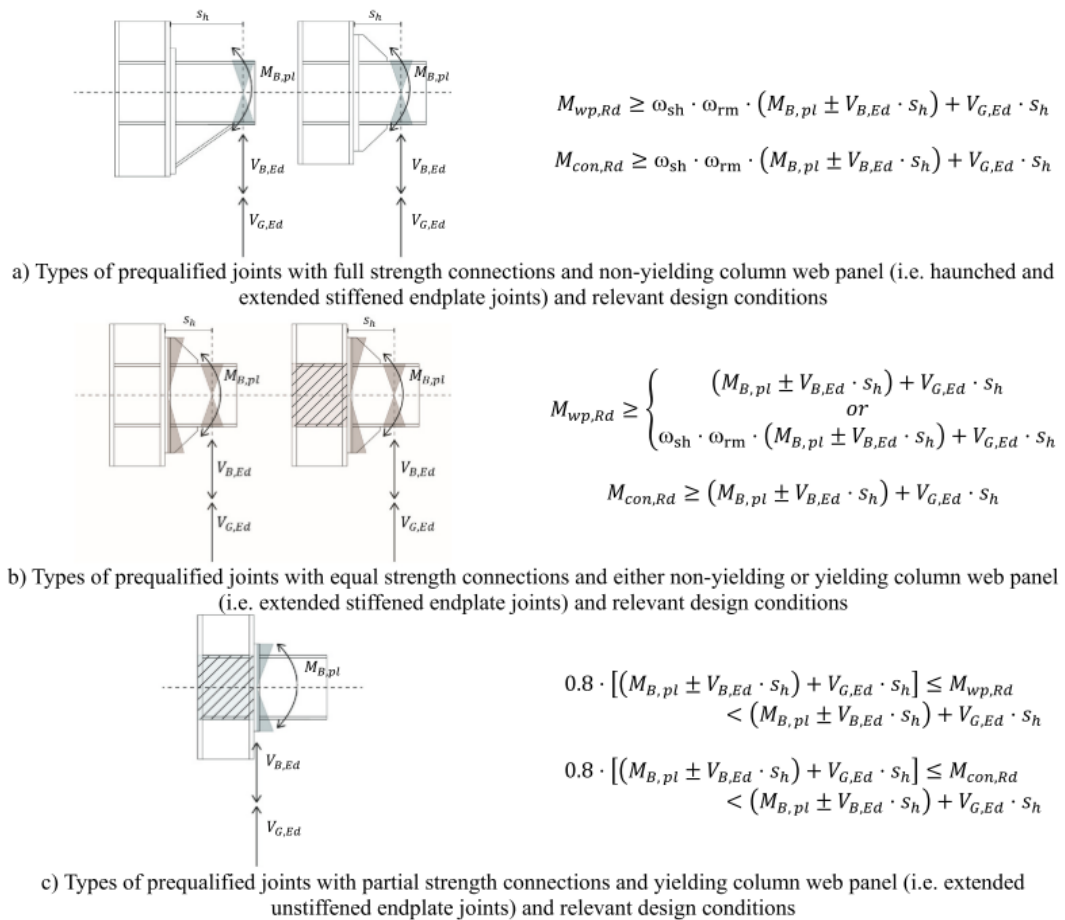


**Figure 2.12: Yielding regions with grey highlights and capacity design requirements for the prequalified joints (Landolfo, 2022).**

There have been concerns about the detrimental impact of the presence of steel-concrete composite interactions over the plastic zone with seismic moment connections (Figures 2.13 and 2.14) (Chen and Chao, 2001; Kim and Lee, 2017). These were attributed to the resulting composite action in jeopardising the concept of the strong-column-weak-beam concept. Despite its significant benefits in enhancing the beam's strength and stiffness under sagging moments, it increases the strain demand in the beam bottom flange near the connection face where the plastic hinges are formed. Also, it could lead to the strengthening rather than weakening of the beam if the slab contribution is not properly accounted for. Previous studies examined the conventional welded steel moment connections and RBS connections with high composite action degrees (Chen and Chao, 2001; Lee et al., 2016; Kim and Lee, 2017; Shaheen et al., 2018). They concluded that the concrete slab and resulting composite action kept contributing to the connections' capacity even when the reinforced concrete slab was cracked and crushed. That could lead to the strengthening rather than weakening of the beam and the early brittle rupture of the beam's bottom flange due to the unforeseen asymmetric behaviour (Chen and Chao, 2001; Lee et al., 2016; Landolfo et al., 2017; Shin et al., 2017a; Shaheen et al., 2018). These findings are consistent with the findings of Sumner et al. (2000), who conducted a test on an interior steel-concrete composite bolted extended end-plate connection as part of the SAC Steel Project. Despite the positive effect of the concrete slab in providing lateral stability to the connecting beam, the bolt rupture and bottom flange buckling were apparent. As stated before, they recommended that the composite action should be low by not placing the shear studs in the zone of the beam's plastic hinges and a gap between the concrete slab and column should be provided. Thus, understanding the composite action effect on the seismic performance of the connections is very important for the erection of new buildings and the retrofit of existing buildings.



**Figure 2.13: Typical plastic zone of the composite RBS specimen tested (Chen and Chao, 2001).**

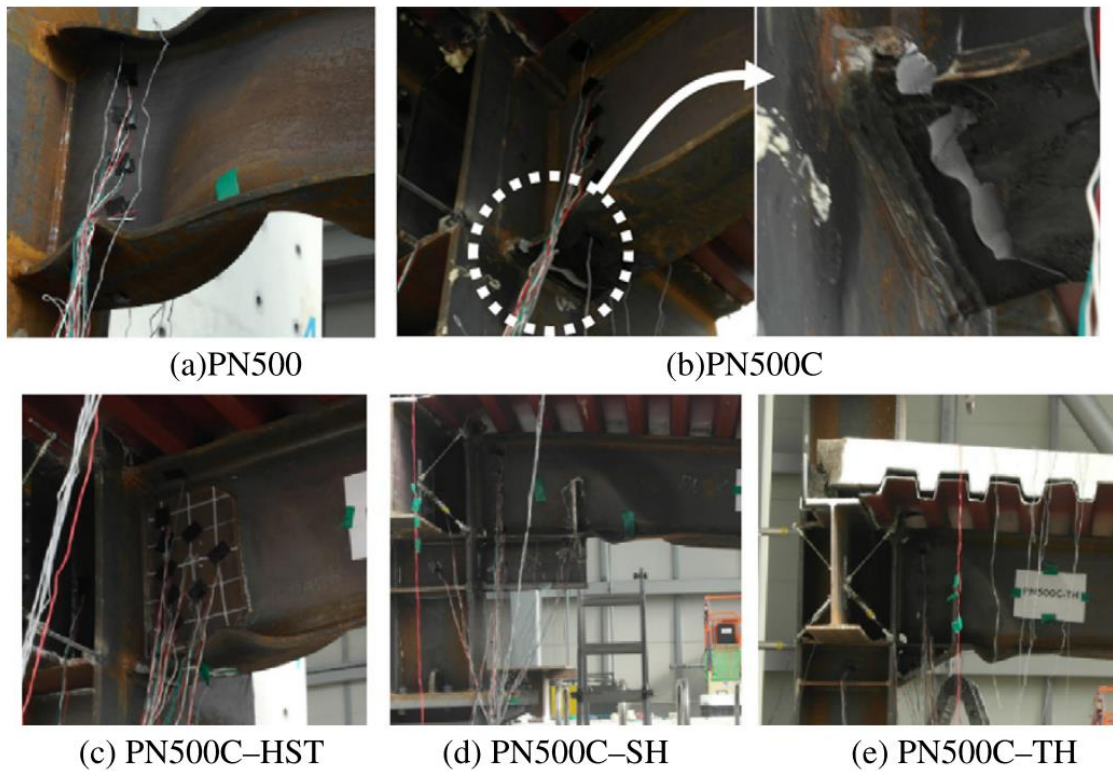


**Figure 2.14: Plastic hinge region after completion of testing (Kim and Lee, 2017).**

Sumner and his collaborators (Sumner et al., 2000b; Sumner et al., 2000a) studied ways to prevent the undesired coupled beam-slab action near connections, finding that the best solution is decoupling their joint action in that place while preserving its midspan. This can be accomplished by suppressing beam shear studs in the protected zone while allowing for a gap between the column and the slab. Laboratory testing has since validated Sumner's approach (Sumner et al., 2000b; Sumner et al., 2000a; Civjan et al., 2000; Civjan et al., 2001; Jones et al., 2002; Zhang and Ricles, 2006a; Zhang and Ricles, 2006b; Lee et al., 2016) and found that damage to the beam is reduced, while structural demands outside the protected zone are mitigated, even leading to a significant reduction of slab cracking (Lee et al., 2016) (Figure 2.15).





**Figure 2.15: Composite RBS connection, before, during and after the test (Lee et al., 2016)**

The behaviour of bolted extended end-plate connections under cyclic loading is complex due to non-linear interactions among connection components through surface contacts and the effect of bolt preload. There are numerous FE studies of seismic and non-seismic bolted extended end-plate connections with and without steel-concrete composite beams in which the researchers considered simplification of the shape of the bolts as rectangular or hexagonal instead of circular (Díaz, Victoria, et al., 2011; Mashaly et al., 2011; Lim et al., 2012; ElSabbagh et al., 2019). Others considered the reduction of the bolt diameter to capture the behaviour of the bolt under monotonic and cyclic loadings (Díaz et al., 2011; Morrison et al., 2017). Further simplifications have been made, including suppressing the contact interaction between the head and nut of the bolt with the plates and tying them to simplify their interactions (Lam and Fu, 2005; Gil et al., 2013; Tsavdaridis and Papadopoulos, 2016; Elflah et al., 2019; Nazaralizadeh et al., 2020). Other techniques used a combination of shell and

solid elements to model the bolted steel beam-to-column joint (Sofias et al., 2014) and model each component of the bolted extended end-plate connections in detail, including the components' contact interactions using contact pairs and bolt preload (Gerami et al., 2011; Sofias et al., 2014; Morrison et al., 2017; EISabbagh et al., 2019). Some of these studies applied symmetry conditions and used different material non-linearities (Figure 2.16).

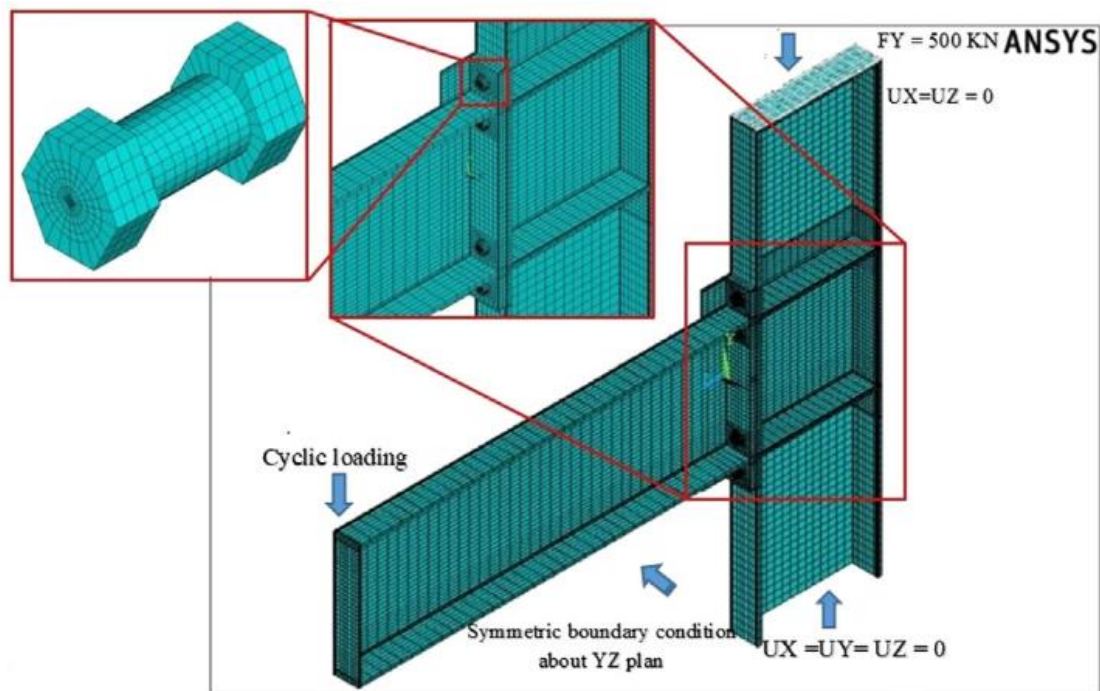


**Figure 2.16: Symmetric boundary conditions (EISabbagh et al., 2019).**

Also, there are some cases of steel-concrete composite bolted extended end-plate connections where bolts and plates are considered to deform monolithically (Lam and Fu, 2005; Vasdravellis et al., 2009; Wang, 2010; Gil et al., 2013). Their FE results showed a good agreement with experimental tests. The ones that simulate steel-concrete composite bolted extended end-plate connections under cyclic loading (Chaudhari, 2017; Wang et al., 2018). Wang et al. (Wang et al., 2018) presented experimental and FE investigations of extended end-plate connections with concrete-filled steel tubular columns under push-release loading, as shown in Figure 2.17. In Chaudhari (2017), the end-plate and bolts were not modelled for the FE validation of all tested specimens. Nevertheless, both of these studies demonstrated a good agreement between FE results and corresponding experimental tests.

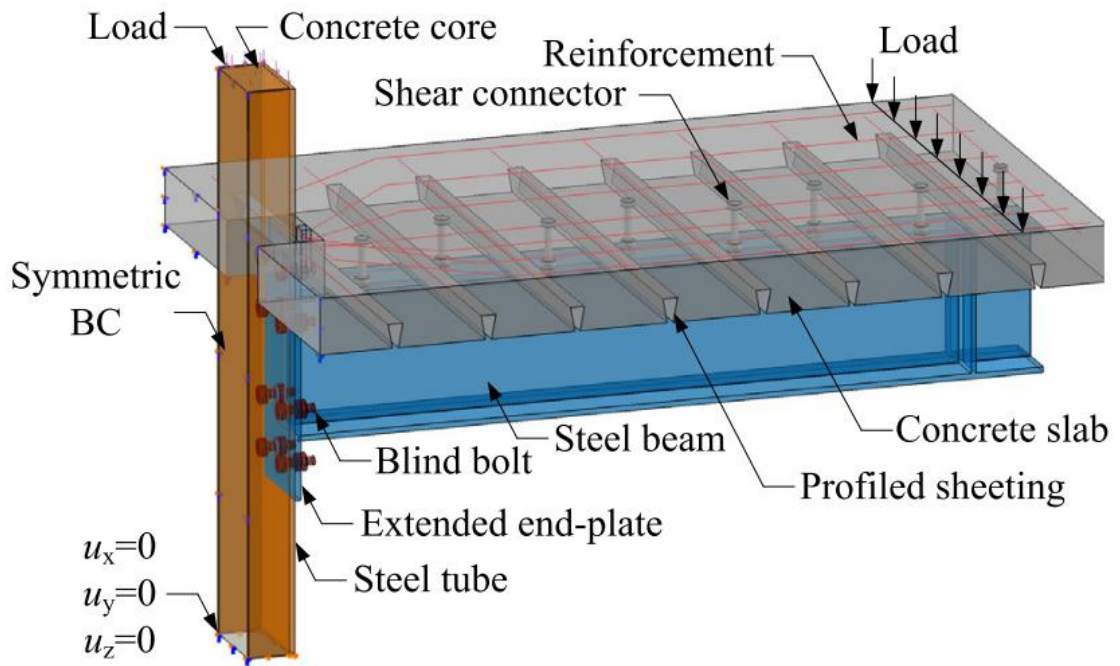


**Figure 2.17: Layout of finite element model (Wang et al., 2018).**

## 2.3 Design criteria

This section presents the main requirements of the relevant design codes of practice. It begins with the main design criteria for steel-concrete composite seismic connections in Eurocode 8. Unlike US codes, Eurocode 8 is not a normative standard design rule that specifies design, detailing, fabrication and quality criteria to achieve the required seismic performance for beam-to-column joints. Thus, prequalified connections requirements from ANSI/AISC 358-16 (2016) and FEMA 350 (2000) are used in the absence of direct design guidance of connections in EC-8 (Landolfo et al., 2010).

### 2.3.1 Eurocode 8

Eurocode 8-1 requires that MRFs be designed such that the formation of plastic hinges resides mainly within beams rather than in columns and connections. To avoid unfavourable performance – for instance, the soft story mechanism and ensuring the development of the strong-column weak-beam mechanism – columns should remain elastic, except at their ends, while plastic failure mode should occur in the beams. Hence, the overall ductile behaviour should be guaranteed by meeting the following criterion of clause 4.4.2.3(4):



$$\frac{\Sigma M_{Rc}}{\Sigma M_{Rb}} \geq 1.3$$

where:

$\Sigma M_{Rc}$  is the sum of design values of the flexural strengths of the columns connected to the joint.

$\Sigma M_{Rb}$  is the sum of design values of the flexural strengths of the beams connected to the joint.

### 2.3.1.1 Connections

In MRFs with beams acting as dissipative elements, connections should be designed at full-strength and with a rotation capacity of at least 35mrad (Eurocode 8-1- 6.6.4(3)). General design rules of non-dissipative connections of dissipative elements are provided in Eurocode 8-1- clause 6.5.5. These rules ensure sufficient connection overstrength to prevent high local plastic strain within a non-dissipative connection. This can be satisfied by applying the following equation (Eurocode 8-1- 6.5.5(3)):

$$R_d \geq 1.1 \cdot \gamma_{ov} \cdot R_{fy}$$

Where:

$R_d$  is the design resistance of non-dissipative welded or bolted connections.

$R_{fy}$  is the plastic resistance of the connected member.

$\gamma_{ov}$  is the overstrength factor = 1.25.

Following Eurocode 8-1/clause 6.2(9), high-strength bolts of grade 8.8 or 10.9 should be used in bolted connections of primary seismic members.

### 2.3.1.2 Composite beams

Despite the benefits of the presence of a floor slab diaphragm, such as axial forces being negligible in beams and enhancing the stiffness against gravity and seismic actions, composite action between the slab and steel beam can impair the strong-column weak-beam concept when not properly accounted for. Eurocode 8-1 clauses 7.7.5(1)P and 7.7.5(2) state that no shear studs should be placed over the plastic hinges area and provide a gap between slab and column faces on all sides of the column to avoid overestimating the capacity of the structure.

### 2.3.2 American codes

Seismic provision (ANSI/AISC 341-16, 2016), prequalified connections (ANSI/AISC 358-16, 2016) and FEMA 350 (FEMA 350, 2000) were developed by the research group SAC Joint Venture to present new seismic design criteria for beam-to-column connections. One of the main criteria in the latter two standards is the beam span-to-depth ratio. This is due to its significant effect on the inelastic behaviour of beam-to-column connections; the increase in member size leads to an increase in strain on the connections, which means the connections become prone to brittle behaviour (FEMA 350, 2000). Both these standards require that the clear span-to-depth ratio of the beam for special steel moment frames should be equal to 7 or greater.

ANSI/AISC 341-16 (2016) adopts a strong-column weak-beam mechanism that requires the sum of the design values of the flexural strengths of the columns to be higher than that of the beam at each joint. The design procedure of extended end-plate connections in ANSI/AISC 358-16 (2016) also aims to design such connections to have sufficient strength to ensure the formation of plastic hinges within the connected beam. The intent of the design procedure of RBS connections in ANSI/AISC 358-16 (2016) and FEMA 350 (2000) is to act as a seismic fuse and weaken the beam at a specific location. Both these connections satisfy the requirement of strong-column weak-beam in seismic provision ANSI/AISC 341-16 (2016). A rotation capacity of a minimum of 0.04 rad is recommended for seismic design with no more than 20% strength degradation of the connection (ANSI/AISC 341-16, 2016).

More detailed recommendations regarding the acceptance criteria for allowable and permitted rotations of various connection types based on three primary performance levels are provided by ASCE/SEI 41-17 (ASCE, 2017). These performance levels are Immediate Occupancy (IO), Life Safety (LS) and Collapse Prevention (CP), which categorise the connection's ability to withstand earthquake forces. Connections are generally classified into two main types based on their strength and stiffness: fully and partially restrained. RWS connections can be defined as fully restrained connections; they are not explicitly mentioned in ASCE/SEI 41-17 (ASCE, 2017). Table 2.1 presents the acceptance criteria for the two aforementioned seismic connection types – Reduced Beam Section (RBS) and extended end-plate connections.

Table 2.1: Acceptance criteria from ASCE/SEI 41-17

Connection	Acceptance criteria		
	IO	LS	CP
RBS	0.025–0.00015d	0.0525-0.00023d	0.07-0.0003d
Extended end-pale (yield of end plate)	0.010	0.035	0.035

Note: d is the beam depth

## 2.4 Structural behaviour and failure modes of perforated beams

This section outlines the behaviour and failure modes of steel-concrete composite and non-composite (bare steel) perforated beams. The similarity in the behaviour to RWS connections is the reason for the review. For instance, one of the most critical failure modes considered in the design of RWS connections and perforated beams is the Vierendeel mechanism (VM) (see Figure 2.18). For this reason, understanding the behaviour and influence of the web opening in composite and non-composite beams is essential for a better understanding RWS connections. Different shapes and numbers of web openings are presented, with particular emphasis on single circular web openings.

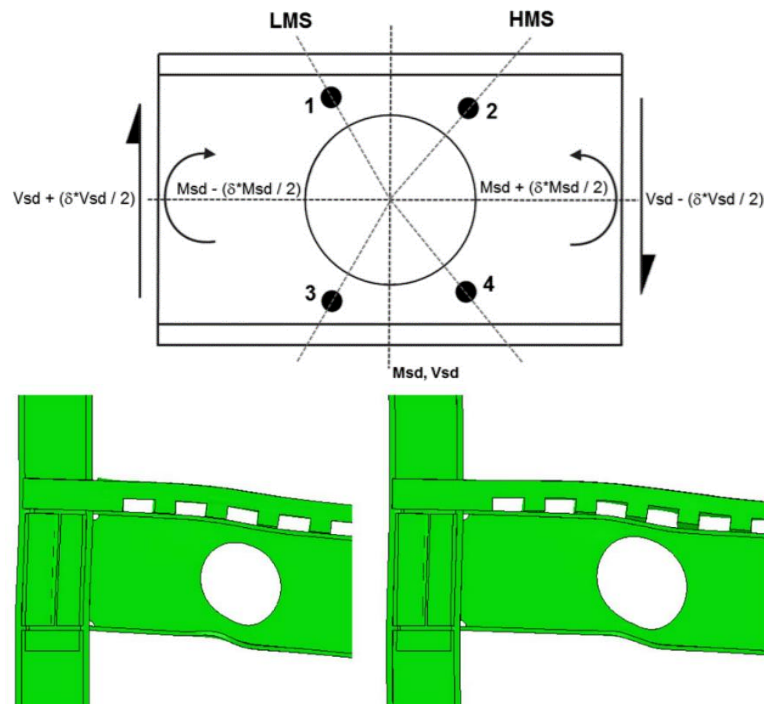
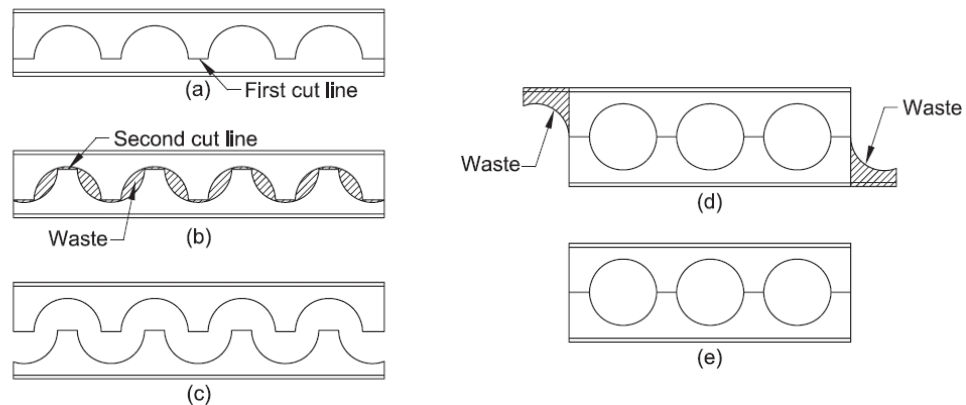


Figure 2.18: Vierendeel Mechanism (Chung et al., 2001; Shaheen et al., 2018).

Owing to the widespread application of perforated beams, which includes cellular beams and beams with web openings, a great deal of research on their behaviour and design has been conducted. Cellular beams, manufactured through a specific process that involves splitting and re-welding an entire beam in an offset position, as shown in Figure 2.19, are contrasted with beams having single web openings. The latter, forming the primary focus of this thesis, are created by cutting individual openings into an existing beam, as exemplified in Figure 2.20. While cellular beams aim for a high strength-to-weight ratio along the entire beam length, beams with single web openings are more about accommodating specific requirements at particular locations along the beam. The manufacturing process for cellular beams leads to a more efficient material distribution for load resistance, whereas single web opening beams may require additional reinforcement around the openings.



**Figure 2.19: Manufacturing of a cellular beam (Fares et al., 2016).**



**Figure 2.20: Laser cutting of web opening (Qiao, Guo, et al., 2022).**

The steel-concrete composite perforated section consists of two Tee-sections above and below the web opening (Figure 2.21), with the top Tee-section comprising the composite slab-beam and the bottom Tee-section being bare steel. In Figure 2.21, a composite beam is displayed; the ensuing behaviour is equally applicable to steel beams. The applied global bending moment and shear force induce three local forces on the concrete slab and perforated steel beam (Liu and Chung, 2003). The applied global bending moment is transferred by a couple of axial forces in Tee-sections above and below the web opening, as illustrated in Figure 2.22. These local axial forces cause a tensile yielding in the bottom Tee-section or/and crushing of the concrete slab (Darwin, 2000; Lawson and Hicks, 2011). The global shear force is transferred through the opening by a couple of local shear forces, creating secondary “Vierendeel” moments in the top and bottom Tees (see Figure 2.22). These secondary moments lead to the formation of four plastic hinges at the four corners of the web opening, known as the VM, as illustrated in Figure 2.18. The VM physically manifests when the steel reaches its yield capacity at the Tee-section ends due to the combination of these local forces. This mechanism is a ductile failure and is critical in the presence of large web openings (Lawson and Hicks, 2011). It is worth mentioning that in the presence of a composite slab, VM causes cracking of the concrete slab, as shown in Figure 2.23d (Darwin, 2000). This mechanism is critical in the presence of large web openings (Lawson and Hicks, 2011).

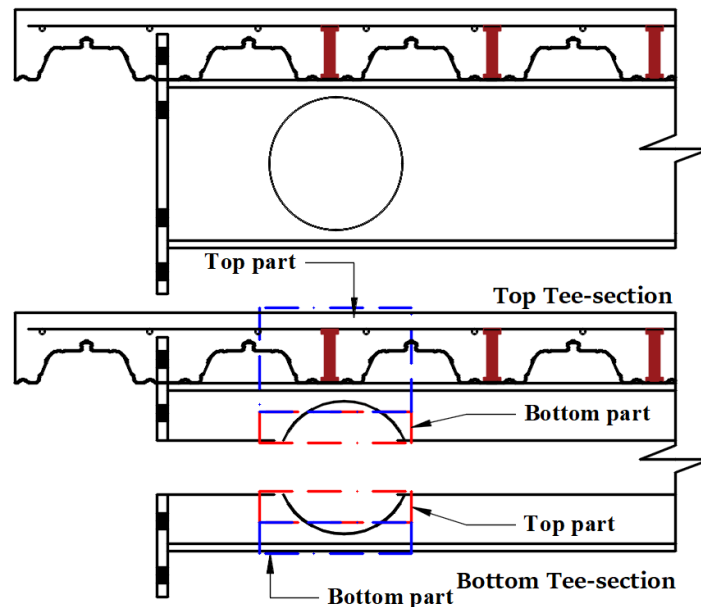


**Figure 2.21: Tee-sections of the perforated beam.**

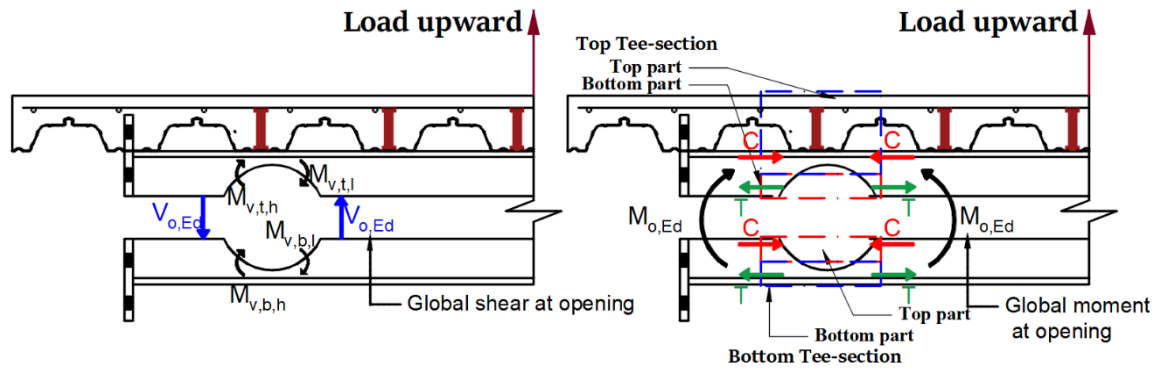


**Figure 2.22: Global moment and shear forces around the web opening**

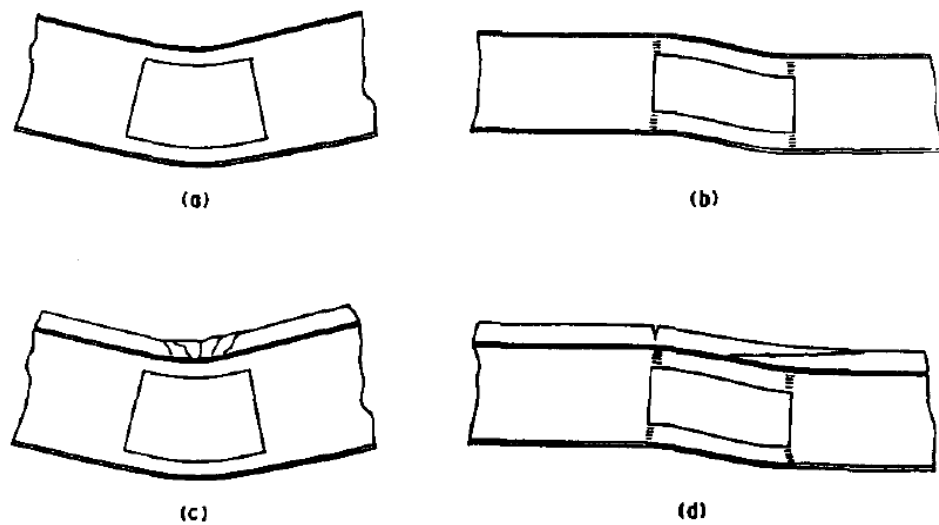


**Figure 2.23: Failure modes at web openings, (a) steel beam, pure bending, (b) steel beam, low moment-shear ratio, (c) composite beam with solid slab, pure bending, and (d) composite beam with solid slab, low moment-shear ratio (Darwin, 1990).**

The incorporation of a single web opening introduces three new key failure modes, specifically: (1) shear failure because of the reduction in the shear capacity, (2) flexural failure because of the reduction in moment capacity, and (3) VM (Chung, 2012). These modes are influenced by the web openings' shapes, sizes and locations (Darwin, 2000; Tsavdaridis and D'Mello, 2012). Moreover, the reduction in load-carrying capacity is dependent on the type of loading, the geometry of the beam, and the shear-to-moment interaction at the centreline of the web opening, as displayed in Figure 2.23 (Darwin, 1990; Lawson and Hicks, 2011; Zeytinci et al., 2021). It is observed that both shear failure and the VM may coincide around the web opening (Chung et al., 2003; Lagaros et al., 2008). Such failure modes of the perforated beam could be controlled by adjusting the web opening location and size (critical length for rectangular and elliptical web opening shapes) (Liu and Chung, 2003; Chung et al., 2003; Lagaros et al., 2008; Yang et

al., 2009; Tsavdaridis and D'Mello, 2012; Tsavdaridis et al., 2017; Erfani and Akrami, 2017; Shaheen et al., 2018).

In the design of the beam with a single web opening, the primary procedure involves assessing the moment and shear capacities at the web opening, in addition to the Vierendeel moment (Chung et al., 2001; Lawson and Hicks, 2011; Chung, 2012). The presence of a concrete slab can enhance Vierendeel bending resistance due to the local composite action between the top steel Tee-section and the concrete slab (Lawson and Hicks, 2011; Fares et al., 2016). However, major cracks can occur due to vertical deflection between two ends of the web opening, as shown in Figure 2.24. These can lead to a significant reduction in the load-carrying capacity of the composite perforated beam, which leads to a significant drop in ductility (Patrick, 2001).

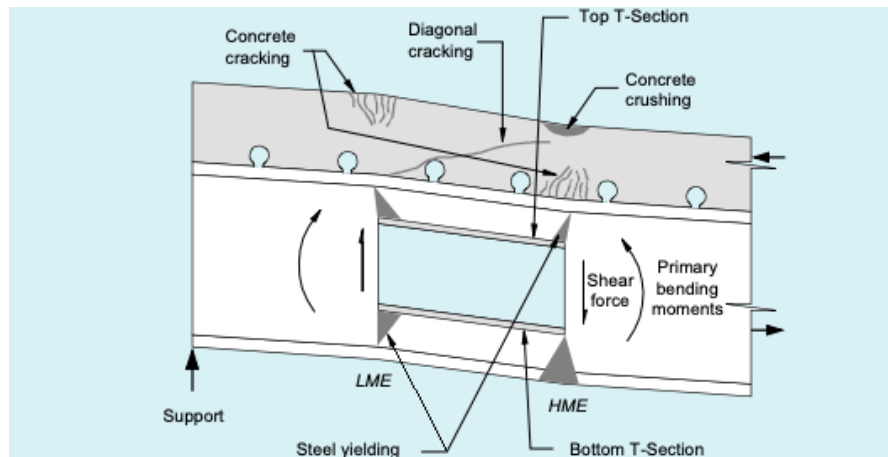


**Figure 2.24: Behaviour of composite perforated beam at ultimate load (PATRICK, 2001).**

According to SCI P355 guidance (Lawson and Hicks, 2011), Vierendeel bending resistance is considered as the sum of the bending resistances of the four corners in a perforation (two for each Tee-section), plus the contribution due to composite action between the top Tee-section and the concrete slab, and can be expressed as:

$$2M_{bT,NV,Rd} + 2M_{tT,NV,Rd} + M_{vc,Rd} \geq V_{Ed} l_e$$

where  $M_{bT,NV,Rd}$ ,  $M_{tT,NV,Rd}$  and  $M_{vc,Rd}$  are the contributions from the bottom Tee-section, top Tee-section and concrete slab, respectively.  $V_{Ed}$  is the design shear force at the opening at the LMS of the opening, as shown in Figure 2.25.  $l_e$  is the effective opening length for Vierendeel bending.

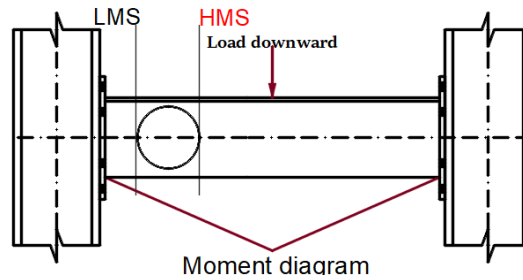


**Figure 2.25: High and low moment sides.**

SCI P355 guidance also provides a design process to calculate the plastic bending resistance at the opening's centreline. This is done by first determining the plastic neutral axis (PNA) position using plastic stress blocks in a perforated composite beam. The forces in the Tee-sections and the concrete slab must be in equilibrium. Thus, two situations are possible: with the PNA in the concrete slab and the top Tee-section, as illustrated in Figure 2.26.

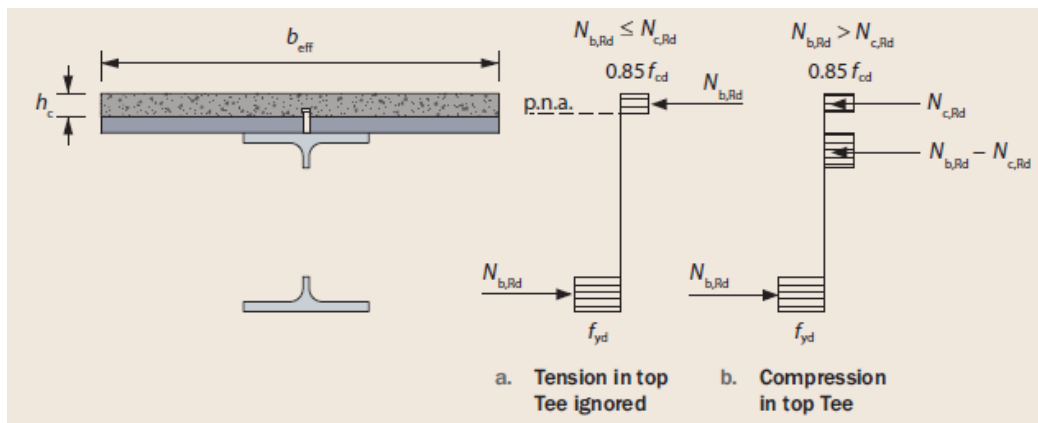


**Figure 2.26: Plastic stress blocks in a perforated composite beam (Lawson and Hicks, 2011).**

## 2.5 Prequalified Connections: Reduced web section (RWS) connection.

RWS connections make use of two concepts. The first is the use of perforated beams such as cellular steel beams, and the second is the 'strong-column and weak-beam' concept. RWS connections offer a competitive solution for retrofitting buildings, as making perforations on the beam web can be done with relative ease from the floor below while strengthening the beam-column connection using supplementary plates or trimming of flanges for making in situ RBS connections would be highly disruptive because that course of action requires partial demolition of floors overlaid on the beams. The most usual final configuration with and without a slab is depicted in Figure 2.27.



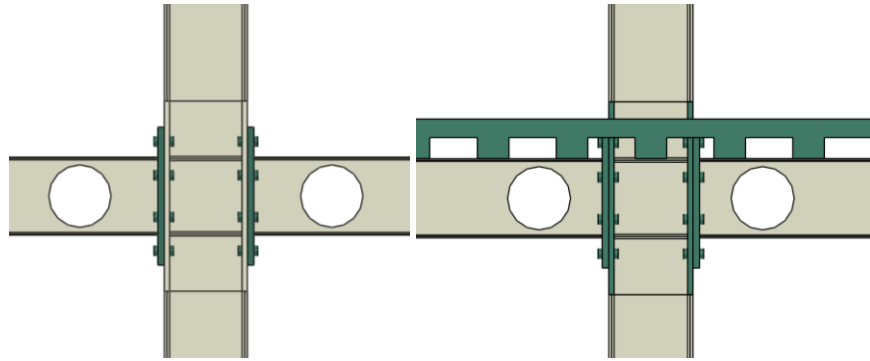


**Figure 2.27: RWS connection.**

The concept of using RWS connections as ductile fuses is derived from the beams with single or multiple openings (aka cellular beams). SCI P355 guidance provides the main failure modes of perforated composite beams and their associated design equations. The guidance presented in SCI P355 is derived from the Tee-section approach (TSA), which was initially introduced for composite perforated beams. This approach can also be utilised to determine the capacities of non-composite perforated beams by disregarding the composite slab's contribution. Figure 2.28 summarises the associated failure modes of a single web opening, which are also applicable to RWS connections. The three main failure modes of concern for RWS connections are bending of the beam at the opening, shear of the beam at the opening, and Vierendeel bending.

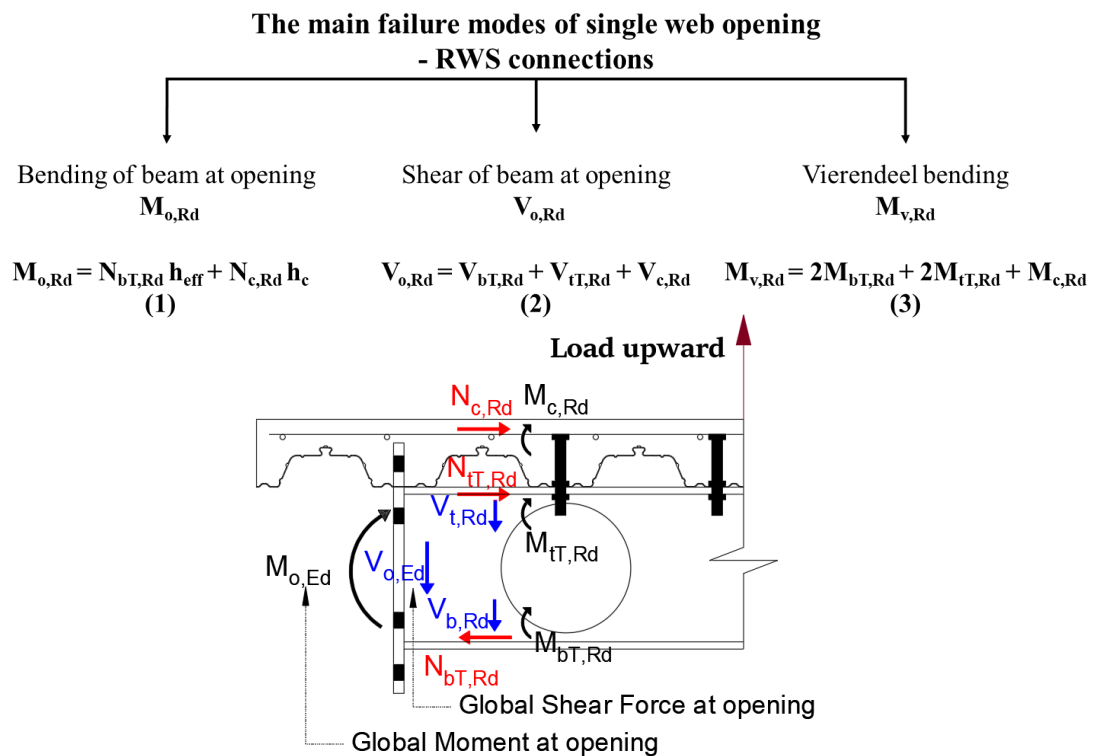


**Figure 2.28: Main failure modes of single web opening – RWS connections.**

The most common yielding mode of RWS connections is through the VM, similar to a cellular beam, that involves local yielding of the Tee-sections of the perforations, starting in the corner of the perforations and eventually leading to the formation of four plastic hinges as displayed in Figure 2.29. The VM is a highly ductile and stable yield mechanism that occurs in RWS connections. This results in the redistribution of global actions to prevent plastic deformation in non-ductile elements (Tsavdaridis and Papadopoulos, 2016; Shin et al., 2017b; Tsavdaridis et al., 2017). This load redistribution allows for extensive rotation ductility if the formation of plastic hinges controls local buckling and torsion (Yang et al., 2009; Tsavdaridis et al., 2014; Erfani and Akrami, 2017). The plastic hinges always form in the low moment side (LMS) before the high moment side (HMS) – in a cantilever configuration – and its occurrence depends on the global moment-shear ratio (Chung et al., 2001; Tsavdaridis and D'Mello, 2012).

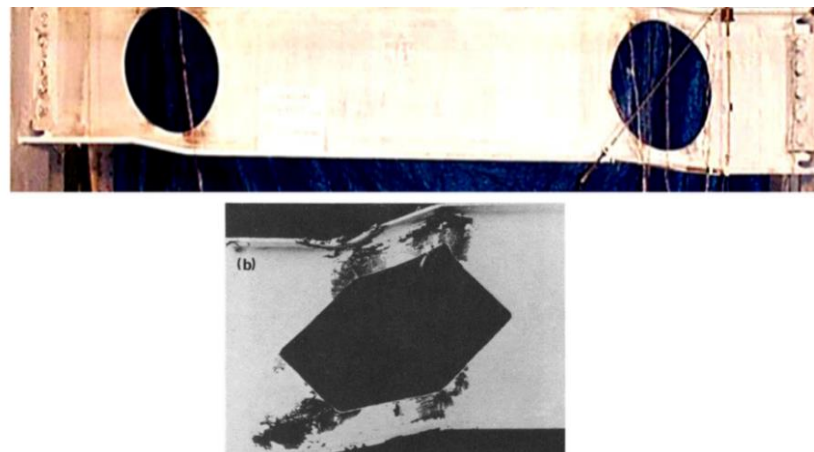


**Figure 2.29: Vierendeel mechanism (Kerdal and Nethercot, 1984; Shin et al., 2017a)**

This ductile mechanism limits the shear along the beam, thus capping demands outside protected zones (Tsavdaridis et al., 2021). The size of the web opening and its location within a high-shear zone may cause a non-ductile failure due to tearing and out-of-plane buckling. Chung et al. stated that both shear failure and the VM may coincide around the web opening (Chung et al., 2003; Lagaros et al., 2008). High global shear forces and an extensive critical length of the opening are required to promote such a ductile mechanism and cap deformation demands on non-ductile elements (Chung et al., 2003; Tsavdaridis and D'Mello, 2012; Tabar et al., 2022). Therefore, the failure mode of the perforated section could be controlled by adjusting the web opening location and size (critical length for rectangular and elliptical web opening shapes) (Liu and Chung, 2003; Chung et al., 2003; Lagaros et al., 2008; Yang et al., 2009; Tsavdaridis and D'Mello, 2012; Tsavdaridis et al., 2017; Erfani and Akrami, 2017; Shaheen et al., 2018).

As the VM allows for large deformations in the inelastic range, there is potential for using RWS beams to endure earthquake actions where the seismic hazard is low, leading to design guidelines for their use in supporting static loads (Aschheim, 2000; Lawson and Hicks, 2011). This has led to research about the behaviour of RWS connections when subjected to cyclic actions (Yang et al., 2009; Tsavdaridis et al., 2014; Shin et al., 2017a; Erfani and Akrami, 2017; Shin et al., 2017b; Zhang et al., 2019; Erfani et al., 2020; Davarpanah et al., 2020a; Tsavdaridis et al., 2021; Tabar et al., 2022).

In the literature review, it was found that the circular opening of RWS connections has a satisfactory seismic behaviour in moving the plasticity away from the column face and without a significant compromise to the connection capacities, providing that the proper size and location of the web opening is chosen (Tsavdaridis and D'Mello, 2011; Tsavdaridis and D'Mello, 2012; Tsavdaridis et al., 2017). The maximum diameter ( $d_o$ ) of the circular web openings was 0.8 of the steel beam depth ( $h$ ), and can be used to ensure the Vierendeel mechanism will occur (Tsavdaridis and D'Mello, 2012; Tsavdaridis et al., 2014; Tsavdaridis and Papadopoulos, 2016; Tsavdaridis et al., 2017; Boushehri et al., 2019). This mechanism can lead to additional rotation of the beam-to-column joint, which, in turn, will increase the ductility of the structure. The end-distance from the column face to the web opening centerline ( $S_o$ ) is a key parameter to gain the full benefit of the VM and the strong-column-weak-beam mechanism. While different values of  $S_o$  were used in the previous research, namely,  $0.5h$ ,  $0.65h$ ,  $0.75h$ ,  $0.8h$ ,  $0.87h$ ,  $h$ ,  $1.25h$ ,  $1.3h$ ,  $1.5h$ , and  $1.74h$  (Tsavdaridis et al., 2014; Tsavdaridis et al., 2017; Shaheen et al., 2018; Boushehri et al., 2019). However, there are some geometric (i.e. practical) limits mentioned in the SCI P355 and in the AISC design guide 31 for the minimum spacing of the end post ( $S_e$ ), which are  $S_e \geq 0.5d_o$  and  $S_e \geq 3$  in ( $\sim 76.2\text{mm}$ ) respectively, (Lawson and Hicks, 2011; Fares et al., 2016).

Testing of RWS connections under monotonic loading (Jia et al., 2021), cyclic load with and without an axial force on the column (Shin et al., 2017b; Zhang et al., 2019; Tsavdaridis et al., 2021; Bi et al., 2021), pseudo-dynamic (Yang et al., 2009), and column removal (Lin et al., 2021; Lin et al., 2022; Qiao, Xie, et al., 2022), has demonstrated their ability to develop plasticity at the web opening and facilitate the implementation of the strong-column-weak-beam framework. Moreover, results of these experimental and numerical studies have established that RWS connections can act as a ductile fuse with acceptable behaviour under different types of loading while limiting structural instability and protecting non-ductile elements (Tsavdaridis et al., 2014; Davarpanah et al., 2020a; Erfani et al., 2020; Du et al., 2021; Zeytinci et al., 2021; Dong et al., 2021; Bi et al., 2021; Tabar et al., 2022).

It is generally acknowledged that beams are primary dissipative elements in MRFs, adhering to the strong-column-weak-beam concept. In line with this concept, RWS connections have been demonstrated to enhance energy dissipation through the yielding of the perforated section (Shin et al., 2017a; Shin et al., 2017b; Shaheen et al., 2018; Tsavdaridis et al., 2021; Bi et al., 2021; Tabar et al., 2022; Guo et al., 2023). However, at first sight, RWS connections seem incapable of high ductility as they reduce the shear resistance of the web. Capacity design principles aim to ensure that the shear resistance is larger than the demands induced by plastic mechanisms to prevent tearing and other fragile failure modes. However, RWS connections showcase a high resiliency. Particularly, tests considering column removal indicate that loads can be transferred around perforations, allowing for catenary action in this highly demanding condition (Lin et al., 2021; Lin et al., 2022; Qiao et al., 2022) (see Figures 2.30, 2.31 and 2.32).

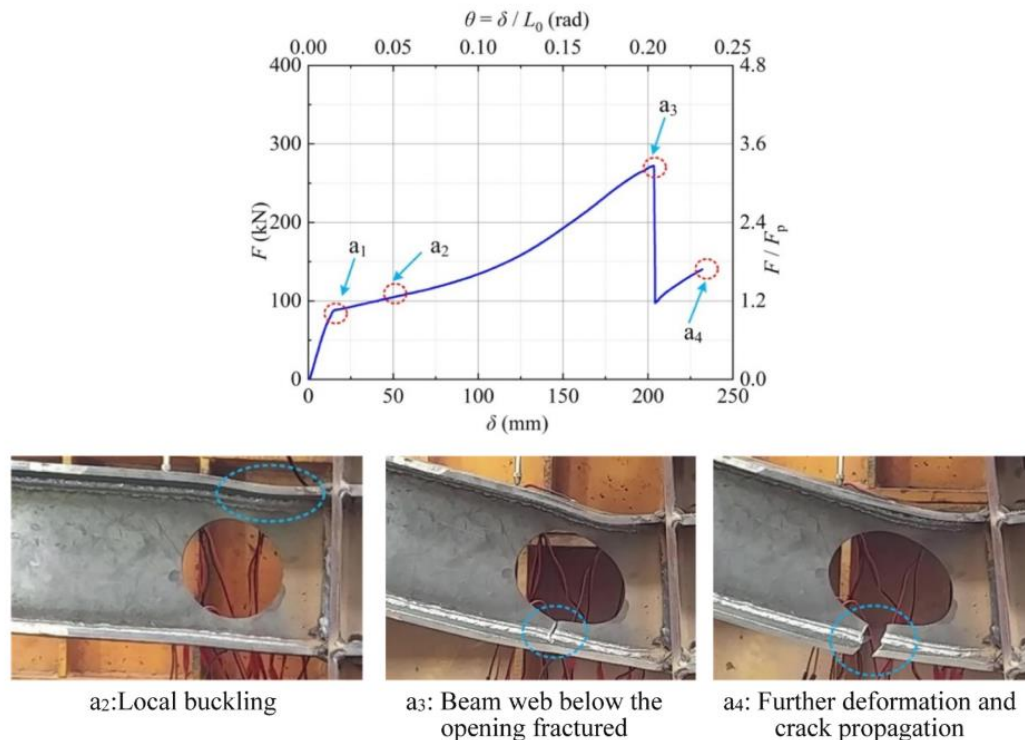


**Figure 2.30: Progressive collapse test results of specimen RWS (Qiao, Xie, et al., 2022).**

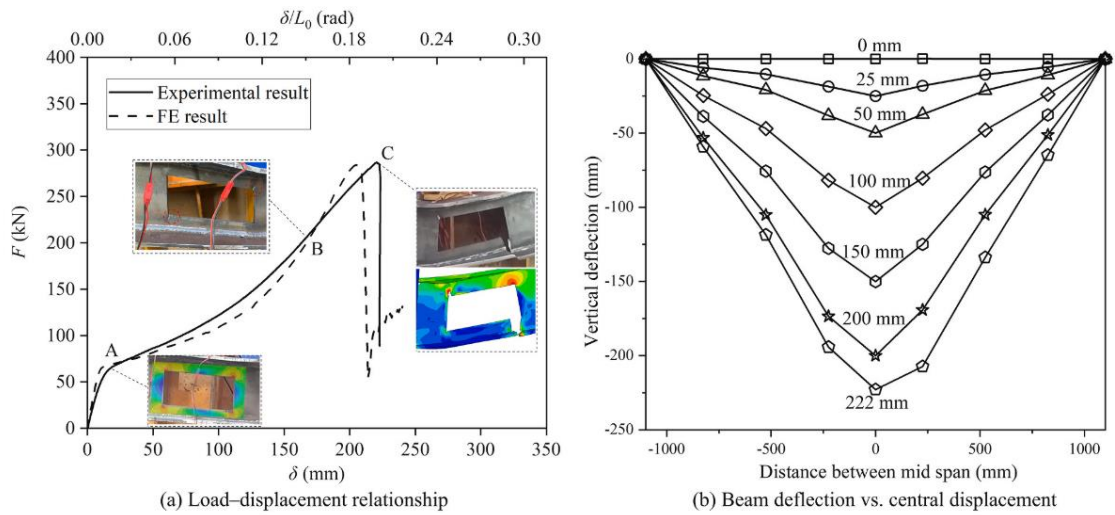
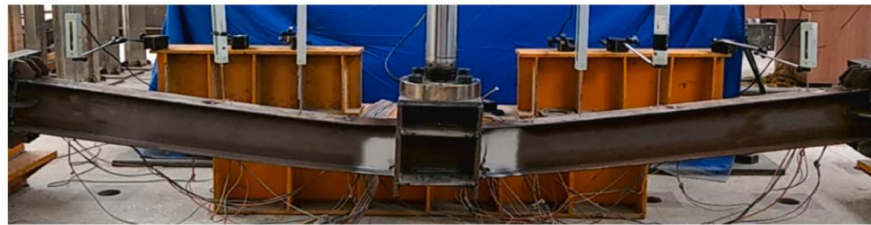


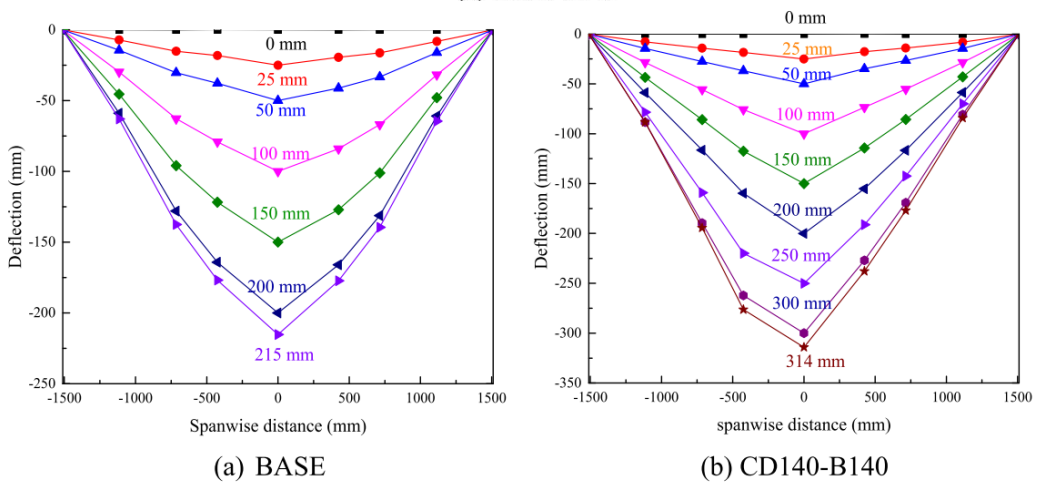
Figure 2.31: Catenary action of welded RWS connections (Lin et al., 2022).



(a) BASE



(b) CD140-B140



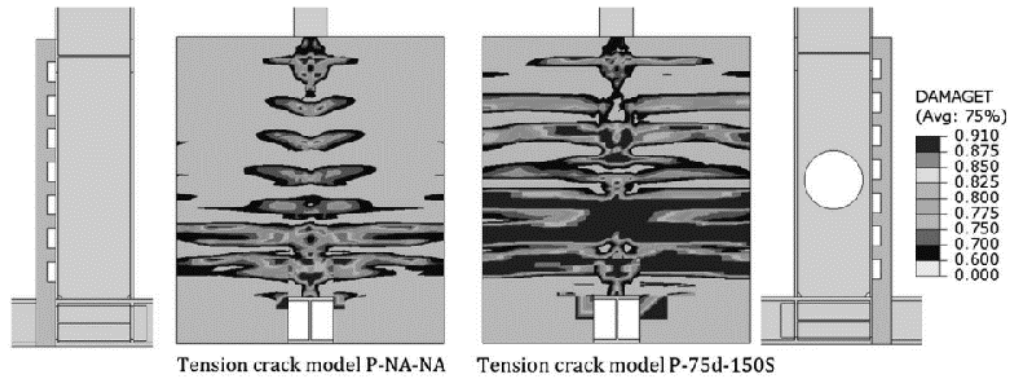
(a) BASE

(b) CD140-B140

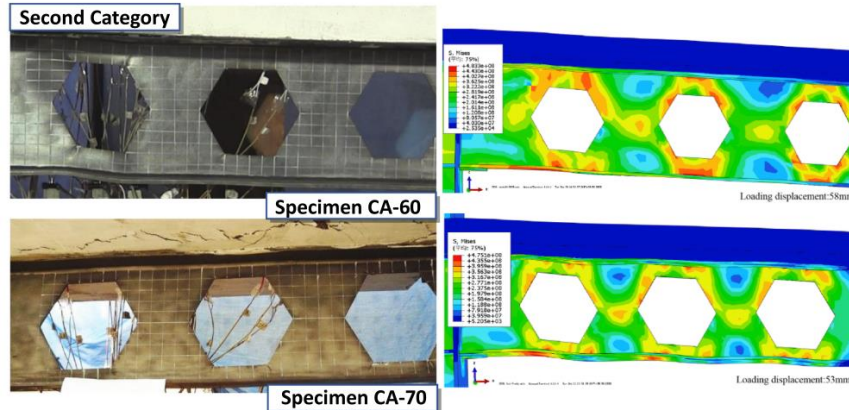
Figure 2.32: Overall deflection of specimens (Lin et al., 2021).

Investigations into composite RWS connections with a single circular web opening (Shaheen et al., 2018) with multiple hexagonal (castellated) web openings (Bi et al., 2021) or multiple circular (cellular beam) web openings (Guo et al., 2023) established their efficiency in harnessing high shear forces near the column face (Shaheen et al., 2018; Bi et al., 2021; Guo et al., 2023) (see Figure 2.33). It has been observed that when the web opening diameter equals  $0.5h$  and  $0.8h$ , the contribution of the composite slab increases the moment capacity by an average of 25.9% and 65.5%, respectively. Similarly, the study by Bi et al. (2021) reported comparable contributions from the composite slab for web openings with diameters of  $0.5h$  and  $0.8h$ , at 25% and 77.5%, respectively. These findings indicate that the larger the opening size, the more pronounced the composite effect of the floor slab becomes. This value is close to what has been accounted for in other composite flooring systems, and thus, decoupling beam and slab response by suppressing shear transfer studs could be a reasonable course of action (CEN, 2005d; ANSI/AISC 358-16, 2016; ANSI/AISC 341-16, 2016). Despite the utilisation of large size of web opening in high shear zone (near connection), the VM generally governed the failure of all studied RWS connections (Yang et al., 2009; Li et al., 2011; Guo et al., 2011; Tsavdaridis et al., 2014; Erfani and Akrami, 2017; Naughton et al., 2017; Zhang et al., 2019; Boushehri et al., 2019; Tsavdaridis et al., 2021), whilst meeting performance requirements of ANSI/AISC 358-16, ANSI/AISC 341-16 and Eurocode 8 (CEN, 2005d; ANSI/AISC 358-16, 2016; ANSI/AISC 341-16, 2016).

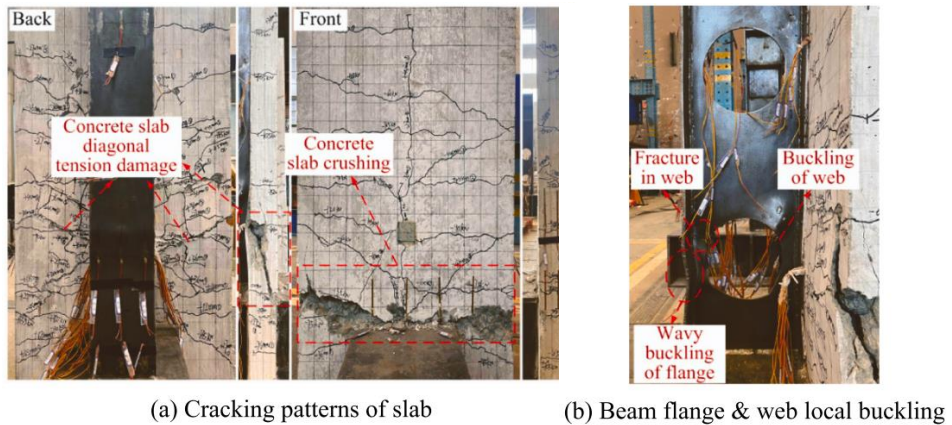




**Effect of web opening on damage in slab (Shaheen et al., 2018).**



**Comparison of test and FE failure (Bi et al., 2021).**



**Final damage patterns in the specimen (Guo et al., 2023).**

**Figure 2.33: Experimental and numerical Investigations into RWS connections.**

The presence of welded shear studs over the protected zone could compromise the attainment of the strong-column-weak-beam framework. If composite action is not properly accounted for, it could strengthen the connection rather than weaken it. This is consistent with the findings of Shaheen et al. (2018), who only examined composite RWS connections with joint action with the slab over the opening. Their study concluded that small to medium web opening sizes should be considered, as large openings compromise their stable hysteretic response (see Figures 2.34 and 2.35).

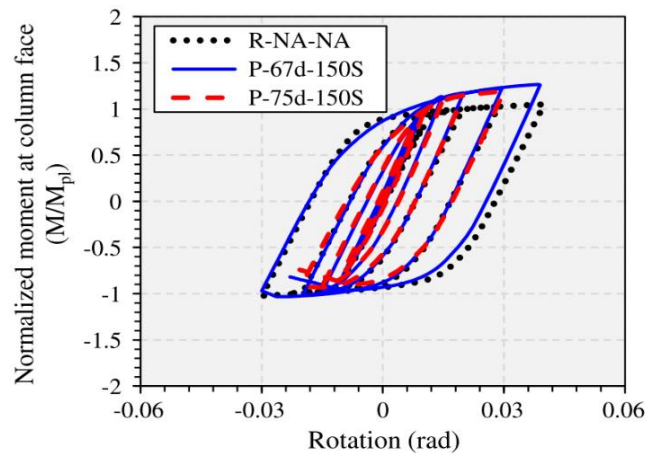


**Figure 2.34: Effect of the web opening size on the capacity.**

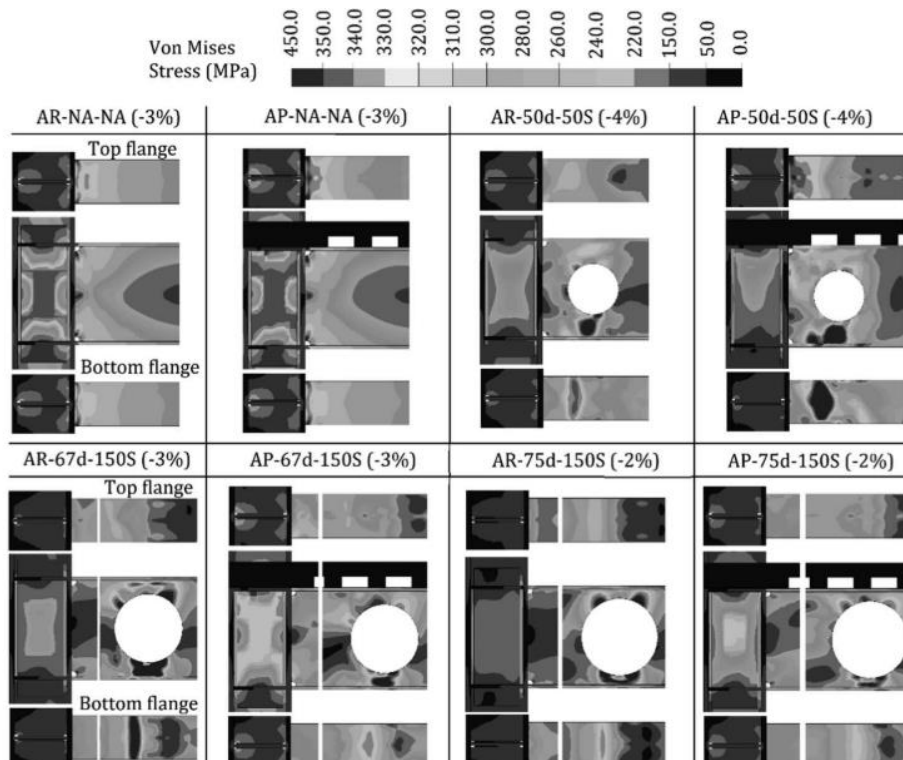


**Figure 2.35: Stress distribution of different RWS models.**

The hysteretic behaviour of steel-concrete composite welded and bolted extended end-plate (BEEP) RWS connections can arise from complex plastic deformations across more than one of the connection components (especially in BEEPs). Given the range of components that may undergo deformation in elastic and plastic regions, predicting the hysteretic responses of BEEP-RWS connections could be challenging. In the past decade, there has been a strong push toward the development of robust guidance and numerical models and acceptance criteria for design and promote the use of RWS connections in MRFs



in seismic areas (Tsavdaridis and D'Mello, 2012; Tsavdaridis et al., 2014; Akrami and Erfani, 2015; Tsavdaridis et al., 2017; Erfani and Akrami, 2017; Shaheen et al., 2018; Boushehri et al., 2019; Erfani and Akrami, 2019; Davarpanah et al., 2020a; Erfani et al., 2020; Zeytinci et al., 2021). This extensive research has resulted in patents and software developments (Tsavdaridis et al., 2014; Tsavdaridis and Papadopoulos, 2016; Tsavdaridis et al., 2017; Naughton et al., 2017; Shaheen et al., 2018; Boushehri et al., 2019; Ferreira et al., 2022; Degtyarev and Tsavdaridis, 2022). Given the significance and continuity of this work, it is necessary to provide a comprehensive understanding of the key parameters that influence the cyclic response of RWS connections, both with and without composite slabs.

## **2.6 Summary**

The literature review highlighted the challenges posed by asymmetric yield mechanisms in steel-concrete composite MRFs during earthquakes, leading to structural compromises and damage, particularly in beam bottom flanges. Existing retrofitting strategies, such as decoupling slabs and beams in protected zones, often face practical limitations. To address these challenges, RWS connections serve as ductile fuses, requiring minimal structural alterations with a single perforation in the beam web. This solution simplifies manufacturing and retrofitting and helps prevent out-of-plane instability. RWS connections localise failures, fostering a Vierendeel mechanism that enhances seismic performance and mitigates asymmetric yield effects. These practical implications underscore the importance of our research in the field of seismic engineering.

While the literature acknowledges the potential benefits of RWS connections, a significant knowledge gap exists regarding their response in steel-concrete composite structures. The one that does exist was a numerical study showing that composite action should be considered due to its effects on the behaviour of the seismic connections under cyclic loads. However, the effect of the presence and absence of composite action (bolted or/and welded shear studs) over the web opening has yet to be studied. Additionally, while previous research highlights the importance of web opening size and location on RWS performance, a comprehensive understanding of the effects of presence/absence composite action and capacity design principles still needs to be investigated.

This thesis directly addresses these research gaps by aligning its objectives with overcoming these limitations and aiming to bridge them by conducting experimental tests to significantly enhance the existing knowledge base on RWS performance under seismic loads. Detailed finite element analysis was also employed to identify key factors governing the cyclic response of double-sided

extended end-plate/RWS connections with and without composite engagement over the web opening. Additionally, comprehensive parametric assessments extend observations from experimental results in this thesis, shedding light on key factors influencing seismic performance. Finally, through compiling test and FEA databases from this research and existing literature to establish a comprehensive database, seeking to evaluate the capacity design ratio effect and assess the applicability of existing design guidelines, such as SCI P355, thereby advocating for the widespread adoption of RWS connections in seismic regions. This knowledge will ultimately facilitate a more robust and expansive understanding of RWS connections, supporting the development of improved design practices and standards in seismic engineering. The summary of experimental and numerical studies on RWS connections is tabulated in Appendix A.

## Chapter 3

### Preliminary Finite Element Analysis

#### 3.1 Introduction

The lack of experimental and numerical studies on the cyclic response of steel-concrete composite extended end-plate and reduced web section (RWS) connections has been manifested. In light of this gap, it becomes imperative also to consider the inherent complexities in steel-concrete composite bolted extended end-plate connections subjected to cyclic loading. These connections exhibit complex behaviour due to the range of components that may undergo plastic deformation. Consequently, while distinct, modelling and predicting the hysteretic responses of such components possesses similar challenges. To name a few, there is sliding and friction between several components, such as the concrete-steel and the steel-steel interfaces. Also, there are secondary effects arising from preloading bolts, and buckling and stretching when subjected to reversible loads. This requires detailed rules for matching node behaviour on distinct types of components/elements, balancing accurate finite element (FE) results against the need to reduce computational time and storage requirements.

This chapter presents a preliminary FE analysis to increase understanding of the behaviour of joint slab-beam action of RWS connections. This was achieved by formulating parametric high-fidelity FE models in Abaqus© (ABAQUS, 2019), to represent with detail the interaction of all structural elements in the connection. The FE model is benchmarked firstly by validating against the findings of an experimental investigation performed in beams without perforations (Chaudhari, 2017; Chaudhari et al., 2019). After reaching close agreement with the experimental results, a parametric study with 48 different models was analysed, employing European beam and column sections. These models studied different configurations with varying (1) web opening diameter ( $d_o$ ), (2) the end distance from the connection face to the centreline of the web opening ( $S_o$ ) and (3) the presence and absence of composite interaction over the protected/plastic zone (i.e., web opening) to ensure effective coupling and decoupling of the beam and the slab.

## 3.2 Finite element model validation

### 3.2.1 Model description

This study considers a cruciform arrangement to test the structural capacity of the RWS column connection. The cruciform arrangement allows for direct estimation of the drift capacity of beam-column connections and closely represents the behaviour of an inner joint in a multi-storey frame (NZS3404:1, 1997). Furthermore, benchmarking of the finite element model is done by replicating results obtained by Chaudhari (Chaudhari, 2017; Chaudhari et al., 2019) by testing a bare steel joint (BSF) and a steel full-section beam-concrete composite slab (FI-SU). Both types of specimens employed extended end-plate connections, shown in Figure 3.1. Detailing of the connection was done in accordance with the New Zealand standards (NZS3404:1, 1997). Continuity plates were welded on both sides of the column. The 25mm extended end-plate connections include four rows of two bolts (M24 class 8.8) that were subjected to a prestress tension of 212 kN. The thicknesses of rib stiffeners and continuity plates were 12mm and 16mm, respectively. The boundary and loading conditions employed in FE models simulated the ones in the experimental tests. The ACI loading protocol (ACI, 2005) considering displacement control was applied, shown in Figure 3.2

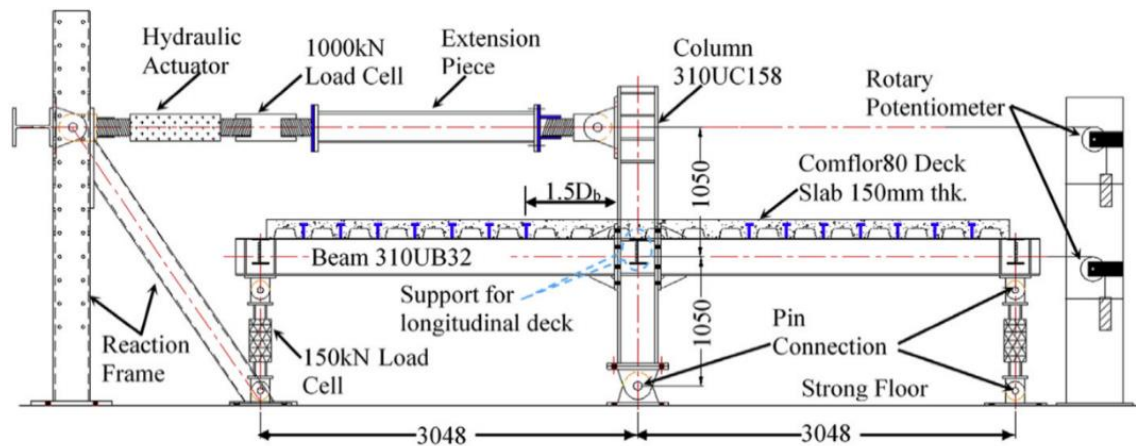
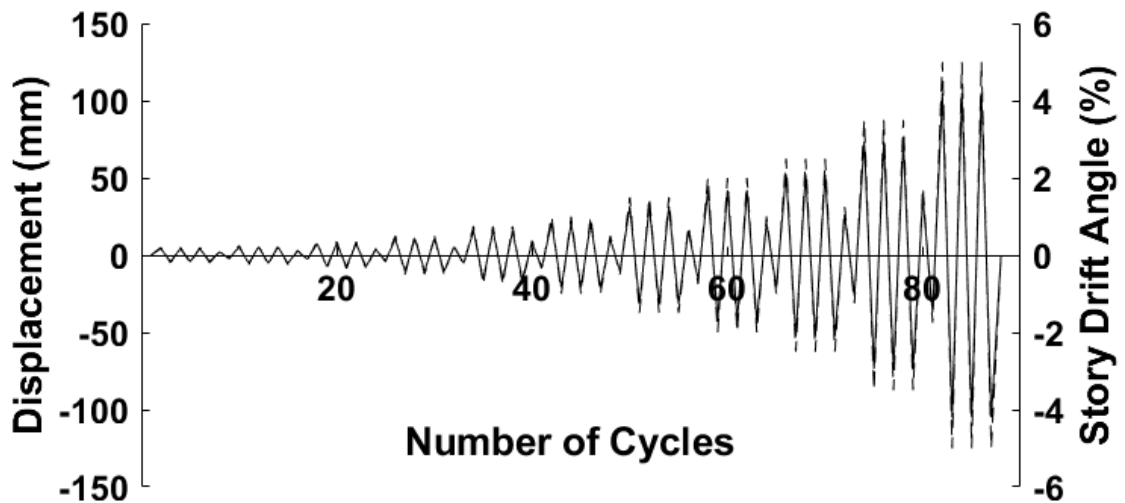


Figure 3.1: Elevation of test setup (Chaudhari, 2017; Chaudhari et al., 2019).



**Figure 3.2: Displacement Control Loading Regime of ACI report T1.1-01 (ACI, 2005).**

### 3.2.2 Element type

The concrete slab, the panel zone, bolts, end plates, and shear studs were modelled using 8-node solid elements with reduced integration (element type C3D8R). Beams, stiffeners, and top and bottom parts of the column were modelled using 4-node shell elements with reduced integration (S4R), as shown in Figure 3.3. This modelling technique of using a combination of 3D shell and 3D solid elements was adopted to increase accuracy in simulating the behaviour of the steel-concrete composite bolted extended end-plate whilst decreasing computation time and memory usage, compared to what would be required if all elements were modelled as solids. Reinforcement steel bars were represented using truss elements (2-node linear, T3D2), as they can only endure uniaxial tension and compression. The metal deck was not modelled because it is primarily used as formwork for the placement of concrete, whilst its inclusion would increase the complexity of the model without aggregated value, as the absence of metal decking affects the pattern of cracks in the concrete slab but not the structural capacity of connection (Darwin and Donahey, 1988; Shaheen et al., 2018). This is explained by the fact that the interaction of shear studs (number of shear studs) with the concrete slab is the most critical factor that governs the capacity of the connection, instead of allocation of the steel deck, which acts primarily as workform (Darwin and Donahey, 1988; Shaheen et al., 2018). Furthermore, the inclusion of metal decking in the model may lead to numerical instabilities that could end in the early termination of the analysis (Baskar et al., 2002).

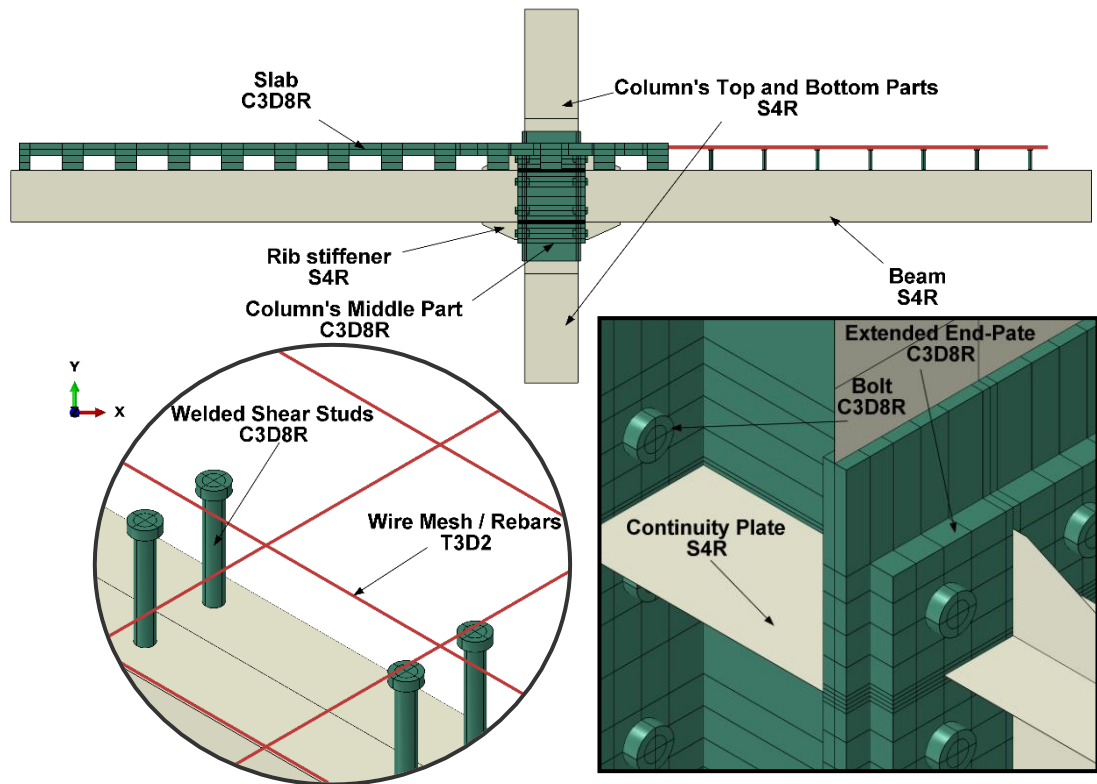


**Figure 3.3: Selected element types for FE model.**

### 3.2.3 Contact modelling

Modelling contact interactions are very critical for steel-concrete composite bolted extended end-plate connections. This importance arises because the bending resistances of such connections depend on the collaborative functioning of all components, where forces are transferred through contact interactions. Moreover, the combination of 3D shell and 3D solid models adopted in this FE analysis, along with the imposed cyclic loading, requires careful treatment to avoid convergence failures. This necessity is heightened due to the high level of nonlinearity expected during the FE analysis.

Interactions amongst diverse components to simulate the experimental test are in accordance with one of the following approaches:

- Tie constraints (equal displacements) to simulate the welding between steel elements were applied (Figure 3.4).
- Normal and tangent interactions considering hard contact and a friction coefficient equal to 0.2 (which corresponds to the case of untreated rolled

surfaces (CEN, 2005b; Chaudhari, 2017) were adopted while allowing for finite sliding to simulate contact amongst steel elements (Figure 3.5).

- Frictionless normal and tangent interactions with displacement control to simulate steel-concrete contact were used (Figure 3.6).
- Embedded elements for interaction of concrete, rebar and tie-studs within the slab were utilised (Figure 3.7).

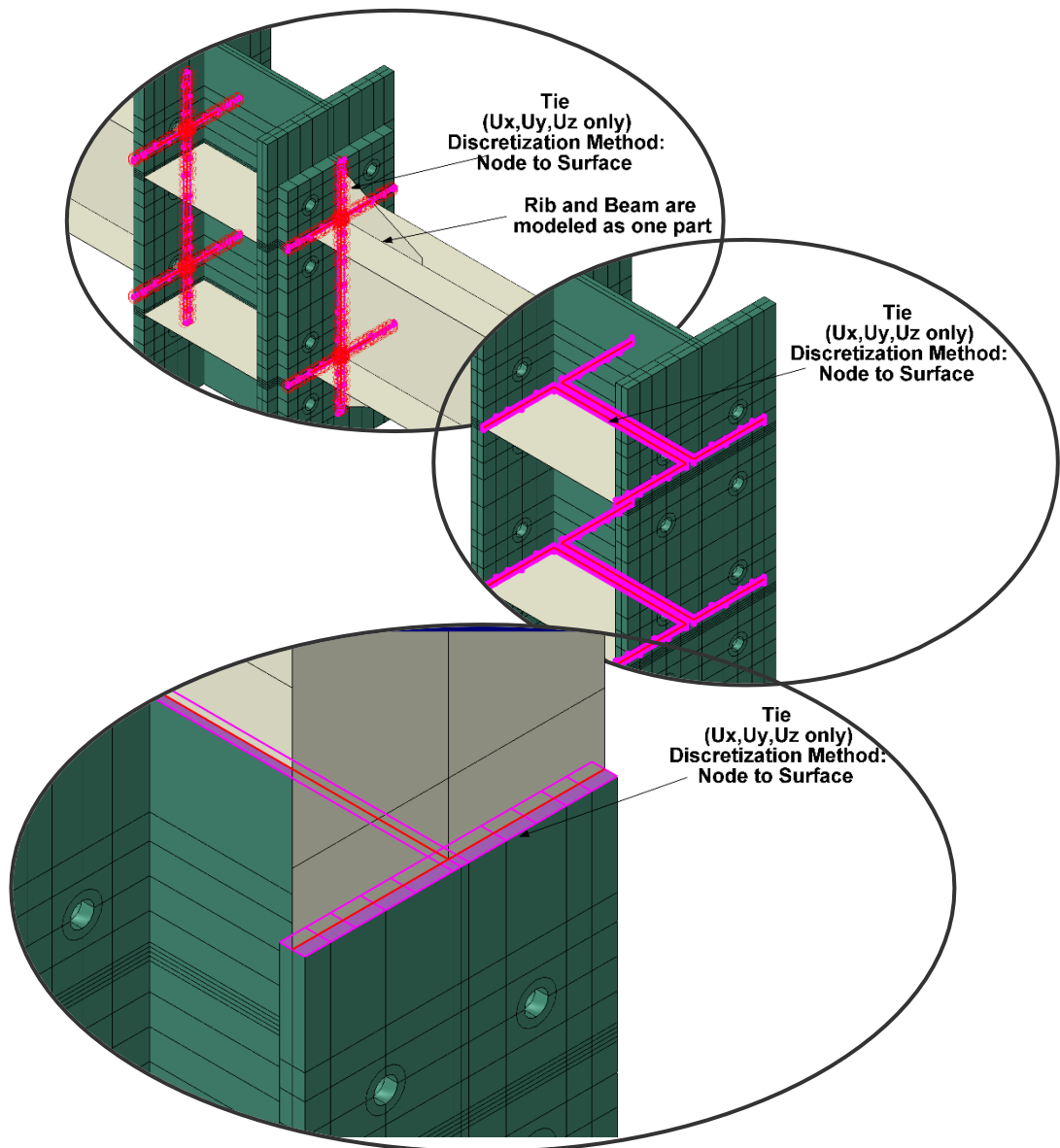


**Figure 3.4: Tie constraints.**

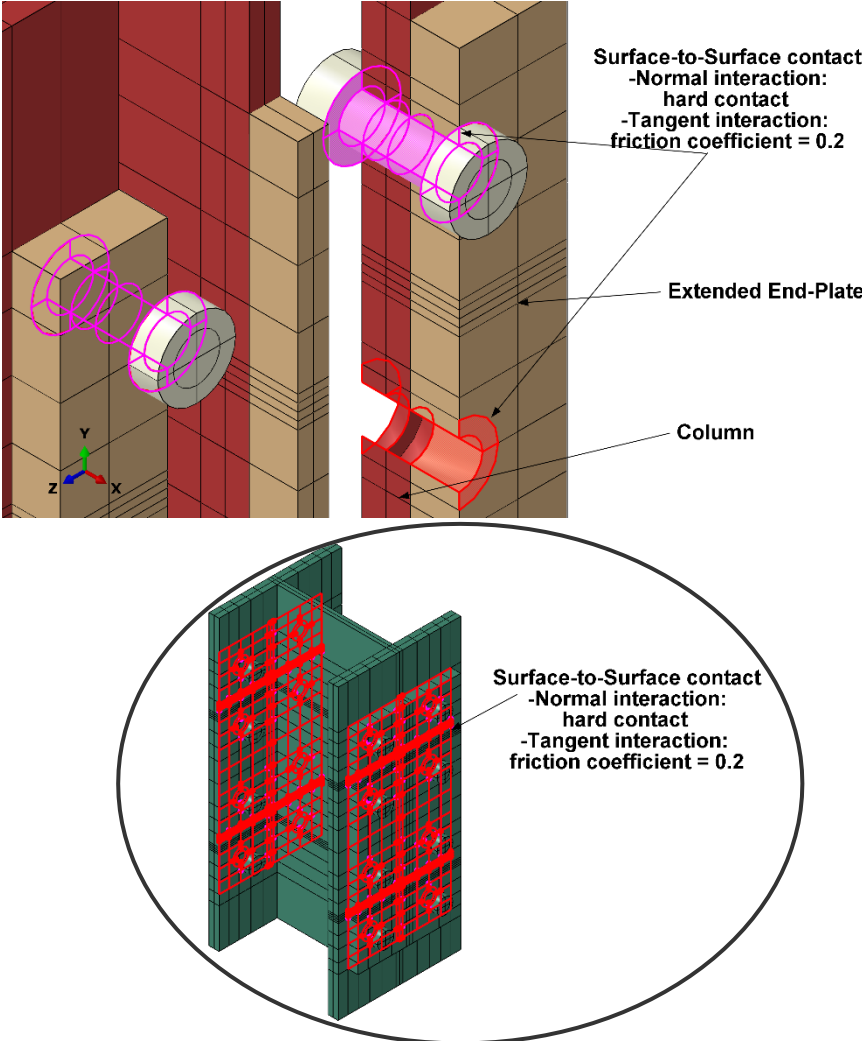


**Figure 3.5: Normal and tangent interactions between steel components.**



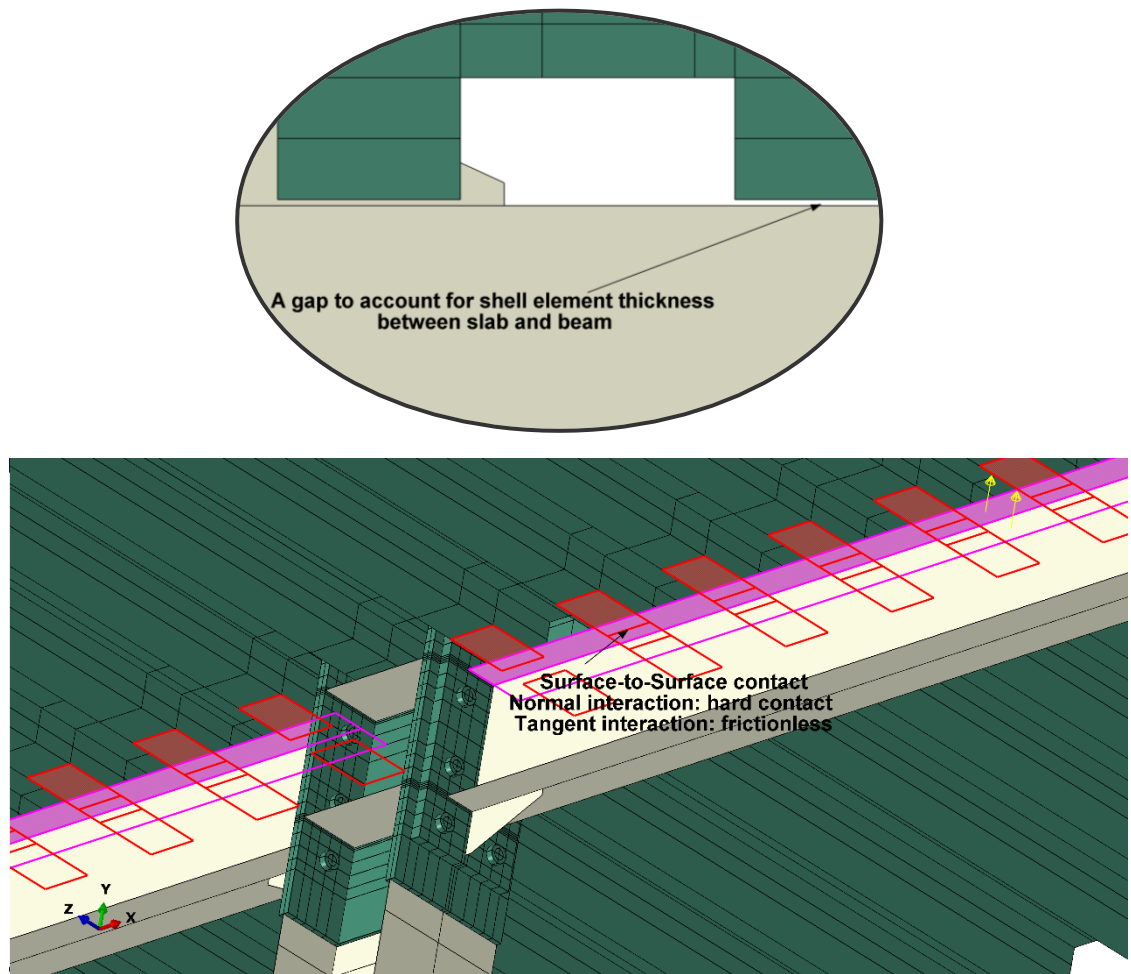


Figure 3.6: Frictionless contact between concrete slab and steel beam.

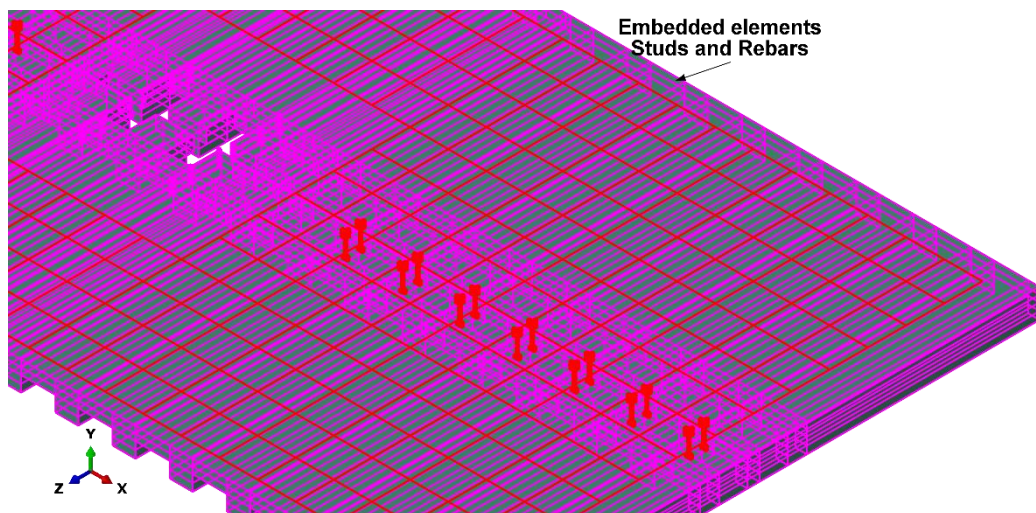


Figure 3.7: Embedded element technique.

### 3.2.4 Boundary and loading conditions

The boundary conditions have a strong influence on the lateral-torsional stability, the deformation capacity, and, eventually, the accuracy of the replicated results. Therefore, the applied boundary and loading conditions were consistent with the tests observed by Chaudhari et al. (2019), aiming to achieve highly accurate FE results. Figure 3.8 illustrates the translations and rotations of pin and roller supports, as well as the out-of-plane restraint. The modelling of these boundary conditions was simplified by employing the “kinematic coupling constraints” option in ABAQUS (2019). Similarly, the cyclic displacement applied to the column's tip also used the kinematic coupling constraint option. Furthermore, preloading forces of 211.8 kN were applied to simulate the tightening of bolts using the “Bolt Load” option.

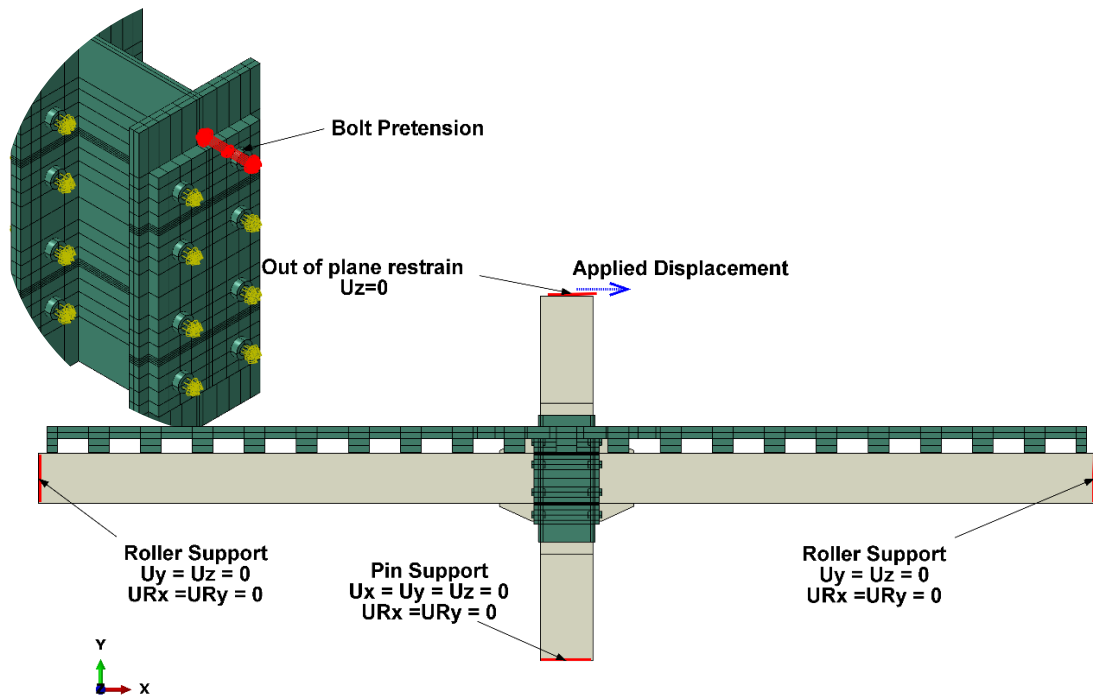
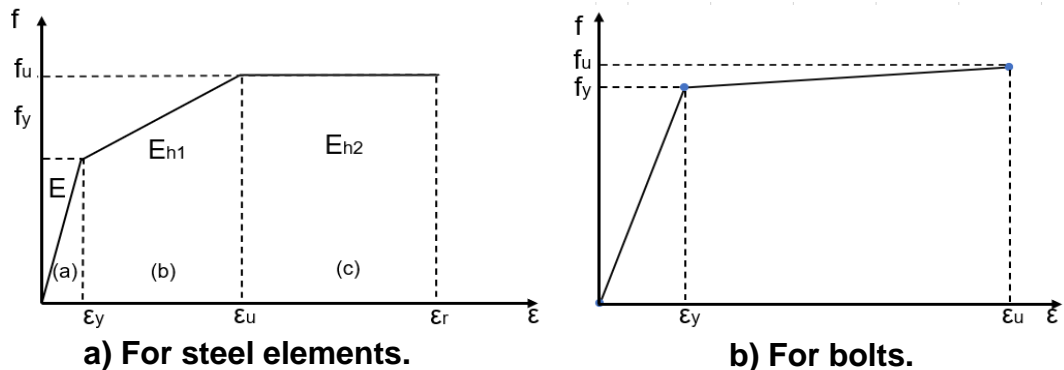


Figure 3.8: Boundary condition and bolts pretensions.

### 3.2.5 Material model

#### 3.2.5.1 Steel

Steel was modelled considering a bilinear stress-strain relationship with adaptative parameters, representing a combined isotropic and kinematic hardening material, in accordance with the formulation implemented in ABAQUS®. This material model was allocated to the main steel structural elements (beam, column and extended end-plate), as shown in Figure 3.9, using yield and ultimate stresses from coupon test results provided in Chaudhari (2017). The three points from stress-strain curves, as shown in Figure 3.9, were used to reduce computational time and storage requirements. The ultimate strain for which peak stress is observed,  $\epsilon_u$  was set equal to 15 times the yield unitary strain,  $\epsilon_y$ . Whilst the strain at which fracture is observed,  $\epsilon_r$  was set up at 10 times  $\epsilon_u$  in accordance with (Díaz et al., 2018). A value of  $\epsilon_u$  equal to 0.05 was enforced for bolts, while the fracture was considered to happen upon achievement of peak resistance. An elastic-perfectly-plastic model was adopted for steel elements outside the panel zone and rebar. Nominal properties were considered for all materials, as assessing the effects of variability during manufacturing is out of the scope of this study.



**Figure 3.9: Material stress–strain curve for beam, column, and connection (Díaz et al., 2018)**

#### 3.2.5.2 Concrete

The concrete slab was modelled using a concrete damaged plasticity (CDP) model based on the constitutive law presented in the Eurocode 2 (CEN, 2004) and the exponential tension softening model (Cornelissen et al., 1986). The stress-strain relation for the normal concrete's compression behaviour is defined in Eurocode 2 (CEN, 2004) by an equivalent uniaxial stress-strain curve, as shown in Figure 3.10. Several models can be used to express the tension-softening behaviour of normal concrete, such as linear, bilinear and exponential.

The exponential expression was adopted (Figure 3.11) as it has been judged to be the most practical realistic model, in accordance with results obtained by Cornelissen et al. (1986) and Ahmed and Tsavdaridis (2022). The average value of three concrete compression cylinders  $f_{cm}$  tests, as provided by Chaudhari (2017), was used to model concrete's compression behaviour. The axial tensile strength  $f_t$  of the concrete was taken as 10% of the average compressive strength value  $f_{cm}$  in accordance with (Qureshi et al., 2010).

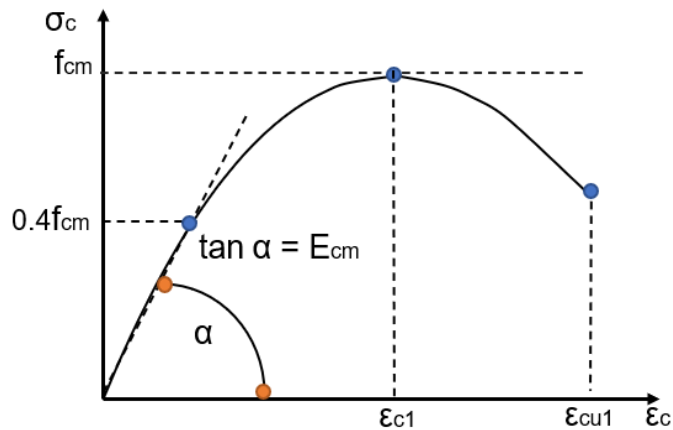


**Figure 3.10: Schematic representation of the stress-strain curve for structural analysis - Eurocode 2 - (CEN, 2004).**

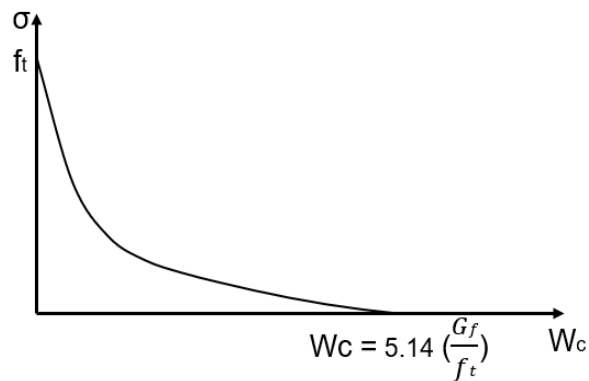


**Figure 3.11: Exponential tension softening (Ahmed and Tsavdaridis, 2022).**

### 3.2.6 Geometric nonlinearity

Geometric nonlinearity was considered to ensure buckling occurs when the FE mode becomes unstable. Therefore, small geometric imperfections must be introduced before performing the nonlinear FE analysis. Eigen buckling analyses were initially performed to introduce a geometric imperfection. As suggested in Tsavdaridis and D'Mello (2009), the first shape of Eigenmode was selected and scaled by the recommended factor of  $t_w/200$ . Figure 3.12 shows the first shape of the Eigenmode adopted.

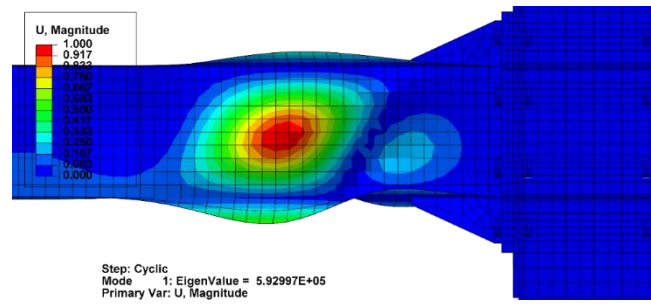


**Figure 3.12: First shape of Eigenmode.**

### 3.2.7 Mesh sensitivity analysis

A mesh sensitivity analysis was conducted using various mesh sizes to evaluate the calculation time, storage, and accuracy of the results. Based on the mesh sensitivity analysis as displayed in Figures 3.13 and 3.14, the element sizes ranged between 30mm for steel and 35 mm for the slab, which is enough to capture the effects of stress concentration features that are observed during laboratory testing (Chaudhari et al., 2019). The element sizes of the bolts and shear studs were 15 mm and 6 mm, respectively. This resolution provides close agreement with experimental results but with a significant reduction in time and computing resources, as shown in Figures 3.13 and 3.14.

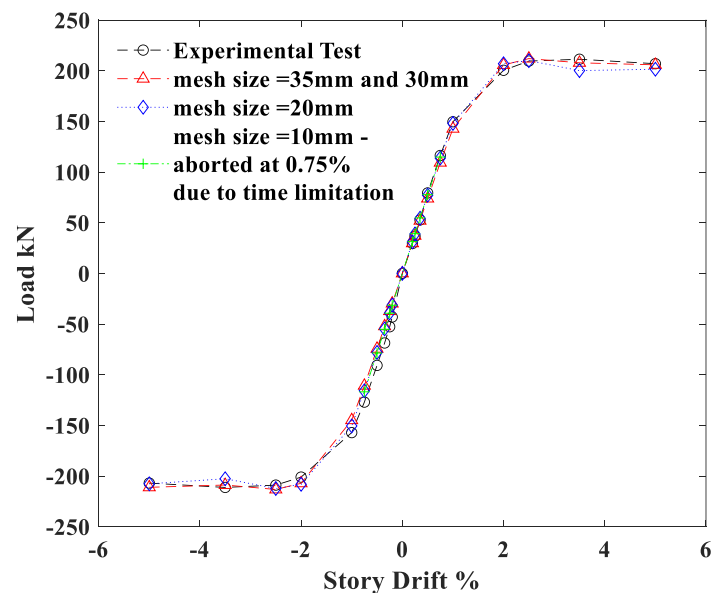


**Figure 3.13: Skelton curves for all FE models in mesh sensitivity analysis.**

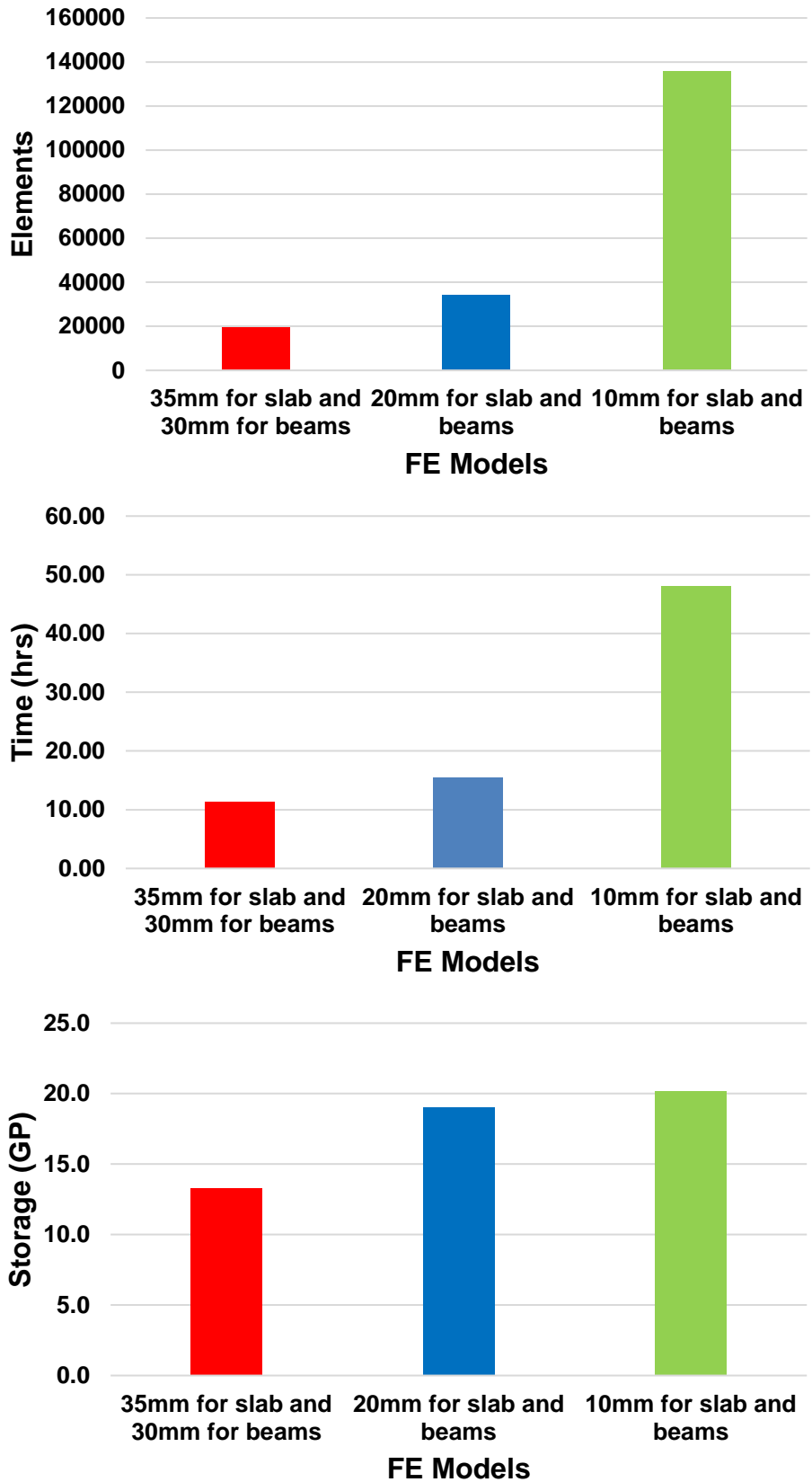
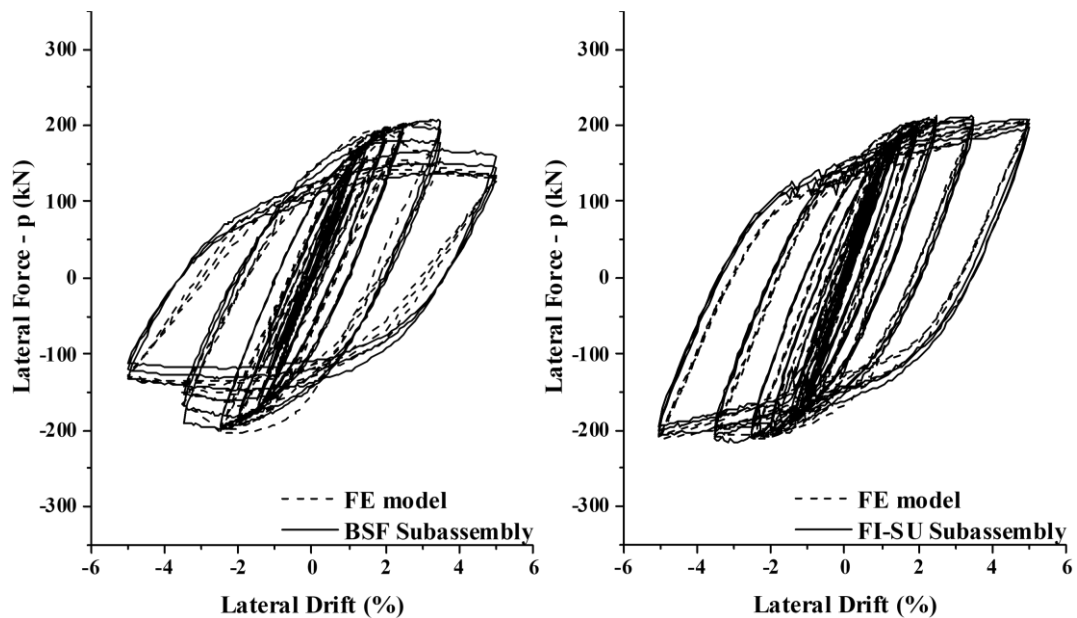


Figure 3.14: Comparison between FE models in mesh sensitivity analysis.

### 3.3 FE models benchmarking

The proposed numerical model is capable of reproducing the displacement-load hysteresis curves of both benchmarking experiments well (Chaudhari, 2017; Chaudhari et al., 2019). Behaviour before yielding, stiffness degradation and hysterical energy dissipation are closely simulated as differences between load-story drift ordinates diverge less than 6% for the model without a slab (BSF); while becoming less than 4% for the model with a slab (FI) as shown in Figure 3.15. In addition, the model captures well residual deformations, and yield and failure modes. Particularly, it reproduces closely flange buckling and slab cracking, both features being showcased in Figures 3.16 and 3.17. Therefore, the numerical model is reliable enough for attaining the objectives of this analysis.



**Figure 3.15: Comparison of Hysteresis Behaviour of FE Result with the Test Results of Chaudhari (2017).**



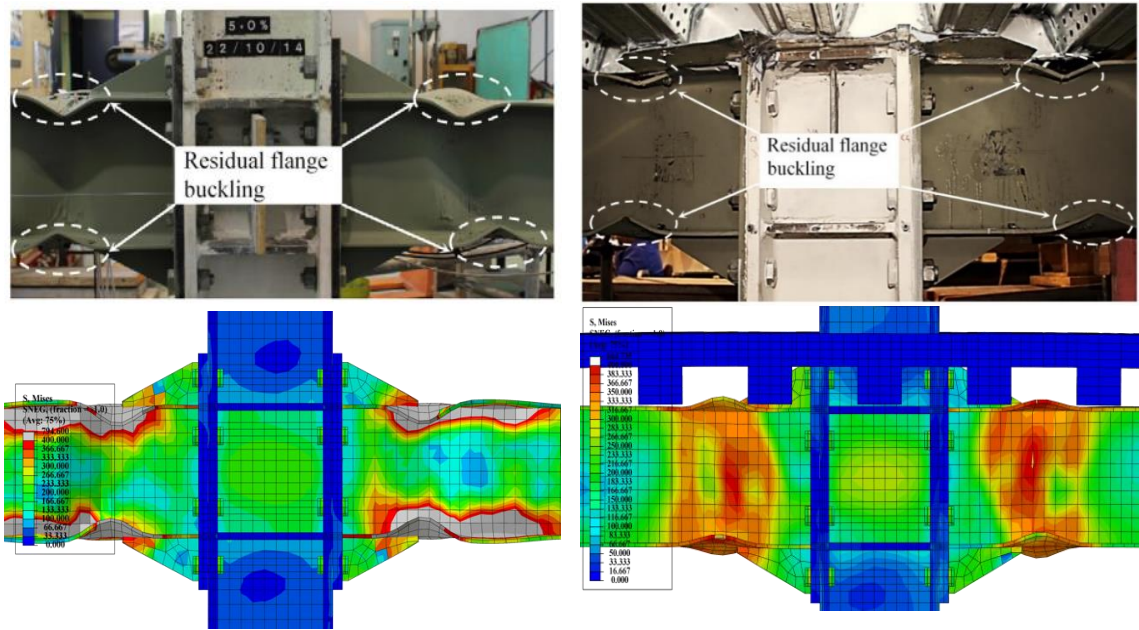


**Figure 3.16: Comparison of local buckling between experimental tests (Chaudhari, 2017; Chaudhari et al., 2019) and FE model (with render the thickness of the shell elements).**

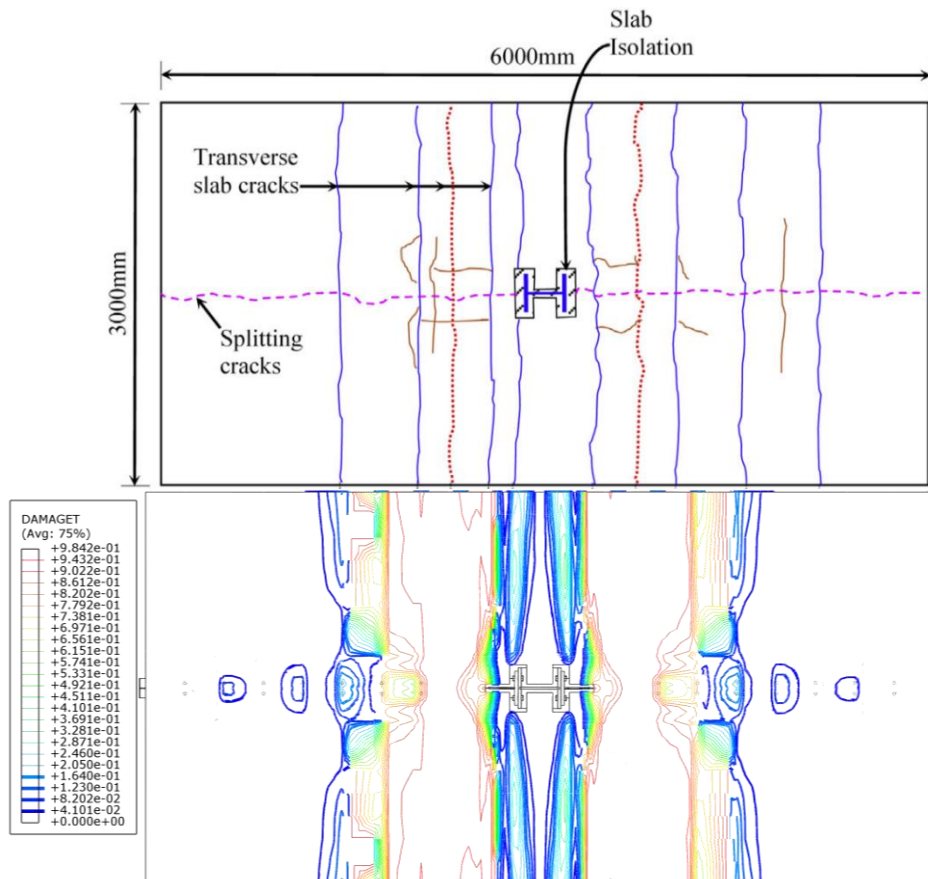


**Figure 3.17: Comparison of concrete cracks between experimental test (Chaudhari, 2017; Chaudhari et al., 2019) and FE model.**



### 3.4 Parametric study

#### 3.4.1 Model description

Using the modelling approach outlined in the previous sections, a parametric study was undertaken to study the effects of varying configurations of the RWS connection on response to cyclic actions. The focus was made on the following:

- i) End-distance from the face of extended end-plate connections to the web opening centreline ( $S_o=0.5h, 0.65h, 0.80h, h, 1.2h$ . Where  $h$  is the overall section height of the steel beam),
- ii) Web opening diameter  $d_o= 0.5h, 0.65h, 0.80h$ . and
- iii) Allocation of shear studs on the protected zone (either absent or present), leading to the provision of 9 to 7 stud rows over the whole length of the beam. The first case represents high beam-slab coupling, while the second represents low beam-slab coupling.
- iv) Both composite and non-composite RWS connections were examined simultaneously in terms of performance and load-carrying capacity.

The parameters, including web opening size and location, were chosen based on a combination of literature review and considerations for achieving a balance between maximising the benefits of the Vierendeel mechanism and maintaining adequate beam strength. This selection ensured practical relevance and facilitated comparison with existing research, as the chosen range of diameters and end-distances are commonly employed in RWS connections (e.g. (Boushehri et al., 2019). Additionally, the limitations of the end-post width ( $S_e$ ) were adhered to by following SCI P355 guidance (Lawson and Hicks, 2011). The baseline model is comprised of compact European beam and column sections, which comply with code specifications stated in Eurocodes 3, 4 and 8. Rib stiffeners were avoided, while 6 mm doubler plates were provided to strengthen and stiffen the panel zone. Table 3.1 summarises the properties of all structural elements allocated. The model was excited by a drift time history in accordance with the prequalification protocol defined in AISC 341 (ANSI/AISC 341-16, 2016), as shown in in Figure 3.18. A gap of 25mm around the column perimeter for all cases was provided, as shown in Figure 3.19 (ANSI/AISC 358-16, 2016), EN 1998-1 clause 7.7.5(1P) and (2) (CEN, 2005d). A slab thickness of 150mm corresponding to a Comflor80 metal deck was considered for all models, as done in (Chaudhari, 2017; Chaudhari et al., 2019). The characteristics of all specimens and the naming convention for each one are presented in Table 3.2 and Figure 3.20, respectively.

**Table 3.1: The dimensions and the detailed configuration of the connection in the parametric study.**

Element	Section type	Material
Slab	-----	Concrete $f'c = 30$ MPa, Rebar $f_y = 515$ MPa.
Beam	IPE300	S355
Column	HEB320	S355
Extended end-plate	530x260x25	S355
Bolt	M24	Class 10.9
Continuity plate	279x144.25x16	S355
Doubler plates	730x279x6	S355

Note: The concrete slab, studs and steel rebars were kept the same as in the experimental test (Chaudhari, 2017; Chaudhari et al., 2019).

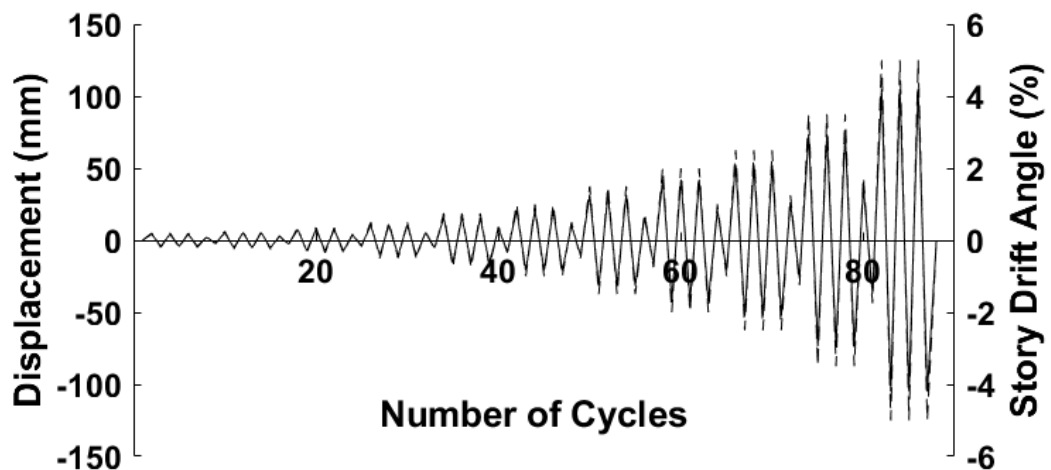


**Figure 3.18: AISC 2016 loading protocol (ANSI/AISC 341-16, 2016).**

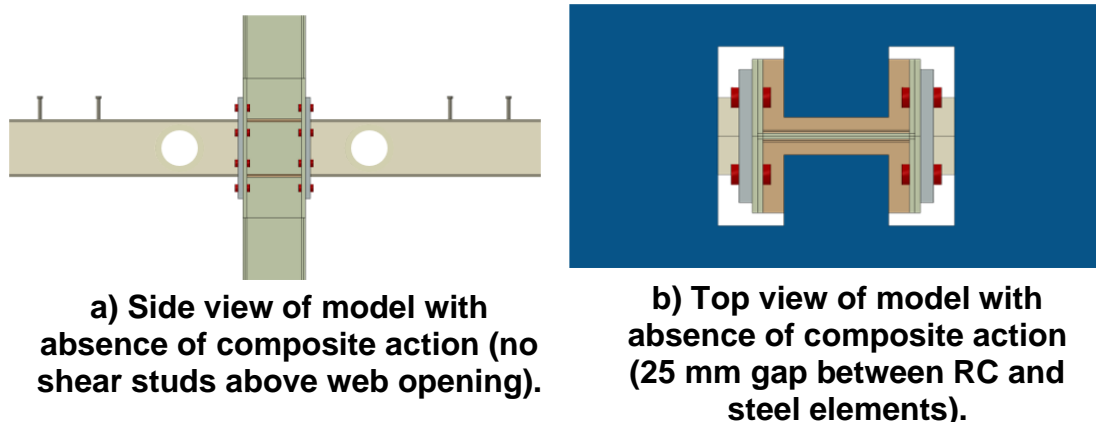


**Figure 3.19: Model with absence of composite action.**

Table 3.2: Summary of assessed specimens.

Model	Number of shear studs' rows	Composite action	Diameter $d_o$	End distance $S_o$	SCI P355
NR-NC	N/A	N/A	N/A	N/A	N/A
NR-C-H	9	High	N/A	N/A	N/A
NR-C-L	7	Low	N/A	N/A	N/A
R-C-H-50d-50S	9	High (presence) composite action	150	150	Yes
R-C-H-50d-65S			150	195	
R-C-H-50d-80S			150	240	
R-C-H-50d-100S			150	300	
R-C-H-50d-120S			150	360	No
R-C-H-65d-50S			195	150	
R-C-H-65d-65S			195	195	Yes
R-C-H-65d-80S			195	240	
R-C-H-65d-100S			195	300	
R-C-H-65d-120S			195	360	No
R-C-H-80d-50S			240	150	
R-C-H-80d-65S			240	195	
R-C-H-80d-80S			240	240	Yes
R-C-H-80d-100S			240	300	
R-C-H-80d-120S			240	360	
R-C-L-50d-50S	8	Low (absence) composite action	150	150	Yes
R-C-L-50d-65S			150	195	
R-C-L-50d-80S			150	240	
R-C-L-50d-100S			150	300	
R-C-L-50d-120S	7		150	360	No
R-C-L-65d-50S	8		195	150	
R-C-L-65d-65S			195	195	Yes
R-C-L-65d-80S			195	240	
R-C-L-65d-100S			195	300	
R-C-L-65d-120S	7		195	360	No
R-C-L-80d-50S	8		240	150	
R-C-L-80d-65S			240	195	
R-C-L-80d-80S			240	240	Yes
R-C-L-80d-100S	7		240	300	
R-C-L-80d-120S			240	360	
R-NC-50d-50S	N/A	Non-composite models	150	150	Yes
R-NC-50d-65S			150	195	
R-NC-50d-80S			150	240	

R-NC-50d-100S			150	300	
R-NC-50d-120S			150	360	
R-NC-65d-50S			195	150	No
R-NC-65d-65S			195	195	Yes
R-NC-65d-80S			195	240	
R-NC-65d-100S			195	300	
R-NC-65d-120S			195	360	
R-NC-80d-50S			240	150	No
R-NC-80d-65S			240	195	Yes
R-NC-80d-80S			240	240	
R-NC-80d-100S			240	300	
R-NC-80d-120S			240	360	

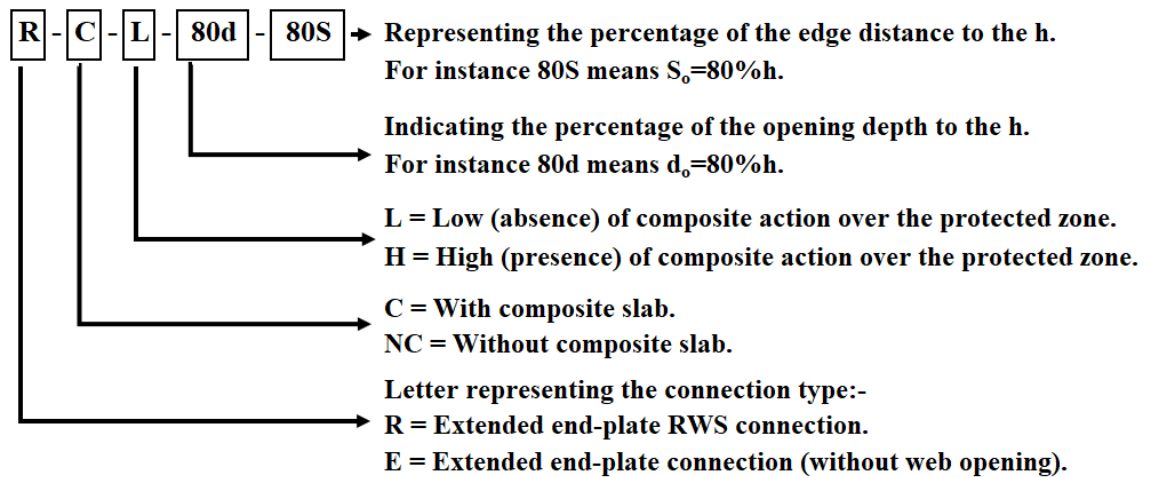
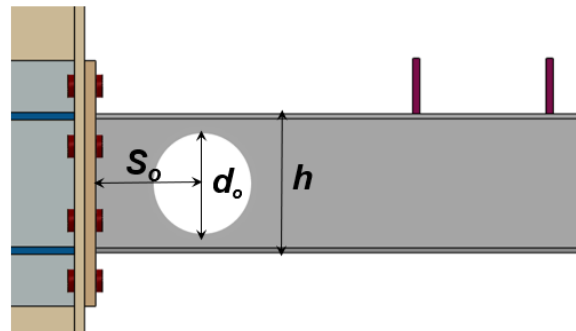


Figure 3.20: Model identifier.

### 3.4.2 Nominal capacities of the protected zones

All RWS connections were designed based on the strength of the connected steel solid-webbed beam section, denoted as  $M_{pl,a,Rd}$ , of a partial/equal-strength connection according to Eurocode 3, Eurocode 4, and Eurocode 8 (CEN, 2005a; CEN, 2005b; CEN, 2005c; CEN, 2005d). Nominal (code-specified) load-bearing capacities of the connection are expected to be governed by the full plastification of the reduced cross-section. For the case where joint slab-beam action is prevented, the nominal moment capacity is given by Eq.3.1:

$$M_{pl,Rd,RWS} = f_y \left( W_{pl} - \frac{d_o^2 t_{w,b}}{4} \right) \quad (3.1)$$

Where  $M_{pl,Rd,RWS}$  is the plastic moment considering an idealised elastoplastic material model for perforated steel section,  $f_y$  is the yield stress,  $W_{pl,y,b}$  is the plastic modulus of the steel section,  $d_o$  is the perforation diameter and  $t_{w,b}$  is the beam web thickness.

The nominal capacity of the composite section is calculated considering joint deformation of both the slab and the beam. Firstly, the steel deck is transformed into an equivalent uniform thickness slab by matching their cross-sectional areas. For this study, a 100 mm thick equivalent slab ( $t_{s,e}$ ) is found. This leads to a “virtual analysis gap” of 50 mm due to the difference amongst the equivalent thickness and the actual thickness of the steel deck. Then the effective width of the composite slab ( $b_e$ ) is calculated according to code specifications (CEN, 2005c) finding that it is 8 times the equivalent slab thickness, namely, 800 mm. The comparable cross-section for assessing the nominal moment capacity is shown in Figure 3.21.

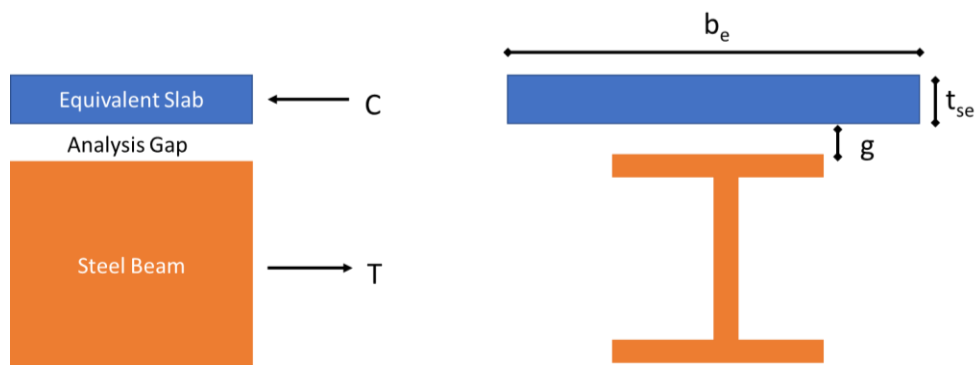


**Figure 3.21: Equivalent composite section for nominal moment capacity assessment, sagging moment.**

Then it is possible to consider Whitney's equivalent rectangular stress theory (CEN, 2005c) to find the ultimate capacity of the ensemble. Firstly, peak compressive and tensile actions on both beam and slab must be calculated, following Eqs. 3.2, and 3.3:

$$C = 0.85 f'c b_e t_{se} \quad (3.2)$$

$$T = f_y (A_g - t_w d_o) \quad (3.3)$$

where  $C$  is the compression force in the cross-section,  $f'c$  is the nominal compression resistance of concrete in the slab,  $b_e$  is the thickness of the equivalent T section to account for shear lag in the slab,  $t_{s,e}$  is the slab thickness,  $T$  is the tension load on the cross-section, and  $A_g$  is the gross cross-section of the steel beam without perforations). In this case, the tension capacity of the beam at the reduced cross-section is lower than the compression action that can be sustained within the slab. Consequently, the neutral axis will be within it. The depth of the equivalent uniform stress field is given by:

$$a = \frac{T}{0.85 f'c b_e} \quad (3.4)$$

Then the moment capacity of the cross-section can be computed by multiplying the tensile action by its lever arm on the cross-section, leading to the following expression for the nominal moment capacity ( $M_{pl,Rd}$ ):

$$M_{pl,Rd} = T \left( \frac{h}{2} + g + t_{se} - \frac{a}{2} \right) \quad (3.5)$$

Where  $h$  is the beam depth,  $g$  is the gap due to the difference between the real thickness of the steel deck and its equal-area idealization. For the hogging moment, the compression fibre is on the bottom, while the steel within the slab allows for an increase of the internal tensile action. However, only minimum reinforcement to prevent cracking due to shrinkage was provided, and consequently, its effect on capacity can be ignored. If that is the case, the hogging moment capacity will be the same as provided by the beam alone, in accordance with Eq. 3.1. A summary of the diverse nominal moment resistances is provided in Table 3.3.

**Table 3.3: Nominal moment capacities of main specimen typologies.**

Specimen	Nominal Moment Resistance [kN-m]	
	Sagging	Hogging
Non composite, Solid webbed beam	223	223
Non composite, $d_0 = 0.80h$	187	187
Non composite, $d_0 = 0.65h$	199	199
Non composite, $d_0 = 0.5h$	209	209
composite, Solid webbed beam	485	223
composite, $d_0 = 0.80h$	360	187
composite, $d_0 = 0.65h$	388	199
composite, $d_0 = 0.5h$	416	209
The capacity of the connection, $M_{(c,Rd)}$ , designed following the components method outlined in Eurocode 3-1-8 (CEN, 2005b) equal 216 kN.m		

### 3.5 Parametric results

Lateral load and interstorey drift relationships are depicted in Figures 3.22, 3.23 and 3.24. For all cases, wide and stable hysteresis cycles without pinching are observed. Likewise, drifting away from the zero ordinate is at most slight, indicating that residual deformations are symmetrical, following the loading protocol. This indicates that buckling of end plates and yielding outside protected zones was mild, leading to symmetrical strain reversals.

The analysis was terminated when the specimen reached an interstorey drift of 6%; a loss of moment capacity larger than 20% of the maximum value was observed; the analysis failed to converge or there was a failure of any of the shear studs or bolts in the end plate. The great majority of RWS of specimens (84%) achieved the 6% threshold and all exceeded a 4% interstorey drift demand. The latter is the performance standard that a connection must satisfy if it is going to be used in special moment-resisting frames, according to AISC-341 16 specifications (ANSI/AISC 341-16, 2016). Results are summarised in Tables 3.4 and 3.5.

In addition to the RWS specimens that met the 6% threshold criteria, it is essential to note that a subset of specimens did not satisfy this criterion during the analysis. These specimens exhibited deviations from the expected response. Although the proportion of specimens that did not meet the 6% threshold was relatively small (16%), it is imperative to understand the factors contributing to their performance, as discussed in Section 3.5.3. A further thorough examination of these FE models revealed that these specimens experienced more severe buckling of end plates, flange/web buckling and yielding outside protected zones, resulting in a brittle response.

Table 3.6 showcases the observed moment capacity of the beam normalized by the bare section nominal moment capacity (without a slab). At most, it is observed that peak moment resistance reaches 1.5 times the nominal capacity of the bare, reduced steel section. Contrarily, for all perforation sizes considered in this study, the moment capacity of the composite cross-section ranges between 1.9 and 2 times the capacity of the beam with perforations at the critical (smallest) cross-section (Table 3.3). This is expected as full plastification of the reduced cross-section solely in tension is unlikely to happen before the full development of the Vierendeel mechanism along the perforation edges. For that reason, it is more sensible to express the maximum moment capacity of the connection in terms of the plastification moment of the bare steel reduced section, according to Eq.3.1, and presented in Table 3.6.



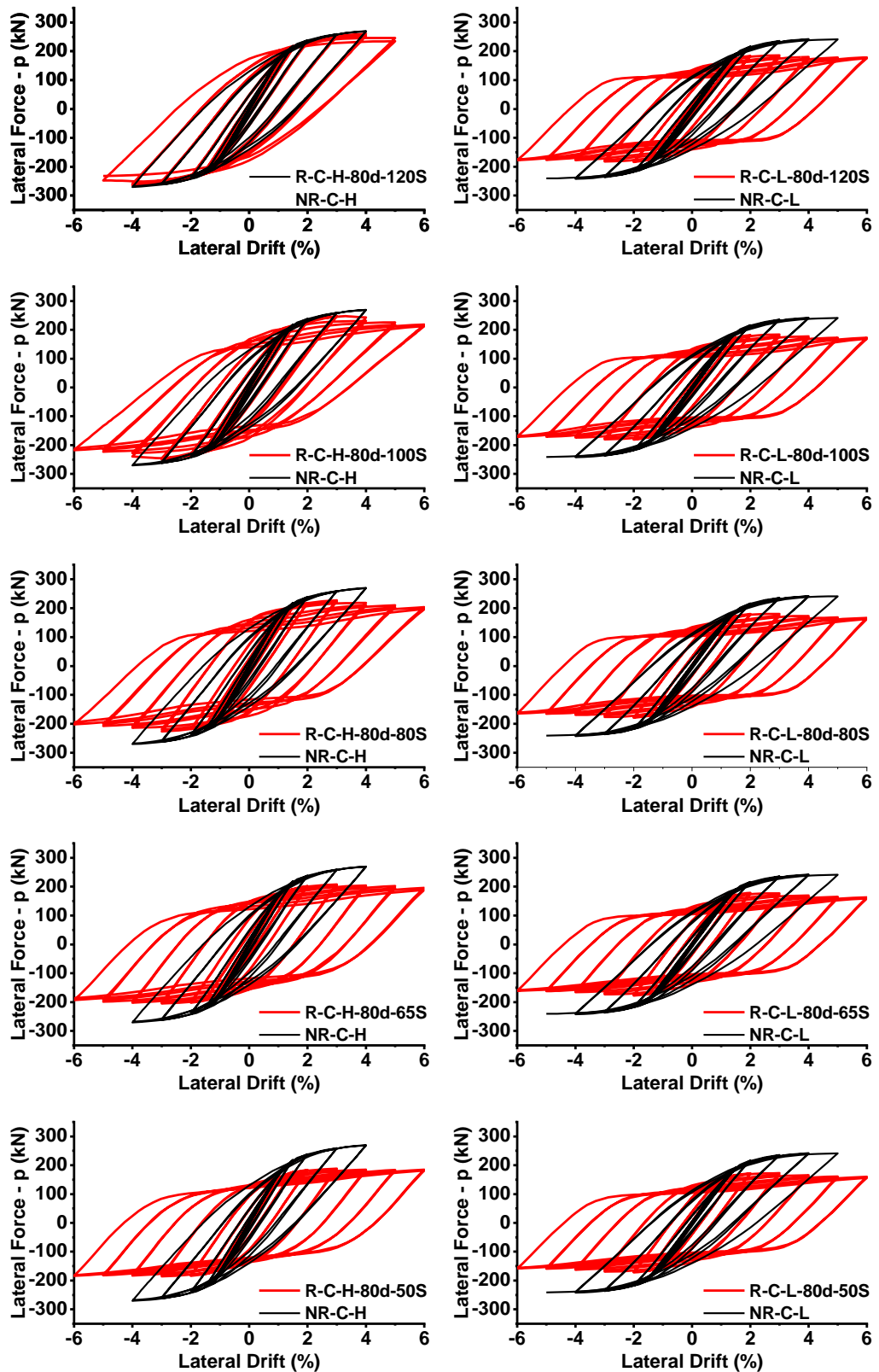


Figure 3.22: Hysteretic curves of solid model and models with the diameter of the opening equal to  $0.8h$ .

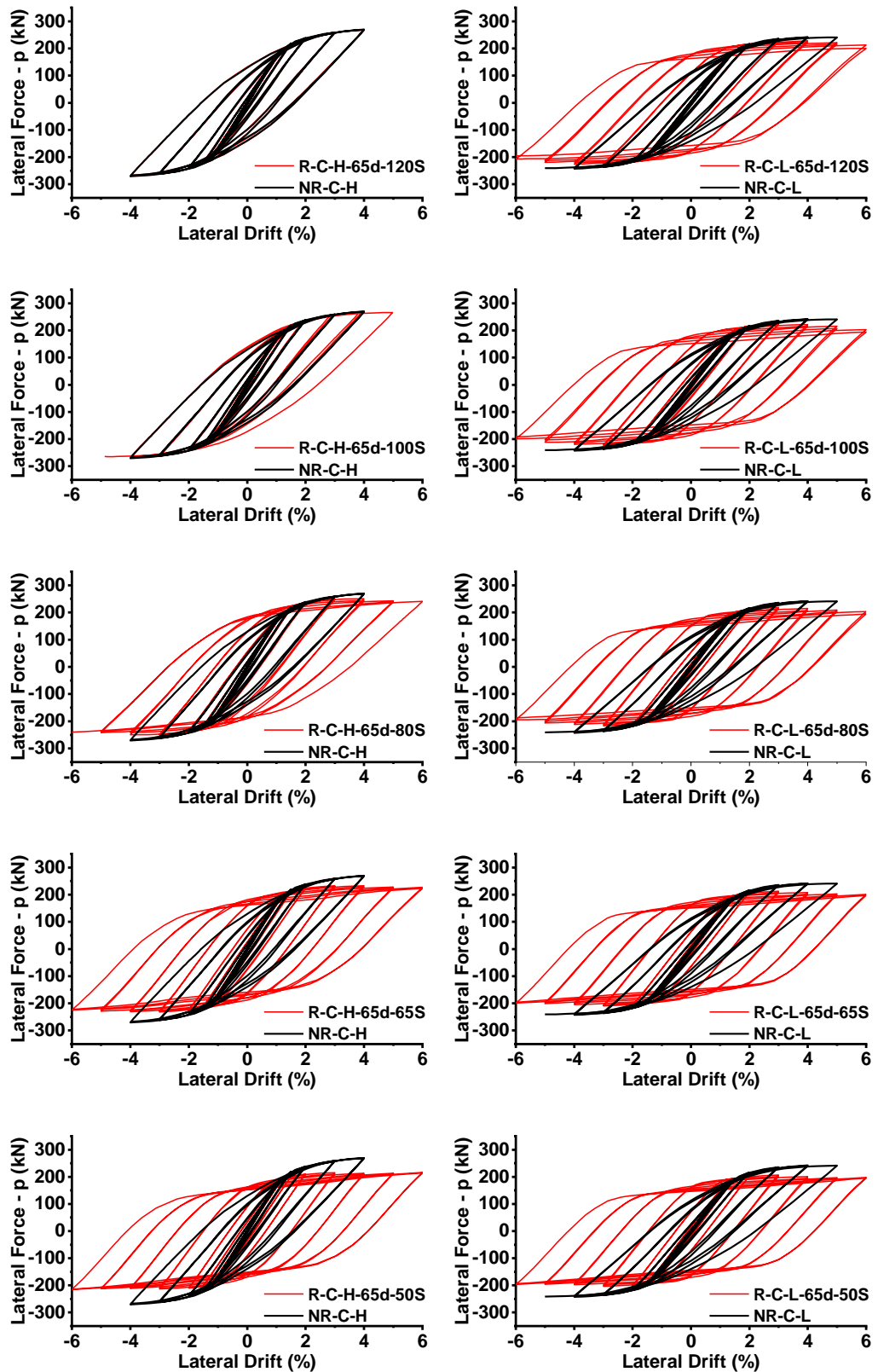


Figure 3.23: Hysteretic curves of solid model and models with the diameter of the opening equal to  $0.65h$

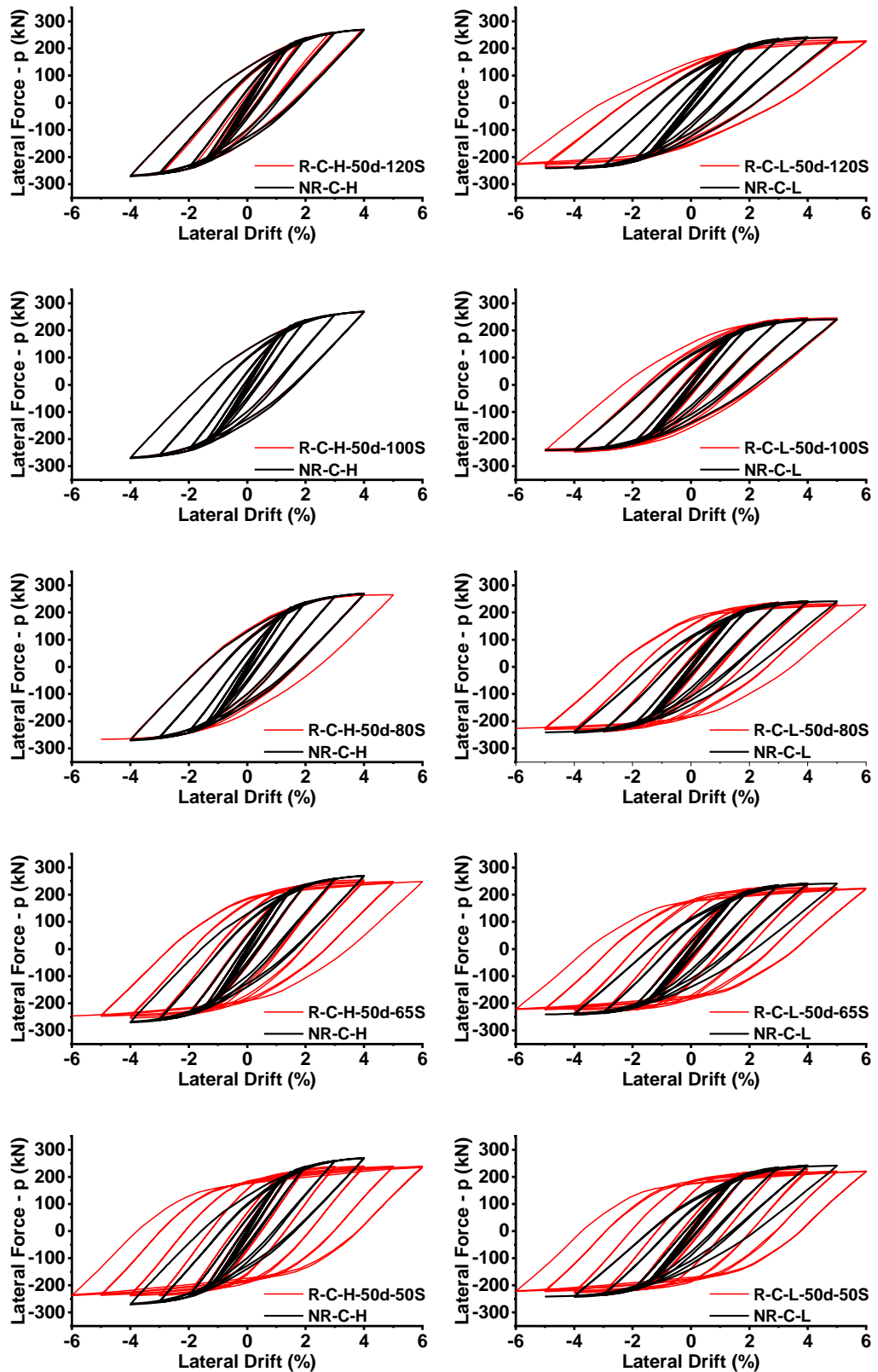


Figure 3.24: Hysteretic curves of solid model and models with the diameter of the opening equal to  $0.5h$ .

**Table 3.4: Load capacity, initial stiffness and strength degradation of all connections.**

Models	Lateral Load (kN)		Initial rotational stiffness $K_i$ (kN.rad)	Strength degradation (%)	
	sag	hog		sag	hog
NR-C-L	242.0	242.4	30912	0.4	0.6
NR-C-H	269.5	270.3	38920	0.0	0.0
NR-NC	232.1	230.1	24612	16.4	15.6
R-C-L-80d-120S	185.6	183.6	28868	3.6	3.2
R-C-L-80d-100S	183.7	181.1	28924	6.2	5.6
R-C-L-80d-80S	180.0	179.2	31248	7.9	8.3
R-C-L-80d-65S	178.1	177.2	31248	8.8	9.1
R-C-L-80d-50S	172.4	171.9	31080	7.4	8.1
R-C-H-80d-120S	260.8	264.6	36232	5.8	6.4
R-C-H-80d-100S	247.6	249.4	36400	11.8	12.8
R-C-H-80d-80S	227.4	226.0	36120	10.6	10.9
R-C-H-80d-65S	207.7	204.6	35532	5.9	5.8
R-C-H-80d-50S	188.2	185.8	34384	2.0	1.1
R-NC-80d-120S	182.0	180.3	23660	21.3	21.3
R-NC-80d-100S	178.5	177.3	23688	20.1	20.4
R-NC-80d-80S	173.6	173.4	23688	19.8	20.7
R-NC-80d-65S	175.4	175.1	23688	21.4	22.2
R-NC-80d-50S	169.7	169.0	23688	22.2	22.6
R-C-L-65d-120S	227.7	226.4	30156	6.8	8.8
R-C-L-65d-100S	224.8	223.5	32900	9.8	10.9
R-C-L-65d-80S	218.1	216.3	32956	7.1	10.0
R-C-L-65d-65S	212.3	209.8	32956	5.5	5.0
R-C-L-65d-50S	206.5	203.9	32956	4.4	3.6
R-C-H-65d-120S	268.5	269.2	37716	0.0	0.0
R-C-H-65d-100S	266.1	268.0	37659	0.2	1.5
R-C-H-65d-80S	250.2	251.0	37604	3.8	4.5
R-C-H-65d-65S	232.9	231.8	37352	2.7	2.7
R-C-H-65d-50S	216.0	215.7	36904	0.0	0.0
R-NC-65d-120S	217.3	214.9	24304	16.7	21.1
R-NC-65d-100S	211.4	210.7	24248	14.4	14.8
R-NC-65d-80S	208.7	208.4	24276	19.3	19.3
R-NC-65d-65S	204.8	204.4	24304	15.9	16.8
R-NC-65d-50S	201.7	201.4	24304	20.0	19.4
R-C-L-50d-120S	241.7	242.1	30632	5.7	6.3
R-C-L-50d-100S	247.5	248.4	33600	4.2	5.2
R-C-L-50d-80S	240.6	238.9	33600	5.4	5.5
R-C-L-50d-65S	234.1	234.3	33628	4.6	5.0
R-C-L-50d-50S	229.0	228.1	33628	3.6	2.6

Continued Table 3.4

Models	Lateral Load (kN)		Initial rotational stiffness $K_i$ (kN.rad)	Strength degradation (%)	
	sag	hog			sag
<b>R-C-H-50d-120S</b>	269.6	270.9	38360	0.0	0.0
<b>R-C-H-50d-100S</b>	268.8	269.9	38360	0.0	0.0
<b>R-C-H-50d-80S</b>	267.0	268.8	38360	0.7	1.0
<b>R-C-H-50d-65S</b>	254.6	253.7	38304	2.6	2.8
<b>R-C-H-50d-50S</b>	239.9	238.3	38052	0.3	0.3
<b>R-NC-50d-120S</b>	229.4	226.7	24472	15.0	14.6
<b>R-NC-50d-100S</b>	225.7	224.0	24472	16.0	15.4
<b>R-NC-50d-80S</b>	223.9	222.7	24472	16.9	15.1
<b>R-NC-50d-65S</b>	221.9	221.2	24500	16.5	15.5
<b>R-NC-50d-50S</b>	220.9	220.5	24528	14.4	14.5

Table 3.5: Interstory drift deformation capacity of all specimens.

Models	Yield rotation $\theta_y$ (%rad)		Ultimate rotation $\theta_u$ (%rad)		Ductility		Dissipated energy (kN.m)
	sag	hog	sag	hog	sag	hog	
NR-C-L	1.79	1.79	5.00	5.00	2.79	2.79	15.27
NR-C-H	1.59	1.59	4.00	4.00	2.52	2.52	13.95
NR-NC	2.14	2.14	6.00	6.00	2.80	2.80	27.26
R-C-L-80d-120S	1.39	1.39	6.00	6.00	4.32	4.32	23.26
R-C-L-80d-100S	1.35	1.35	6.00	6.00	4.44	4.44	23.00
R-C-L-80d-80S	1.25	1.25	6.00	6.00	4.80	4.80	23.22
R-C-L-80d-65S	1.24	1.24	6.00	6.00	4.84	4.84	22.74
R-C-L-80d-50S	1.35	1.35	6.00	6.00	4.44	4.44	22.25
R-C-H-80d-120S	1.63	1.65	5.00	5.00	3.07	3.03	21.55
R-C-H-80d-100S	1.50	1.50	6.00	6.00	4.00	4.00	27.86
R-C-H-80d-80S	1.39	1.39	6.00	6.00	4.32	4.32	28.15
R-C-H-80d-65S	1.33	1.31	6.00	6.00	4.51	4.58	27.73
R-C-H-80d-50S	1.21	1.21	6.00	6.00	4.96	4.96	23.50
R-NC-80d-120S	1.65	1.65	6.00	6.00	3.64	3.64	23.54
R-NC-80d-100S	1.65	1.64	6.00	6.00	3.64	3.66	23.49
R-NC-80d-80S	1.60	1.60	6.00	6.00	3.75	3.75	23.30
R-NC-80d-65S	1.60	1.60	6.00	6.00	3.75	3.75	22.73
R-NC-80d-50S	1.55	1.55	6.00	6.00	3.87	3.87	20.96
R-C-L-65d-120S	1.75	1.75	6.00	6.00	3.43	3.43	30.21
R-C-L-65d-100S	1.60	1.60	6.00	6.00	3.75	3.75	30.73
R-C-L-65d-80S	1.50	1.50	6.00	6.00	4.00	4.00	30.61
R-C-L-65d-65S	1.50	1.45	6.00	6.00	4.00	4.14	27.64
R-C-L-65d-50S	1.40	1.40	6.00	6.00	4.29	4.29	26.81
R-C-H-65d-120S	1.51	1.51	4.00	4.00	2.65	2.65	14.00
R-C-H-65d-100S	1.51	1.51	4.98	4.88	3.30	3.23	13.92
R-C-H-65d-80S	1.50	1.50	6.00	6.00	4.00	4.00	27.20
R-C-H-65d-65S	1.38	1.38	6.00	6.00	4.35	4.35	30.66
R-C-H-65d-50S	1.29	1.29	6.00	6.00	4.65	4.65	26.97
R-NC-65d-120S	1.95	1.90	6.00	6.00	3.08	3.16	28.34
R-NC-65d-100S	1.90	1.89	6.00	6.00	3.16	3.17	28.54
R-NC-65d-80S	1.88	1.88	6.00	6.00	3.19	3.19	28.71
R-NC-65d-65S	1.75	1.80	6.00	6.00	3.43	3.33	28.87
R-NC-65d-50S	1.80	1.80	6.00	6.00	3.33	3.33	28.10
R-C-L-50d-120S	1.80	1.80	6.00	6.00	3.33	3.33	24.38
R-C-L-50d-100S	1.69	1.69	5.00	5.00	2.96	2.96	17.73
R-C-L-50d-80S	1.68	1.69	6.00	6.00	3.57	3.55	25.46
R-C-L-50d-65S	1.61	1.61	6.00	6.00	3.73	3.73	28.83
R-C-L-50d-50S	1.60	1.60	6.00	6.00	3.75	3.75	29.72

Continued Table 3.5

Models	Yield rotation $\theta_y$ (%rad)		Ultimate rotation $\theta_u$ (%rad)		Ductility		Dissipated energy (kN.m)
	sag	hog	sag		sag	hog	
<b>R-C-H-50d-120S</b>	1.58	1.58	3.96	3.98	2.51	2.52	13.92
<b>R-C-H-50d-100S</b>	1.55	1.55	4.00	4.00	2.58	2.58	14.03
<b>R-C-H-50d-80S</b>	1.53	1.53	5.00	5.00	3.27	3.27	14.72
<b>R-C-H-50d-65S</b>	1.45	1.45	6.00	6.00	4.14	4.14	27.16
<b>R-C-H-50d-50S</b>	1.40	1.40	6.00	6.00	4.29	4.29	28.20
<b>R-NC-50d-120S</b>	2.00	2.00	6.00	6.00	3.00	3.00	27.59
<b>R-NC-50d-100S</b>	1.98	1.98	6.00	6.00	3.03	3.03	27.69
<b>R-NC-50d-80S</b>	1.98	1.98	6.00	6.00	3.03	3.03	27.95
<b>R-NC-50d-65S</b>	1.97	1.97	6.00	6.00	3.05	3.05	27.86
<b>R-NC-50d-50S</b>	1.95	1.95	6.00	6.00	3.08	3.08	28.14

Note: Sag = sagging and hog = hogging. They refer to the direction of the applied load. Sag is when the actuator pushes to the right, while hog is when it pulls to the left.

Table 3.6: Attained moment capacities for right beam.

Models	Normalized max $\frac{M_f}{M_{pl,a,Rd}}$		Normalized max $\frac{M_o}{M_{pl,Rd,RWS}}$	
	(sag)	(hog)	(sag)	(hog)
NR-C-L	1.14	-1.05	N/A	N/A
NR-C-H	1.19	-1.22	N/A	N/A
NR-NC	1.03	-1.02	N/A	N/A
R-C-L-80d-120S	1.01	-0.86	1.06	-0.90
R-C-L-80d-100S	0.96	-0.86	1.03	-0.92
R-C-L-80d-80S	0.88	-0.88	0.97	-0.96
R-C-L-80d-65S	0.86	-0.86	0.96	-0.96
R-C-L-80d-50S	0.89	-0.83	1.01	-0.94
R-C-H-80d-120S	1.34	-1.20	1.40	-1.25
R-C-H-80d-100S	1.38	-1.12	1.48	-1.20
R-C-H-80d-80S	1.30	-0.97	1.42	-1.06
R-C-H-80d-65S	1.17	-0.90	1.31	-1.00
R-C-H-80d-50S	1.03	-0.83	1.17	-0.94
R-NC-80d-120S	0.80	-0.80	0.84	-0.83
R-NC-80d-100S	0.79	-0.78	0.84	-0.84
R-NC-80d-80S	0.77	-0.77	0.84	-0.84
R-NC-80d-65S	0.78	-0.77	0.86	-0.86
R-NC-80d-50S	0.75	-0.75	0.85	-0.85
R-C-L-65d-120S	1.10	-1.01	1.08	-0.99
R-C-L-65d-100S	1.06	-1.02	1.06	-1.02
R-C-L-65d-80S	1.05	-0.99	1.08	-1.01
R-C-L-65d-65S	1.00	-0.95	1.05	-1.00
R-C-L-65d-50S	1.01	-0.91	1.07	-0.97
R-C-H-65d-120S	1.15	-1.22	1.13	-1.20
R-C-H-65d-100S	1.22	-1.21	1.22	-1.21
R-C-H-65d-80S	1.29	-1.14	1.32	-1.17
R-C-H-65d-65S	1.20	-1.04	1.26	-1.08
R-C-H-65d-50S	1.11	-0.95	1.17	-1.01
R-NC-65d-120S	0.96	-0.95	0.94	-0.93
R-NC-65d-100S	0.94	-0.93	0.94	-0.93
R-NC-65d-80S	0.92	-0.92	0.95	-0.94
R-NC-65d-65S	0.91	-0.90	0.95	-0.94
R-NC-65d-50S	0.89	-0.89	0.95	-0.94
R-C-L-50d-120S	1.23	-1.05	1.15	-0.98
R-C-L-50d-100S	1.21	-1.08	1.16	-1.03
R-C-L-50d-80S	1.21	-1.05	1.18	-1.03
R-C-L-50d-65S	1.20	-1.03	1.19	-1.03
R-C-L-50d-50S	1.18	-1.01	1.19	-1.03
R-C-H-50d-120S	1.16	-1.23	1.08	-1.15



Continued Table 3.6

Models	Normalized max $\frac{M_o}{M_{pl,Rd,RWS}}$		Normalized max $\frac{M_o}{M_{pl,Rd,RWS}}$	
	(sag)	(hog)	(sag)	(hog)
<b>R-C-H-50d-100S</b>	1.17	-1.22	1.12	-1.17
<b>R-C-H-50d-80S</b>	1.25	-1.22	1.22	-1.19
<b>R-C-H-50d-65S</b>	1.28	-1.15	1.27	-1.15
<b>R-C-H-50d-50S</b>	1.20	-1.08	1.21	-1.10
<b>R-NC-50d-120S</b>	1.01	-1.00	0.95	-0.93
<b>R-NC-50d-100S</b>	1.00	-0.99	0.95	-0.94
<b>R-NC-50d-80S</b>	0.99	-0.99	0.97	-0.96
<b>R-NC-50d-65S</b>	0.98	-0.98	0.98	-0.97
<b>R-NC-50d-50S</b>	0.98	-0.97	0.99	-0.99

Note:  $M_{pl,a,Rd}$  = nominal plastic strength of the connected steel beam;  $M_{pl,Rd,RWS}$  = nominal plastic strength of the connected perforated steel beam based on equation (1);  $M_{c,Rd}$  = 215.6 kNm, the design resistance of the joint according to Eurocode 3 (CEN, 2005a);  $M_f$  = maximum beam moment at column face;  $M_o$  = maximum beam moment at the centre of web opening.

### 3.5.1 Effect of web opening diameter ( $d_o$ )

Results for perforated beams with an opening equal to 80% of the beam's height indicate that the nominal capacity of the bare beam is reached if low composite action is present, as peak moment ranges between 0.9 and 1.06 the nominal value, being 0.94 the average for the hogging moment and 1.00 for the sagging moment. This is expected as the slab provides an additional constraint to buckling and bending of the upper plastic hinges that make up the Vierendeel mechanism. Yet, as the ratio is close to one, it can be considered that both the Vierendeel Mechanism and the yielding of the critical cross-section are concurrent. When high composite action is enforced, moment capacity increases sizably but is not enough to reach what is expected for the composite section, which is close to double the plastification moment of the bare section alone with tension in the upper flange and compression at the bottom (Table 3.3). The average values for the ratio between the peak moment observed and the nominal capacity of the bare steel section are 1.09 and 1.36 for hogging and sagging moment capacity, while minimum and maximum values are 0.94 and 1.48. As observed in the previous case, there is a significant difference between sagging and hogging moments, which is explained by the additional constraint on buckling. There is a slight reduction in capacity as the perforation is made closer to the column, but the data does not indicate a clear trend. Still, it is a good course of action to follow

SCI P355 guidelines in that regard; thus, allowing for a space of at least one perforation diameter from the column face to the centre of the perforation.

When composite action is impeded in specimens with  $d_o = 0.8h$  (i.e., non-composite), the peak moment reaches values that range between 0.86 and 0.83 of the nominal capacity, being similar for both sagging and hogging moment. Avoidance of shear transfer studs allows for relative slippage between the steel section and the slab; thus, buckling is more likely to occur, making behaviour being controlled by the development of the Vierendeel mechanism along the opening edges. On other hand, results indicate that there is a limited role of the spacing between the column face and the perforation.

All cases reached a story drift of 6%, except the specimen with high composite action with the first perforation allocated at a distance from the column equal to 1.2 times the height of the beam (R-C-H-80d-120S). As the analysis was terminated at this threshold, ductility estimates are lower-bound. Still, cases where there is low or high beam-slab interaction show interstorey drift ductility larger than 4, while for cases where the interaction was prevented, it ranges between 4 and 3 (Table 3.5).

Lower diameter perforations (0.65h and 0.5h) uncover the effect of overextending the distance between the column face and the centre of the perforation. For spacings,  $S=1.2h$  and  $1.0h$  the observed ultimate interstorey drift is less than 6%; yet, it is larger than 4.0% or close to this value (values of 3.96% were obtained for specimen R-C-H-50d-120S) indicating that even for these configurations, performance would allow for inclusion in special moment frames (ANSI/AISC 341-16, 2016). Nevertheless, going beyond SCI P355 recommendations is not advisable and can diminish deformation capacity significantly.

The ratio of peak moment capacity to nominal resistance reduces significantly as the opening size becomes smaller. For  $d_o = 0.65h$  and beams with high composite action; the average value is 1.22 for the sagging moment and 1.13 for the hogging moment, which is 10% less than was observed for the beam with  $d_o = 0.8h$ , whilst the difference is marginal for the hogging moment. For  $d_o = 0.5h$  with high composite action; averages for ratios of observed peak resistances and nominal values for sagging and hogging moment are 1.18 and 1.15 respectively. Thus, for that case, capacity increases as a by-product of strengthening of T-stubs following the Vierendeel mechanism, rather than true composite action. For  $d_o = 0.5h$  and  $0.65h$  specimens with low and no composite action, resistance ranges between 1.19 and 0.93 times the nominal capacity, observing comparable results for both sagging and hogging moments.

### 3.5.2 Strength degradation

Load capacity was checked at the end of the last load cycle. Table 3.4 shows strength degradation for all models. Remarkably, the great majority (84%) of RWS specimens reached an interstorey drift of 6% while being able to attain a capacity larger than 80% of the maximum observed value. In all cases, peak achieved moments in hysteresis cycles whilst drift demand was less than 4% were larger than 80% of the maximum, making all specimens compliant with the requirements for their deployment into special moment frames, according to AISC (ANSI/AISC 358-16, 2016).

All non-composite RWS and solid models (i.e., no slab) experienced a large strength degradation of up to 22.6% due to the absence of bracing which makes them susceptible to lateral-torsional buckling. Whilst for beams with low-composite action, where a limited number of studs is provided even in the protected zone; but not enough for full shear transfer amongst slab and beam, strength loss is at most 10.9% and the average reaches 6.3%. For beams with full composite action, even with studs within the protected zone, the average strength degradation reaches 3.2%, but the result is highly influenced by outliers where large openings are provided ( $d_o = 0.8h$ ). Clearly, the slab has a positive effect in controlling out-of-plane buckling of the reduced web section, making it highly unlikely if the perforation diameter is equal or less than 0.65 times the beam depth. For larger diameters, namely, 80% of the beam's depth, noticeable but limited, strength degradation is observed, reaching, at most 12.8%.

### 3.5.3 Failure modes and stress and strain distribution

As stated before, all specimens reached a 4% interstorey drift demand without significant loss of structural integrity, making them suitable for use in special moment frames. Moreover, most achieved a 6% interstorey drift without losing their load-bearing capacity. However, there are significant differences in how this performance was achieved, as outlined in Table 3.7. It is worth noting that specific failure mechanisms are identified through individual scrutiny of each model, aiding in the understanding of observed responses.

In overall terms, the provision of perforations leads to a protected zone where inelastic action can happen without global instability, as shown in Figures 3.25-3.32. This is accomplished by yielding through the Vierendeel Mechanism and plastification of the reduced cross-section. The latter also induces buckling without tearing the bottom flange due to strain reversals in tension and compression. These mechanisms preserve the gravitational load-bearing capacity of the connection, thereby allowing for extensive deformation capacity.

**Table 3.7: FE results of the contribution of composite action for right beam and failure modes.**

Model	Number of shear studs' rows	Contribution of composite action		Failure modes
		Sag	Hog	
NR-C-H	9	15.8%	20.5%	BF & BE
NR-C-L	7	10.6%	3.5%	BF & BE
R-C-H-80d-120S	9	66.6%	50.8%	VM, BF, & BE
R-C-H-80d-100S		74.9%	43.0%	VM, BF, & BE
R-C-H-80d-80S		69.3%	26.1%	VM
R-C-H-80d-65S		51.5%	16.7%	VM
R-C-H-80d-50S		37.6%	10.9%	VM
R-C-H-65d-120S		19.9%	28.9%	BF, FB, & BE
R-C-H-65d-100S		30.5%	29.9%	BF, FB, WB & BE
R-C-H-65d-80S		39.8%	24.3%	BF, WB & BE
R-C-H-65d-65S		32.9%	14.7%	FB, & WB
R-C-H-65d-50S		24.1%	6.9%	FB, & WB
R-C-H-50d-120S		13.9%	23.3%	BF, FB, & BE
R-C-H-50d-100S		17.3%	23.7%	BF, FB, & BE
R-C-H-50d-80S		25.8%	23.8%	BF, FB, & BE
R-C-H-50d-65S		29.9%	18.0%	BF, FB, WB & BE
R-C-H-50d-50S	22.7%	11.1%	FB, WB & BE	
R-C-L-80d-120S	7	25.8%	8.2%	VM
R-C-L-80d-100S		21.9%	9.7%	VM
R-C-L-80d-80S	8	15.1%	14.4%	VM
R-C-L-80d-65S		11.6%	11.1%	VM
R-C-L-80d-50S		18.6%	11.2%	VM
R-C-L-65d-120S	7	14.5%	6.8%	VM & WB
R-C-L-65d-100S	8	13.5%	9.8%	VM & WB
R-C-L-65d-80S		14.1%	7.3%	VM & WB
R-C-L-65d-65S		10.8%	5.7%	VM
R-C-L-65d-50S		13.3%	2.7%	VM
R-C-L-50d-120S	7	21.2%	5.3%	BF, FB, & BE
R-C-L-50d-100S	8	21.1%	8.9%	BF, FB, & BE
R-C-L-50d-80S		22.2%	6.7%	BF, FB, & BE
R-C-L-50d-65S		21.6%	5.5%	VM, FB, & BE
R-C-L-50d-50S		20.4%	4.1%	VM, FB, & BE

Note: BF = bolt bending (exceeded its capacity); BE= bending of extended end-plate; FB = flange buckling; WB = web buckling; and VM = Vierendeel mechanism. + ve and - ve refer to sagging and hogging moments of the right beam, respectively.

Although inelastic action is prevented on the column, bending of bolts and buckling of end plates are observed. These undesired, potentially fragile phenomena occur in RWS specimens with low composite action and with a perforation diameter of 0.5 times the beam height only (Figures 3.25 and 3.26). For RWS specimens where shear studs are provided in the protected zone, they occur in almost all cases. For specimens with a perforation diameter equal to  $0.8h$ , the formation of the Vierendeel mechanism is inevitable (Figures 3.29 and 3.30). Also, it developed in those specimens with a perforation diameter equal to  $0.65h$  having low composite action (Figures 3.27 and 3.28).

However, it must be stressed that these undesired events occur for a large interstorey drift demand, in excess of 4% and could be potentially limited if capacity design principles are applied considering the specific features of RWS connections, as detailing is done in accord with testing for non RWS specimens. Possible strategies are: designing end plates to consider the effective plastification capacity of the composite section, whilst accounting for steel strain hardening, and elimination of shear studs above the plastic zone, to allow for the formation of Vierendeel mechanism, alike bare steel beams. It must be stressed that out of plane instability and tearing of structural elements, either beams, columns or joints was avoided.

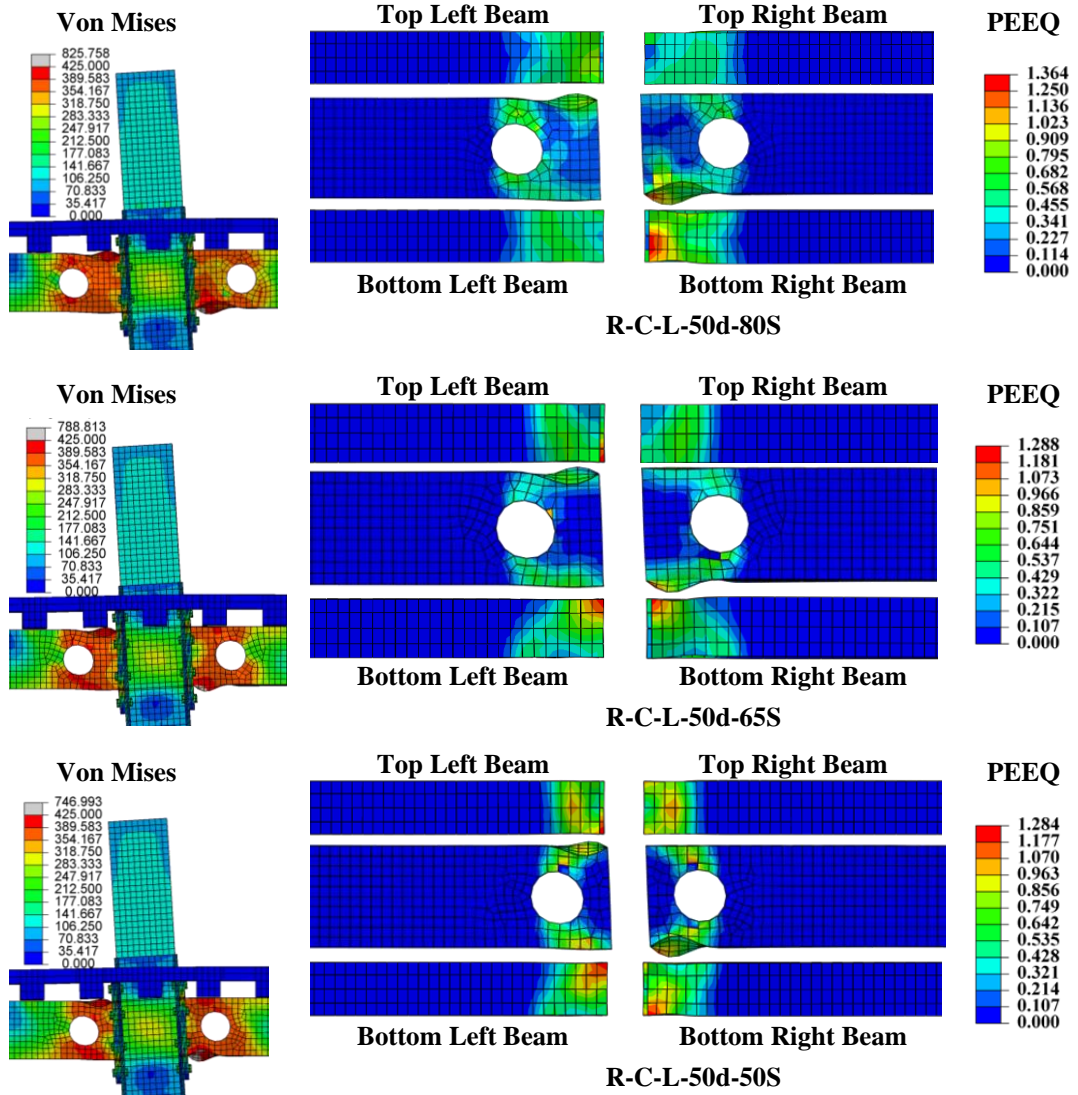


Figure 3.25: PEEQ and stresses distribution in last cycle of RWS models with  $d_o = 0.5h$  and  $S_o$  were complied with SCI P355 guidance (no shear studs over the protected zone).

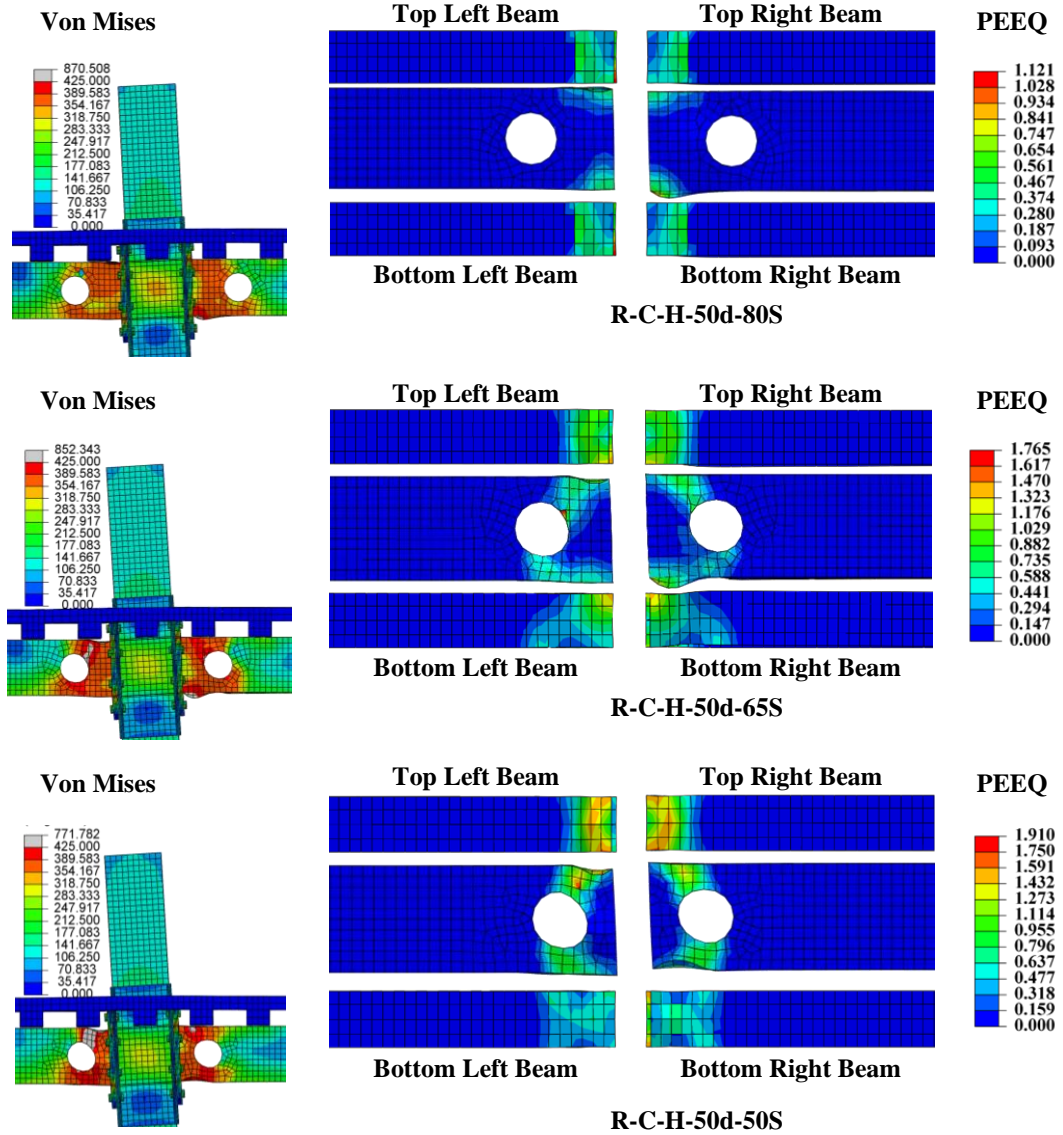


Figure 3.26: PEEQ and stresses distribution in last cycle of RWS models with  $d_o = 0.5h$  and  $S_o$  were complied with SCI P355 guidance (presence of shear studs over the protected zone).

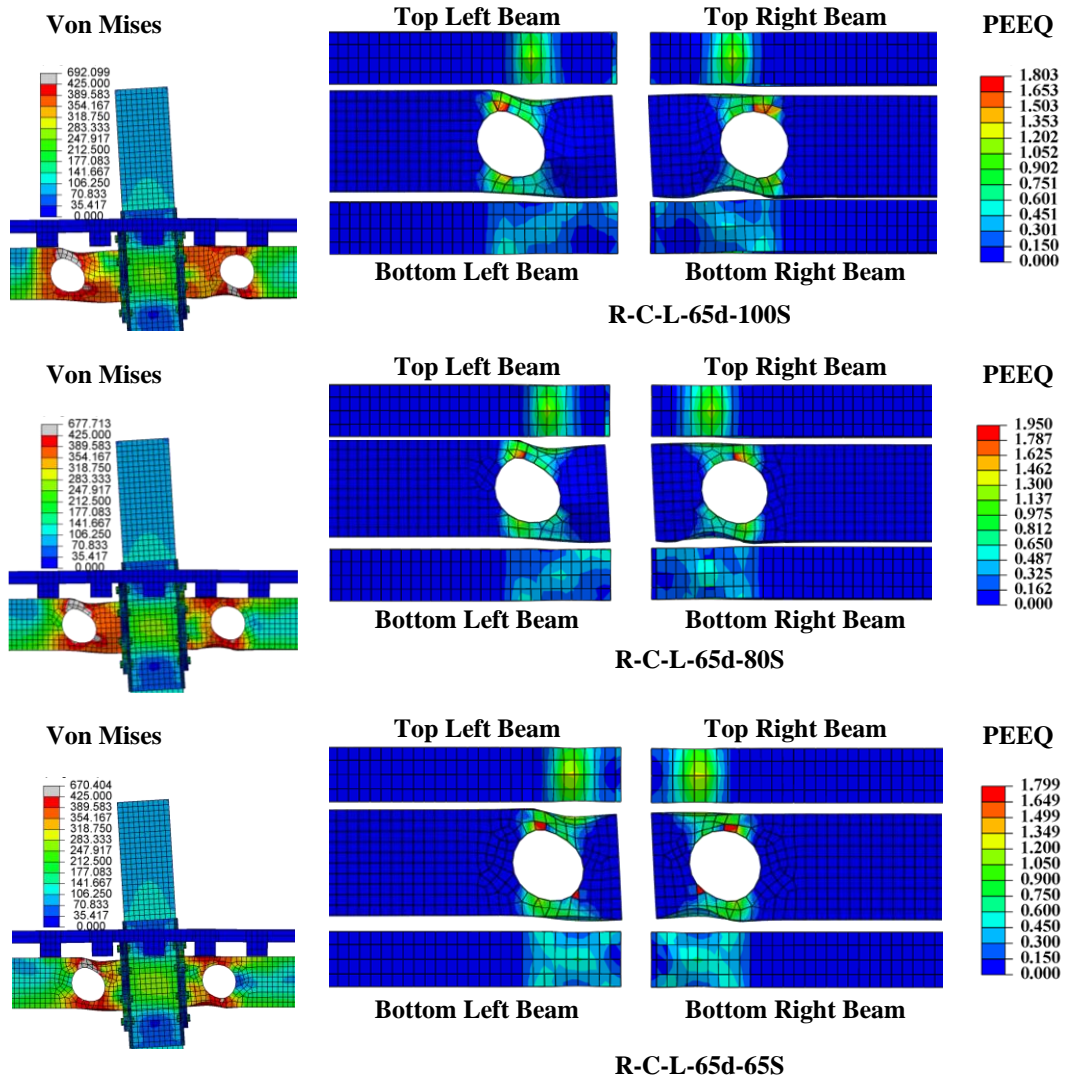


Figure 3.27: PEEQ and stresses distribution in last cycle of RWS models with  $d_o = 0.65h$  and  $S_o$  were complied with SCI P355 guidance (no shear studs over the protected zone).



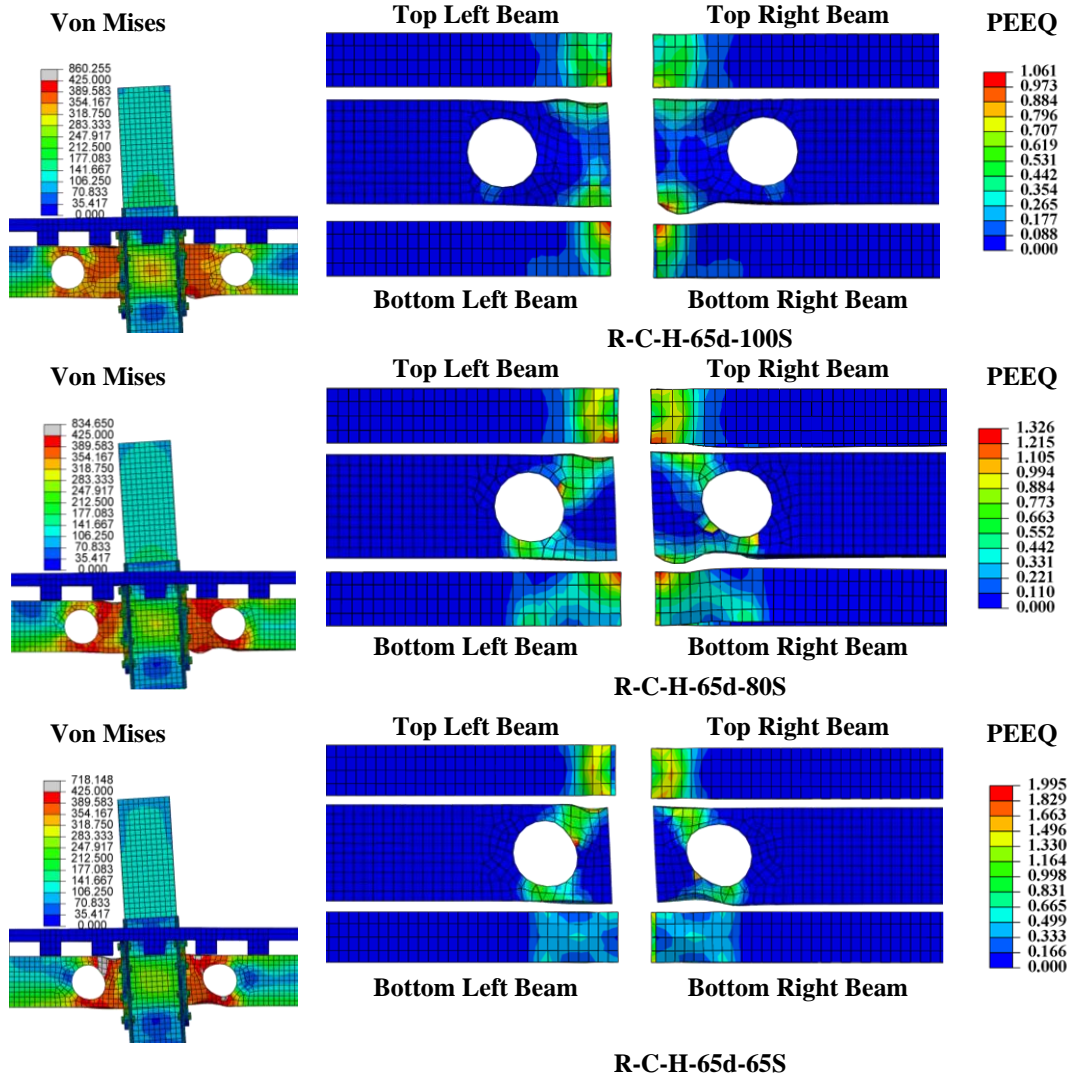


Figure 3.28: PEEQ and stresses distribution in last cycle of RWS models with  $d_o = 0.65h$  and  $S_o$  were complied with SCI P355 guidance (presence of shear studs over the protected zone).

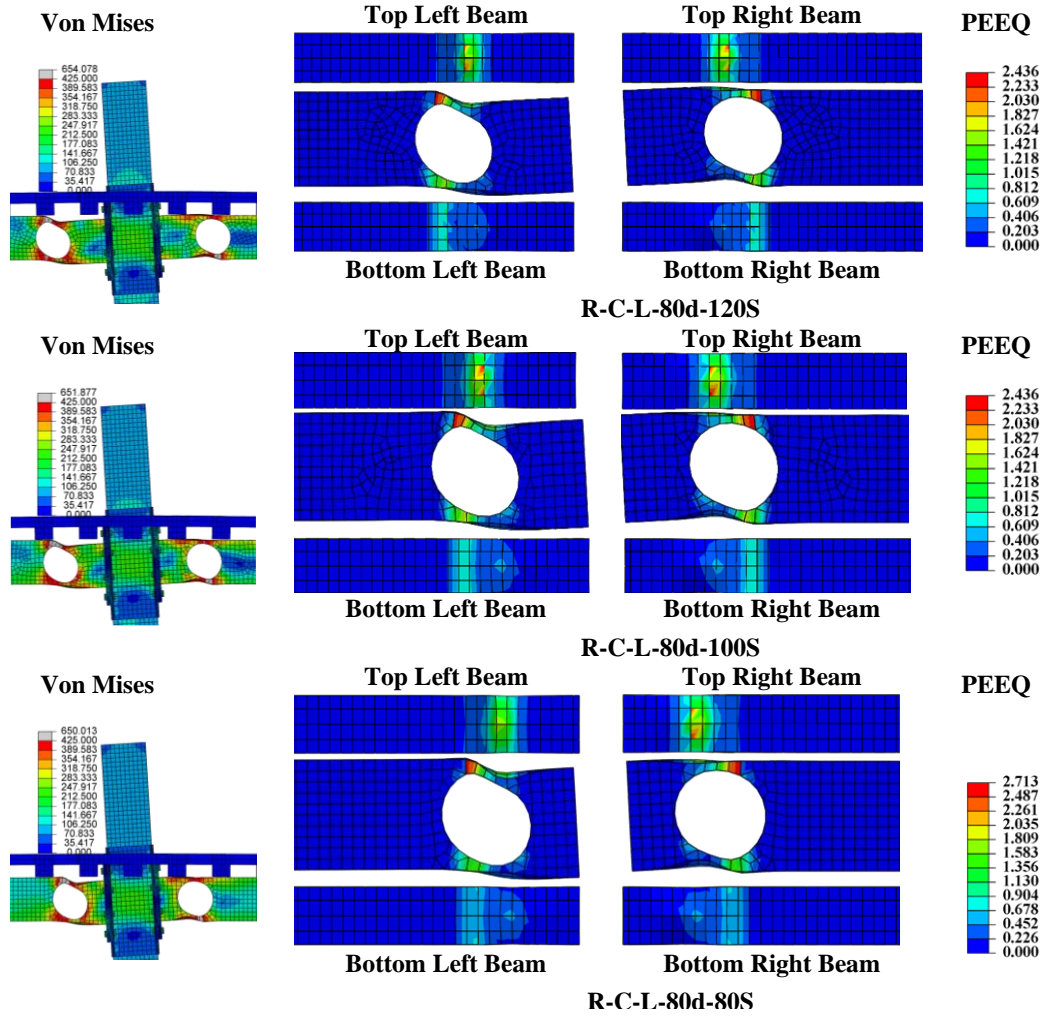


Figure 3.29: PEEQ and stresses distribution in last cycle of RWS models with  $d_o = 0.8h$  and  $S_o$  were complied with SCI P355 guidance (no shear studs over the protected zone).

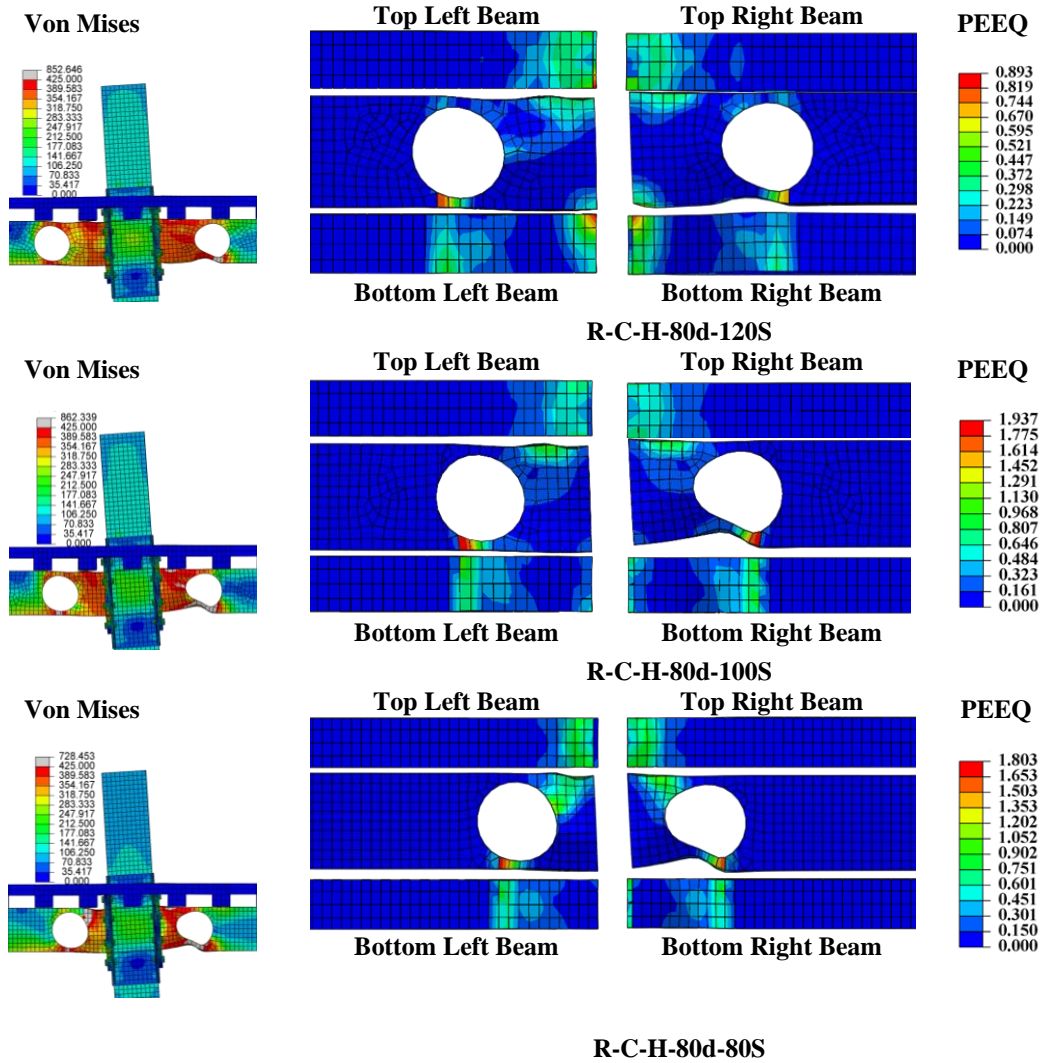
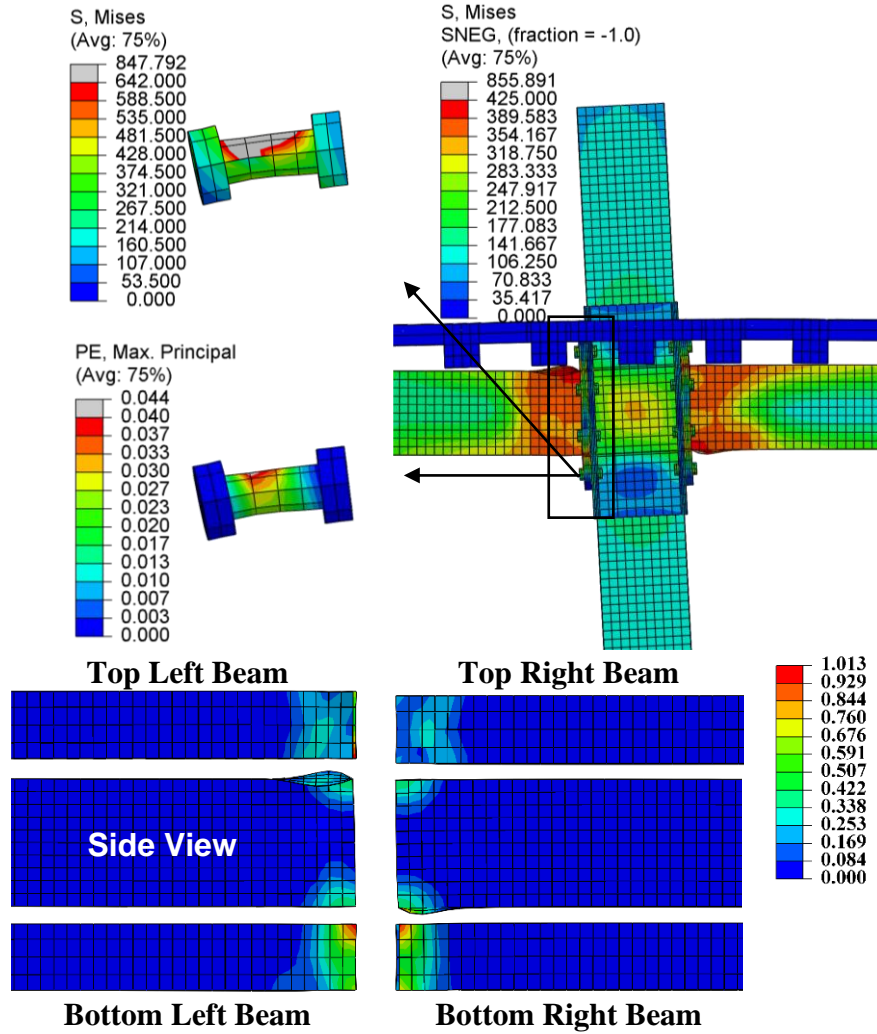


Figure 3.30: PEEQ and stresses distribution in last cycle of RWS models with  $d_o = 0.8h$  and  $S_o$  were complied with SCI P355 guidance (presence of shear studs over the protected zone).

**Low composite action**



**Figure 3.31: Distribution of PEEQ and Von Mises stresses of composite solid model (NR-C-L) in last cycle in the hysteretic curve**

**High composite action**

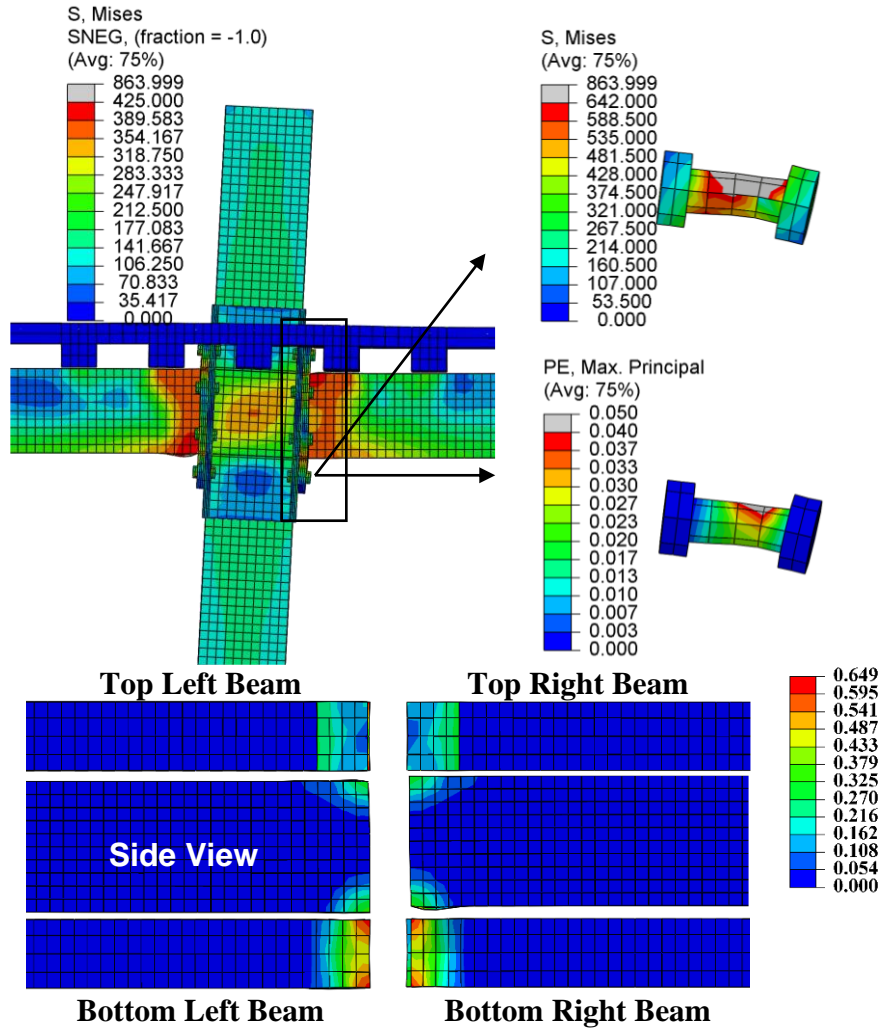


**Figure 3.32: Distribution of PEEQ and Von Mises stresses of composite solid model (NR-C-H) in last cycle in the hysteretic curve.**

### 3.5.4 Damage patterns on the slab.

Figures 3.33 and 3.34 depict different patterns of slab damage in both tension and compression, for models where there is high and low composite action. Clearly, there is extensive cracking in tension for all cases, indicating that reducing the number of shear studs may allow for some relative slippage, as hinted by the cap on moment resistance, but joint deformation is still important, leading to adverse transfer of shear strain into the concrete slab.

Contrarily, compressive crushing shows a more varied behaviour depending on the degree of coupling of the beam and the slab. For low composite action, damage is limited, particularly when the opening diameter is  $0.65h$  or larger. Rather, it happens due to stress concentration in the vicinity of the web opening. For high composite action, damage is more widespread, indicating that the slab plays a critical role by supporting compressive stresses. Among specimens with high composite action, damage is lowest when the opening is  $0.80$  times the beam depth. Yet, this case displayed the largest structural efficiency, as the average peak moment reached  $1.38$  times the nominal capacity of the bare beam. This is explained by the fact that reducing the cross-section of the beam to the greatest extent, limits excess tensile actions within the cross-section; therefore, balancing compressive actions are lower, and induced damage is consequently milder.

It seems that the best efficiency is achieved by providing large openings and allowing for mild crushing and cracking of the concrete slab, which in turn provides a supplementary energy dissipation mechanism along with hysteretic energy dissipation due to the attainment of early plastic deformations around the web openings (Vierendeel mechanism). The best efficiency was defined by scrutinizing the pattern and intensity of the crushing and cracking in the slab of each specimen while considering crucial factors such as energy dissipation and ductility. This approach can be applied to RWS connections with low and high composite action.



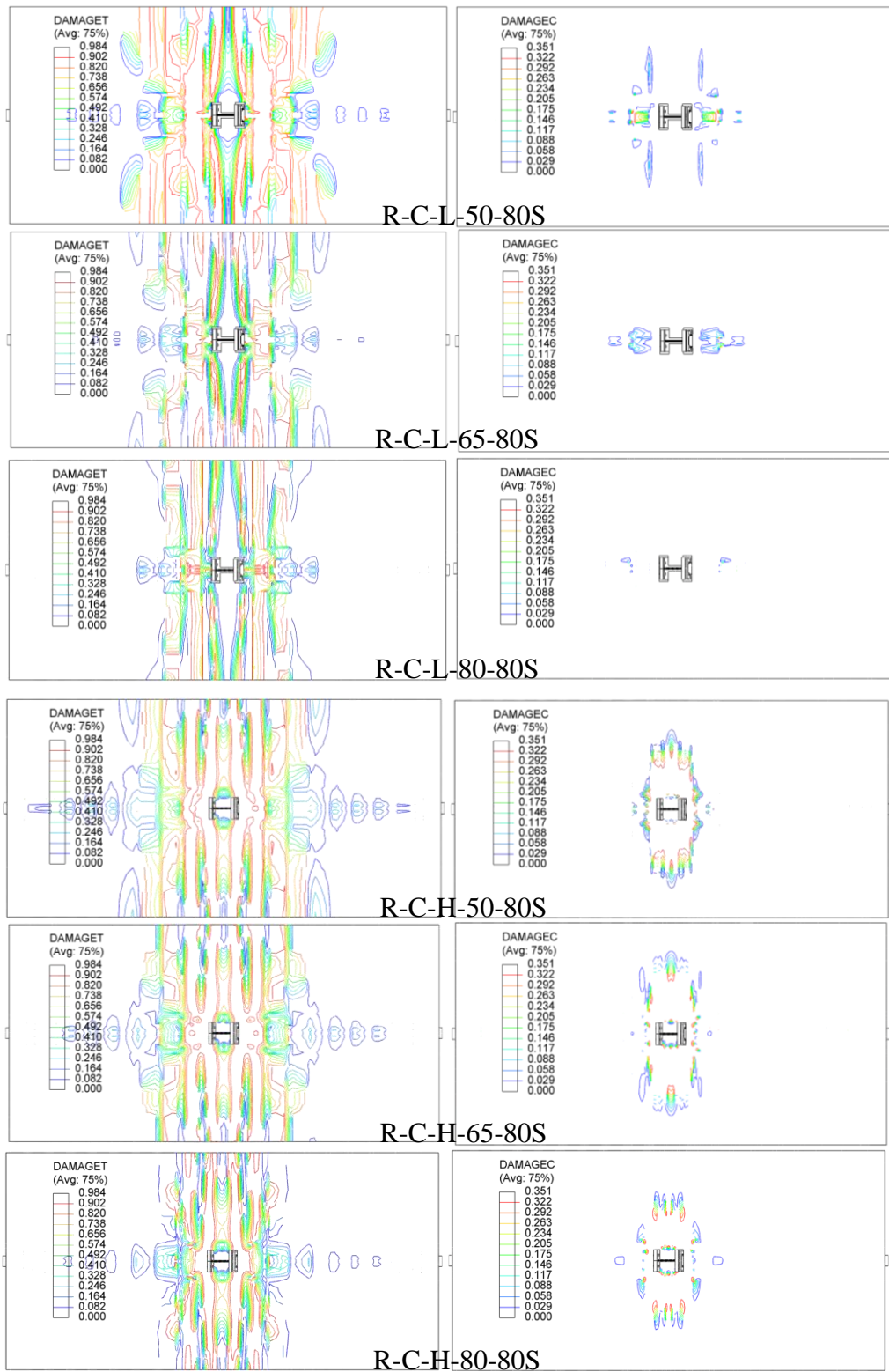


**Figure 3.33: Concrete slab cracking and crushing patterns for different RWS connections.**

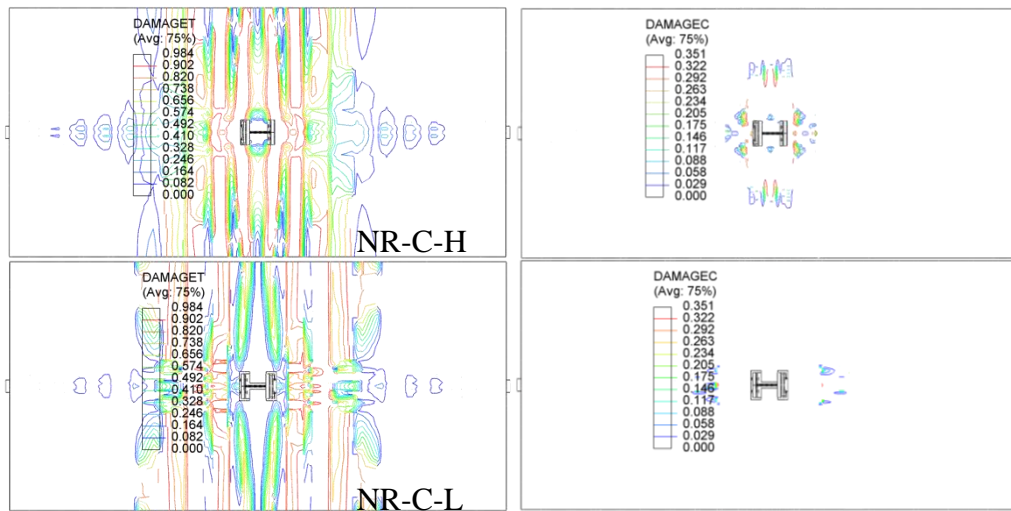


**Figure 3.34: Concrete slab cracking and crushing patterns for different solid webbed-beam connections.**

### 3.5.5 Contribution of composite action

The contribution of low and high composite action to the overall strength capacity is shown in Table 3.7. The average contribution values for specimens with low composite action are 17% and 7.8%, for sagging and hogging moments, respectively. While for those with high composite action, the average values are 37% and 23.5% for sagging and hogging moments, respectively. This hints that composite action keeps contributing to the overall moment capacity even if the reinforced concrete slab is extensively cracked and crushed. Thus, it could lead to the strengthening rather than weakening of the connection if it is not properly accounted for. Thus, understanding the composite action effect on the seismic performance of the connections is very important for accounting for overstrength in both erection of new buildings and seismic retrofit.

The RWS models with low composite action have a low contribution of composite action to the overall strength capacity, ranging between 2.7% and 25.8 (Table 3.7). This is an advantage to those specimens in terms of the ease of predicting the strength capacity, which would be based on the plastic bending capacity of the bare steel beam section. For RWS models with high composite action, the contribution of composite action to the overall strength capacity ranged between 6.9% and 74.9%, noticeably higher. Consequently, ignoring slab effects in the design of RWS models where high composite action is allowed, can lead to unsafe design.

Interestingly, cracking and crushing of concrete were observed to be lower for a perforation size of  $0.8h$  than what was registered for perforation sizes equal to  $0.65h$  and  $0.5h$  (Figure 3.33). Albeit explicit consideration of the slab in design



may lead to a slight reduction of damage within it, the main reason for doing it is to preserve the strong column-weak beam design paradigm.

### 3.6 Discussion

Results indicate that composite RWS connections offer a large deformation capacity, of 4% interstorey drift, while keeping a moment capacity of at least 80% of the peak value, without inducing damage to columns and joints. Particularly, tearing of structural elements is prevented, being the most relevant non-ductile phenomena failure of bolts in the beam-column connection and shear transfer studs between the slab and the beam.

It was found that achieving the full nominal resistance of the composite section, which would be theoretically expected to be around twice the bare steel section capacity, proved unlikely. While specimens achieved peak resistances close to this value under cyclic loading (Table 3.6  $M_f/M_{pl,Rd}$ ), they typically reached a maximum of 1.4 times the nominal capacity. This was observed when shear transfer studs were placed in the protected zone (i.e., high composite action). This large divergence can be explained by the characteristics of the reversible deformation demand being imposed on the model. Reversion of strains within the beam compromises its capacity to endure compressive actions when compared to a slab that doesn't go through it. Crushing becomes more likely after tensile cracking in previous cycles. Consequently, it is possible that maximum moment capacity becomes closer to what is expected for the full composite section if monotonic loads are imposed instead.

On the other hand, the numerical model supports the idea that decoupling the beam and the slab (i.e., non-composite) is a sensible approach for limiting non-linear action outside the protected zone. Moment capacity approaches the nominal capacity of the beam, even allowing for a 20% lower value for the sagging moment. This is expected as the slab offers an additional constraint for local buckling when a sagging moment is imposed, while the likelihood of out-of-plane deformation increases when compression is observed in the bottom flange when the moment reverses.

Comparatively, best results are obtained for fully coupled RWS beam -to- column connections of 80% of the beam height, and spacings between the perforation and the column face between one perforation diameter and one time the beam height, which is in accord with specifications SCI P355 guidance (Lawson and Hicks, 2011). For these conditions, represented by specimens R-C-H-80-100S and R-C-H-80d-80S, the connection reaches the highest ratio between peak moment capacity and the nominal moment resistance of the bare steel reduced

section (1.48 for the sagging moment, and 1.20 for the hogging moment for the first while 1.42 and 1.06 for the latter); being both able to accommodate 6% interstorey drifts. Albeit, resistance is not symmetrical, differences amongst sagging and hogging moments are half of what is expected for the bare steel reduced section, allowing for a more stable behaviour when subjected to large displacement demands. This is particularly relevant for the retrofitting of new buildings as decoupling of slabs and beams could be avoided, focusing instead on making perforations solely on the beam's web. This will reduce costs and speed up work.

The advantages of limiting composite action only to the protected zone are not clear in terms of diminishing concrete cracking. Results indicate that despite this course of action, tensile cracking on the slab is as extensive as to what is observed for the fully composite action, but maximum achieved moments are lower. Clearly, studs outside the protected zone induce at least partial strain compatibility between the slab and the beam; which leads to this undesired outcome. Also, complete avoidance of composite action is feasible, as done with other structural engineering solutions (Zhang and Ricles, 2006a; Zhang and Ricles, 2006b; Lee et al., 2016). However, the elimination of composite action (no holding) over the plastic zone in the RWS connections, led to the standard formation of the Vierendeel mechanism, like the case of bare steel beams. On other hand, RWS connections with high composite action have shown different behaviour due to the high contribution of the composite slab to the overall strength. Hence, the use of low composite action is preferable to avoid high strain demand on the bottom flange of the beam as well as cracking and crushing of the concrete slab, whilst it does not jeopardize the strong column-weak beam paradigm, following what is observed in US Standards and practice using reduced beam section (RBS) connections.

Thus, the general rules for all types of non-dissipative connections in dissipative zones of the structure specified at (ANSI/AISC 341-16, 2016) can be applied to bolted extended end-plate RWS connections as follows:

$$M_{j,Rd} \geq 1.1 \cdot \gamma_{ov} \cdot (M_{pl,Rd,RWS} + V_{Ed} \cdot S) \quad (3.6)$$

Where  $M_{j,Rd}$  is the design resistance of the joint,  $\gamma_{ov} = 1.25$  (the overstrength factor),  $V_{Ed}$  is the shear force corresponding to the formation of a plastic hinge in the connected beam,  $S$  is the end distance between the connection face and the centerline of the web opening.

### 3.7 Summary

A high-definition finite element model was calibrated considering cyclic tests performed on full-section beams with composite slabs, designed to attain high ductility. The calibration of the model allowed for parametric assessments of the behaviour of composite beam-column joints with reduced web section beams. The focus was made on the diameter opening (0.8, 0.65 and 0.5 times the beam height); the distance from its centre to the column face (1.2, 1.0, 0.8 and 0.5 times the beam height) and the absence and presence of composite action over the protected zone

All assessed specimens achieved an interstorey drift of 4%, showcasing stable hysteresis cycles without pinching or residual deformations in a particular direction when subjected to symmetric cyclic loads. The great majority (84%) of specimens reached an interstorey drift of 6%. Tearing of columns, joints and beams was adverted, being the most critical failure mode the failure of shear studs between the slab and the beam and the tearing of bolts in the end-plate connection. In certain cases, bolt failures in the end plate were observed. However, this happened for drift demands in excess of 4% and they could be avoided by adjusting capacity design principles for these novel connections. Thus, they can be potentially used in special moment frames as specified in AISC 341 (ANSI/AISC 341-16, 2016).

The moment capacity of the full composite section ranges between 1.9 and 2 times the capacity of the bare steel section for all cases studied. The RWS connections achieved peak moment capacities significantly lower than what is expected for full composite beam-slab action. At most, the peak moment reached 1.5 times the nominal moment capacity of the bare RWS steel section ( $\frac{M_o}{M_{pl,Rd,RWS}}$ ), reaching an average of 1.36 times in specimens where the perforation was 80% of the beam's height; particularly, when full composite action was enforced for sagging moment. For the hogging moment, values close to 1.09 times the nominal capacity are observed. When composite action is restricted, moment capacity ranges between 1.06 for the sagging moment and 0.9 for the hogging moment. It must be stressed that these results are observed for cyclic demands, and consequently there is a reversion of strains within the slab, which can compromise its capacity to sustain extensive compression. Contrarily, for monotonic loads, strains don't reverse within it and consequently larger peak moments could be achieved.

Thus, numerical simulations hint that RWS connections could be an option for both retrofitting existing structures and new buildings, even when extensive deformation capacity is required. Moreover, the limited increase in moment

capacity due to the slab effect indicates that coupling of the slab and the beam have a less critical effect compared to what is observed for beams without perforations, hence providing a cap on overstrength phenomena. This is highly desirable for retrofitting existing structures where decoupling of both the slab and the beam could not be feasible. Based on this study, the design of a composite bolted extended endplate RWS connection for rehabilitation or a new seismic connection should be based on the nominal plastic bending capacity of the reduced steel beam  $M_{pl,Rd,RWS}$ , similar to what is observed for the design of an RBS connection.

## Chapter 4

### Experimental Investigation

#### 4.1 Introduction

The present chapter extends work done in Chapter 3 and by Shaheen et al. (2018) that showcased the potential of such structural fuses and their suitability for seismic applications. This paper goes a step further by experimentally investigating the effects of the presence of bolted shear studs on the cyclic behaviour of composite reduced web section (RWS) connections, aiming to augment available data to expand on the current status quo.

The use of bolted shear studs could overcome the obstacle of replacing damaged beams in the aftermath of moderate earthquakes. Albeit they are not as ductile as other shear transfer solutions, they maintain their integrity and impede extensive deformation of the contact between slab and beam. Hence, such demountable bolts have been introduced as practical alternatives to traditional solutions for facilitating beam decoupling from slabs, and enabling reuse (Moynihan and Allwood, 2014; Ataei et al., 2016; Ataei et al., 2017; Liu et al., 2017; Yang et al., 2018; Sencu et al., 2019; Ataei et al., 2019; Girão Coelho et al., 2020; Chiniforush et al., 2021). The combination of structural fuses, namely RWS, bolted end-plate connections (Tartaglia et al., 2019) and bolted shear studs may provide a cost-effective structural system for speedy seismic rehabilitation. Henceforth, one of the goals of this study is to assess if the provision of bolts to connect beams and slabs is robust enough to prevent extensive deformation of the beam/slab contact and allow for practical separation of both elements during the replacement of damaged parts whilst temporary support is provided.

This chapter describes the arrangement of the experimental works, the test apparatus, and the investigation results into the performance of steel-concrete composite reduced web section (RWS) connections subjected to cyclic loading. It also describes the design of the specimen, the test setup details, the loading protocol, the specimens' details, instrumentation and interpretation of the test results, and the test observations and results.

## 4.2 Experimental work

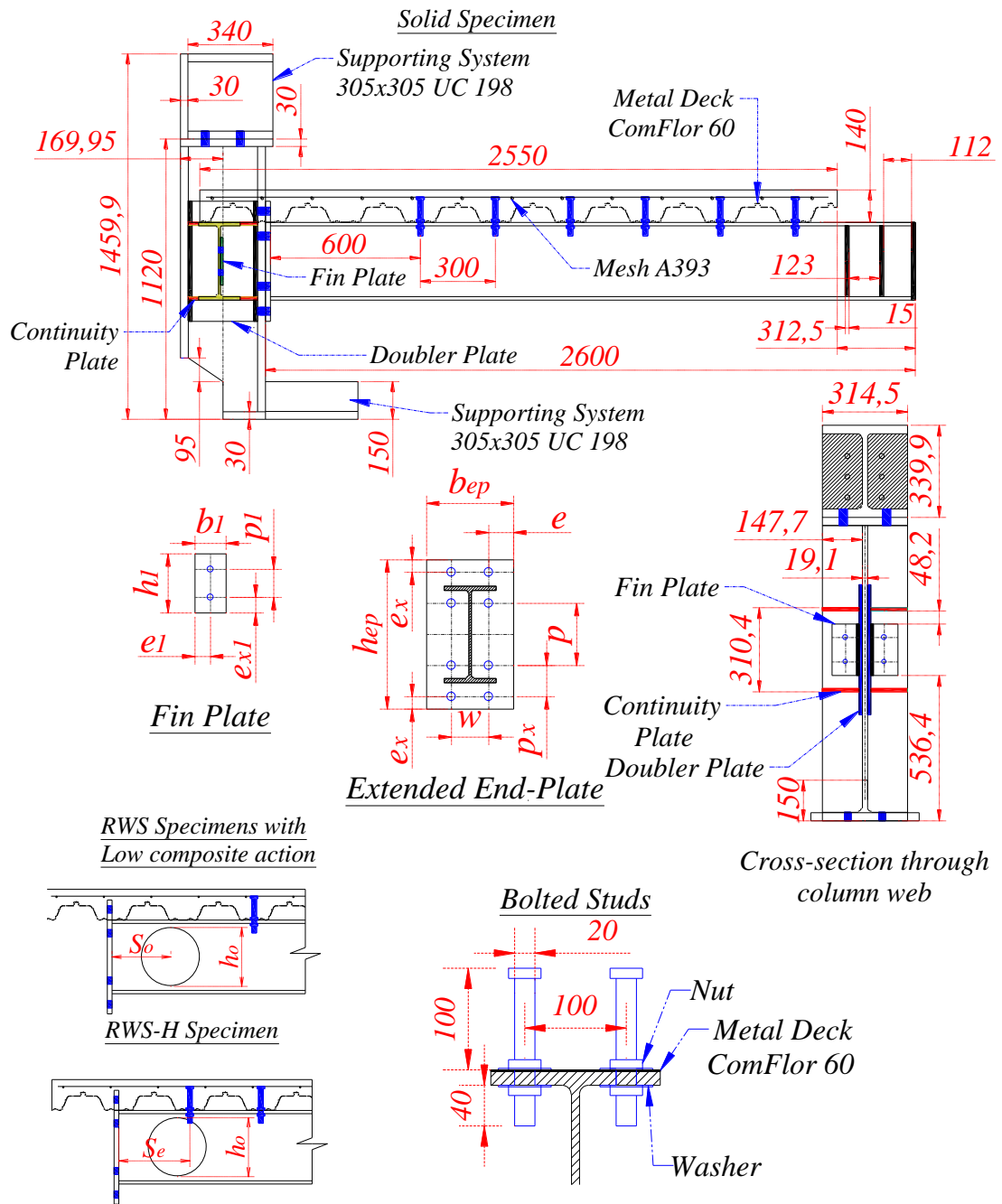
### 4.2.1 Design and details of the composite connection specimens

In this test campaign, cyclic load testing on full-scale specimens of four identical steel-concrete composite connections in terms of sizes and material (Table 4.1 and Figure 4.1). Summary of specimen characteristics and material nominal capacities are provided in Tables 4.1 and 4.2. All specimens represented an exterior unstiffened extended end-plate connection in a moment-resisting frame (MRF).

**Table 4.1: Specimen test matrix.**

Specimen ID	Solid Specimen	RWS-L-retrofit*	RWS-L	RWS-H
<b>Connection Type</b>	EEP	EEP RWS		
<b>Composite action</b>		Low (L)		High (H)
$d_o$	-	0.8h	0.8h	0.8h
$S_o$		1h	0.8h	0.8h
$M_{c,Rd}$ (kNm)	300.2			
$M_{pl,a,Rd}$ or $M_{pl,Rd,RWS}$ (kNm)	300.2	257.1		
$M_{c,Rd}/M_{pl,a,Rd}$	1	1.17		
<b>Joint Category</b>	Partial-strength	Full-strength		
<b>Primary and secondary beams</b>	305x165 UB 54			
<b>Column</b>	305x305 UC 198			
<b>Extended end-plate (EEP)</b>	480x280x20 mm			
<b>Bolts</b>	M27 Gr. 10.9 with preloading force of 321 kN			
<b>Slab</b>	140 mm			
<b>Metal deck</b>	ComFlor 60			
<b>Two rows of bolted shear connector</b>	M20x160 mm - Gr. 8.8 with preloading force of 40 kN			
<b># of rows of bolted shear connectors</b>	6			7
<b>Mesh A393</b>	Φ10-200x200 mm			

Note:  $h$  = height of the beam;  $80d$  = means the diameter of the web opening is equal to 80% of  $h$ ;  $80S$  = means the end-distance is equal to 80% of  $h$ . \* A web opening was created into the solid specimen and then retested for rehabilitation purposes.  $M_{c,Rd}$  = joint capacity.  $M_{pl,Rd,RWS}$  = the nominal plastic bending capacity for the steel section with a web opening =  $F_{y,b} (W_{pl,y,b} - \frac{d_o^2 \cdot t_{w,b}}{4})$ .



	Extended end-plate	Fin plate	
	M27 Gr. 10.9	M20 Gr. 10.9	
$t_{ep}$	20	$t_1$	10
$b_{ep}$	280	$b_1$	100
$h_{ep}$	480	$h_1$	190
$w$	120	$e_{x1}$	50
$e_x$	100	$e_1$	50
$p_x$	40	$p_1$	90
$e$	80	<b>Doupler Plate</b>	480x246.7x12
$p$	200	<b>Continuity Plate</b>	277.1x135.7x12

Figure 4.1: Dimensions of test specimens (mm).

Table 4.2: Nominal capacities specimens.

Specimen	steel section / composite section	Moment resistance (kNm)		Shear resistance $V_{o,Rd}$ (kN)	Vierendeel bending resistance $M_{V,Rd}$ (kN)
		+ve (upward)	-ve (downward)		
Solid Specimen	$M_{pl,a,Rd}$	300.3	300.3	545	-
	$M_{pl,Rd}$	499.6	385.6	545	-
RWS-L-retrofit	$M_{o,a,Rd}$	265.3	257.1	142.9	10.42
	$M_{o,Rd}$	265.3	257.1	156.7	11.64
RWS-L	$M_{o,a,Rd}$	265.3	257.1	142.9	9.97
	$M_{o,Rd}$	265.3	257.1	156.7	12.56
RWS-H	$M_{o,a,Rd}$	265.3	257.1	142.9	18.14
	$M_{o,Rd}$	272.4	257.1	156.7	20.13

Note:  $M_{pl,a,Rd}$  and  $M_{pl,Rd}$  = plastic moment resistance of steel and composite solid webbed beam, respectively, according to Eurocode 3 (CEN, 2005a) and Eurocode 4 (CEN, 2005c).  $M_{o,a,Rd}$  and  $M_{o,Rd}$  = plastic moment resistance of steel and composite solid webbed beam, respectively, according to SCI P355 guidance and SCI P428 guidance (Girão Coelho et al., 2020).

The specimens were designed based on the nominal plastic bending capacity  $M_{pl,a,Rd}$  of the connected steel solid-webbed beam of a partial-strength connection without considering the composite action contribution in accordance with Eurocode 3, Eurocode 4 and Eurocode 8 (CEN, 2005a; CEN, 2005b; CEN, 2005c; CEN, 2005d). The incorporation of web opening makes the connection go from partial- to full-strength as the capacity of the connected steel beam is reduced. Steel-concrete composite RWS connections complied with SCI P355 guidance and SCI-P428 guidance (Girão Coelho et al., 2020) terms of end-distance, diameter and bolted shear studs.

The first composite specimen was a partial-strength extended end-plate connection with a solid-webbed beam (hereinafter referred to as the solid specimen). The solid specimen was subjected to cyclic loading, until it reached close to 70% of its positive/sagging moment capacity, thus simulating the effects of moderate seismicity over time, for rehabilitation purposes. Then, a web opening was created, and the specimen was re-tested. It is worth mentioning that the beam was perforated off-site, so the composite slab was dismantled and new M27 bolts were provided.

The re-tested (second) specimen is referred to as the RWS-L-retrofit specimen which was the second specimen to be tested. This allows for benchmarking the



effects of residual strains and stresses induced by previous earthquake events. The other two specimens were steel-concrete composite RWS connections. The difference between them is the presence or absence of bolted shear studs above the web opening (i.e., composite action).

The presence/absence of bolted studs above the web opening was used to classify the specimens as having high (H) or low (L) composite action according to Eurocode 8-1 clause 7.7.5 and ANSI/AISC 358-16 (CEN, 2005d; ANSI/AISC 358-16, 2016) as shown in Figure 4.1. All four specimens had a 25 mm gap between the connection's components and reinforced concrete (RC) slab, to avoid the crushing and cracking of the concrete following ANSI/AISC 358-16 and Eurocode 8-1 clause 7.7.5(2) (CEN, 2005d; ANSI/AISC 358-16, 2016).

A cantilever testing setup was selected to benchmark behaviour. This was accomplished by providing a strong stocky column in such a way that its deformation is negligible. The highly ductile beam section was chosen based on the width-to-depth and span-to-depth ratios according to seismic provisions ANSI/AISC 341-16 and 358-16 (ANSI/AISC 341-16, 2016; ANSI/AISC 358-16, 2016) and in such way that it was feasible to test them in the available facilities.

#### **4.2.2 Specimen preparation**

The specimens were fabricated and cast by the supplier. The steelwork (welding and drilling) was carried out by the steel fabrication company. The diameter of the pre-drilled holes in the end plate was 30 mm, which provided a clearance of 3 mm for the M27 bolts, according to CEN (2011). The diameter of the pre-drilled holes in the beam top flange was 21 mm, which provided a clearance of 1 mm for the M20 bolted shear connectors, according to SCI P428 (Girão Coelho et al., 2020). A clearance of 1 mm was provided for the bolted shear connectors to minimise slippage (Girão Coelho et al., 2020). The clear height of shear connectors above the beam flange was equal to 100 mm, as recommended in SCI P428 (Girão Coelho et al., 2020) (Figure 4.2). The preloaded M27 Grade 10.9 bolts were tightened using a torque wrench, according to EN 1090-2 (CEN, 2011), to obtain a preloading force of 321 kN and the demountable M20 Grade 8.8 bolted shear connectors with double nuts were tightened to 100 Nm. This torque value was taken from Moynihan and Allwood (2014) to ensure the bolted shear connectors would be within an elastic range and could be utilised for another cycle of use.



**Figure 4.2: The height of the bolted shear connector above the top beam flange (mm)**

The shuttering and formwork for the specimens are shown in Figure 4.3. The composite beams were cast on their own without a column or secondary beams. They were assembled in the laboratory, as the column and secondary beams were designed to be free of damage and to work as a support system. Ready-mix concrete was used and was cast for all the specimens at the same time. Cubes and cylinders were prepared from the same ready-mix concrete used for the specimens. The ready-mix concrete class was 25/30, with a maximum aggregate size of 20 mm with a 140-mm slump.



**Figure 4.3: Shuttering of test specimen.**

### 4.2.3 Test setup and loading protocol

The test setup consisted of a full-scale one-sided composite extended end-plate RWS connection (see Figures 4.4 – 4.6). The experimental works were carried out on the strong floor at the Heavy Structures Laboratory in the School of Civil Engineering at the University of Sheffield. The test setup was designed to minimize deformation contributions from the column. Thus, the back, top and bottom of the strong column were fixed within the testing rig frame. Loading plates were used to on-site weld the specimens to the actuator due to the height limitation of testing the rig frame, which would lower the head of the actuator below the beam.

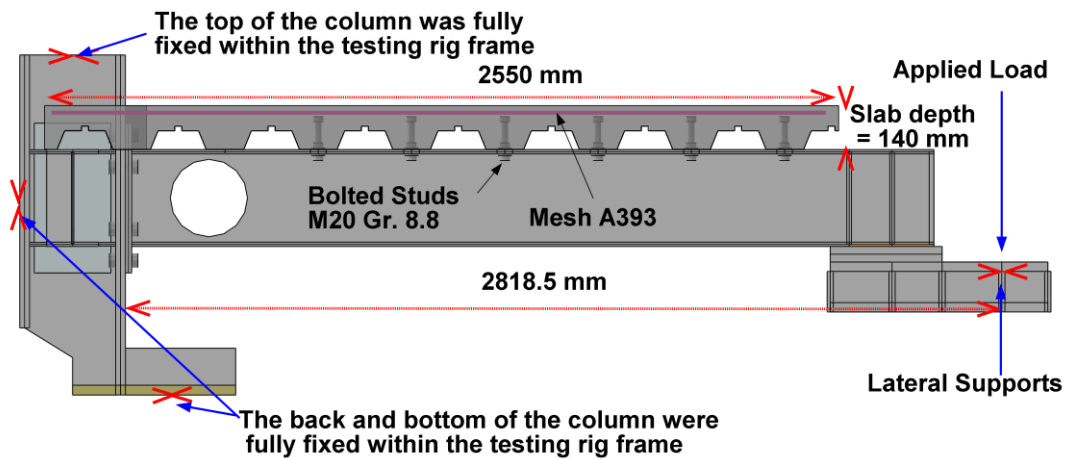


Figure 4.4: Experimental test setup – side view.

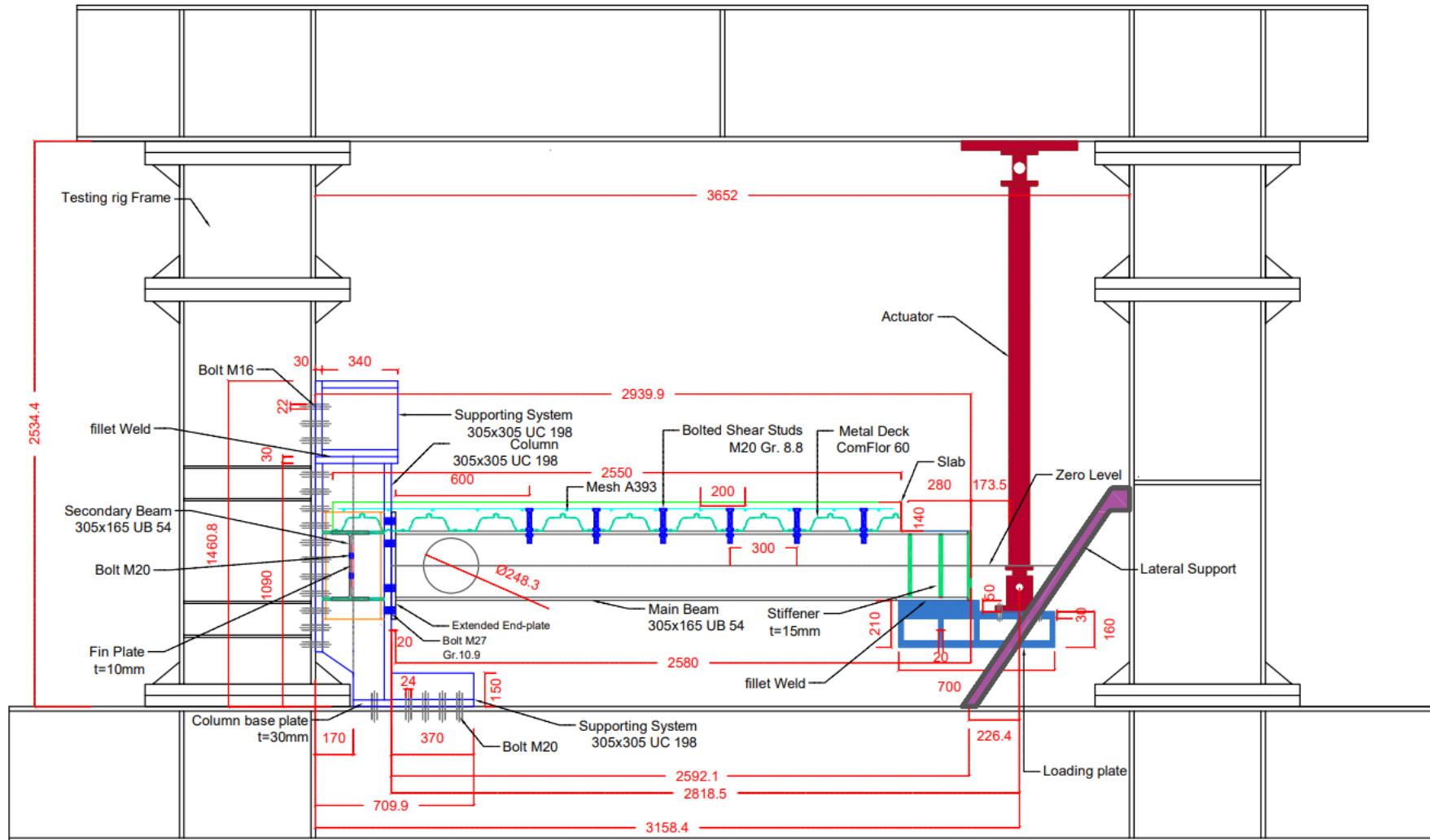
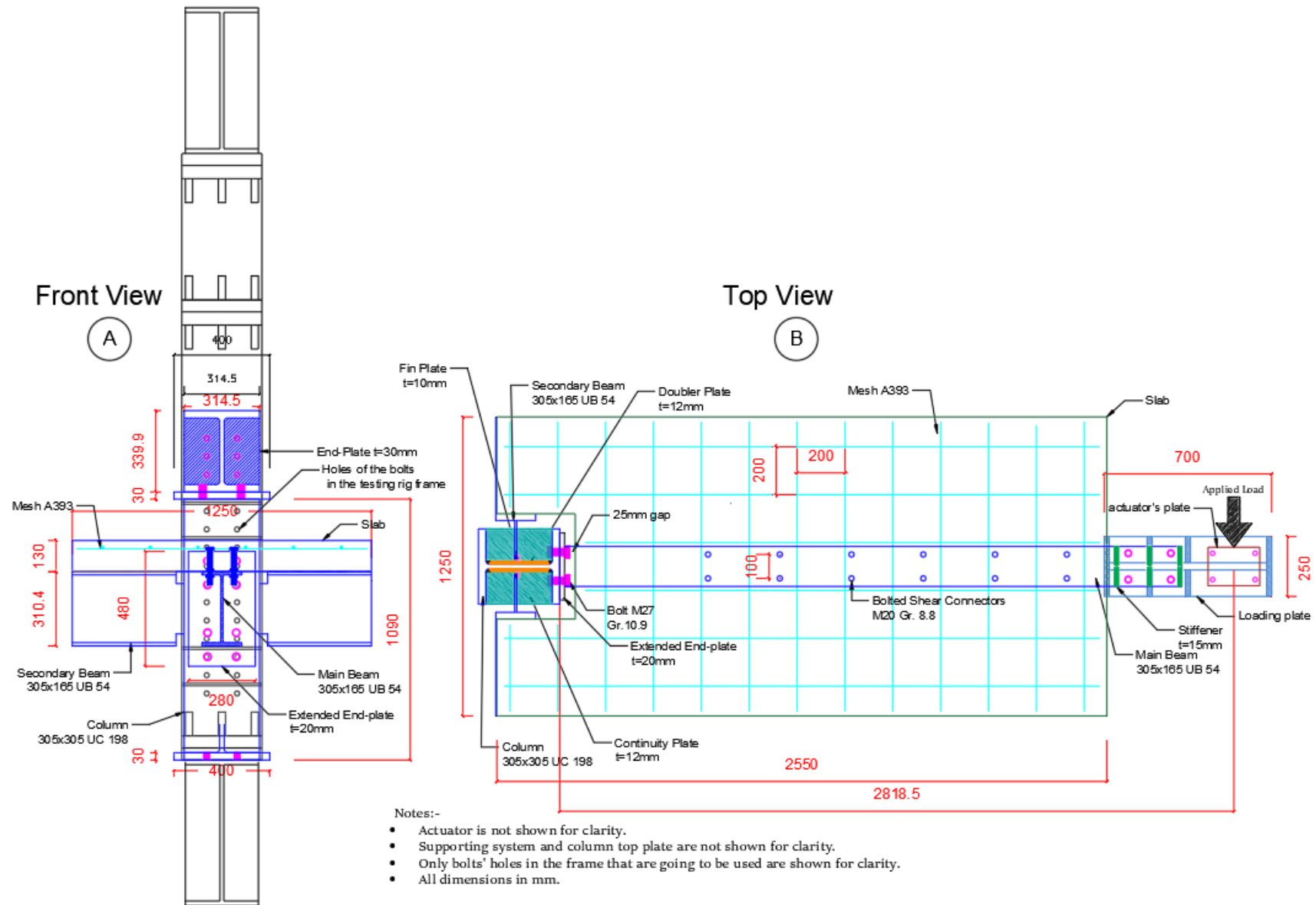


Figure 4.5: Experimental test setup – side view (mm)



**Figure 4.6: Experimental test setup – front and top view (mm)**

The concrete slab provides additional lateral support, making the use of lateral restraints redundant all over the beam. However, lateral restraints were provided at the point of the actuator connection, to set boundary conditions that resemble what is generally expected in buildings. The distance between the column face and the actuator loading point was 2818.5 mm. A two-way actuator of 130 kN capacity (i.e., upward and downward) was used to apply a cyclic load at the beam tip.

The cyclic quasi-static test followed the loading protocol in the AISC Seismic Provisions for qualifying the RWS connection for special and intermediate MRFs, as shown in Figure 4.7 (ANSI/AISC 341-16, 2016). This loading protocol was selected for two reasons. Namely, it was used in the research campaign by SAC Joint Venture to prequalify the seismic connections (FEMA 350, 2000; ANSI/AISC 358-16, 2016) and its wide acceptance in the research community. The cyclic tests were under displacement control with a loading rate of 0.5 mm/s. This low loading rate was chosen to allow for the evaluation of structural behaviour in the post-elastic range, as it can track softening behaviour and various damaging states of interest and avoid dynamic effects.

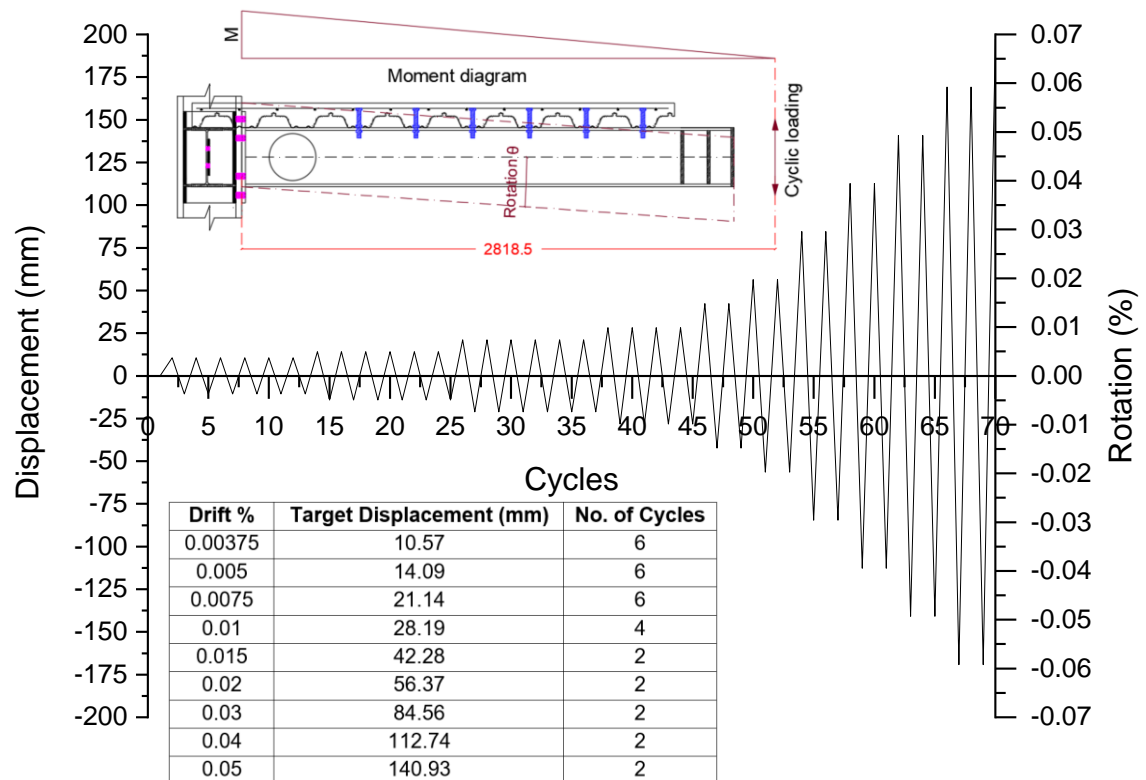


**Figure 4.7: Cyclic loading protocol.**

### 4.2.4 Instrumentation

The general instrumentation layout for the test setup is shown in Figure 4.8. Each specimen was calibrated to measure the strain, rotation, displacement, and load at various locations. Instruments such as strain gauges (SG) and rosettes (RG), angular displacement transducers (RT), linear variable differential transformers (LVDT) and load cells were installed at the regions of expected inelastic deformations, deflection, and slippage. The instruments were connected to the data logger.

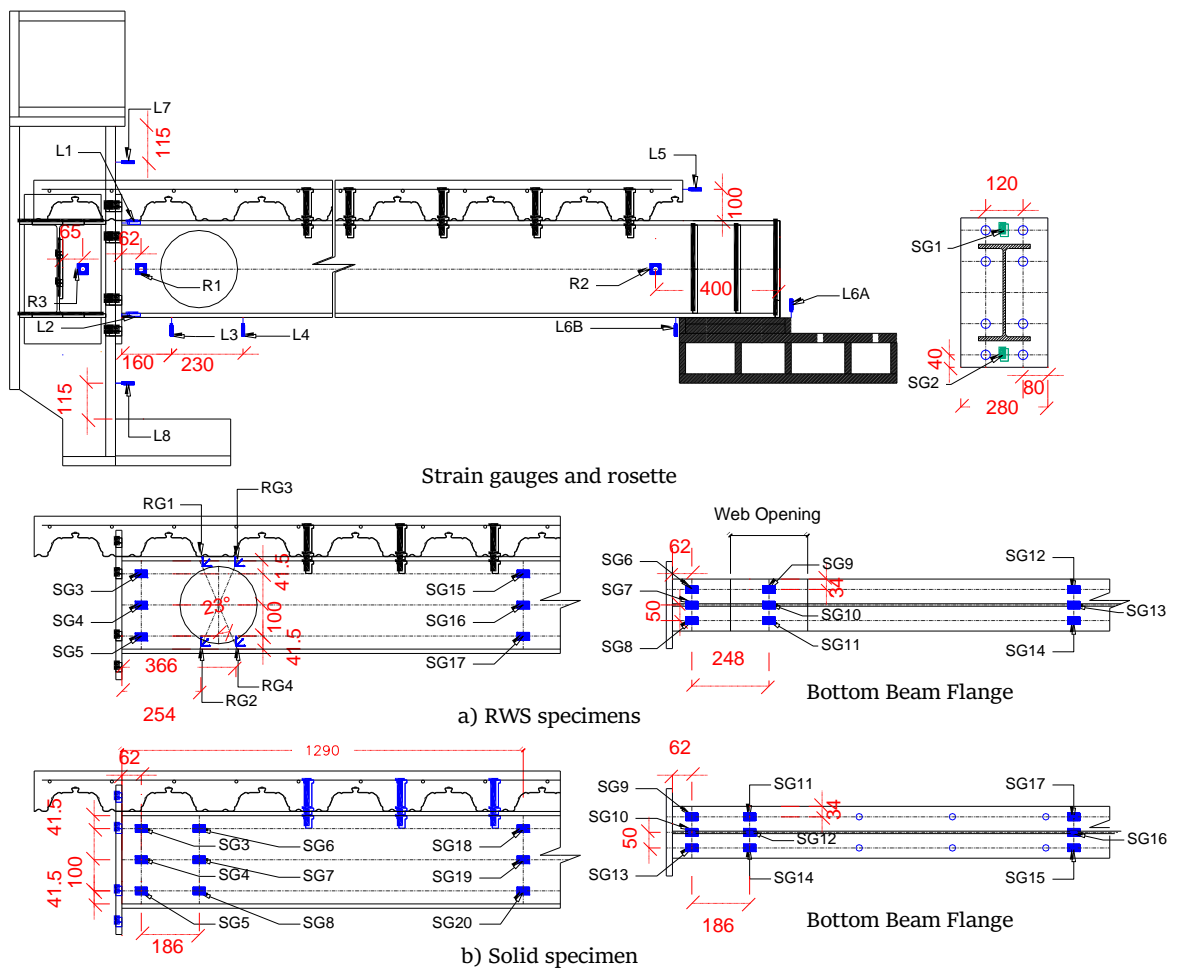


**Figure 4.8: Instrumentation layout (mm).**

The actuator was provided with a calibrated load cell to enable the total applied load at the end of each beam to be measured. The measurement of this force enables the beam moment to be determined. SGs were also placed at the top and bottom of the extended endplates to measure the strain. The web and bottom flange of the beams were mounted by SGs in several locations (near and far from the connection face). This helped to monitor the stress/strain concentration along the beams. RGs were mounted in the vicinity of the web openings to measure the stress distribution in the RWS connections and understand their failure mechanisms.

Deformation of the panel zone was not allowed as the specimens were designed using a strong column-weak beam concept, which means the panel zone should remain elastic. Hence, LVDTs were placed at the column ends to capture any potential displacement. This helped to evaluate the rigidity of the fixed supports. In addition to the internal displacement measurement of the actuator, the following LVDTs and RT were also placed:

- Two horizontal LVDTs (L1 and L2) to measure the end-plate slip/deflection.
- Two vertical LVDTs (labelled L3 and L4) to measure the web openings deflection.
- One horizontal LVDT (L5) to measure the composite slab slip.
- Two vertical LVDT (L6A and L6B) at beam tip to compare the actuator displacement and to evaluate if any slippage or failure would occur in the loading plates.
- Two horizontal LVDTs (L7 and L8) to measure any possible movement of the column.
- Two RTs (R1 and R2), to measure the total rotation of the beam at the connection region in the case of R1, while in R2, the rotation of the beam end was measured.
- R3 was mounted to measure any possible rotation of the panel zone.



#### 4.2.5 Interpretation of the test results

This section describes the test data interpretation of the different beam-to-column subassemblies. The specimen behaviour was presented by various parameters, such as applied load, beam displacement, connection rotation, beam rotation and energy dissipation. Global hysteretic behaviour was represented by a plot of the applied moment at the column face ( $M$ ) versus the total rotation ( $\theta_{tot}$ ).  $M$  was calculated by the load applied ( $P$ ) at the actuator multiplied by the span from the column face to the centre of the actuator. The total rotation of the connection ( $\theta_{tot}$ ) is the sum of the extended end-plate (EEP) rotation ( $\theta_{EEP}$ ), RWS rotation ( $\theta_{RWS}$ ) and beam rotation ( $\theta_{beam}$ ), as shown in the following equation 4-1.

$$\theta_{tot} = \theta_{EEP} + \theta_{RWS} + \theta_{beam} \quad \text{Eq. (4-1)}$$

The extended end-plate rotation was obtained through L1 and L2 installed at the top and bottom of the extended end plate divided by the distance between them ( $Z$ ), as in the following equation:

The RWS rotation ( $\theta_{RWS}$ ) was determined by the following relationship:

$$\theta_{EEP} = \frac{\Delta_{L2} - \Delta_{L1}}{Z} \quad \text{Eq. (4-2)}$$

$$\theta_{RWS} = \frac{\Delta_{L4} - \Delta_{L3}}{z_{RWS}} \quad \text{Eq. (4-3)}$$

Finally, the beam rotation ( $\theta_{beam}$ ) was obtained through the following relationship:

$$\theta_{beam} = \frac{\Delta_{actuator}}{span} \quad \text{Eq. (4-4)}$$

The ductility and energy dissipation are key behaviour measurements to evaluate the connection performance under seismic loads. These measurements can be evaluated from the moment-rotation (M-R) hysteresis curves under gradually increased cyclic load. The ductility ratio ( $D_{\theta}$ ) is defined as  $\theta_u / \theta_y$ , where  $\theta_y$  is the rotation corresponding to the yield point, and  $\theta_u$  is the ultimate rotation corresponding to the ultimate point on the M-R curve. The energy dissipation was calculated by summing up the area under the M-R hysteresis loop of the whole cycles.

Figure 4.9 shows the change in steel stress-strain relationship (Hibbeler, 2017) and the change in stress distribution through the composite cross-section from elastic to plastic stress blocks (Davison and Owens, 2012). It is assumed that the composite beam bottom flange is fully yielded when its strain reaches  $5\varepsilon_y$ , where  $\varepsilon_y$  is the yield strain for steel grade S355 (Davison and Owens, 2012). In this case, the positive moment reaches nearly 95% of the plastic moment capacity of the composite cross-section. Hence, the recorded strains from the tests were

interpreted based on these figures to understand the behaviour and failure modes of the specimens.

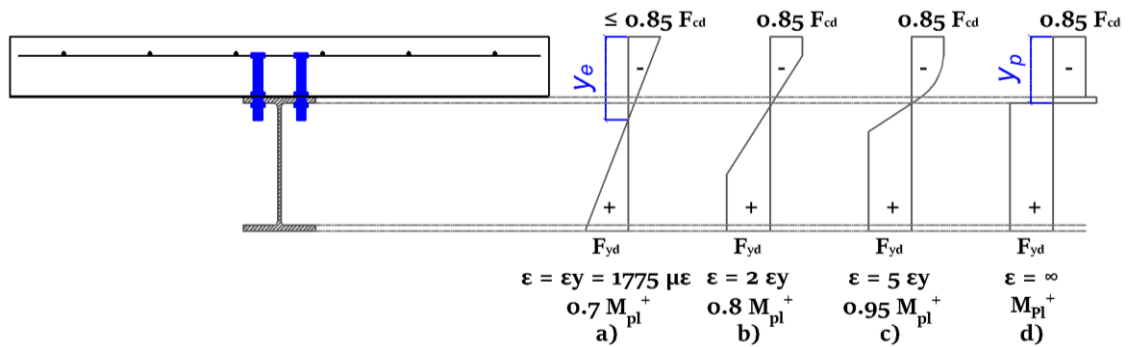


**Figure 4.9: Elastic, elastic-plastic and plastic stress distributions in a composite section (Davison and Owens, 2012).**

#### 4.2.6 Material properties

The mechanical properties of the steel beam (305x165 UB 54) grade S355 were obtained through monotonic coupon tensile testing. The test coupon was prepared according to BS EN ISO 6892-1 (2009). The tensile coupon dimensions are shown in Figure 4.10. Three of the coupons were cut from the flanges and three were cut from the web. The test coupons were tested using universal testing machine available at the structural laboratory of University of Leeds. The stress-strain curves of the steel section coupons are shown in Figure 4.11. The concrete strength of the compression cylinder tests was determined at 7-day, 14-day and 28-day. The average values of the three compression cylinder tests of RWS-L and RWS-H specimens are shown in Table 4.3.

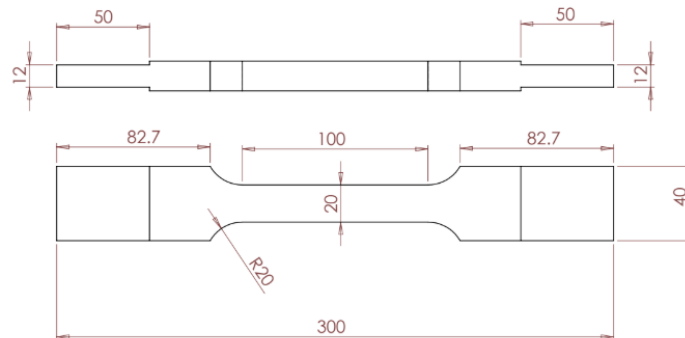


**Figure 4.10: Coupon details.**

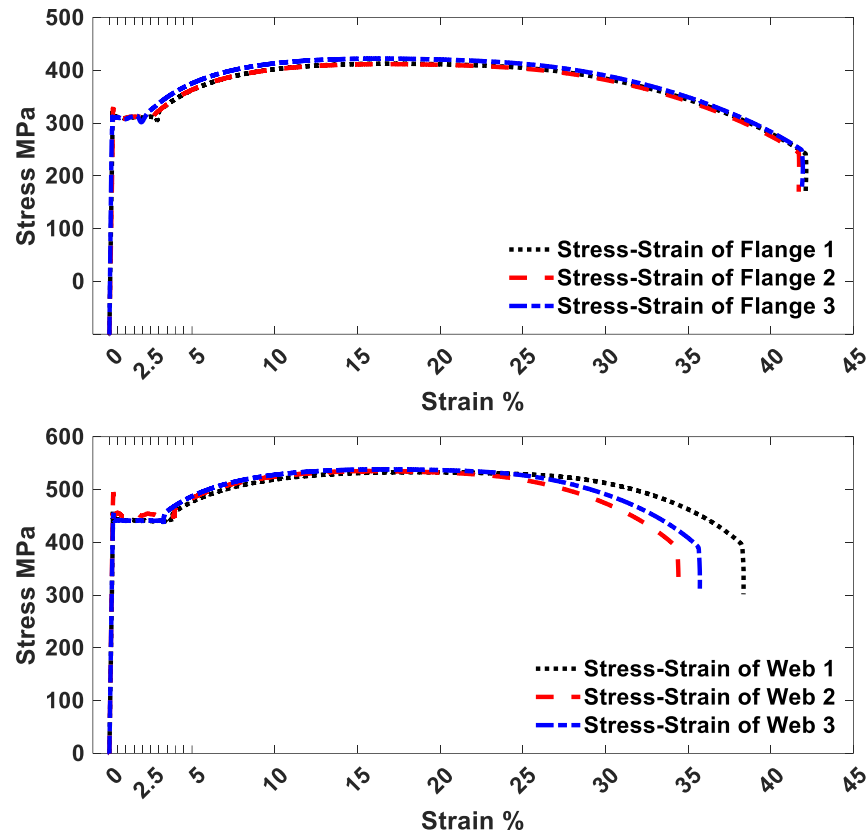


Figure 4.11: : Stress-strain curves of steel section coupons.

Table 4.3: Concrete compressive cylinder strengths

Designation	Compressive Cylinder Strength (MPa)			
	Sample 1	Sample 2	Sample 3	Average
RWS-L	31.8	31.3	30.7	31.3
RWS-H	29.3	32.1	24.8	28.7

Note: The concrete class is C25/30.

## 4.3 Experimental results

### 4.3.1 Solid connection (no web opening)

The solid connection specimen followed the loading protocol until reaching an imposed chord rotation of 0.02rad in both directions. At these points, the solid specimen reached 70% and 80% of its positive and negative moment capacities, respectively (Figure 4.12 and Table 4.4). The stiffness degradations in both directions were less than 20%. No signs of plastic deformation were observed, either through visual inspection, or measurements by strain gauges. This is a likely outcome of the RC slab's contribution to increasing the strength of the connection for hogging moments. At most two lines of micro-cracks within the concrete slab were recorded, as shown in Figure 4.13. Clearly, the onset of yielding in the solid specimen was reached without extensive plastic actions as illustrated in Figure 4.9. All the other steel elements including the demountable bolted shear studs were damage-free. Consequently, the composite slab was disconnected from the beam to create a web opening to simulate a retrofit procedure. Hence, this leads to the RWS-L-retrofit specimen, as shown in in Figure 4.14.

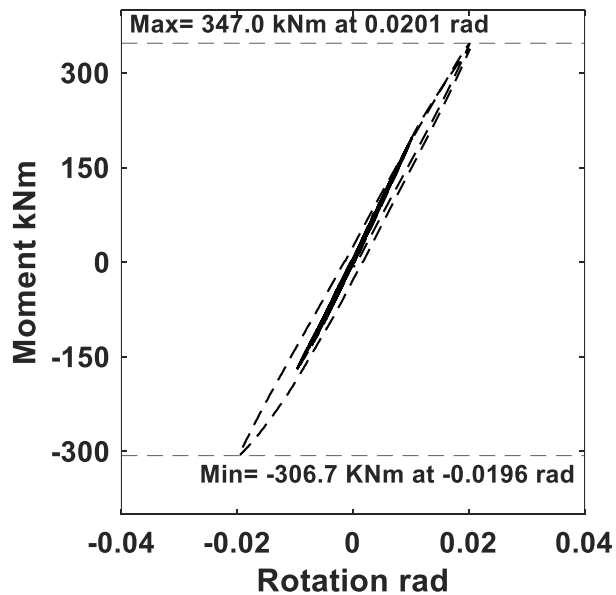
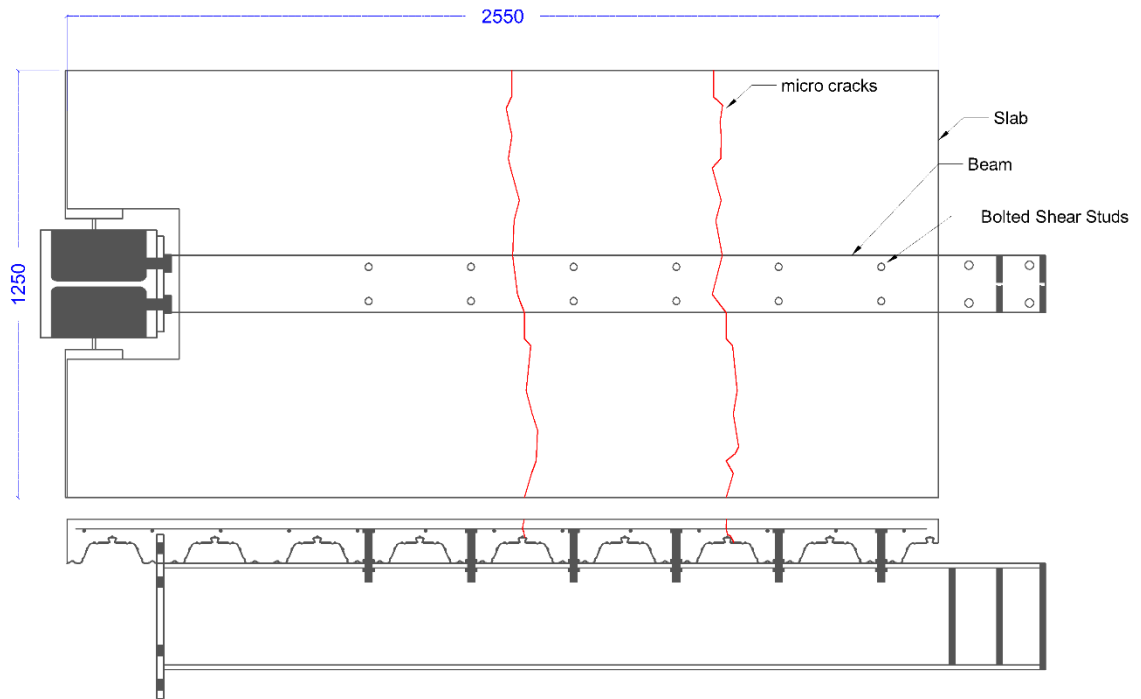


Figure 4.12: Moment-Rotation curve solid connection specimen.

Table 4.4: Results Summary.

		Solid	RWS-L-retrofit	RWS-L	RWS-H
<b>M at column face <math>M_f</math> (kNm)</b>	<b>+ve</b>	347	340.2	339.4	328.7
	<b>-ve</b>	-306.7	-318.5	-293.4	-290.3
<b>M at opening centreline <math>M_o</math> (kNm)</b>	<b>+ve</b>	-	300.3	307.1	290.1
	<b>-ve</b>	-	-281.2	-265.4	-256.2
<b><math>M_f/M_{pl,a,Rd}</math> steel section</b>	<b>+ve</b>	1.16	1.13	1.13	1.09
	<b>-ve</b>	-1.02	-1.06	-0.98	-0.97
<b><math>M_f/M_{pl,Rd}</math> composite section</b>	<b>+ve</b>	0.71	0.69	0.69	0.67
	<b>-ve</b>	- ve $M_f/M_{pl,Rd}$ steel section			
<b><math>M_o/M_{o,a,Rd}</math> steel section</b>	<b>+ve</b>	-	1.17	1.19	1.13
	<b>-ve</b>	-	-1.09	-1.03	-1.00
<b><math>M_o/M_{o,Rd}</math> composite section</b>	<b>+ve</b>	-	1.13	1.16	1.06
	<b>-ve</b>	- ve $M_o/M_{o,a,Rd}$ steel section			
<b><math>\theta_u</math> (rad)</b>	<b>+ve</b>	-	0.0499	0.0499	0.0499
	<b>-ve</b>	-	-0.0499	-0.0498	-0.0499
<b><math>\theta_y</math> (rad)</b>	<b>+ve</b>	0.0201	0.0180	0.0174	0.0168
	<b>-ve</b>	- 0.0196	-0.0169	-0.0150	-0.0148
<b><math>M_y</math> (kNm)</b>	<b>+ve</b>	-	323.9	324.1	318.2
	<b>-ve</b>	-	-294	-279.5	-185.2
<b>Ductility <math>D_\theta = \theta_u/\theta_y</math></b>	<b>+ve</b>	-	2.39	2.91	2.82
	<b>-ve</b>	-	-2.39	-3.46	-3.14
<b>Dissipated energy (kN.m.rad)</b>	<b>+ve</b>	-	35.20	34.87	34.42

Note:  $M_f$  is the applied moment at the column face.  $M_o$  is the applied moment at web opening centreline.



**Figure 4.13: Observed crack pattern in Solid connection specimen (mm).**



**Figure 4.14: Disconnecting the composite slab of the solid specimen to be reused for the next test.**

### 4.3.2 Yielding mode

The development of yielding and plastic hinges in all three RWS connections is presented in Figures 4.15 – 4.17. It is worth reiterating that in this study, low moment side (LMS) and high moment side (HMS) depend on the global applied moment, for instance, the edge of a web opening subjected to lower global moment is LMS (see Figure 4.18). Additionally, each side consists of bottom and top Tee-sections.

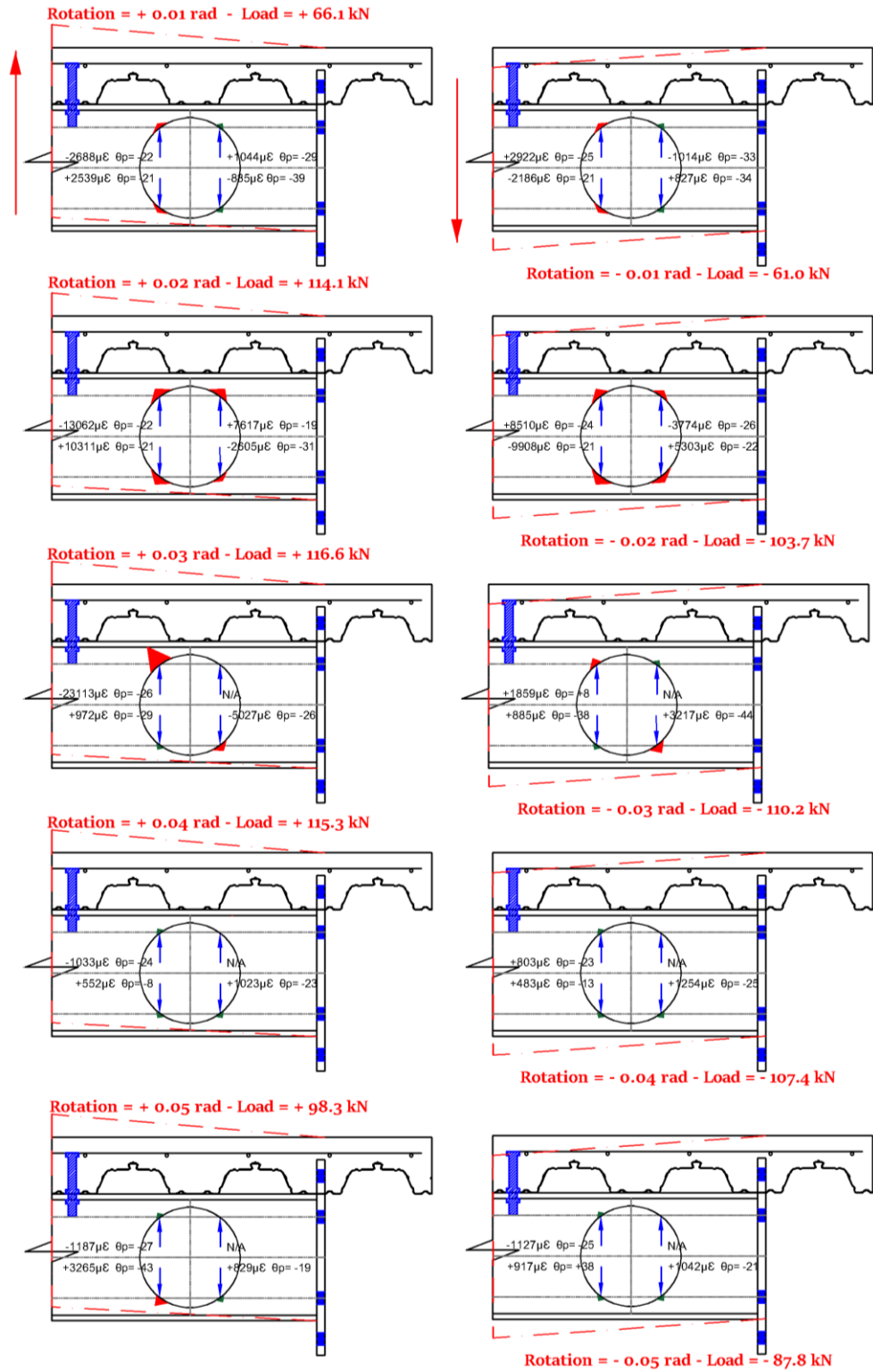


Figure 4.15: Distribution of strain intensity for RWS-L-retrofit connection (N.A. = Not Available due to the loss of the strain gauge during the test).

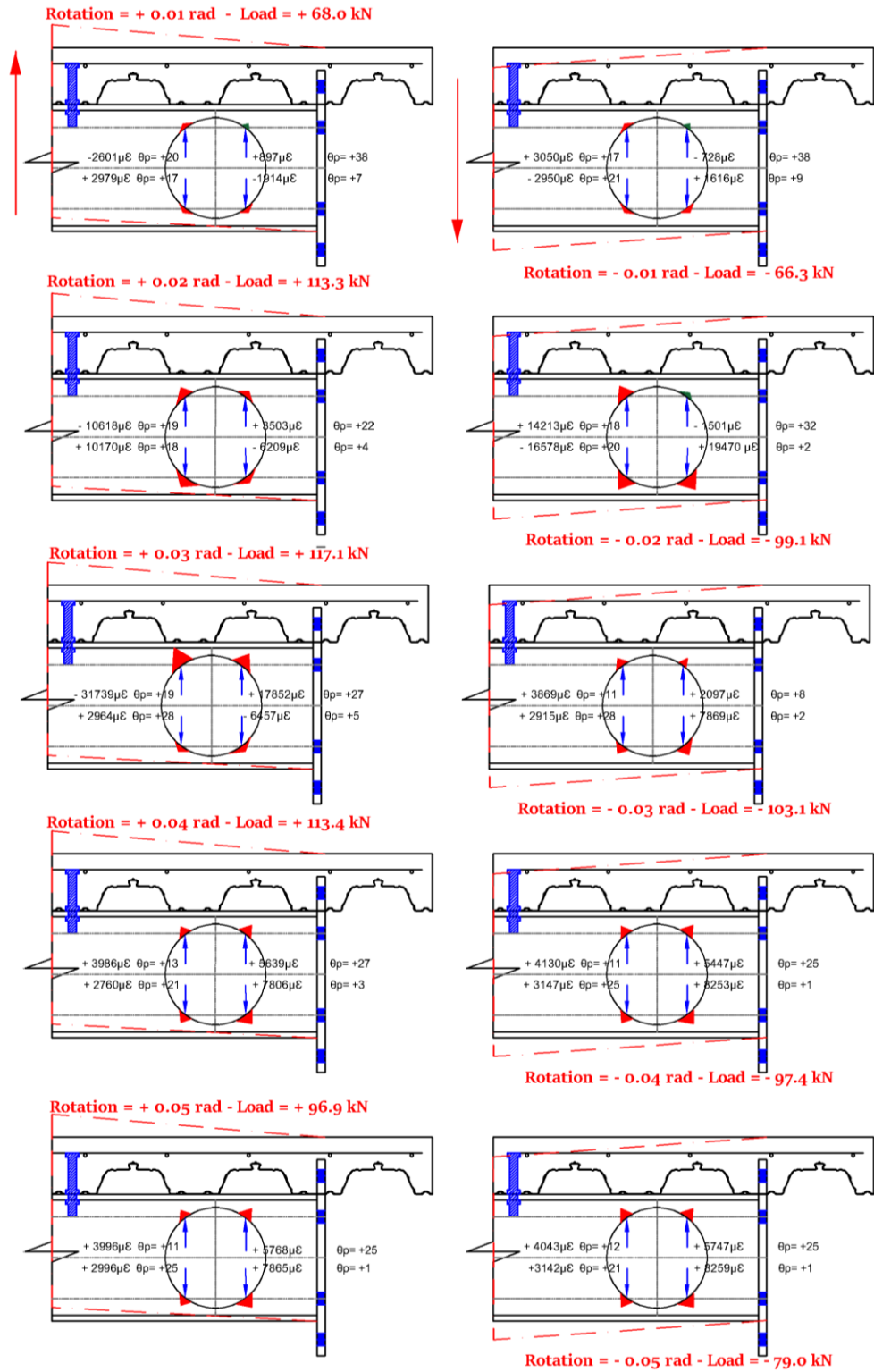


Figure 4.16: Distribution of strain intensity for RWS-L connection.



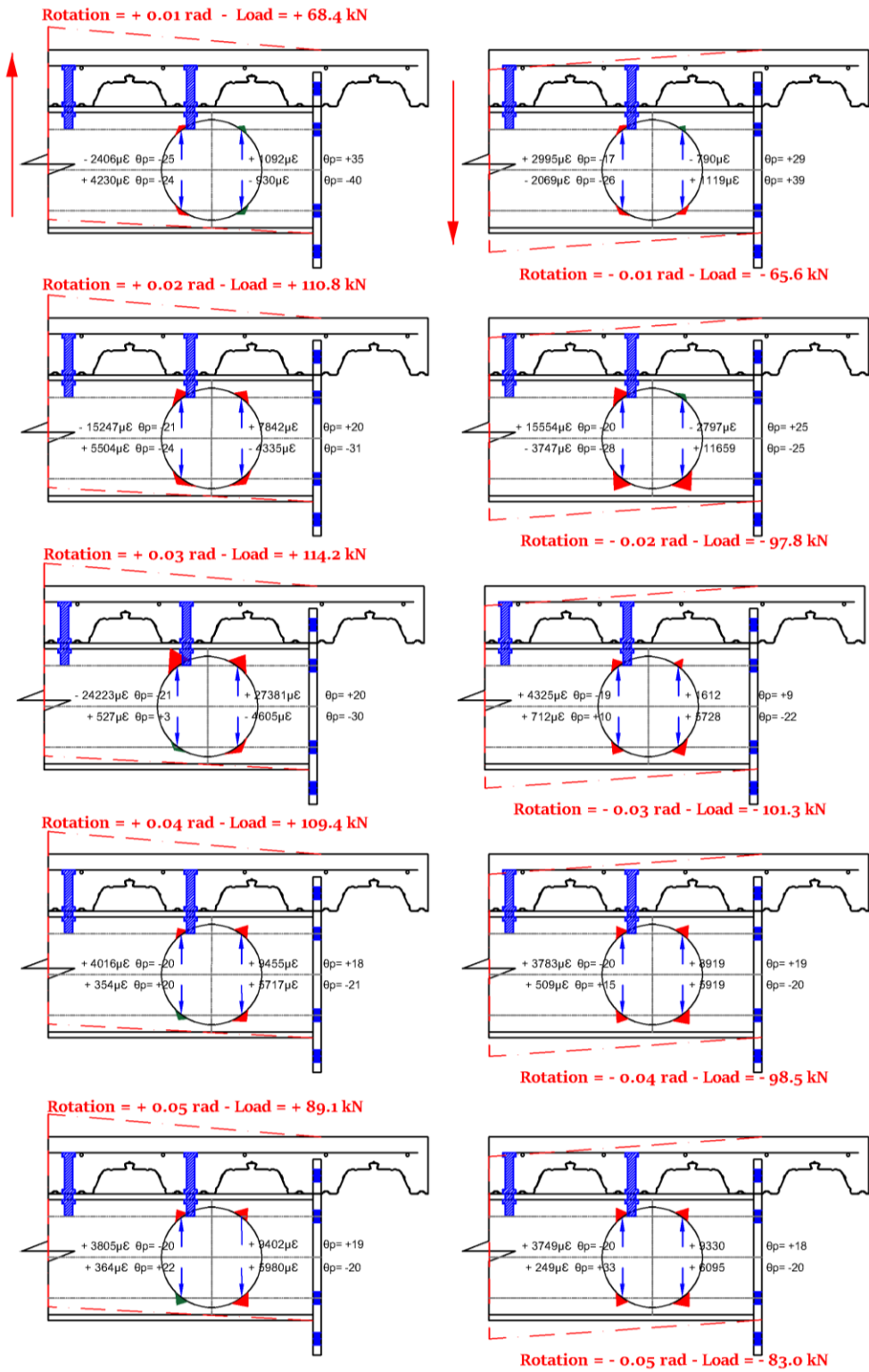
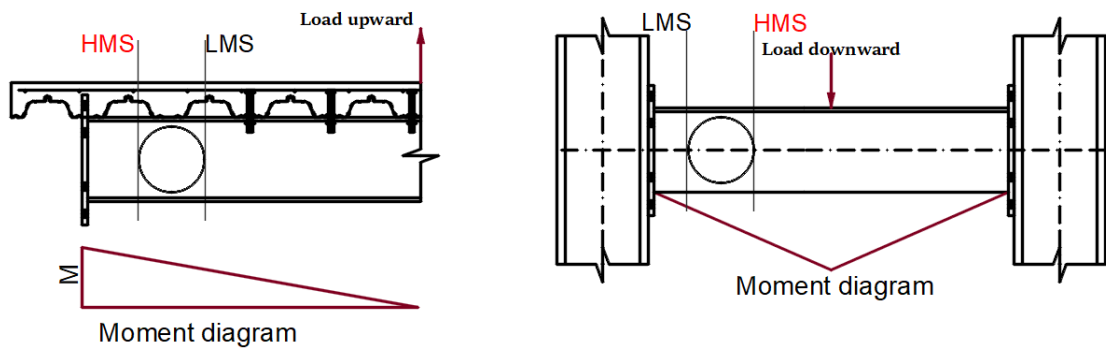


Figure 4.17: Distribution of strain intensity for RWS-H connection.



**Figure 4.18: High and low moment sides.**

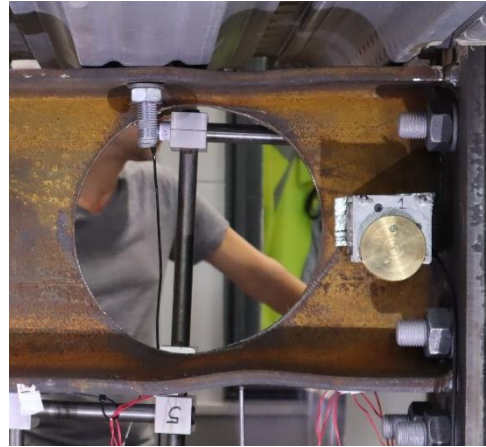
Recorded strains in the vicinity of the web opening in all RWS connections are larger in the LMS than in the HMS. In RWS-H only, the strain demand at LMS was significantly higher than that at HMS. This was attributed to the composite beam-slab engagement as the shear transfer bolts were placed off-centre over the LMS of the web opening thereby increasing the strain demand on the Tee-sections of the LMS. Consequently, yielding initiated earlier in RWS-H at the bottom Tee-section of the LMS than the other RWS connections during the first cycles of 0.01rad (sagging) as illustrated in Figures 4.15 - 4.17. However, the web opening exhibited extensive load redistribution from LMS to HMS in all RWS connections. This can be observed where the Tee-sections of the HMS in all three RWS connections reached yielding before the first two cycles of 0.02rad.

The web opening experienced large deformation in all three RWS connections when subjected to 0.03rad rotation cycles. The first plastic hinges formed in all three RWS connections at the top tee section of LMS. Particularly, in RWS-H, (see Figure 4.19a) there were peeling and hairline cracks starting at the edges of the web opening on the top Tee-section at the LMS.

In all RWS connections, during the first cycle of 0.03rad, the beam top and bottom flanges (above and below the web openings) began to buckle locally when in compression and straighten out when in tension. This behaviour persisted until the 0.04rad rotation cycles. This indicates that four plastic hinges around the web opening occurred (Vierendeel mechanism). Hence, the Vierendeel mechanism was fully developed, allowing for local buckling of the beam in both its top and bottom flanges. It could be concluded that the local yielding of Tees (ductile failure) led to favourable behaviour instead of simple shear failure at the web opening, in all RWS specimens.



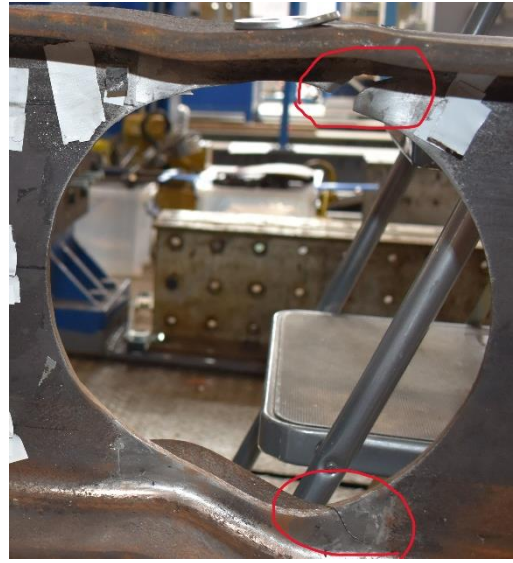
**a) Steel peeling off during 4% rotation.**



**b) Vierendeel mechanism.**



**c) Bolted studs' failure.**



**d) Cracks.**

**Figure 4.19: The failure modes of RWS-H connection.**

### 4.3.3 Hysteretic response

The hysteresis curves for all RWS connections are presented in Figures 4.20 – 4.22. Provision of stable hysteresis cycles with a high energy dissipation capacity at well-defined plastic hinge locations, is fundamental for resilient structural behaviour during and in the aftermath of earthquakes (Bernuzzi et al., 1996). In this study, RWS connections behaved as expected in terms of attaining ductility, mitigating the cracks of concrete slabs, and sustaining higher moments than the bare steel beam's full plastic moment ( $M_{pl}$ ) at 4% rotation in both directions. Thus, all RWS connections were capable of achieving at least an interstorey drift larger than 4%, thereby complying with performance targets set up in of ANSI/AISC 358-16, ANSI/AISC 341-16 and the Eurocode 8 (CEN, 2005d; ANSI/AISC 341-16, 2016; ANSI/AISC 358-16, 2016). It must be stressed that rotation capacity is expected to be larger when deployed in moment-resisting frames due to column flexibility.

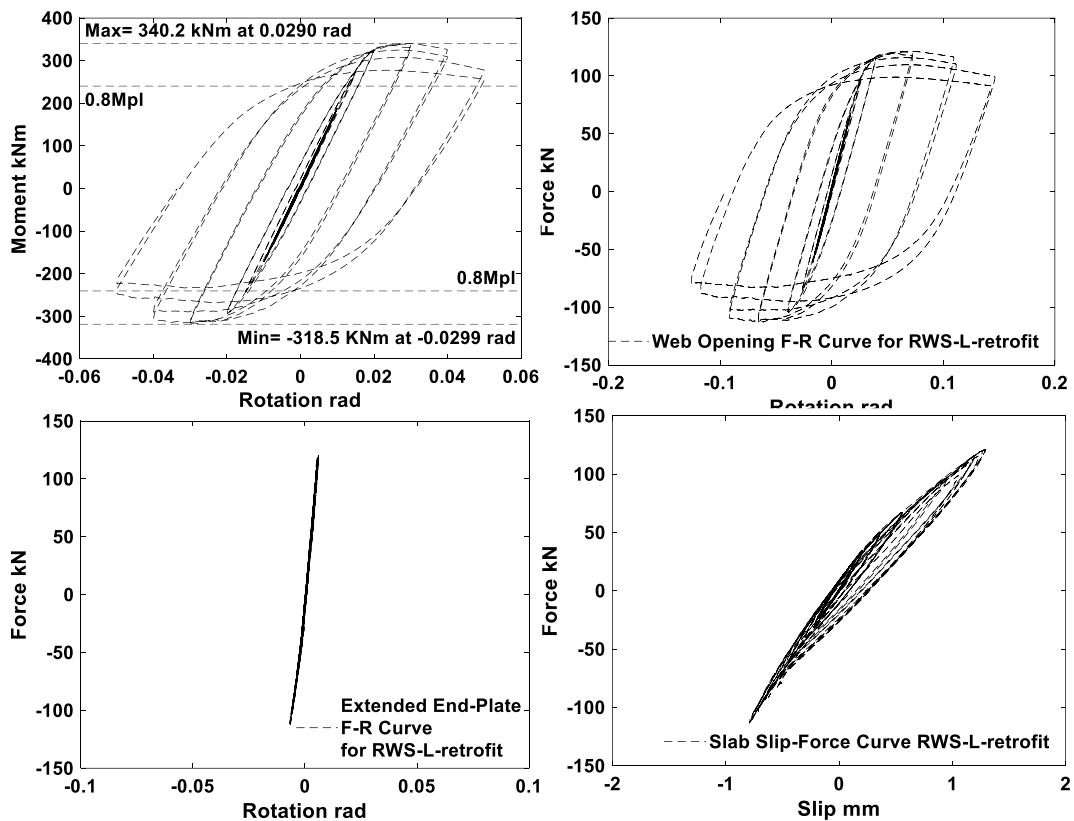


Figure 4.20: Hysteretic curves for RWS-L-retrofit connection.

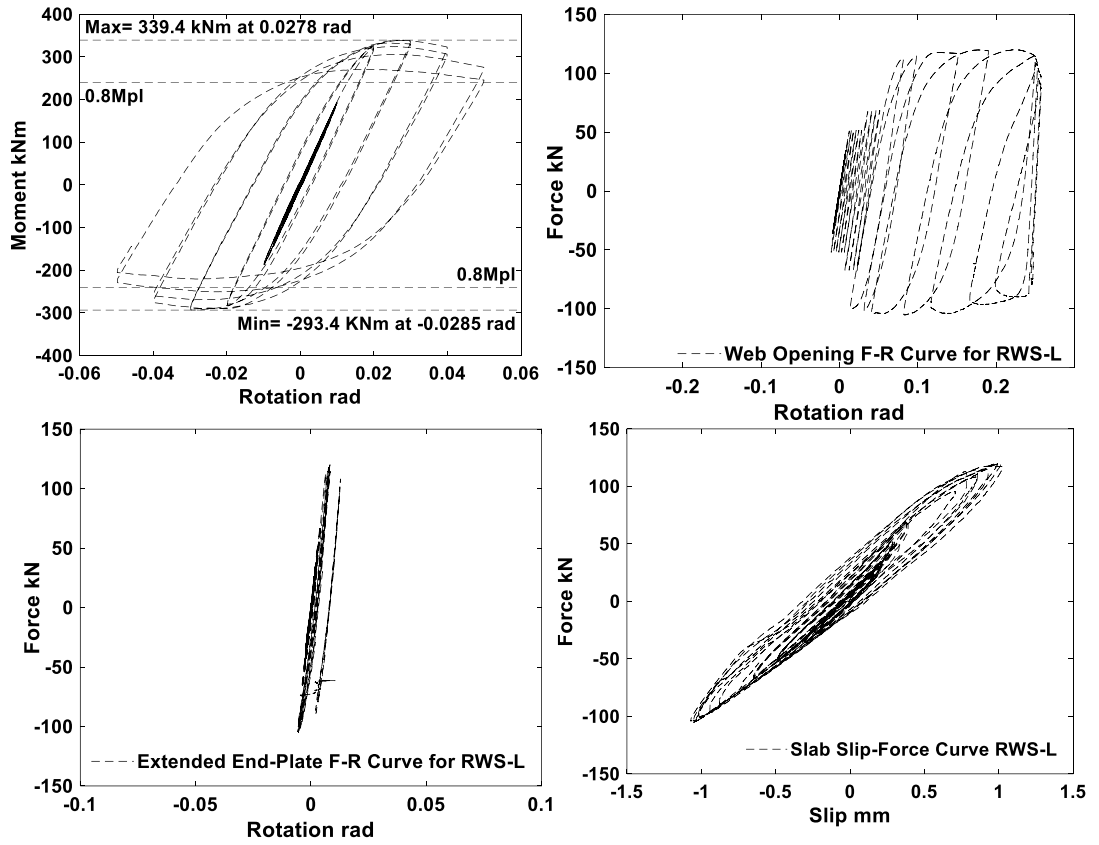


Figure 4.21: Hysteretic curves for RWS-L connection

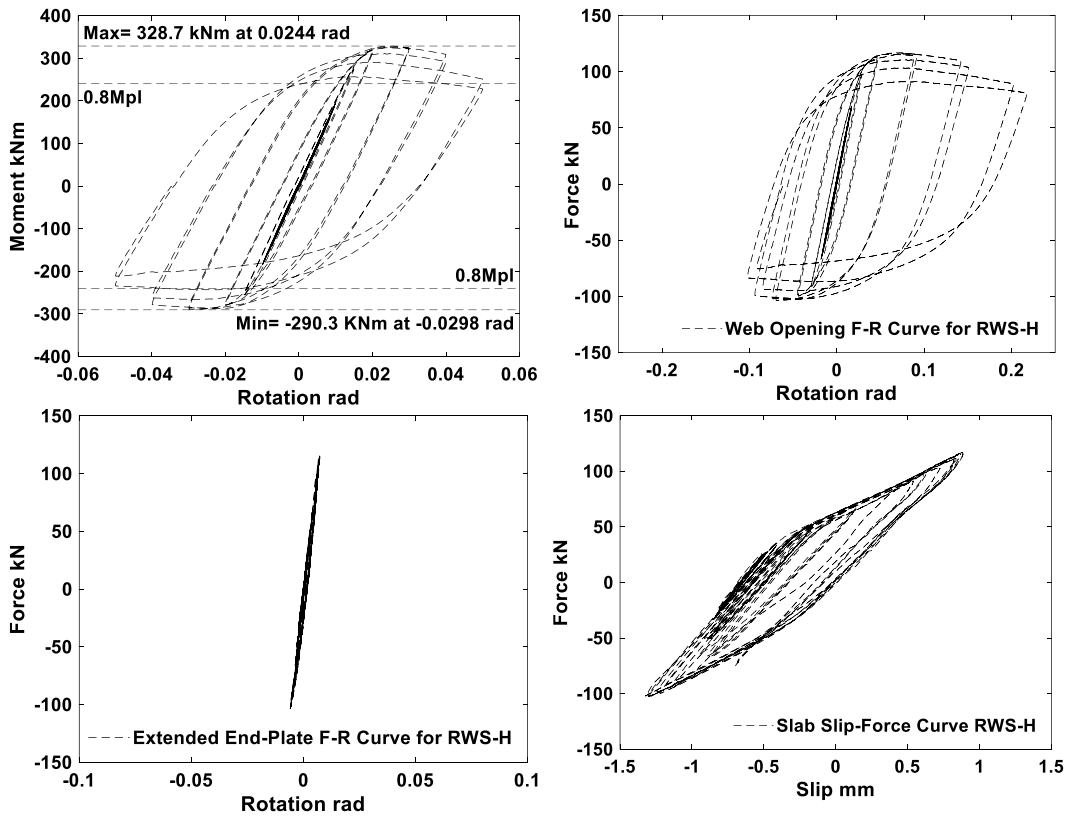
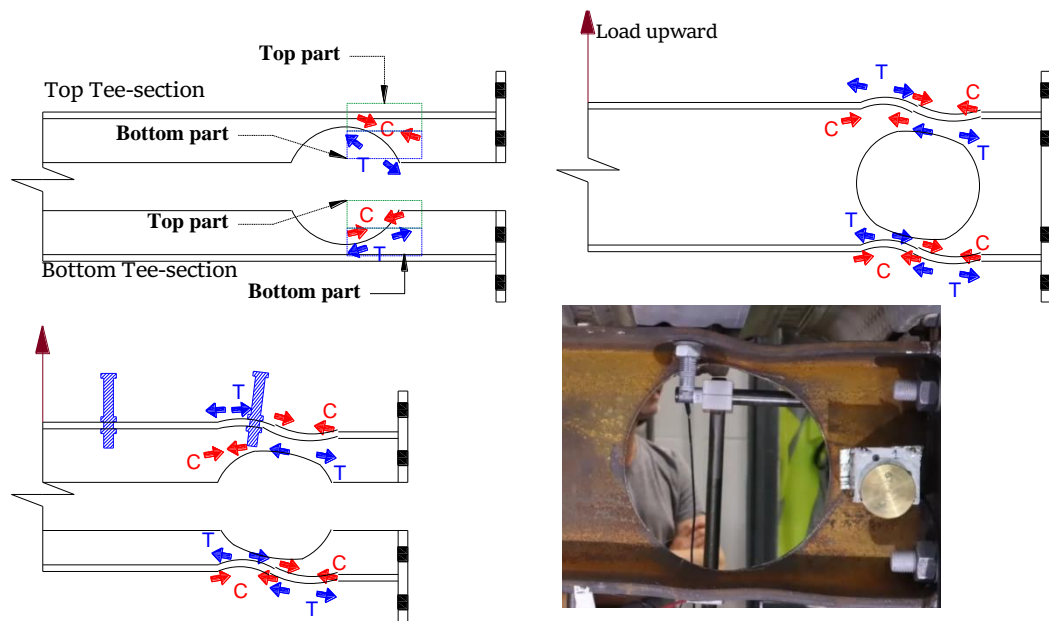


Figure 4.22: Hysteretic curves for RWS-H connection.

Round hysteresis cycles without pinching were observed for all RWS connections. They are the outcome of early local yielding in the vicinity of the web opening, thus, leading to the redistribution of the global actions from LMS to HMS. This redistribution is due to inelastic stresses being concentrated around the web openings, inducing the occurrence of the Vierendeel mechanism in the weakened area of the beam rather than failure within its non-ductile components. Such a mechanism caps the shear forces that can be transferred outside protected zones, in close alignment with capacity design principles.

It was expected that the extra row of studs over the protected zone would lead to early yielding and early failure due to increased stress/strain demand on the bottom flange (Lee et al., 2016). However, energy dissipated well through the Vierendeel mechanism in RWS-H, despite earlier crack initiation in the vicinity of the web opening. This was attributed to the capability of the web opening for redistribution of local forces, counterbalancing the increased stress/strain demand on the bottom flange that led to quick initiation of a crack in the vicinity of the web opening.

Unexpectedly, RWS-H demonstrated lower moment capacity compared to the identical specimen RWS- L (Table 4.4). The extra row of bolted shear studs should have led to a higher moment capacity of the RWS-H specimens when compared with their counterparts. Instead, it increased the stress/strain demand in the top Tee-section Figure 4.22, leading to an earlier onset of yielding in the top Tee-section at LMS due to the location of the extra row of bolts above the LMS. This can be justified by the fact that the web opening consists of two Tee-sections (top and bottom sections) with similar local behaviour under the same global load. Each Tee-section consists of top and bottom parts that exhibit compression and tension under the same action over the cross-section, as illustrated in Figures 4.23 and 4.24. The location of the studs above LMS led the bottom part of the top Tee-section to experience earlier local yielding, which eventually induced earlier crack initiation at the LMS as well. This is a plausible explanation for the lower moment capacity of RWS-H, as this feature was absent in RWS connections without composite action above the web opening.



**Figure 4.23: Illustration of the behaviour of Tee-sections in RWS-H.**

In detail, when subjected to cyclic loading, the top and bottom Tee-sections will be subjected to global/cross-section shear and moment, as well as local axial forces as shown in Figures 4.24 and 4.25. The behaviour of the top and bottom Tee-sections alternates between tension and compression due to the reversible actions expected during earthquakes. Any increase in the global moment will generate local axial forces in the Tee-sections, decreasing their contribution to the capacity of the Vierendeel mechanism (Lawson and Hicks, 2011). An increase in the shear force and critical length will lead to larger moments within the Vierendeel mechanism.

When the applied load goes upward, moments within the Vierendeel mechanism cause the web of the top Tee-section to undergo tension while the flange-web of the top Tee-section exhibits compression at HMS (see Figure 4.24). Under the same conditions, the web of the top Tee-section will experience compression while the flange web and the top Tee-section will be under tension at LMS. Such a complex behaviour can induce early local yielding of Tees before any yielding in the connection and column. This early local yielding results in the stretching of the opening and local buckling of flanges as shown in Figure 4.24. Both are indicators of the formation of the Vierendeel (ductile), mechanism which becomes the dominant mechanism rather than simple shear failure at the web opening, due to the redistribution of the global actions.

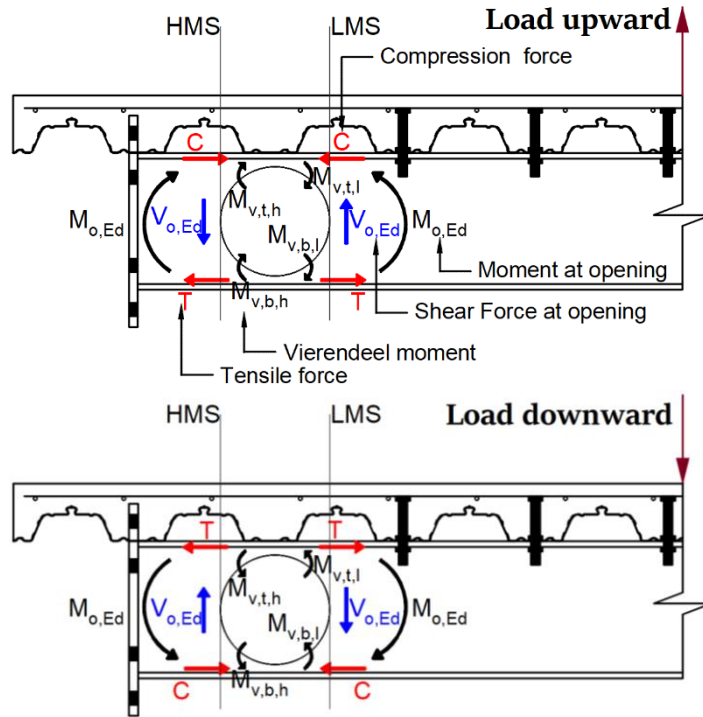


Figure 4.24: Force action at web opening without composite action above the protected zone.

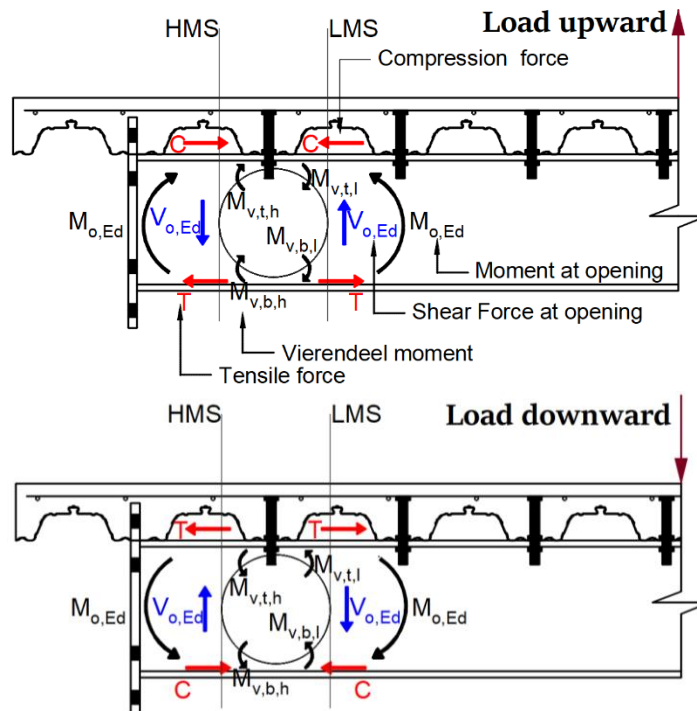
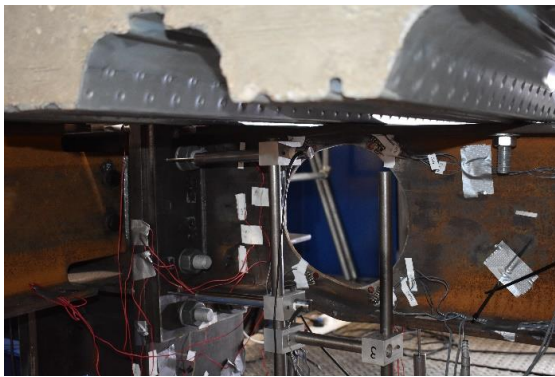


Figure 4.25: Force action at web opening with composite action above the protected zone.



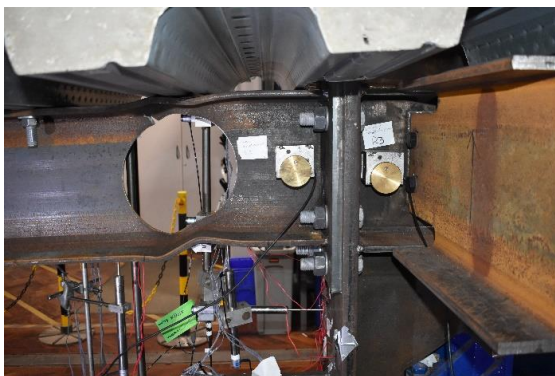
Remarkably, the retrofitted specimen (RWS-L-retrofit), which involved creating a web opening, performed as well as the other RWS connections, despite concrete cone failure (Figure 4.26b). An additional crack line was observed in the slab of RWS-L-retrofit connection (Figure 4.27), in addition to the two lines of micro-cracks that developed in the solid connection as illustrated in Figure 4.13. These two lines of cracks became more visible but did not propagate deeply inside the RC slab in the next test of RWS-L-retrofit. While RWS-L and RWS-H specimens experienced only micro-cracks. Also, slight separation between the deck and the concrete occurred in RWS-L and RWS-L-retrofit (see Figure 4.28). The maximum slab slip in all RWS connections at the maximum load was not more than 1.3 mm in the positive moment and 1.32 mm in the negative moment. This further indicates that significant plastic deformation only occurred in the web opening.



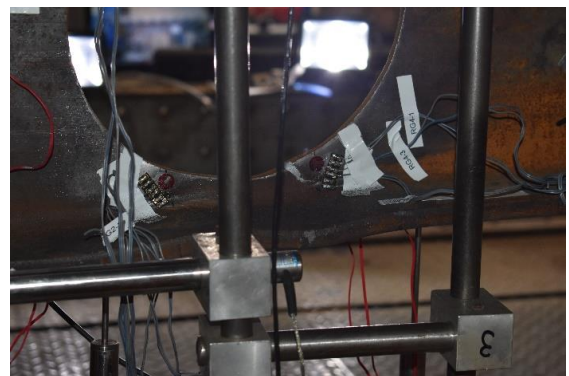
**a) Vierendeel Mechanism.**



**b) Concrete cone failure.**



**c) Top crack at the end of first cycle of 0.05 rad (hogging moment).**



**d) Bottom crack at second cycle of 0.05 rad (sagging moment).**

**Figure 4.26: Failure modes of RWS-L-retrofit specimen.**

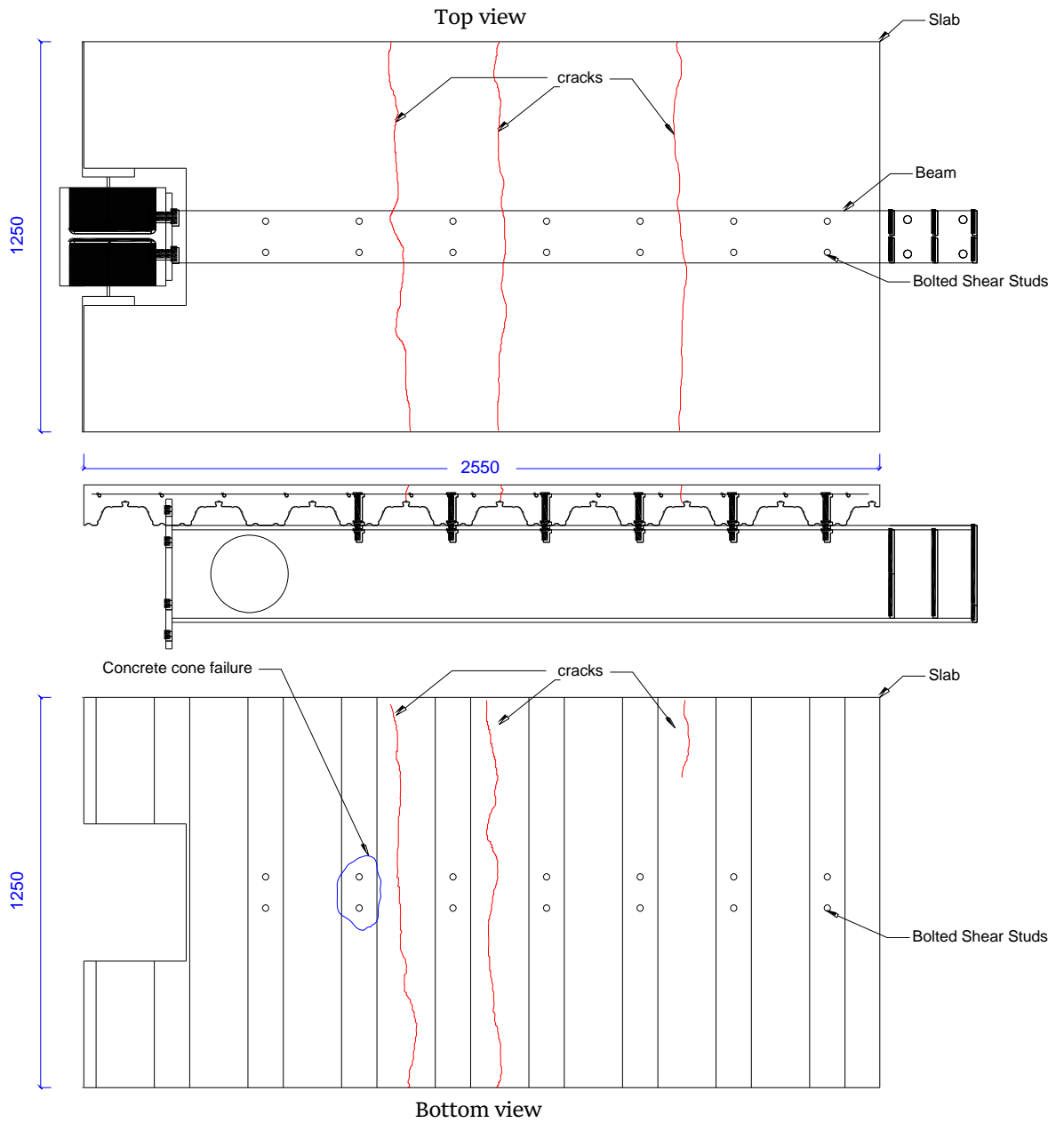


**Figure 4.27: Observed crack pattern in RWS-L-retrofit connection specimen (mm).**

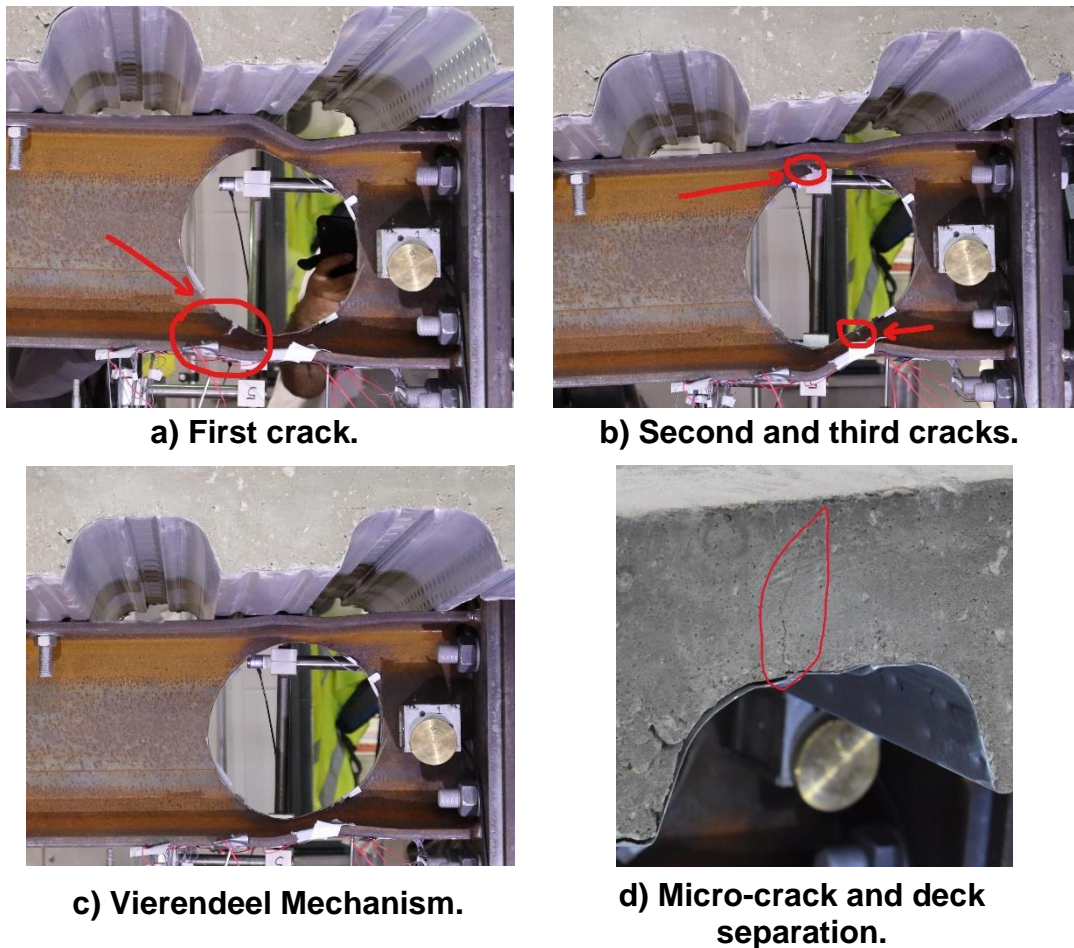


**Figure 4.28: The failure modes of RWS-L connection.**

It seems that both the demountable shear studs and a 25mm gap between the RC slab and steel elements played a key role in mitigating RC slab damage, along with the plastification of the web opening. This could be due to the hole clearance in the steel beam flange which allowed for slippage between the beam and the slab, as well as the fact that plastic deformation occurred in the vicinity of the web opening. The provision of the entirely disconnected beam-to-column joints (i.e., 25mm gap) prevented contact between the RC slab and steel elements, thus limiting force transfer between them. Consequently, the expected failure mode of a ductile frame strong column-weak beam was observed in all the tested RWS specimens (Figures 4.26 and 4.28).

The demountable composite system was found to be capable of quick disassembly, therefore fostering reuse, and/or replacement in case of extensive damage observed at the end of the design life or in the aftermath of a large earthquake. The nuts were easily demounted using an ordinary wrench; even, if there was appreciable bending of the washer, which was the case for the RWS-H specimen.

### 4.3.4 Expected vs. actual resistances

#### 4.3.4.1 Capacity design

The strong-column weak-beam design framework, adopted in both Eurocodes and AISC (CEN, 2005b; CEN, 2005d; ANSI/AISC 341-16, 2016; ANSI/AISC 358-16, 2016) requires that the bending strength of the connection  $M_{j,Rd}$  should be stronger than the bending resistance of the connected beam  $M_{pl,Rd}$ . In this study, the capacity of the connection  $M_{j,Rd}$  that was designed based on the components method in Eurocode 3-1-8 (CEN, 2005b) compared to  $M_{pl,a,Rd}$  and  $M_{o,a,Rd}$  are shown in Table 4.1.

The connection to beam capacity ratio  $M_{j,Rd}/M_{pl,a,Rd}$  of the solid specimen equals one, which falls into the category of partial-strength according to Eurocode 3-8 (CEN, 2005b). In the equal/partial strength category, the plastic deformations occur in both the connection and the beam (Landolfo, 2022). The introduction of the web opening (RWS) into the solid-webbed beam reduced the capacity of the connected beam. Thus, it increased the connection-to-beam capacity ratio  $M_{j,Rd}/M_{o,a,Rd}$  to 1.17 and altered the connection category from partial to full strength.

The adopted capacity design framework was effective for obtaining the expected performance, namely plastic deformations occurred in the web opening only. This means that a web opening effectively constrains inelastic action in the protected zone, away from the joint plate and the column. Henceforth, providing the web opening is a reliable course of action that allows for full-strength connections within the strong column/connection weak beam paradigm.

Ensuring that RWS connections retain their ability to carry gravity forces, even after failure, is critical; especially in the aftermath of an earthquake. In this testing campaign, a large web opening equal to 80% of the beam depth was tested; this exceeds the limitations of the SCI P355 guidance. Moreover, as previously mentioned, the rotation capacity is expected to be greater when deployed in moment-resisting frames than what was observed in these tests, due to the flexibility of the column. As a result, both the column flange and the panel zone would contribute to inter-story drift capacity, preventing cracks in the vicinity of the web opening. Thus, the post-earthquake capacity (e.g., shear capacity) would remain uncompromised, as the Vierendeel capacity of the perforated section has not been reached. The potential risks, such as yielding or buckling of the remaining web sections and their implications for maintaining structural integrity in post-earthquake scenarios, are worth exploring and investigating.

#### 4.3.4.2 Connection Design Moment

Table 4.4 shows the ratios of the applied actions to the design/capacity values. It is worth noting that all hogging (-ve) design capacities for all non-composite and composite, unperforated and perforated beam sections were based on the steel capacities (i.e.,  $M_{pl,a,Rd}$  (Eq. 4.1) and  $M_{o,a,Rd}$  (Eq. 4.2) Error! Reference source not found.). For RWS connections, the average ratios based on the nominal resistance of steel solid-webbed beam (Eq. 4.1) are +1.12 and -1.00 under sagging and hogging moments, respectively. While the average ratios based on perforated steel (Eq. 4.2), are +1.16 and -1.04 under sagging and hogging moments, respectively. Ratio values greater than 1 denote that the composite slab contributes to the overall connection strength.

It is found that under sagging moment, the composite slab contributes to the overall RWS connection strength, regardless of composite engagement. While under hogging moments, the contribution of the composite slab was affected by the location of the web opening. Therefore, the composite action should be considered in the design process due to its contribution. This is because it could jeopardize the strong column-weak beam framework, by strengthening rather than weakening the beam, if it is not properly accounted for. Further experimental and FE investigations are needed to verify the effect of the size and location of web openings on the contribution of the composite slab.

For sagging moments, it can be seen that the plastic stress block method  $M_{pl,Rd}$  overestimates the actual composite section strength (Table 4.4). While the plastic bending resistance of the composite beam section at the web opening  $M_{o,a,Rd}$  according to SCI P355 guidance, underestimates the actual composite perforated beam section strength. In details,  $M_{o,a,Rd}$  based on the SCI P355 guidance provides an overstrength by about 12%. While the plastic stress block method  $M_{pl,Rd}$  does not represent the actual strength and provide less strength than the actual one by about 32%. Hence it is important to comprehend the impact of the composite engagement on RWS connections to consider the overstrength in both new buildings and seismic retrofit.

Regarding moments within the Vierendeel mechanism, the design method of SCI P355 guidance did not accurately predict the actual Vierendeel bending resistance of the perforated beam section that was subjected to cyclic loading (Table 4.5). Under sagging moment, the applied Vierendeel moments were lower than the Vierendeel bending resistance by 26% for RWS connection without composite engagement, and by 50% for RWS-H. While under a hogging moment, the applied Vierendeel moments were, on average, 28% lower than the Vierendeel bending resistance. This also applied to the shear resistance of the

perforated sections as per SCI P355 guidance. On average, the applied shear forces were 26% and 25% lower than the resistances under sagging and hogging moments, respectively.

**Table 4.5: Design resistances vs. applied actions.**

RWS connections		RWS-L-retrofit	RWS-L	RWS-H
$V_{o,Rd}$ (kN)	Steel	142.9		
	Composite	161.2	160.5	160.5
$M_{V,Rd}$ (kNm)	Steel	18.2		
	Composite	18.2		24.5
$V_{Ed}$ (kN)	+ve	120.7	120.4	116.6
	-ve	-113	-104.1	-103
$M_{V,Ed}$ (kNm)	+ve	13.43	13.40	12.98
	-ve	-12.58	-11.59	-11.46
$V_{Ed}/V_{o,Rd}$	+ve	0.75	0.75	0.73
	-ve	-0.79	-0.73	-0.72
$M_{V,Ed}/M_{V,Rd}$	+ve	0.74	0.74	0.53
	-ve	-0.69	-0.64	-0.63

**Note:**  $V_{o,Rd}$  = shear resistance for perforated section and  $M_{V,Rd}$  = Vierendeel bending resistance according to SCI P355 guidance.  $V_{Ed}$  = maximum applied shear force in the test.  $M_{V,Ed}$  = applied Vierendeel moment in the test =  $V_{Ed} l_e$ . Where  $l_e$  is equivalent rectangular opening length.  $M_{V,Rd}$  of RWS-L-retrofit and RWS-L for composite sections were based on the steel sections, because there was no composite engagement over the opening. For -ve  $V_{Ed}/V_{o,Rd}$  and -ve  $M_{V,Ed}/M_{V,Rd}$ , steel section resistances were used (i.e.,  $M_{V,Rd}$  for steel and  $V_{o,Rd}$  for steel).

#### 4.3.5 Strain profile across the steel beam bottom flanges

The strain profiles across the steel beam bottom flanges near the connections and below the web openings are presented in Figures 4.29 and 4.30. It is worth noting that the yield strain of the steel material in these tests equals  $1775\mu$ . The strain on the bottom flange near the connection for RWS-L-retrofit was beyond the elastic limit (in yielding region), but did not reach the plastic region as illustrated in Figure 4.9. The highest recorded strain was  $2866\mu$  at rotation of  $0.03\text{rad}$  under hogging moments. In contrast, for RWS-L and RWS-H, the highest recorded strains on the bottom flanges near the connection were  $10936\mu$  and  $11241\mu$  at a rotation of  $0.05\text{rad}$  under sagging, respectively. The higher strain demands found in RWS-L and RWS-H were approximately 3.8 times those found in the RWS-L-retrofit. This was due to the fact that the location of web openings was closer to the column face in these two connections. This also implies that the strain demand on the bottom flange near the connection was not influenced by the composite engagement, given the negligible difference in the strain demand observed between RWS-L and RWS-H.

Regarding the strain demand on the flange below the web opening, the highest recorded strain was  $7516\mu$  at a rotation of  $0.04\text{rad}$  for RWS-L-retrofit. At the same stage, the recorded strains were  $8524\mu$  and  $9122\mu$  at a rotation of  $0.04\text{rad}$  in RWS-L and RWS-H, respectively. However, the highest recorded strains in RWS-L and RWS-H were  $11907\mu$  and  $12821\mu$  at a rotation of  $0.05\text{rad}$  under hogging, respectively. It was observed that under sagging moments, the strain demands on the flange below the web opening did not exceed  $3329\mu$  for all RWS connections. However, the beam flange below the web opening was in the elastic-plastic region during the cycles of  $0.03\text{rad}$ . It was worth noting that the strain profiles up to the end of the tests across the beam web in all RWS connections did not exceed  $1603\mu$ .



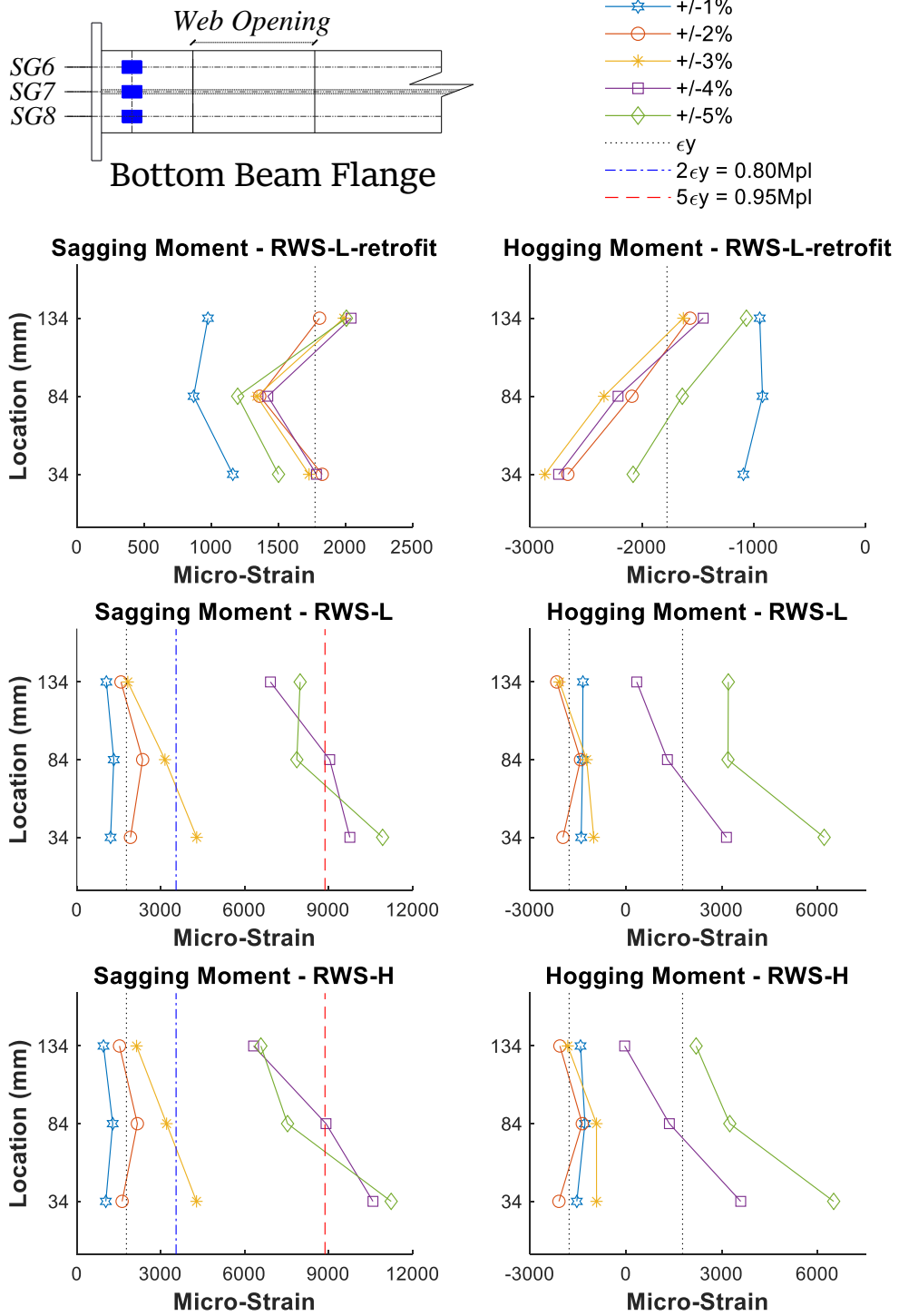


Figure 4.29: Strain profiles for beam bottom flange near the connections.



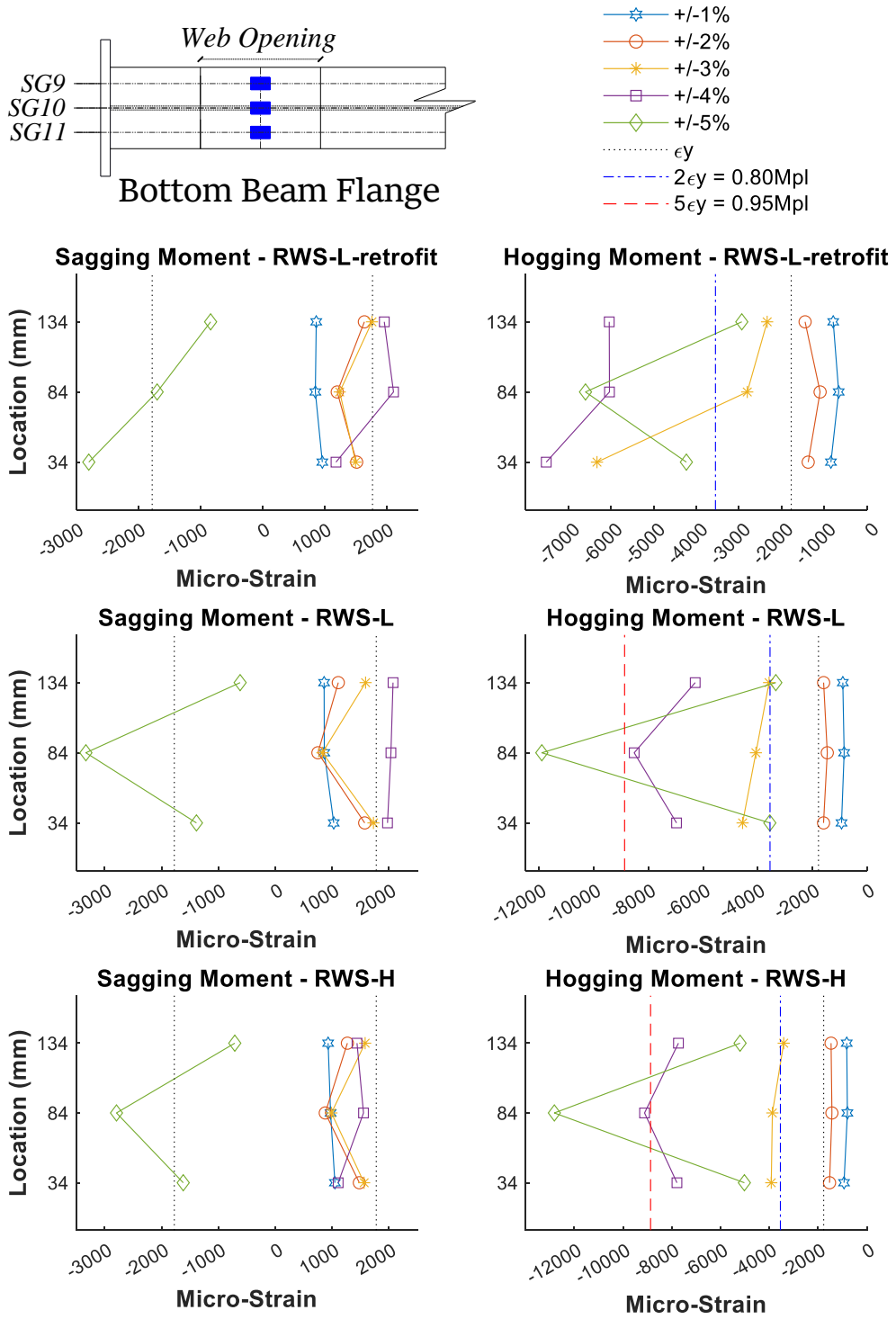


Figure 4.30: Strain profiles for beam bottom flange below the web openings.

## 4.4 Summary

This chapter presents the results of an experimental study on demountable steel-concrete composite RWS connections to assess their adequacy for use in seismic areas. Four demountable steel-concrete composite connection specimens that employed RWS were tested under cyclic loading. The key differences among the specimens were the presence of bolted shear studs over the web opening and the location of the web opening.

One solid-webbed specimen was tested to examine the structural performance of retrofitted connections. This was done by cutting a hole in the web after subjecting the specimen to cyclic loads representing moderate seismicity. The test results showed that the RWS connections were capable of utilizing the perforation's location in a high shear zone. This resulted in the initiation of local yielding in Tee-sections, leading to the dominance of the ductile (Vierendeel) failure mode in the connected beam.

This mechanism is critical to avoid transferring excessive shear forces to the components of such connections. The results also underscored that the component method approach used in Eurocode 3 for joint design should include the effect of web opening on the joint behaviour using the design guidelines of SCI P355 guidance (Lawson and Hicks, 2011). This is due to the reliability of the occurrence of Vierendeel failure mode.

All specimens can accommodate at least a 4% inter-story drift ratio. This would rank the connections as highly ductile, henceforth allowing for their deployment within Special Moment Frames, considering both AISC and Eurocode guidelines.

The size and location as well as the presence of bolted studs over the protected zone influence the strength, rotational capacity, ductility, and energy dissipation of RWS connections. Further experimental and numerical studies are needed to expand data for potential prequalification in existing and next-generation seismic codes for steel design.

## Chapter 5

### Parametric Assessments

#### 5.1 Introduction

Although physical testing provides more accurate and valuable findings, it comes with high costs and is time-consuming. Also, it is impossible to cover the whole range of parameters that are needed for a complete investigation in an experimental study. Finite element (FE) analysis offers acceptable and practical alternatives. However, FE analysis still requires physical testing for benchmarking to be employed for further investigations. Therefore, high-fidelity FE models were developed to simulate the structural behaviour of the four demountable composite RWS connections that were conducted in Chapter 4.

This chapter investigates the cyclic behaviour of demountable steel-concrete composite reduced web section (RWS) connections. The complex hysteresis behaviour of bolted extended end-plate RWS connections is a result of multiple deformable components, making their prediction challenging. To enhance understanding, a high-fidelity FE model was developed, focusing on parameters and, specifically, the presence of composite action over the web opening, diameter, and the end-distance of the web opening. The study, encompassing 285 FE models, aims to quantify and assess the hysteretic response characteristics of RWS connections.

Numerical simulation techniques using the ABAQUS were defined to best replicate the hysteretic behaviour observed in the experimental findings. These techniques also aimed to reduce analysis running time and conserve computer storage without compromising the accuracy of results. Many of these techniques are generally based on the numerical techniques employed in Chapter 3. These include element types, modelling contact interactions, creating partitions, meshing, geometric and material nonlinearities, as well as boundary and loading conditions. For the sake of completeness and convenience, a brief description of these techniques is presented in this chapter, considering the distinctions in the conditions of the test setup and the specimens reported in Chapter 4.

## 5.2 Finite element model validation

### 5.2.1 Numerical modelling

The geometrical and cross-sectional details of the four tested specimens are reported in Chapter 4. In the numerical simulations, a combination of shell (S4R) and solid elements (C3D8R) with reduced integration was employed. The concrete slab, bolts, and bolted shear studs were modelled with 8-node solid elements with reduced integration (element type C3D8R). All other elements were modelled with 4-node shell elements with reduced integration (S4R), as shown in Figures 5.1 and 5.2. The reinforcement steel bars were modelled using a truss element (2-node linear, T3D2), which can carry only tensile and compression loads and exclude any resistance to bending.

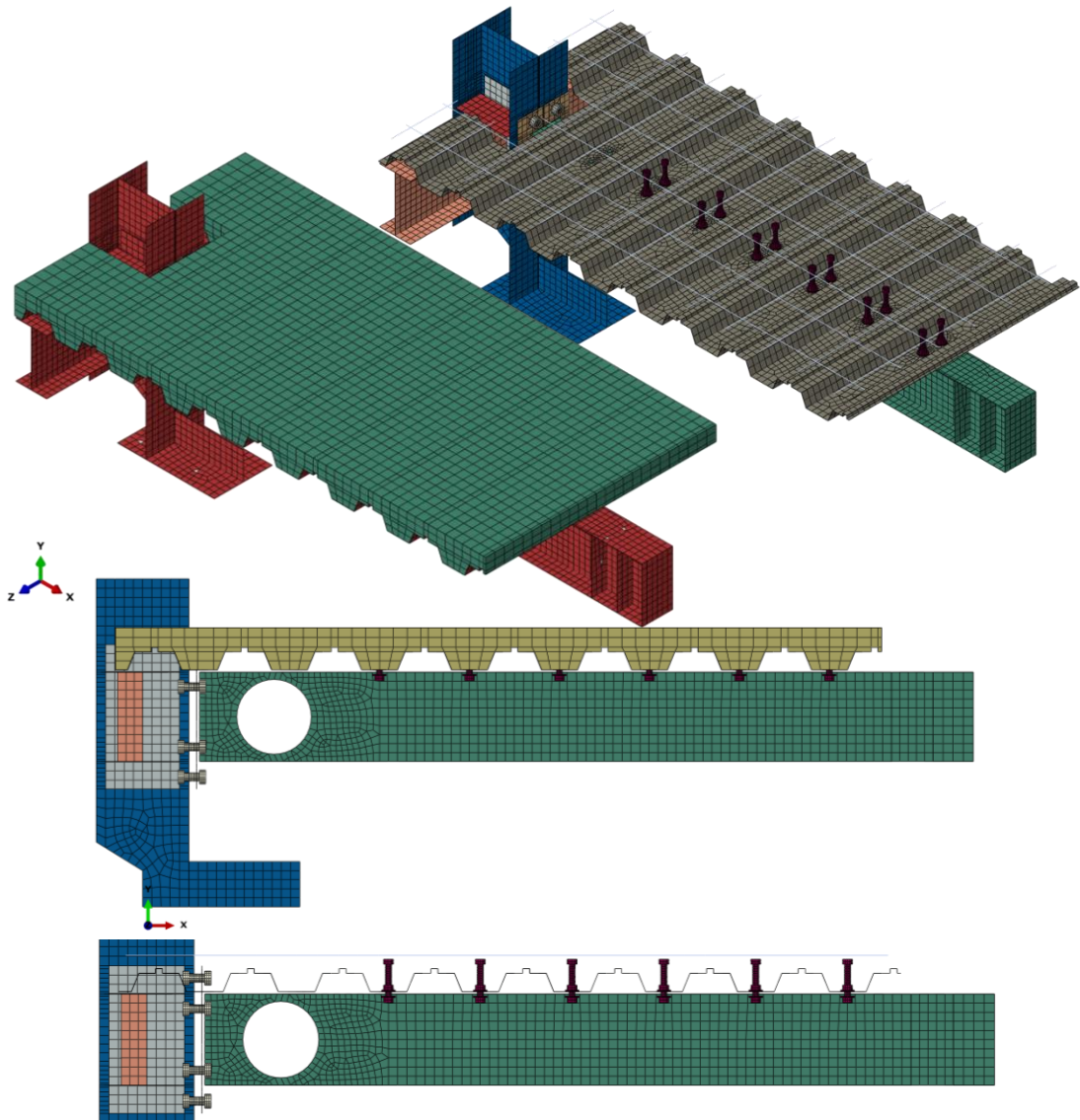
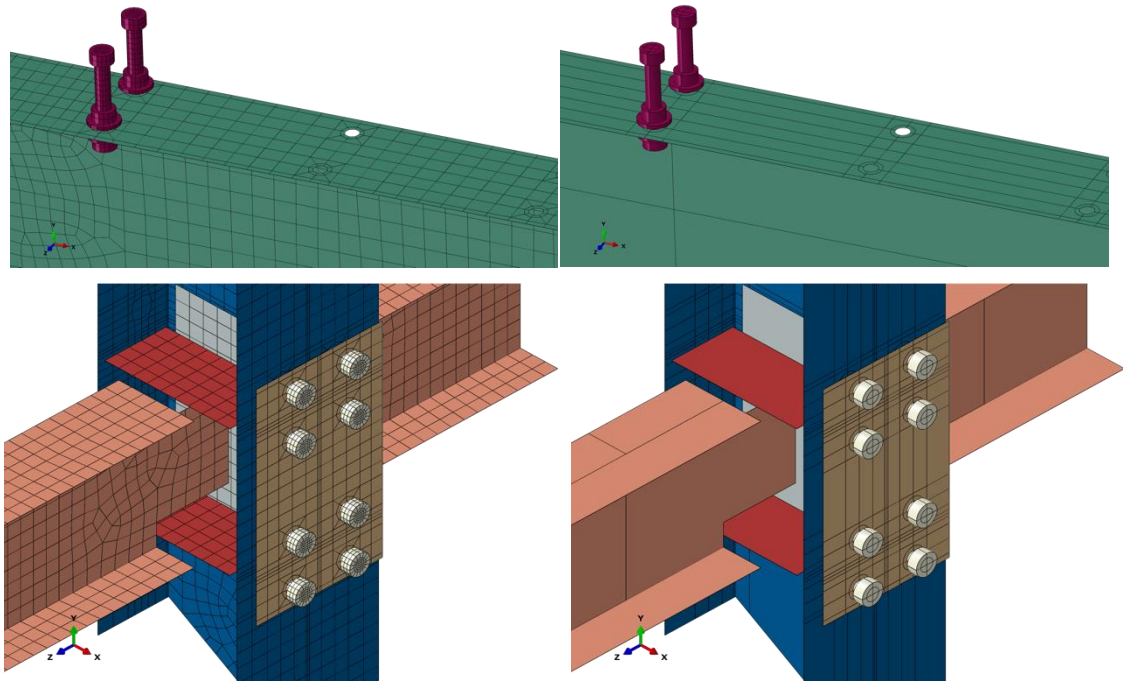


Figure 5.1: Top and side views of FE model with and without slab (shell thickness is not shown).



**Figure 5.2: FE model showing meshes and partitions.**

Tie constraints were applied to simulate the welding between steel elements. Normal and tangent interactions were employed between steel-to-steel elements by defining hard contact and formulation of a friction coefficient equal to 0.2 (which corresponds to the case of untreated rolled surfaces (CEN, 2005a)) and with a finite sliding approach. Tie contact was considered between the reinforced concrete slab and metal deck to avoid numerical instabilities in some parametric FE models, instability which can lead to early termination of the analysis. Also, this modelling technique was adopted to decrease computational time in parametric FE models.

Based on the mesh sensitivity study conducted in Chapter 3 to assess the time, storage, and accuracy of the results, the mesh size for steel, slab, bolts and bolted studs is equal to 30, 50, and 7.5 mm, respectively. A mesh size equal to 20 mm was selected for the main beam with a distance of 600 mm near the connection, as high stresses/strains were expected. The total number of elements was 35,551. These FE modelling techniques were defined to best simulate the hysteretic behaviour of the experimental tests in Chapter 4 and to limit the analysis running time between 11 and 15 hours (i.e., one session on the High-Performance Computer).

The boundary and loading conditions, including the gravity load, were employed in FE models to simulate the ones in the experimental tests in Chapter 4, as illustrated in Figure 5.3. Furthermore, preloading forces were applied to simulate

the tightening of bolts and bolted studs using the “bolt load” (see Figure 5.3). The distribution of residual stresses obtained from testing the solid specimen was applied to the validated FE model of RWS-L-retrofit in order to simulate the effects of moderate seismicity for rehabilitation purposes. Eigenbuckling analyses were initially performed before the main analyses. The first modes were scaled by the recommended factor of  $t_w/200$  in accordance with (Tsavdaridis and D’Mello, 2009) to introduce geometric imperfections accounting for typical local manufacturing tolerances.

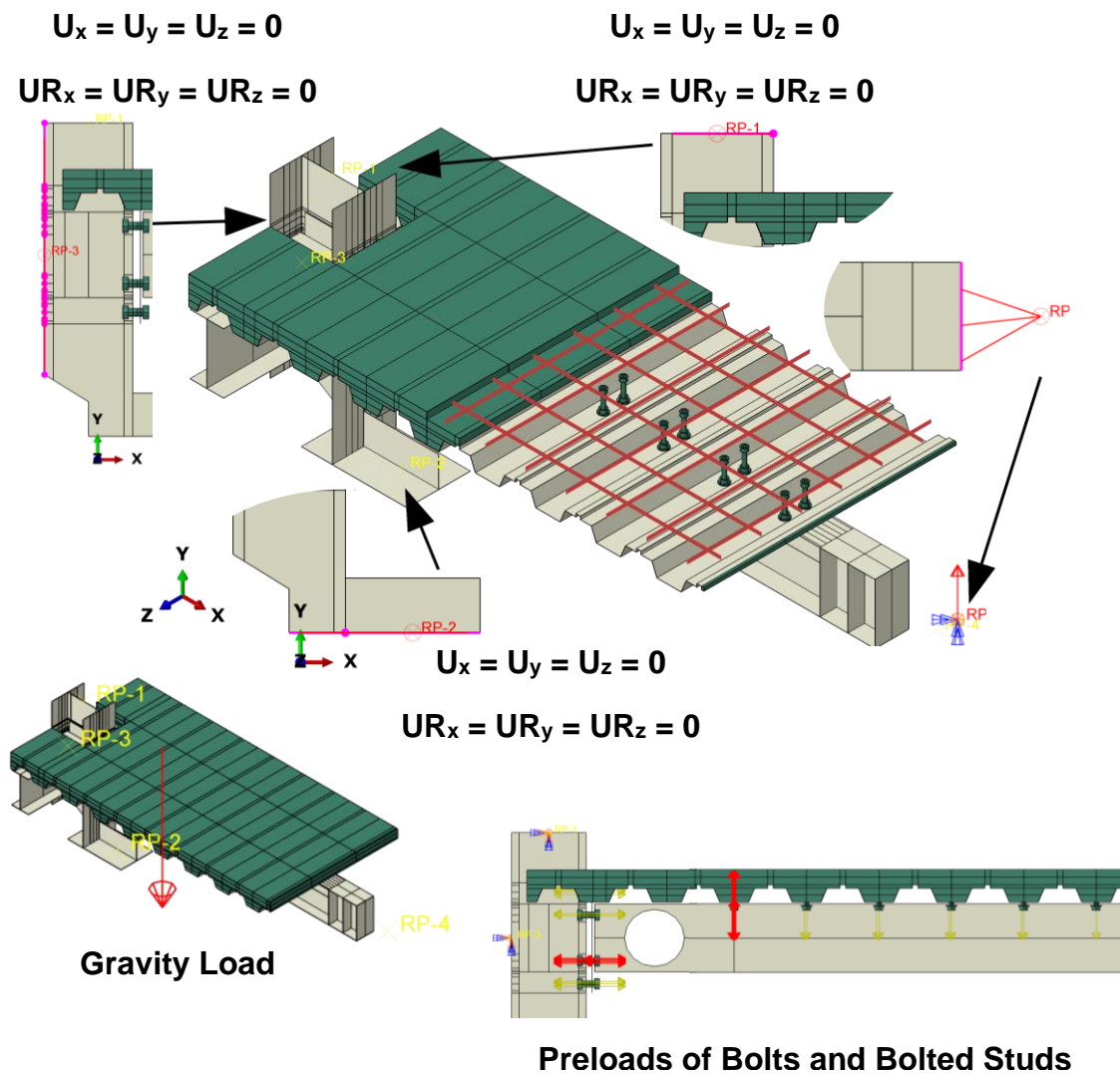
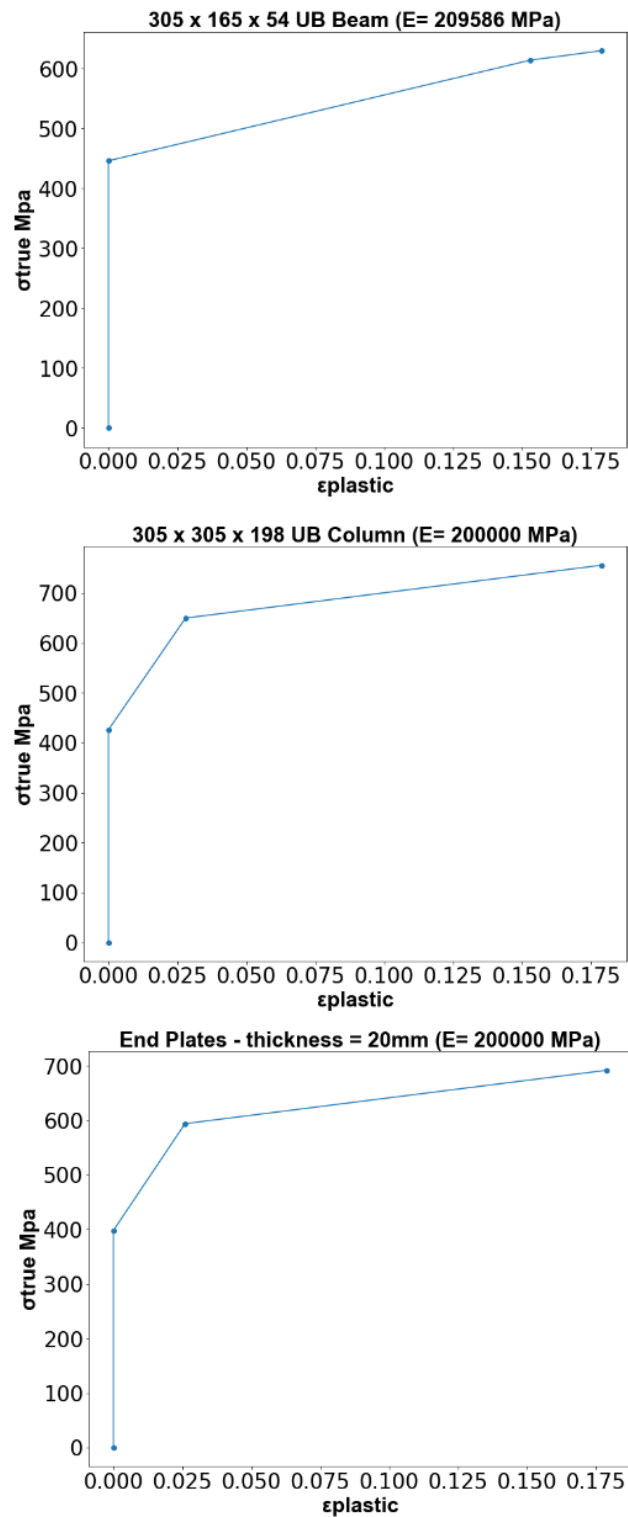


Figure 5.3: Boundary and loading conditions.

### 5.2.2 Material model

The same models that were adopted in Chapter 3 were employed and described herein. Material non-linearities were adopted by employing a combined isotropic and kinematic material-hardening model from ABAQUS for all steel elements, including bolts and bolted shear studs, as shown in Figures 5.4 and 5.5. The average values of tensile tests for the beam web and flange were considered, and nominal values of material properties were taken from the manufacturer's specifications. Three points from stress-strain curves were used to reduce computational time and storage requirements, as shown in Figures 5.4 and 5.5. The ultimate strain ( $\epsilon_u$ ) was equal to  $15\epsilon_y$  for all steel elements and  $10\epsilon_y$  for bolts and bolted shear studs. While  $\epsilon_r$  was set to 0.2 for all steel elements and to 0.05 for the bolts and bolted shear studs. The ductile damage option was used to consider the effect of the cracks that occurred in the vicinity of the web opening during the experimental tests. The values of ductile damage were extracted, as described in the ABAQUS manual, from the tensile tests of beam web that were conducted in the literature. An elastic-perfectly-plastic model was adopted for metal deck and rebar, with strain hardening equal to  $E_{sh} = E/80$  (Chaudhari, 2017). The concrete slab was modelled using a concrete damaged plasticity (CDP) model based on a constitutive law of EC2 (CEN, 2004) and exponential tension softening (Cornelissen et al., 1986) to simulate the concrete crushing and cracking, respectively (see Figures 5.6 and 5.7). The average value of three compression cylinder tests of concrete was used with the axial tensile strength  $f_t$  taken as 10% of the compressive strength of  $f_{ck}$  31.28 MPa (Qureshi et al., 2010).



**Figure 5.4: True stress-strain curve of the beam, column and end-plate.**



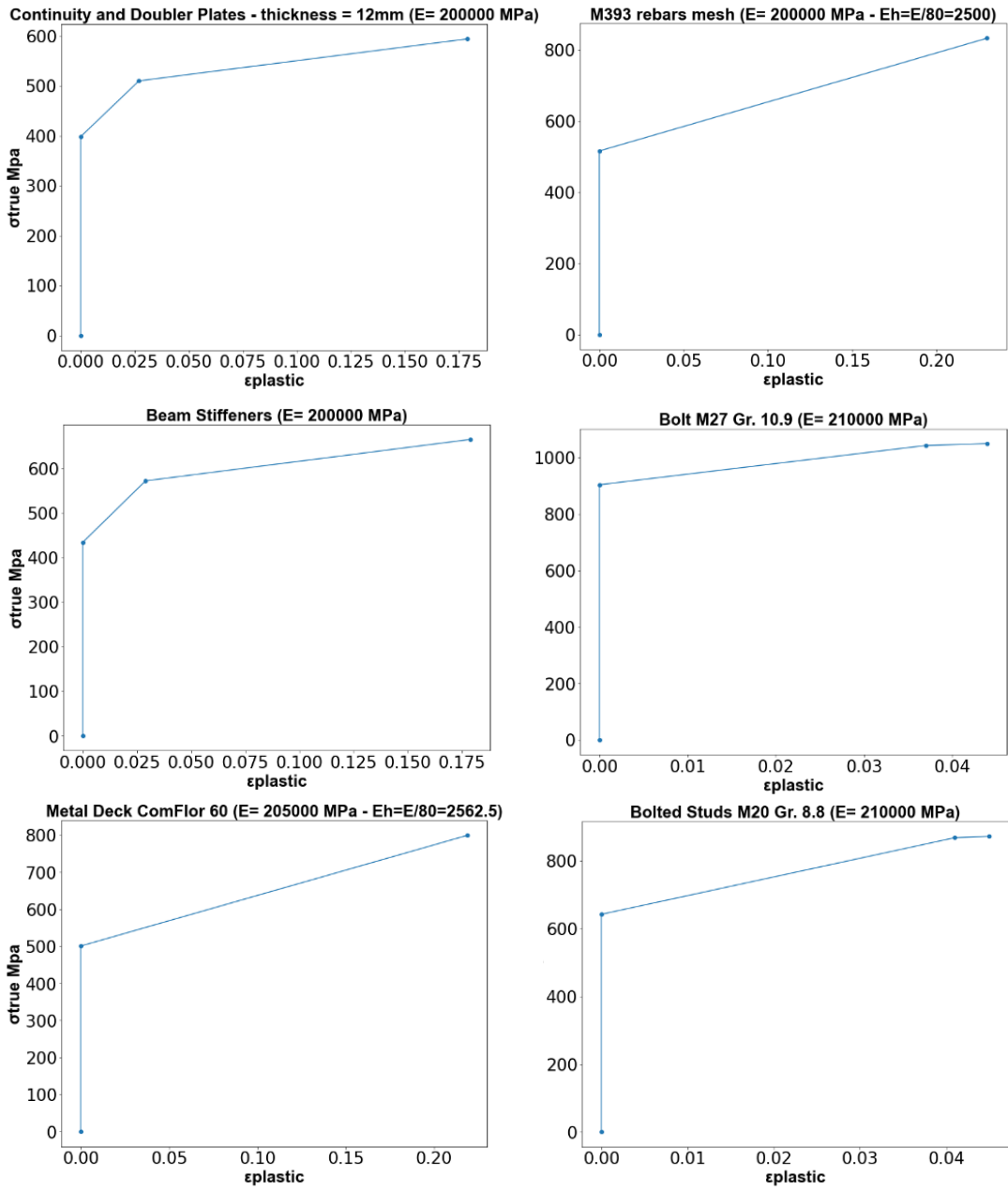
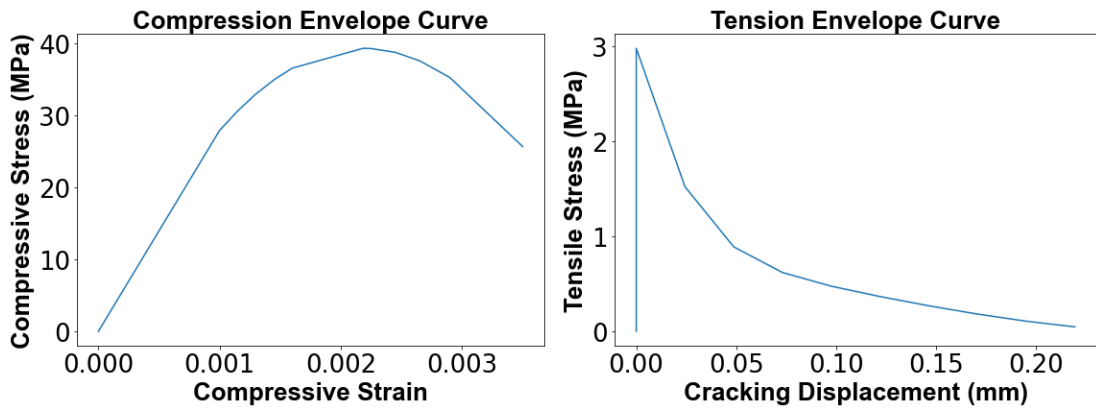
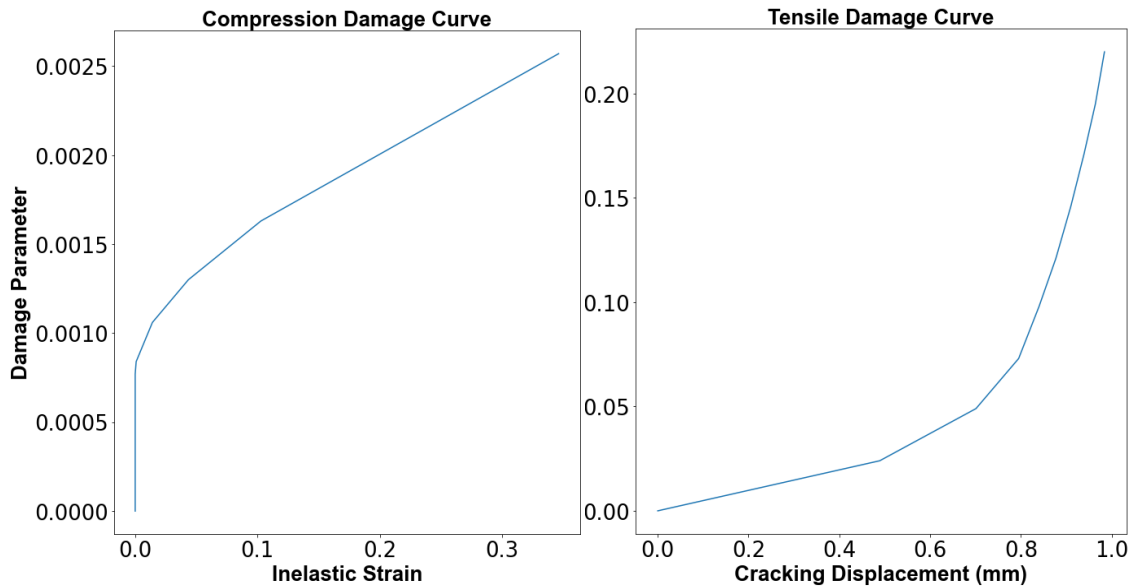


Figure 5.5: True stress-strain curve of the other steel elements.



**Figure 5.6: Uniaxial stress-strain curve of concrete under compression and tension.**



**Figure 5.7: Compression and tensile damage curves.**

### 5.2.3 FE verification

The FE assumptions outlined in previous sections were verified using the cyclic experimental results. Figure 5.8 presents a comparison of the moment-rotation relations at a column face derived from the experimental and FE results. The FE models exhibited behaviour similar to the experimental findings in terms of yielding, stiffness degradation, energy dissipation, and failure modes, as shown in Figures 5.8 - 5.10. The maximum deviation in sagging values between FE simulations and experimental tests ranges between 3% and 6%. Meanwhile, the maximum deviations of 4% were calculated for the hogging capacities. Overall, the FE models effectively reproduce the experimental findings and can be employed in the parametric investigation.

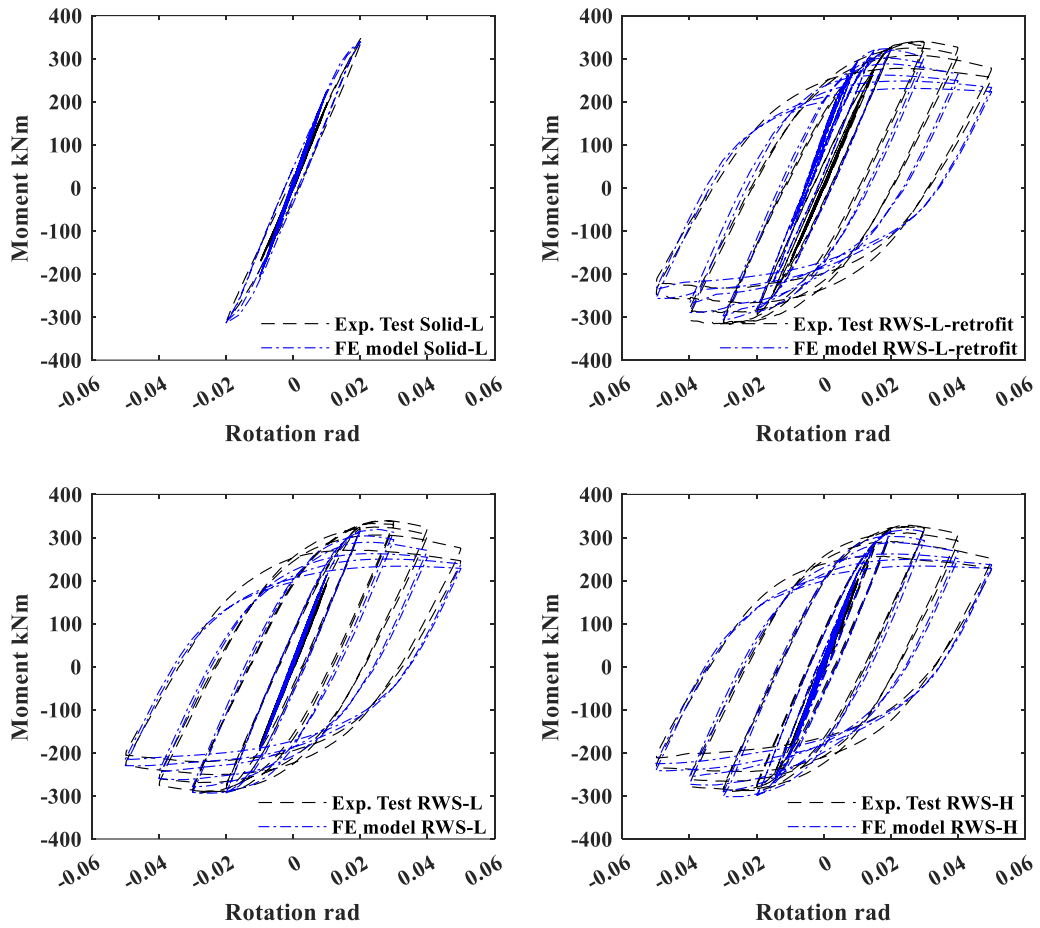


Figure 5.8: Benchmarking of the FEM hysteresis cycles.

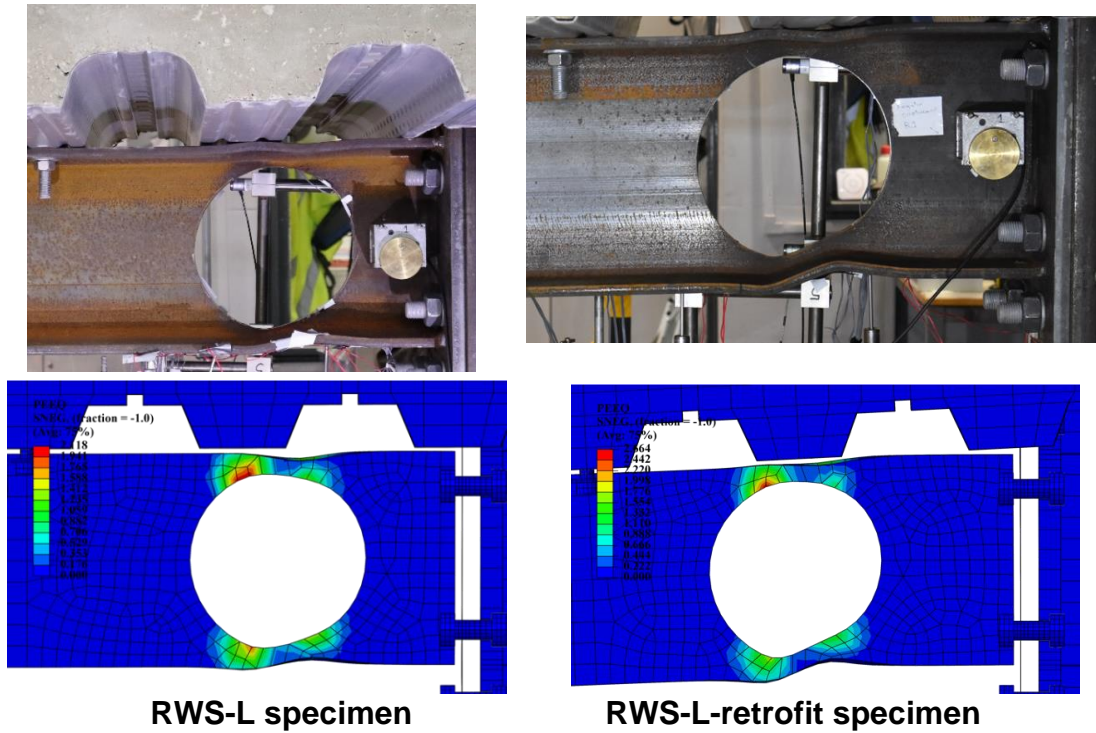


Figure 5.9: Comparison between FE models and tested specimens (shell thickness is not shown).

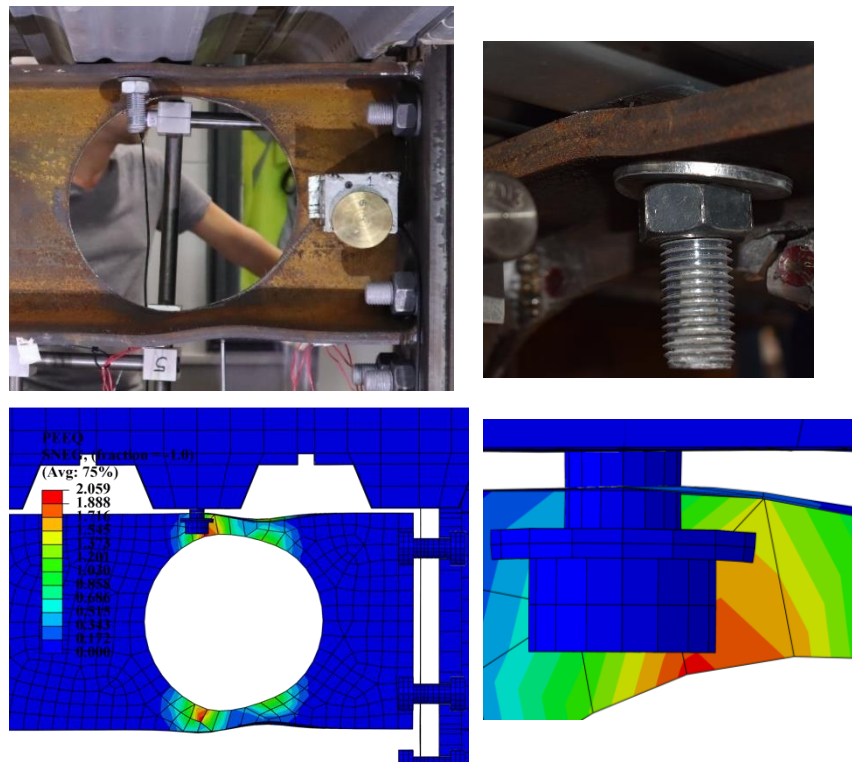


Figure 5.10: Failures of RWS-H.

## 5.3 Parametric investigation

### 5.3.1 Parameters

Following the FE modelling validations, 285 parametric FE models were developed for RWS connections with various configurations, as shown in Table 5.1. Moreover, three FE models of solid-webbed connections (without web opening) were developed for comparison purposes. Table 5.1 presents the three parameters selected to investigate the effect of the presence of composite action over the plastic zone (i.e., web opening) on the performance of a steel-concrete composite bolted extended end-plate RWS connection subjected to cyclic loading. The selection of these parameters facilitates the non-dimensionalisation of all RWS connection results. This allows for creating extensive databases that can be used to develop numerical models and design guidelines for RWS connections, following European Standards.

In this study, the end-distance ( $S_o$ ) complies with SCI guidance which specifies the minimum width of the end-post from the column face to the edge of the web opening. The FE models with a web opening diameter  $d_o$  of 50% of the beam's depth ( $h$ ) start with an end-distance  $S_o$  equal to 50% of  $h$  to comply with SCI P355 guidance. Similarly, for FE models with  $d_o = 0.55h$ , start with  $S_o$  is equal to  $0.55h$ .

This guide applies to all different diameters considered in the study. The presence and absence of bolted shear studs above the web opening were used to classify the specimens as having high (H) or low (L) composite action, respectively, according to Eurocode 8-1 clause 7.7.5 and ANSI/AISC 358-16 (CEN, 2005d; ANSI/AISC 358-16, 2016). The steel elements and concrete slab were kept the same as in the experimental tests in Chapter 4, regarding dimensions and material grades.

**Table 5.1: Parameters.**

* 1) Diameter $d_o$			** 2) End-distance $S_o$		3) The presence of composite action over the web opening (3 Categories)
%	mm	Number of models in each set of diameters	%	mm	
50%	155	15	50%	155	Yes - High composite action
55%	171	14	55%	171	No- Low composite action
60%	186	13	60%	186	without composite slab
65%	202	12	65%	202	<b>Note:</b> High composite action = there are bolted shear studs over the web opening. Low composite action = no bolted shear studs over the web opening. Without composite slab = steel RWS connection. $h$ = height of the beam; $80d_o$ = means the diameter of the web opening is equal to 80% of $h$ ; $80S_o$ = means the end-distance is equal to 80% of $h$ . * FE models with $d_o = 50\%$ starts with $S_o = 50\%$ , FE models with $d_o = 55\%$ starts with $S_o = 55\%$ and so on.  ** All models were compiled to SCI P355 guidance in terms of the width of the end-post. *** Maximum web opening diameter considering the depth of Tee section limitation in accordance with SCI P355 guidance. Therefore, $d_o = 75\%$ and $80\%$ are beyond SCI P355 guidance
70%	217	11	70%	217	
72%***	223	11	72%***	223	
75%	233	10	75%	233	
80%	248	9	80%	248	
<b>Total 95</b>			85%	264	
<b>Number of models in each set of diameter x 3 Categories (1-High, 2-Low and 3-Without composite slab)</b>  <b>Total parametric models = 3 x 95 = 285</b>			90%	279	
			95%	295	
			100%	310	
			105%	326	
			110%	341	
			115%	357	
			120%	372	

### 5.3.2 Connection performance characteristics

This section evaluates the RWS connection's essential characteristics based on the deduced performance parameters of interest, including its stiffness, bending strength and ductility.

#### 5.3.2.1 Deduction of performance parameters

Different methods exist in the literature for determining the yield point on the hysteresis moment-rotation curve; this research employs a specific approach detailed in Figure 5.11. The Ibarra–Medina–Krawinkler (IMK) model (Ibarra et al., 2005) was employed to consistently assess selected response (both strength and deformation) parameters influencing the cyclic response of RWS connections. For consistency with previous experimental and FE studies, the moment is defined as the moment at the column face, and the rotation represents the total rotation of the connections. First, the skeleton moment-rotation ( $M - \theta$ ) curves derived from the hysteretic curves of 285 FE models of bolted RWS connections were employed to identify the hysteresis characteristic points, as shown in Figure 5.11. The skeleton ( $M - \theta$ ) curves, taken at the column face, illustrate the hysteretic behaviour of beam web opening as one component of the extended end-plate RWS connection to be incorporated into the component method adopted in Eurocode 3 Part 1-8 (CEN, 2005b).

Figure 5.11 illustrates the stages of defining the following strength and deformation parameters of the  $M - \theta$  curves using the IMK model (Ibarra et al., 2005):

- The effective yield moment ( $M_{ye}$ ) and its corresponding rotation ( $\theta_y$ ).
- The maximum moment resistance ( $M_m$ ) and its corresponding rotation ( $\theta_m$ ).
- The ultimate moment ( $M_u$ ) and its corresponding rotation ( $\theta_u$ ).
- The elastic ( $K_e$ ), strain-hardening ( $K_s$ ) and post-capping ( $K_c$ ) stiffnesses.

The first parameters to be defined in a hysteretic curve to draw skeleton  $M-\theta$  curves are the initial stiffness ( $K_i$ ) of hysteretic curve and the maximum moment strength ( $M_m$ ). The initial stiffness ( $K_i$ ) of the hysteretic curve is calculated by dividing the first cycle's moment by its rotation ( $K_i = M_i/\theta_i$ ). Knowing  $K_i$  and  $M_{m,Rd}$ , the effective yield moment ( $M_{ye}$ ) is defined as the point of intersection where the tangent line drawn at the point of maximum moment strength ( $M_{m,Rd}$ ) intersects with the line representing the initial stiffness. Then, all corresponding rotations (i.e.,  $\theta_y$  and  $\theta_m$ ) can be defined accordingly. The elastic rotational stiffness ( $K_e$ ) can be defined by the yield moment by its corresponding rotation

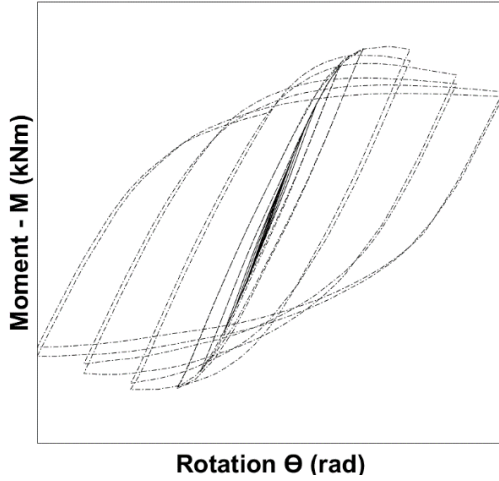
( $K_e = M_{ye}/\theta_y$ ). While the strain-hardening stiffness ( $K_s$ ) and post-capping stiffness ( $K_c$ ), are calculated by the following equations:

$$K_s = \frac{M_m - M_{ye}}{\theta_m - \theta_y} \text{ Eq. 6.1}$$

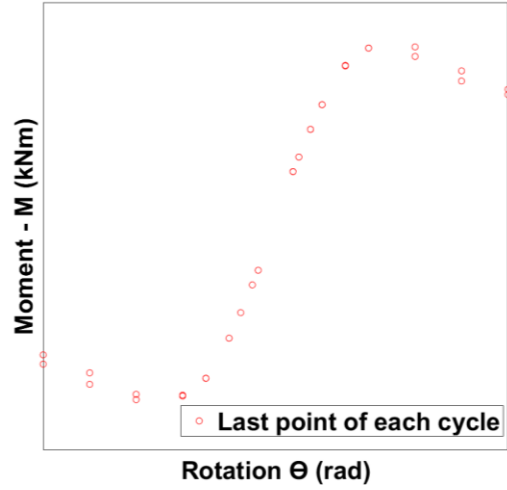
$$K_c = \frac{M_u - M_m}{\theta_u - \theta_m} \text{ Eq. 6.2}$$

In this research, the plastic moment resistance of the connection  $M_{c,Rd}$  is represented by the effective yield moment ( $M_{ye}$ ). The ultimate moment strength ( $M_u$ ) represents the moment of the last cycle in cases where the strength degradation occurs. If skeleton  $M - \theta$  curves do not experience strength degradation,  $M_u$  would be equal to the maximum moment strength ( $M_m$ ).

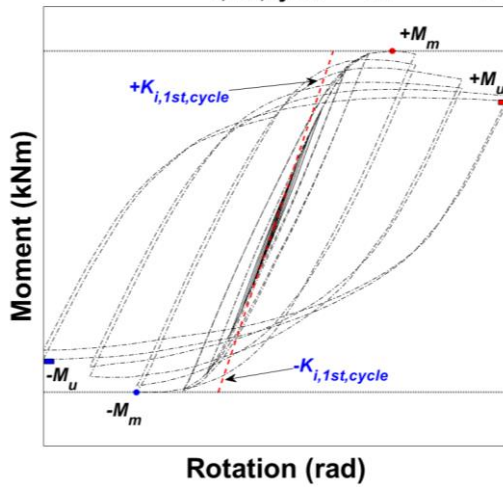
1 - Typical hysteretic M- $\Theta$  curve at column face



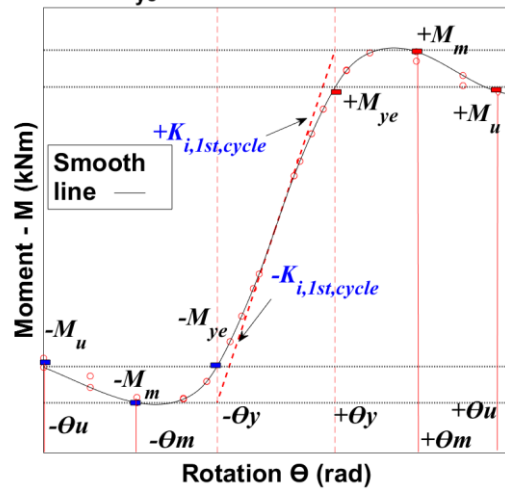
2 - Skeleton M- $\Theta$  curve at column face



3- Defining  $K_{i,1st,cycle}$ ,  $M_m$  and  $M_u$



4- Defining  $M_{ye}$  and all corresponding rotations



5- Defining Stiffnesses

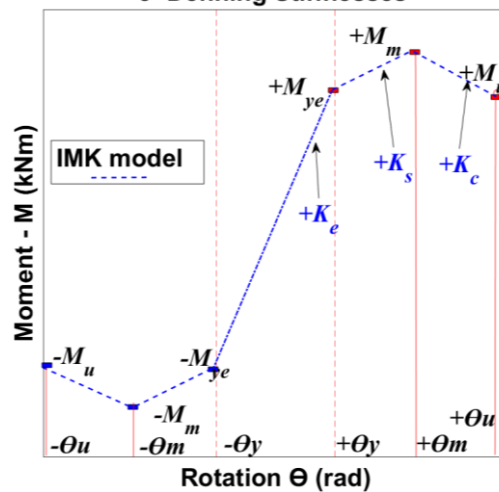


Figure 5.11: Defining the strength and deformation parameters of IMK model.



### 5.3.2.2 Stiffness and bending resistance

Eurocode 3 classifies connections based on their stiffness and strength (CEN, 2005b). In unbraced frames, a connection's stiffness is classified as semi-rigid if its initial stiffness ( $S_{j,ini,EC3}$ ) falls between  $0.5 E_b I_b / L_b$  and  $k_b E_b I_b / L_b$ , where  $k_b$  is equal to 25 for moment-resisting frames (MRFs),  $E_b$  represents the measured steel beam elastic modulus,  $I_b$  is the beam moment of inertia about the section's major axis, and  $L_b$  is the beam length between column centerlines. It is obvious that the Eurocode 3 component method tends to overpredict the elastic stiffness ( $K_e$ ) as shown in Figures 5.12 and 5.13. This observation aligns with the findings of Ding and Elkady (2023). The average difference between the initial stiffness in accordance with Eurocode 3 component method ( $S_{j,ini,EC3}$ ) and the initial stiffness of the first cycle ( $K_i$ ) were about 0.29 and 0.25 under sagging and hogging, respectively. While the average differences between  $S_{j,ini,EC3}$  and the elastic stiffness ( $K_e$ ) based on the IMK model, was roughly 0.23 in both directions.

For strength classification, the connection can be categorised as either full-strength or partial-strength based on the capacity design ratio between the connection and the connected steel beam. According to the European projects of EQUALJOINTS and EQUALJOINTS-Plus (EJs), the connection can be classified as equal-strength if the capacity design ratio equals 1 and the plastic deformations occur in both the beam and the connection (Landolfo, 2022; D'Aniello et al., 2023). The findings of EJs projects are adopted in the new generation of Eurocodes. In the current Eurocode 3-1-8 (CEN, 2005b), an equal-strength connection is categorised as a partial-strength connection. In this research, the connection was designed as equal-strength, based on the nominal plastic bending capacity ( $M_{pl,a,Rd}$ ), of the connected steel solid-webbed beam, without considering the composite action contribution. Thus, the incorporation of web opening alters the strength category of the connection from equal to full strength due to the reduced section.

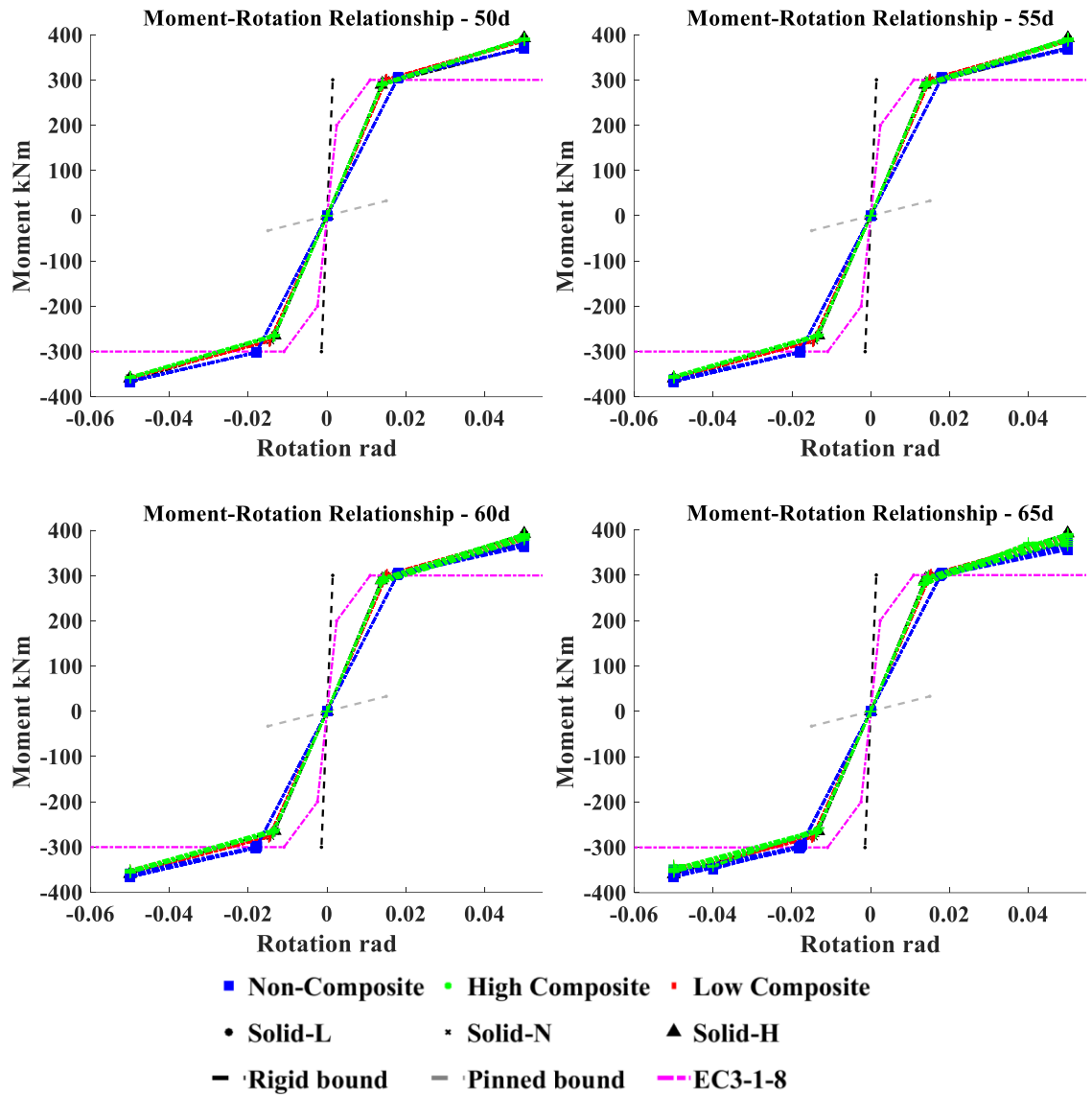
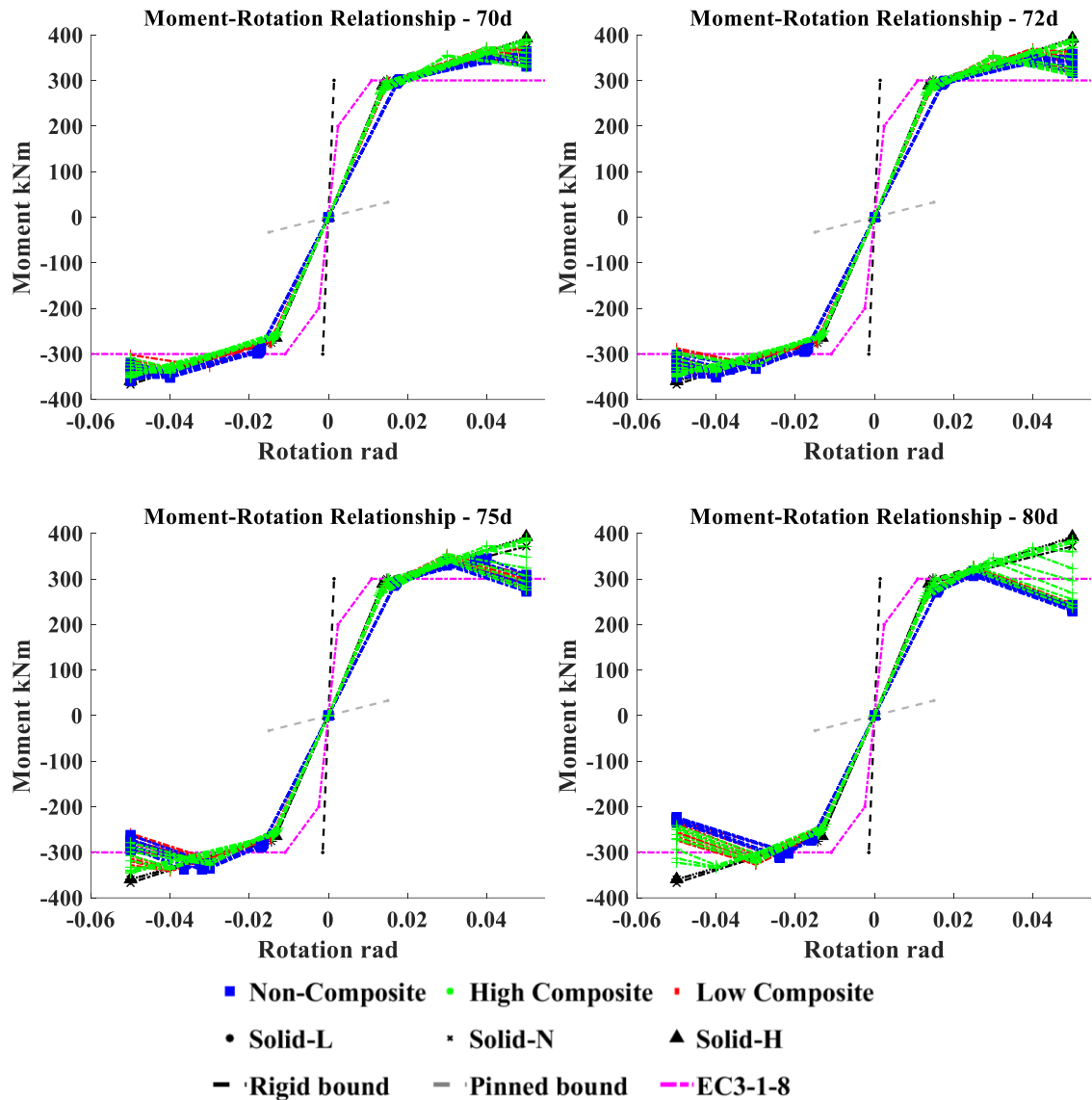


Figure 5.12: Skeleton curves of RWS connections with diameter = 0.5, 0.55, 0.6 and 0.65h.



**Figure 5.13: Skeleton curves of RWS connections with diameter = 0.7, 0.72, 0.75 and 0.8*h*.**

Based on the skeleton curves in Figures 5.12 and 5.13, the average difference between the sagging and hogging strengths was approximately 6%. This was due to the presence of a composite slab, leading to asymmetric behaviour. Another consideration is the fact that the composite slab typically enhances the bending strength of the steel beam. Consequently, the bending strength of the composite beam might surpass that of the column, forcing the plasticity to occur within the column, potentially resulting in local story collapse mechanisms (Elkady and Lignos, 2014). In addition, the growth in bending strength of the connected composite beam increases the shear force demand on the column panel zone (Elkady and Lignos, 2014). The increased demand could lead to significant inelastic shear deformations to the column panel zone of interior joints and may cause brittle failure of the welds between the bottom flange of the steel beam and

the column face (Zhang et al., 2004). In such scenarios, the bending strength of the steel beam could be significantly reduced. This mechanism is not ideal for energy dissipation. The seismic behaviour of the joint, including the panel zone's contribution is beyond the scope of this study, but worth to be investigated with RWS connections.

In this study, the effective yield (plastic) strength ratio ( $M_{ye}/M_{pl,a,Rd}$ ) is employed to evaluate the plastic strength of a connection. All connections (both with and without web opening) developed average strengths of 0.97 and 0.90  $M_{pl,a,Rd}$  for those with low composite action and 0.96 and 0.87  $M_{pl,a,Rd}$  for those with high composite action, under sagging and hogging, respectively. All bare steel connections could achieve the nominal plastic strength of the connected beam  $M_{pl,a,Rd}$ . The effective yield moments (strengths)  $M_{ye}$  of bare steel connections exceeded those with composite slabs. This was expected due to the earlier yielding of the connections with composite slabs, which arises from the increased strain demand on the bottom beam flange. However, the maximum applied moments ( $M_m = M_f$ ) of composite connections (both with low and high action) were higher than those for bare steel beams. This is attributed to the presence of composite slab, which increases the strength of the beam, but, as aforementioned, results in an early yielding of the section.

Beyond the effective yield (plastic) strength, all connections developed a maximum moment ( $M_m = M_f$ ) of 1.23  $M_{pl,a,Rd}$  in sagging and 1.16  $M_{pl,a,Rd}$  in hogging, on average. The minimum normalised moments ( $M_m/M_{pl,a,Rd}$ ) were 1.02 and 0.98 in sagging and hogging strengths, respectively; while the maxima for  $M_m/M_{pl,a,Rd}$  were 1.31 and 1.22 in sagging and hogging strengths, respectively. This variation was highly dependent on the location and size of the web opening, as shown in Figure 5.14. This observation is consistent with previous studies on RWS connections (Yang et al., 2009; Li et al., 2011; Tsavdaridis et al., 2014; Tsavdaridis and Papadopoulos, 2016; Naughton et al., 2017; Erfani and Akrami, 2017; Momenzadeh et al., 2017; Shaheen et al., 2018; Boushehri et al., 2019; Zhang et al., 2019; Nazaralizadeh et al., 2020; Tsavdaridis et al., 2021; Tabar et al., 2022).

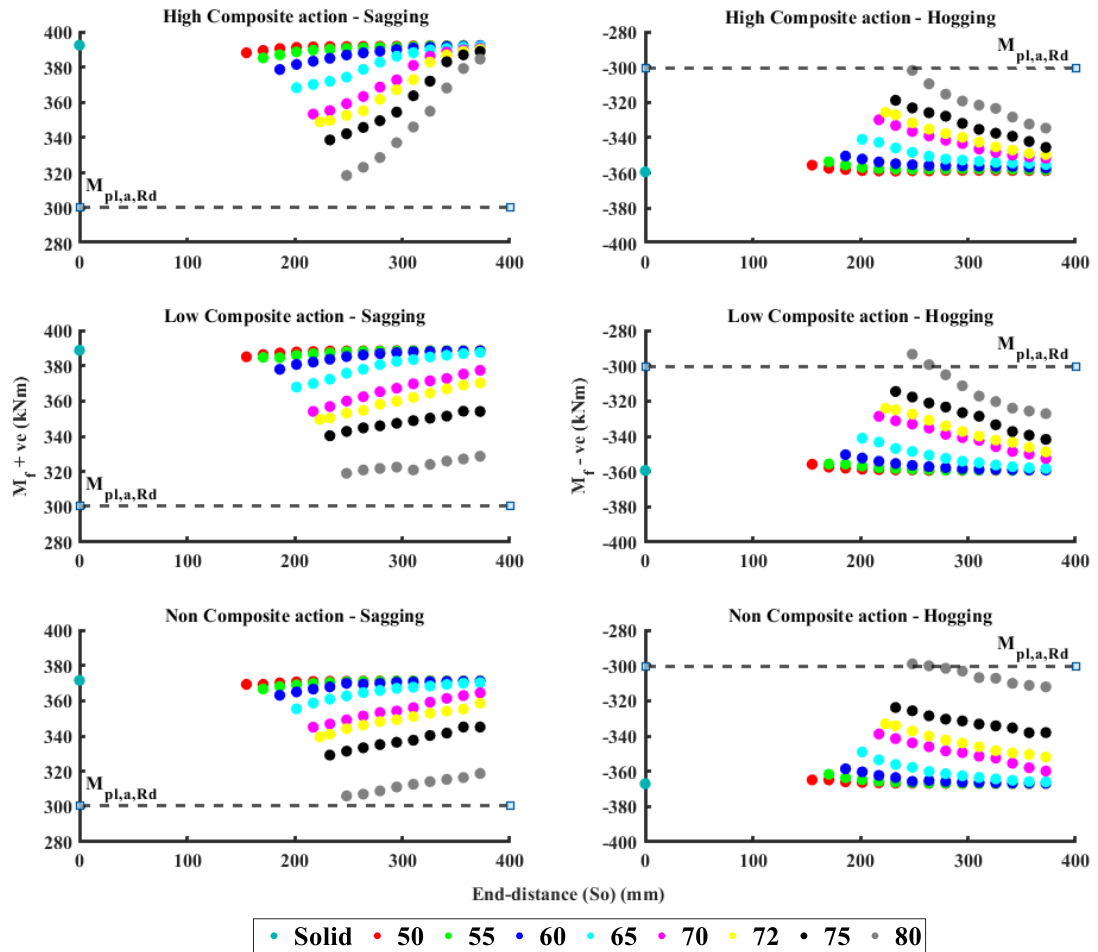


**Figure 5.14: The effect of end-distance ( $S_o$ ) on maximum applied moments at column face ( $M_f = M_m$ ).**

### 5.3.2.3 Hysteretic response

The design of all RWS connections was based on the nominal plastic bending capacity  $M_{pl,a,Rd}$ , of the connected steel solid-webbed beam of a partial-strength connection, without considering the composite action contribution according to Eurocode 3, Eurocode 4, and Eurocode 8 (CEN, 2005a; CEN, 2005b; CEN, 2005c; CEN, 2005d). As it was aforementioned, the strength category of the connection changed from partial to full strength due to the perforated section. In partial-strength connections, the deformations occur in the connection, leading to the pinching mechanism characterised by the reduction in stiffness during reloading after unloading, along with stiffness recovery when displacement is imposed in the opposite direction (FEMA P440a, 2009; D'Aniello et al., 2017). Such a mechanism is associated with the opening and closing of gaps between the end-plate and column flange, which could result in a large reduction in the energy dissipation capacity (FEMA P440a, 2009; D'Aniello et al., 2017).

The pinching mechanism occurred in all solid-webbed connections as well as in RWS connections with diameters equal to  $0.5h$  to  $0.65h$ . Figure 5.15 shows that the pinching mechanism in composite RWS connections with a diameter ( $d_o$ ) and end-distance ( $S_o$ ) equal to  $0.65h$ , was eliminated in the last two cycles of  $0.05\text{rad}$ . This elimination was due to the late full plastification of the perforated section (Vierendeel mechanism), which limited the inelastic deformation in the extended end plate. This can be seen in Figure 5.16, which shows the development of two plastic hinges on the low moment side (LMS). It is worth noting that the LMS is located to the right of the web opening in the cantilever setup. However, the pinching effect became more pronounced when end-distance ( $S_o$ ) increased in the composite RWS connections with a diameter ( $d_o$ ) equal to  $0.65h$ . While all RWS connections with diameters equal to  $0.5h$  to  $0.60h$ , exhibited pinching behaviour, with no signs of the Vierendeel mechanism developing. In this study, all solid-webbed connections and RWS connections with  $d_o$  ranges from  $0.5h$  to  $0.65h$ , did not experience strength degradation up to  $0.05\text{rad}$  where the analysis was stopped to optimise the computational time and storage.

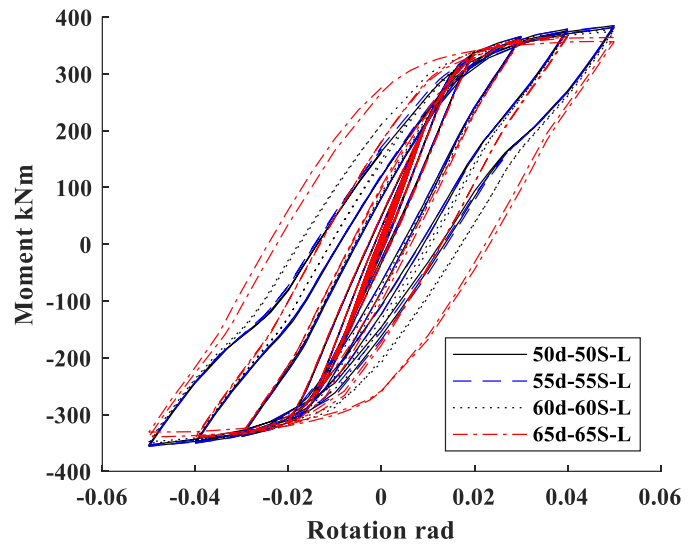
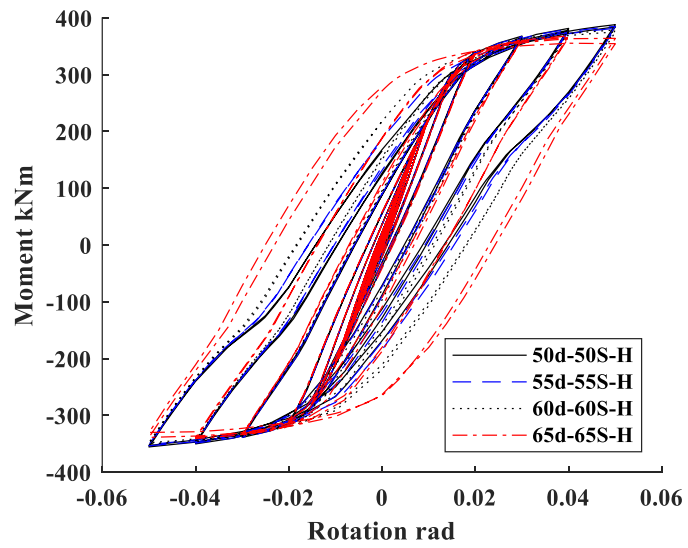


**Figure 5.15: Moment-rotation curves for small to medium web opening with low and high composite action.**

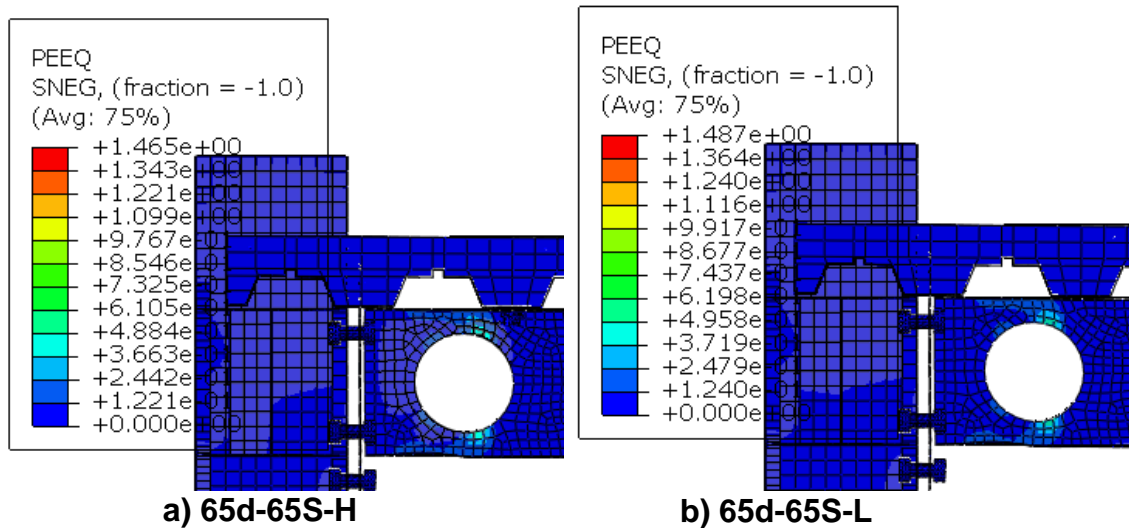


**Figure 5.16: The development of two plastic hinges in LMS.**

When the web opening size increases, it has been observed that the pinching effects become less noticeable. As a result, the connections experience a cyclic strength degradation, as depicted in Figure 5.17. FEMA 440 (FEMA P440a, 2009) differentiates two types of cyclic strength degradation that a structural system might exhibit, namely cyclic degradation and in-cycle degradation (FEMA P440a, 2009). The former occurs in the subsequent loading cycle due to increasing inelastic displacement, while the latter takes place within the same loading cycle because of repeated cyclic displacement. Generally, the cyclic strength degradation could lead to a stable dynamic response of a structural system (FEMA P440a, 2009). In contrast, in-cycle strength degradation might induce dynamic instability in the structural system (FEMA P440a, 2009). All RWS connections experienced cyclic strength degradation, with reductions in strength not exceeding 20% before reaching 0.04rad. Consequently, they satisfy the seismic requirements of ANSI/AISC 358-16, ANSI/AISC 341-16 and Eurocode 8 (CEN, 2005d; ANSI/AISC 358-16, 2016; ANSI/AISC 341-16, 2016).



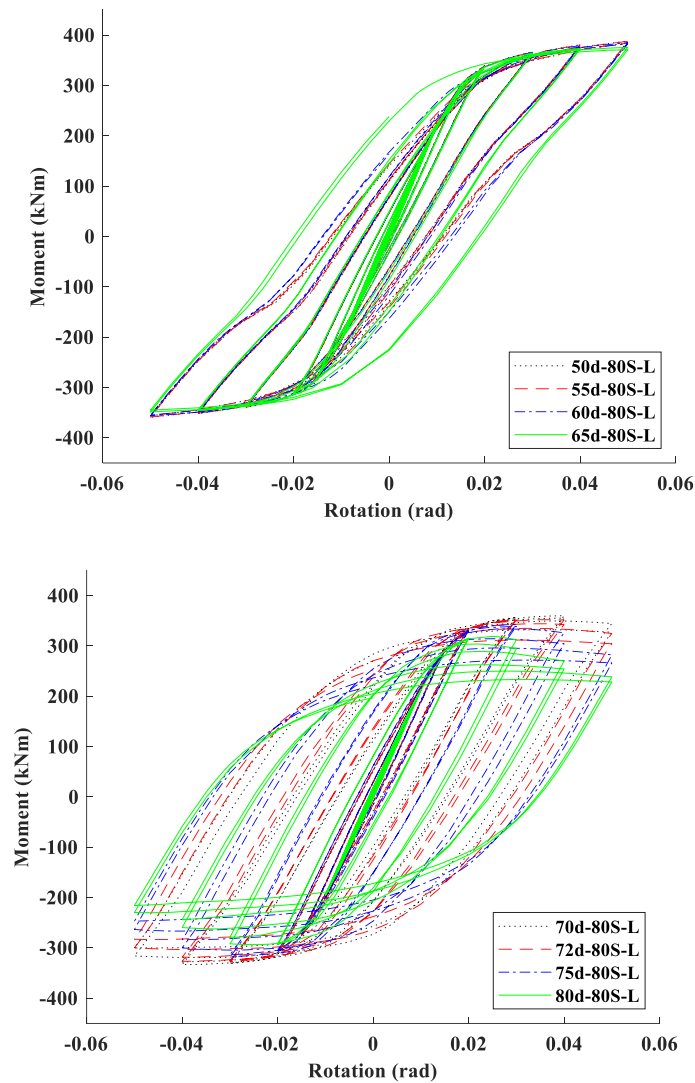


**Figure 5.17: The effect of web opening size on the pinching mechanism.**

Consistent with the findings presented in Chapter 3, it has been found that the efficiency of medium to large web opening sizes in triggering the Vierendeel mechanism in composite RWS connections. Herein, RWS connections with diameters equal to  $0.7h$  to  $0.8h$ , respectively, were able to make the reduced section the main resources of the plasticity. The RWS connections with diameters equal to  $0.7h$  and  $0.72h$  comply with SCI P355 guidance limitations in terms of the web opening size, while the web opening with diameters equal to  $0.75h$  and  $0.8h$  are outside that range. Both sets perform satisfactorily and provide an ideal structural behaviour in terms of stress distribution under cyclic loading without significantly compromising the connection capacity, provided that a suitable location for the web opening is chosen.

#### 5.3.2.4 Ductility and energy dissipation

Ductility and energy dissipation are key seismic response characteristics that need to be present in critical structural elements, aiming for reliable load transfer and redistribution within a structure under seismic loads. Both ductility and energy dissipation are interrelated for the seismic performance of MRFs. The former evaluates the ability of a material or structure to undergo large inelastic deformation without significant reduction in strength and is quantified as the ratio of the ultimate rotation to yield rotation ( $\theta_u/\theta_y$ ). Energy dissipation, on the other hand, assesses the structure's capability to release seismic energy. This is achieved through the development of plastic hinges at predefined locations, which aim to minimise the force transmitted to the structure, thereby preventing accumulated damage. This attribute can be calculated by examining the area enclosed under the outer loop of the hysteresis loops at ultimate rotation.

Figures 5.18 and 5.19 illustrate the effect of web opening size on both ductility and energy dissipation, respectively. RWS connections with high composite action exhibit the highest ductility ratios, as a result of early initiation of yielding due to the high strain demand on the beam's bottom flange. Also, this high strain demand led to a greater ductility under hogging moment in RWS connections with high composite action. The difference between RWS connections with the high and low composite action is approximately 4% and 5%, on average, under sagging and hogging moments, respectively. The outlier in the RWS connection is with a diameter equal to  $0.75h$ , due to an early termination of the analysis at  $0.04\text{rad}$  under a hogging moment. However, this should not distort the observation that as the web opening size increases, the ductility also increases. Conversely, ductility decreases as the web opening location moves away (i.e., as end-distance increases). Non-composite RWS connections exhibit lower ductility ratios compared to composite connections. This is likely due to their relatively high yield rotations, which aligns with the findings of Shaheen et al. (2018).

Regarding energy dissipation, RWS connections with low composite action exhibit the highest values when the diameter ranges from  $0.72h$  to  $0.8h$  among all connections. For diameters ranging from  $0.5h$  to  $0.7h$ , connections with high composite action dissipate more energy than their counterparts with low composite action. This observation is also consistent for connections with solid-webbed beams. For connections with non-composite slabs, the dissipated energy increases as the web opening size increases. As observed with the ductility predictions, the dissipated energy decreases as the location of the web opening moves further away, or in other words, as the end distance increases. Among all connections, the solid-webbed beam connection has the lowest energy dissipation values. Therefore, it can be concluded that incorporating web

openings effectively enhances energy dissipation through the plastification of the reduced section (i.e., the Vierendeel mechanism).

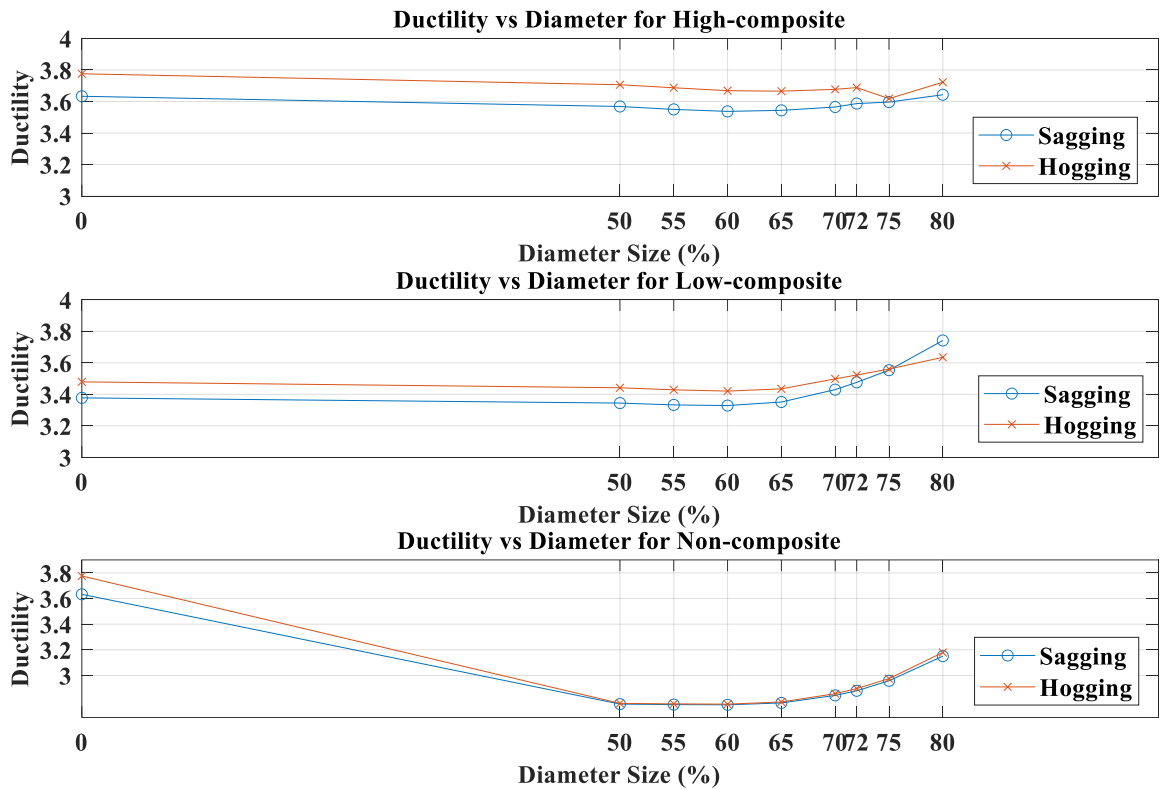
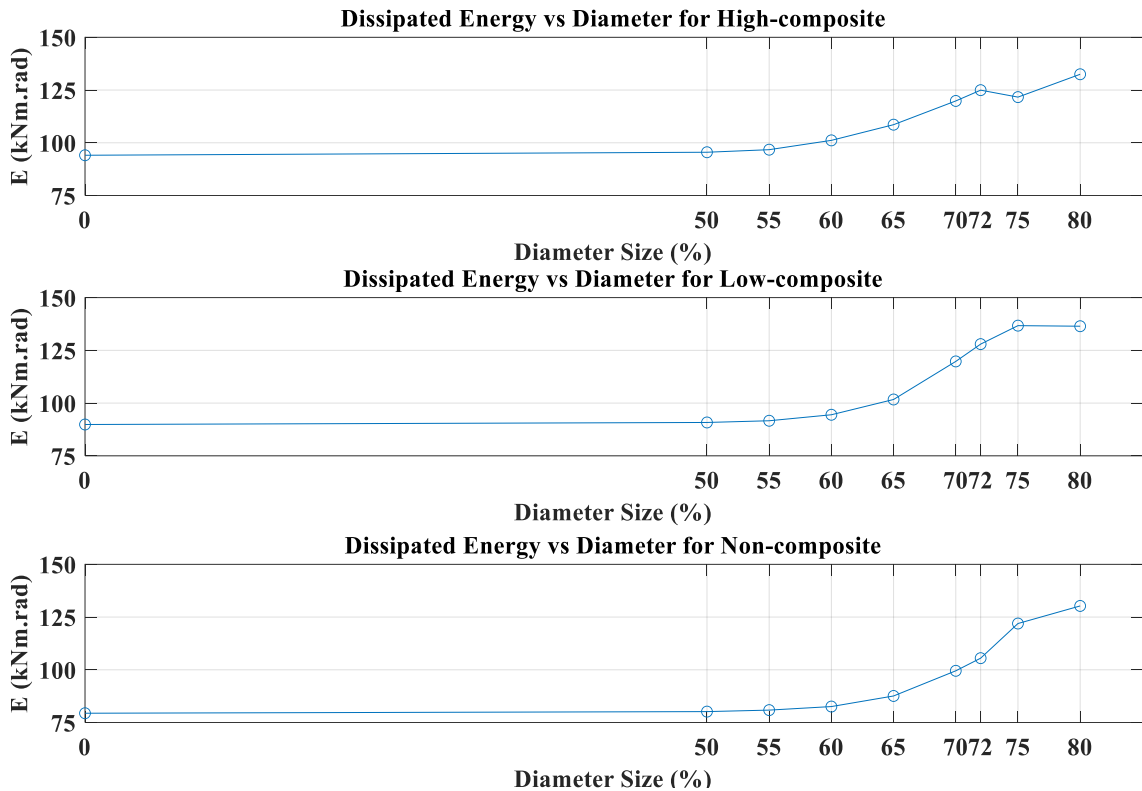


Figure 5.18: The trend of the ductility vs diameter (on average).



**Figure 5.19:**The trend of the dissipated energy vs diameter (on average).

### 5.3.2.5 Contribution of the composite slab

Figure 5.20 showcases the contribution of the composite slab to the overall strength of the connections under sagging. This is unlike when the connection is under hogging. Due to the presence of the composite slab, the cyclic response of connection is asymmetric, unlike bare steel counterparts, which behave symmetrically under reversed loading. In simpler terms, when the connection is under compression, the composite slab (top section of the composite beam) is active. In contrast, when the connection is under tension, only the steel section is active.

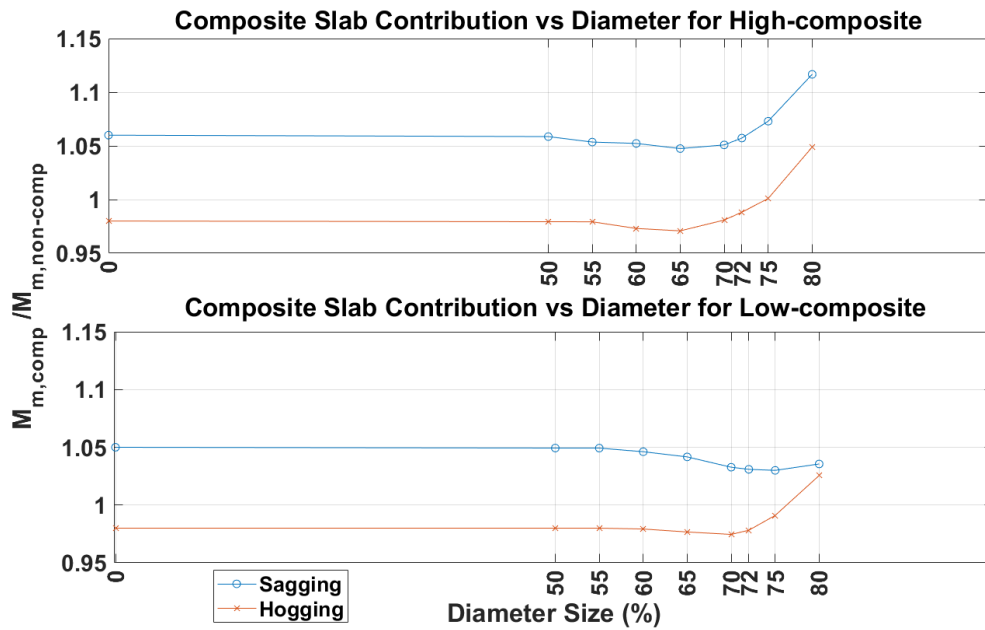


**Figure 5.20: Contribution of composite slab to maximum strength of the connections (on average).**

Despite this, the maximum strengths of the connections were slightly similar between the RWS connections with and without bolted studs over the web opening (protected zone), for most diameter sets (i.e.,  $0.5h$  to  $0.7h$ ). This similarity can be attributed to the elimination of contact between the concrete slabs and the extended end-plates and columns (i.e., 25mm gap) in all connections. This 25 mm gap restricts the force transfer from the concrete slab to the extended end plates and columns. Consequently, the additional row of bolted shear studs provided in the RWS connections with high composite action, does not affect the overall strength of the connection, although it did have an impact on ductility in which the presence of composite action leads to early yielding.

For RWS connections with diameters ranging from  $0.72h$  to  $0.8h$ , the contribution of the composite slab increases in both sagging and hogging directions. With RWS connections of diameter of  $0.8h$ , the composite slab contributes, on average, 5% to the overall strength. It is also observed that as the web opening location moves further away, the contribution of the composite slab increases. This observation aligns with the previous study of Shaheen et al. (2018) and with Chapter 3 on composite RWS connections. These findings suggest that, in general, when using bolted shear studs, the strength of the composite connection is more predictable than with the traditional welded shear studs, which could contribute up to a 60% contribution (Shaheen et al., 2018). Another key observation is that the level of damage (in the form of cracking and crushing) remained minimal, largely because of the oversized holes for bolted shear studs.

### 5.3.2.6 Applicability of SCI P355 guidance

The hysteresis behaviour of bolted extended end-plate RWS connections with demountable composite slabs can arise from complex deformations that span multiple connection components (e.g., web opening, end-plate, bolts, etc.). Given the range of components that may undergo deformation in elastic and plastic regions, predicting the hysteresis behaviour of such connections could be challenging. In the literature, there is no consensus on computing the moment capacity of RWS connections ( $M_{RWS,Rd}$ ).

In this study, the IMK model (Ibarra et al., 2005) is employed to determine the effective yield moment ( $M_{ye}$ ) representing the moment capacity of RWS connections. This approach is followed because the design guidance in Eurocode 3 (CEN, 2005a) and SCI P355 guidance rely on the nominal (or measured) yield strength ( $f_y$ ) to compute the expected capacity of a member. The expected plastic bending capacity of a steel beam is typically defined based on the nominal (or measured) yield strength ( $f_y$ ) multiplied by the plastic section modulus of the major axis ( $Z$ ) in accordance with Eurocode 3 (CEN, 2005a). Additionally, the bending of the beam at the opening ( $M_{o,a,Rd}$ ) as per SCI P355 guidance (excluding the composite slab contribution) is determined as the product of the following;

- i. area of the two Tee sections ( $A_{T,e,o}$ );
- ii. the yield strength ( $f_y$ ); and,
- iii. the effective depth between the centroid of the Tees ( $h_{eff}$ ).

Although the effective yield moment ( $M_{ye}$ ) typically is slightly higher than the connection's expected moment capacity ( $M_{j,Rd}$ ) (Lignos and Krawinkler, 2011), the  $M_{ye}$  of the skeleton  $M - \theta$  curves is a reasonable estimation of the moment capacities of RWS connections. The difference between the maximum moment  $M_m$  and the effective yield moment ( $M_{ye}$ ) can be considered as the additional strength possessed by the connection due to strain-hardening and second-order effects that develop resulting from deformations across multiple connection components.

The effective yield moments ( $M_{ye}$ ) obtained from the skeleton  $M - \theta$  curves are compared with the bending of the beam at opening ( $M_{o,a,Rd}$ ) in accordance with SCI P355 guidance. The outcomes indicate that the  $M_{ye}/M_{o,a,Rd}$  have an average ( $\mu$ ), standard deviation ( $\sigma$ ), minimum (min), and maximum (max) of 1.06, 0.03, 0.95 and 1.13 under sagging, respectively. The ratio of  $M_{ye}/M_{o,a,Rd}$  under hogging,  $\mu$ ,  $\sigma$ , min and max of -1, 0.05, -0.89 and -1.1, respectively. A general tendency is detected that the SCI P355 guidance could predict the moment strength of bolted extended end-plate RWS connections with demountable

composite slab under cyclic loads. The findings show an acceptable strain-hardening ratio  $M_m/M_{ye}$  of 1.26, on average. Table 5.2 displays the average ( $\mu$ ), standard deviation ( $\sigma$ ), minimum (min), and maximum (max) for different sets of diameters.

**Table 5.2: Statistics for different sets of diameters based on the ratio of  $M_{ye}/M_{o,a,Rd}$ .**

$d_o$	Composite (H/L) / Non-composite	average $\mu$		max		min		$\sigma$	
		+ve	-ve	+ve	-ve	+ve	-ve	+ve	-ve
50	High	1.02	-0.93	1.02	1.00	-0.91	-0.93	0.01	0.01
	Low	1.05	-0.96	1.05	1.04	-0.95	-0.97	0.00	0.00
	Non-comp	1.06	-1.05	1.07	1.06	-1.05	-1.06	0.00	0.00
55	High	1.03	-0.94	1.04	1.01	-0.92	-0.95	0.01	0.01
	Low	1.06	-0.97	1.07	1.05	-0.96	-0.98	0.01	0.01
	Non-comp	1.07	-1.06	1.08	1.07	-1.06	-1.07	0.00	0.00
60	High	1.04	-0.95	1.06	1.01	-0.93	-0.96	0.02	0.01
	Low	1.07	-0.98	1.08	1.05	-0.96	-0.99	0.01	0.01
	Non-comp	1.09	-1.07	1.09	1.07	-1.06	-1.08	0.01	0.01
65	High	1.05	-0.96	1.07	1.00	-0.93	-0.97	0.03	0.02
	Low	1.07	-0.99	1.09	1.04	-0.96	-1.00	0.02	0.02
	Non-comp	1.09	-1.08	1.10	1.08	-1.06	-1.09	0.01	0.01
70	High	1.05	-0.96	1.09	0.99	-0.92	-0.98	0.04	0.02
	Low	1.06	-0.98	1.09	1.03	-0.95	-1.01	0.02	0.02
	Non-comp	1.09	-1.08	1.11	1.07	-1.06	-1.10	0.01	0.01
72	High	1.05	-0.96	1.10	0.98	-0.92	-0.98	0.05	0.02
	Low	1.05	-0.98	1.08	1.02	-0.95	-1.01	0.02	0.02
	Non-comp	1.09	-1.07	1.10	1.07	-1.05	-1.09	0.01	0.01
75	High	1.05	-0.96	1.12	0.97	-0.92	-0.99	0.05	0.02
	Low	1.04	-0.97	1.06	1.01	-0.93	-1.00	0.02	0.02
	Non-comp	1.07	-1.06	1.09	1.06	-1.04	-1.07	0.01	0.01
80	High	1.04	-0.95	1.13	0.95	-0.90	-0.98	0.07	0.03
	Low	1.00	-0.95	1.02	0.97	-0.89	-0.99	0.01	0.03
	Non-comp	1.04	-1.02	1.05	1.02	-1.00	-1.03	0.01	0.01

Note:  $d_o$  = diameter,  $\mu$  = average and  $\sigma$  = standard deviation.

Figure 5.21 shows the average change in the Vierendeel ratio  $M_v/M_{v,Rd}$  (excluding the composite slab contribution) as diameter changes. It is observed that as the web opening size increases, the Vierendeel ratio also increases. Furthermore, the contribution of the composite slab to Vierendeel capacity grows as the web opening size increases. However, the end-distance ( $S_o$ ) has only a trivial effect on the Vierendeel capacity. It can be concluded that SCI P355 guidance overestimates the Vierendeel bending capacity of the RWS connections. Further data incorporating varied geometric and material parameters is essential to confidently assess the Vierendeel bending capacity of the RWS connections.

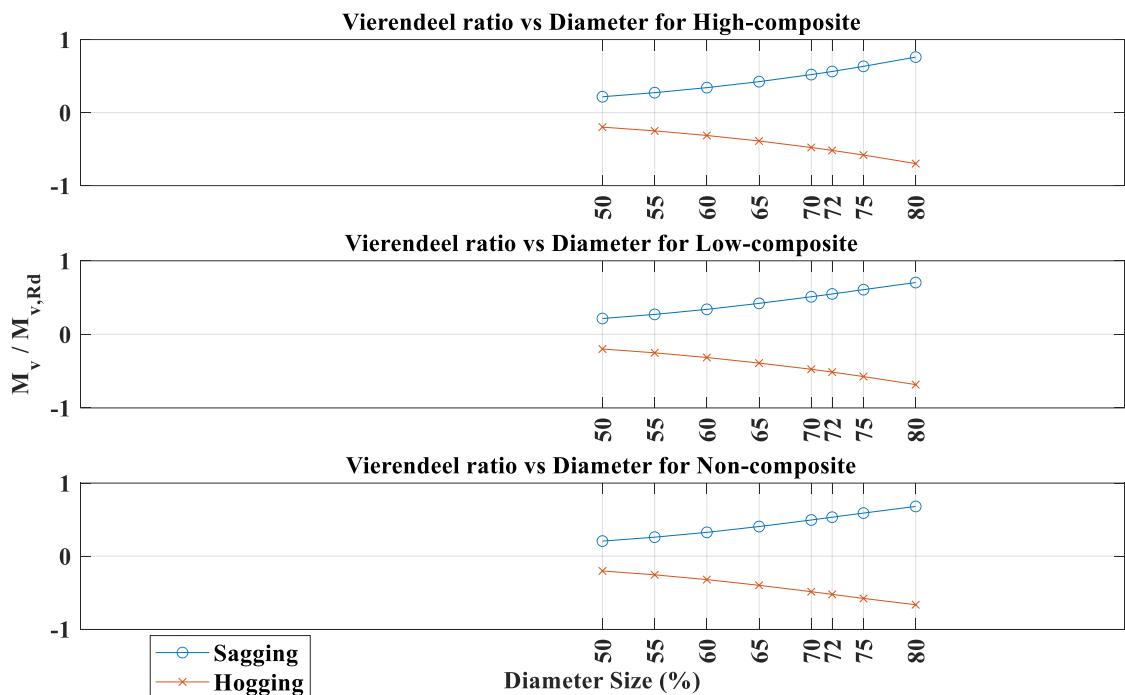


**Figure 5.21: The change in Vierendeel ratio vs the change in diameter (on average).**

### 5.3.2.7 Capacity design ratio

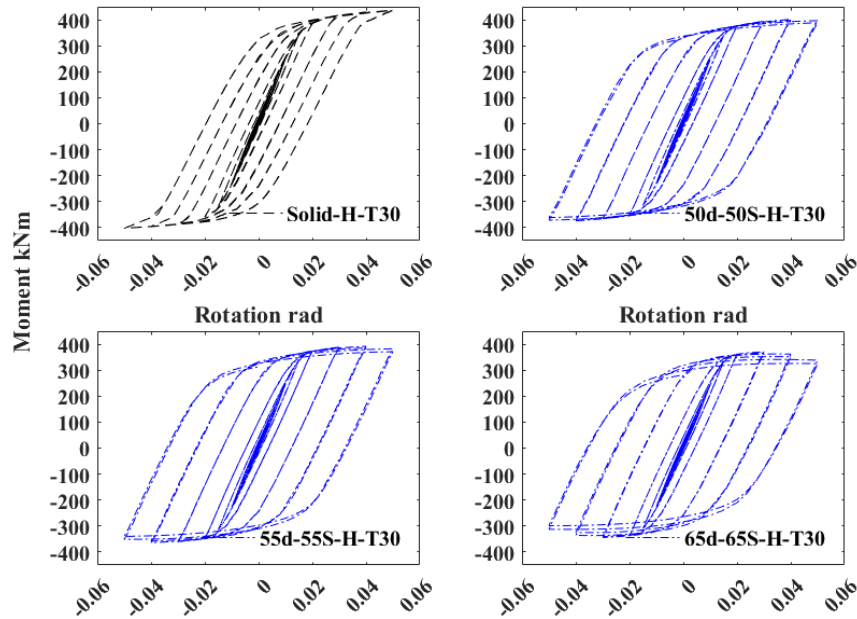
All RWS connections were designed based on the connected steel solid-webbed beam section strength  $M_{pl,a,Rd}$ , of a partial/equal strength connection, without considering the composite action contribution according to Eurocode 3, Eurocode 4, and Eurocode 8. Aiming that the incorporation of web opening alters the strength category of the connection from partial to full strength due to the reduction in the strength of the connected steel beam section. However, there is no consensus in the literature on the extent of reductions in strength which arise due to the size and location of the web opening.



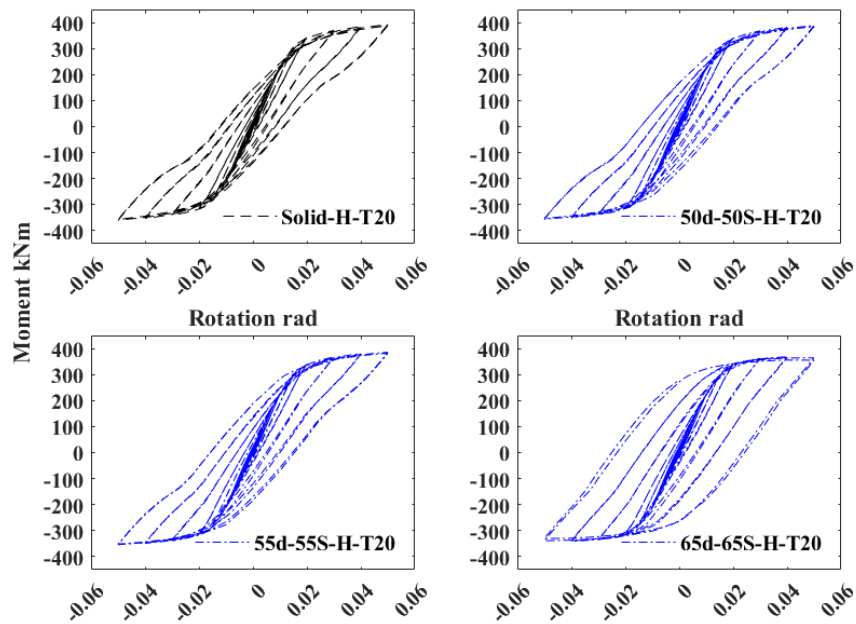
Knowing the amount of reduction in the moment capacity of the connected beam will change the capacity design ratio of the column/connection to the connected “**steel-concrete composite**” beam. This is significant in the retrofit of the existing buildings to optimise the resources in choosing the better size and location of the web opening to achieve the required capacity design ratio. Many studies have demonstrated the ability of a large web opening in the high shear zone to develop a ductile (Vierendeel) mechanism (Yang et al., 2009; Li et al., 2011; Tsavdaridis et al., 2014; Tsavdaridis and Papadopoulos, 2016; Naughton et al., 2017; Erfani and Akrami, 2017; Momenzadeh et al., 2017; Shaheen et al., 2018; Boushehri et al., 2019; Zhang et al., 2019; Nazaralizadeh et al., 2020; Tsavdaridis et al., 2021; Tabar et al., 2022). However, this is not always the case, as Shaheen et al. (2018) concluded that small to medium web opening sizes should be considered owing to the negative impact of large web openings on the cyclic behaviour of composite RWS connections. The findings of the experimental and FE studies in Chapters 3 and 4 highlighted the importance of the capacity design ratio in the design of RWS connections. Thus, understanding the capacity design ratio as well as the composite action effects on the seismic performance of the RWS connections is critical for both new and existing buildings.

Figure 5.22 presents a comparison between the full-strength connection and the equal/partial-strength connection. Both connections are identical in terms of the presence of composite action over the protected zone, as well as the size and material of steel and concrete sections. The only difference lies in the thickness of the end plates; the full-strength connection has a thickness of 30mm, while the equal/partial-strength connection has a thickness of 20mm. This resulted in a 5% increase in the capacity of the connection. The comparison has been conducted using small-to-medium diameters of web openings ( $0.5h$ ,  $0.55h$ , and  $0.65h$ ). The pinching phenomenon occurred in both types of solid-webbed connections. In the partial/equal strength connection, the extended end-plate is the main source of plastic deformation, hence the pinching effect is more pronounced than in the full-strength connection. As the diameter increases, the pinching effects diminish, especially in the full-strength connection. This is consistent with the findings in Chapter 3 that proved the efficiency of introducing the web opening to alter the strength category and make the reduced section in the beam the main element to dissipate energy by developing plasticity. The results confirm the findings of Shaheen et al. (2018) regarding the small-to-medium web opening sizes, as the high capacity design ratio was provided. It can be concluded that when a high-capacity design ratio is provided, low to medium web opening sizes should be used and vice versa. However, the capacity design ratio should be further studied to better comprehend it. It is worth noting that large diameters have not been

used in this comparison as their efficiency in inducing yielding in the beam has been established, provided that the proper location is chosen.



a) Thickness of end-plate = 30 mm  $\frac{M_{j,Rd}}{M_{pl,a,Rd}} = 1.06$  (full-strength connection).



b) Thickness of end-plate = 20 mm  $\frac{M_{j,Rd}}{M_{pl,a,Rd}} = 1$

Figure 5.22: Comparison between two different connections with high composite action in terms of capacity ratio.

## 5.4 Summary

The hysteretic response characteristics of demountable steel-concrete composite RWS connections have been quantified and assessed in this chapter. This assessment is based on a comprehensive parametric high-fidelity FEA database that comprises 285 models. The parametric results were subsequently employed to gain a better understanding of the local cyclic behaviour of composite RWS connections. It is important to note that the findings of this study are confined to the specimens and design assumptions used in this research. Response parameters derived from skeleton moment-rotation  $M-\theta$  relationships, including stiffness, strength, and ductility, were evaluated. Additionally, the contribution of the composite slab to the overall strength of the RWS connection was investigated by comparing the composite RWS connections to their RWS steel counterparts. Both the bending moment  $M_{o,a,Rd}$  and Vierendeel bending  $M_{v,Rd}$  capacities, in accordance with SCI P355 guidance, were also assessed. From available trend plots and hysteretic results, the following major conclusions could be drawn from this study:

- As the web opening size increases, the pinching effects diminish.
- RWS connections with diameters equal to  $0.7h$  to  $0.8h$ , efficiently triggered the Vierendeel mechanism under cyclic loads.
- Ductility increases with the increase of the size of the web opening but decreases as the end distance increases.
- RWS connections effectively enhance energy dissipation through the plastification of the perforated section.
- For composite RWS with diameters set equal to  $0.7h$  to  $0.8h$ , ductility and energy dissipation increase up to 13% and 57%, respectively, with a reduction in capacity up to 19%, compared to a solid-webbed connection.
- The decision to incorporate a web opening should consider the capacity design ratio between the column, connection, and beam.
- In this study, an equal capacity design ratio between the connection, and beam, was used, and

- For RWS connections with the **presence** of composite action, the ideal  $d_o/S_o$  ratio is 1.
- For RWS connections with the **absence** of composite action, the ideal  $d_o/S_o$  ratio between 0.8 and 1 is recommended, provided that the end-post distance adheres to the requirements specified in SCI P355 guidance.
- The presence of bolted shear studs over the protected zone influences ductility, potentially leading to early yielding of the perforated section.
- The strength of composite RWS connections with bolted shear studs is more predictable than that with traditional welded shear studs. On average, a demountable composite slab contributed about 5% to maximum strength.
- The SCI P355 guidance could be employed to estimate the bending moment at the opening of RWS connections with demountable composite slabs under cyclic loads.

## **Chapter 6**

### **Capacity Design Assessment**

#### **6.1 Introduction**

The main focus of this chapter is to assess how the capacity design ratio affects the response of both bare-steel and steel-concrete composite reduced web section (RWS) connections in terms of ductility, energy dissipation, and equivalent viscous damping. Three main steps were pursued as follows:

##### **i. Utilisation of validated Finite Element (FE) models**

The chapter begins by leveraging two FE models validated in Chapter 3. A new parametric study was conducted using New Zealand steel section profiles, the same as those used in the Chaudhari et al. (2019) tests. This was a significant shift from the previous parametric study's approach in Chapter 3, where the European section profiles were used. The rationale for reverting to New Zealand sections in Chapter 6 was to enrich and diversify the existing database, thereby broadening the range of steel sections analysed and facilitating a more comprehensive analysis of RWS connection behaviour.

##### **ii. Analysis of parametric study results from Chapter 5**

The chapter then delves into an in-depth analysis of the results obtained from the parametric study conducted in Chapter 5. The first two steps (i and ii) were analysed together which served as a reliable starting point for assessing the response of single-sided and double-sided RWS connections.

##### **iii. Compilation and extrapolation of literature data**

Lastly, the chapter includes a comprehensive compilation and extrapolation of both experimental and numerical non-dimensionalised results from existing literature with results derived from Chapter 3 (European sections). This effort was aimed at further investigating the characteristics of RWS connections. By integrating and extrapolating this data, the chapter contributes to a more robust and expansive understanding of RWS connections, supporting the development of improved design practices and standards in seismic engineering.

## 6.2 Deduced response parameters of the collected RWS database

The response parameters of the parametric numerical investigations (Section 6.3) and the collected RWS database (Section 6.4) were deduced using one or both of the following two methods. The first method manually extracted numerical values from moment-rotation ( $M - \theta$ ) curves based on the Ibarra–Medina–Krawinkler (IMK) model, as mentioned in Chapter 5. For the second method, in cases where full ( $M - \theta$ ) curves are absent in the literature (i.e., the assembled RWS connections database), the data was extracted from tabulated results found in research papers within the literature. Both test and numerical results were normalised concerning the nominal plastic moment capacity of the steel solid webbed-beam sections.

For a fair comparison, the energy dissipation and equivalent viscous damping for both sagging and hogging moments were calculated. These calculations utilised key response parameters (both normalised moments and rotations) as described in Chapter 5 and depicted in Figure 6.1. Both tri-linear and bi-linear skeleton ( $M - \theta$ ) curves based on the IMK model (Ibarra et al., 2005) were employed. The tri-linear skeleton ( $M - \theta$ ) curve is detailed in Chapter 5. The bi-linear skeleton ( $M - \theta$ ) curve was used for two specific cases. The first case applied when the connection did not undergo strength degradation, thus equating  $M_u$  with  $M_m$  and  $\theta_u$  with  $\theta_m$ . The second case was used when the corresponding rotation and/or moment data was unavailable in the tabulated results from literature. For instance, if  $M_u$  and  $\theta_m$  were not provided while  $M_m$  and  $\theta_u$  were available, then a bi-linear skeleton ( $M - \theta$ ) curve was used. It is worth mentioning that this research utilises a specific method (shown in Figure 5.11 in Chapter 5) to define the yield point on the moment-rotation hysteresis curve.

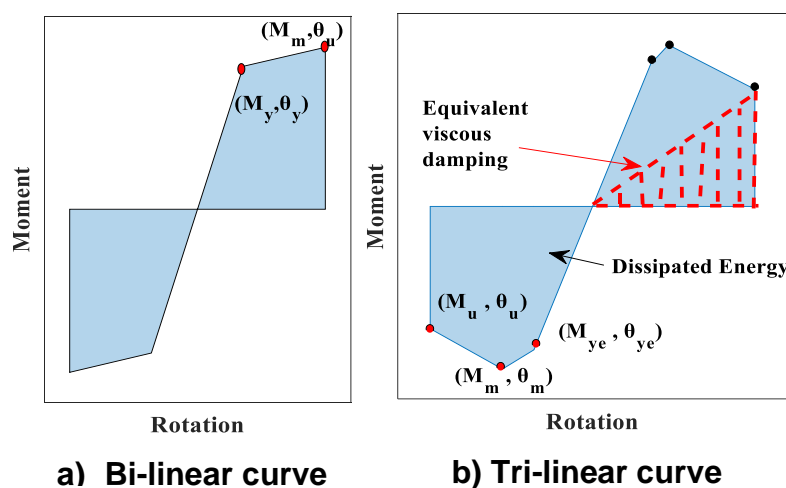


**Figure 6.1: Skeleton moment-rotation curves used for the collected RWS database.**

## 6.3 Parametric numerical investigations

### 6.3.1 Synopsis

In Europe, adopting partial-strength connections is permissible, provided that their ductility and rotational capacity are experimentally verified according to Eurocode 8 (CEN, 2005d). Such connections are cost-effective, with extended end-plate joints being about 30% cheaper than full-strength, thereby reducing post-earthquake repair costs (Tartaglia et al., 2019). Nonetheless, full-strength connections are often preferred as they obviate the need for the experimental verification requirements of Eurocode 8 (CEN, 2005d). The findings of Chapters 3, 4 and 5 have demonstrated the ability of RWS connections to reclassify a connection from partial- to full-strength while still leveraging the full benefit of the ductile (Vierendeel) mechanism. This was due to the reduction of the beam web section, resulting in a reduction of the beam's capacities, making the web opening behave as a fuse. Henceforth, inelastic action is precluded in the connection.

Following the numerical validations (see Chapters 3 and 5), a further parametric investigation was conducted for selected parameters (see Figure 6.2 and Tables 6.1 and 6.2) to ensure a well-informed assessment of ductility, energy dissipation and equivalent viscous damping coefficient of RWS connections. A total of 504 RWS (single- and double-sided) connections and 6 solid webbed-beam connections counterparts were assessed, and both bare steel and composite connections were considered. The composite connections are divided into low and high slab-beam interaction groups (i.e., absence and presence of composite action above the protected zone). Welded and bolted shear studs were used in double-sided and single-sided connections, respectively.

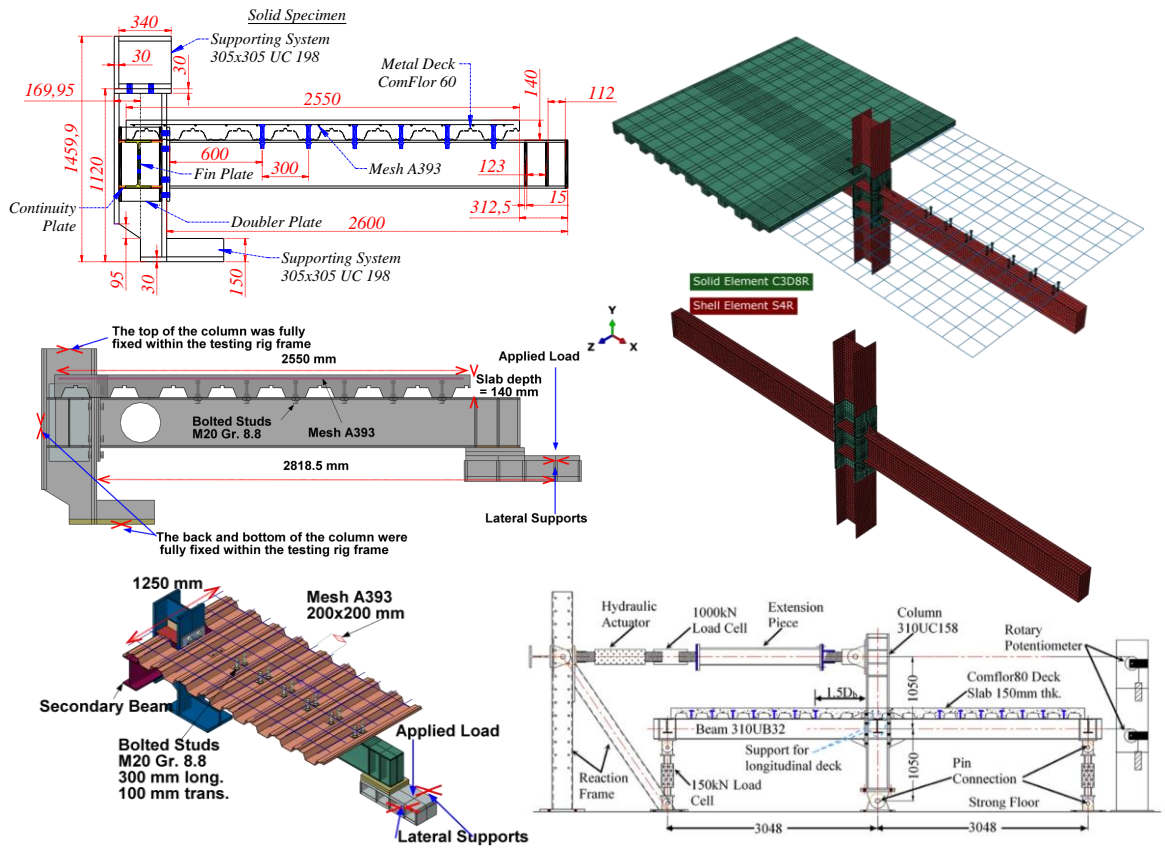


Figure 6.2: Test set-ups and FE model for tests of Chapter 4 on the left and tests of (Chaudhari et al., 2019) on the right.

Table 6.1: Summary of validated tested specimens.

Specimen	RWS	Composite interaction*	Studs	Connection arrangement
Solid connection**	No			
RWS-L-retrofit**	$d_o = 0.8h$ $S_o = 1h$	No	Bolted	single-sided $\frac{M_{c,Rd}}{M_{pl,a,Rd}} = 1$
RWS-L**	$d_o = 0.8h$	Yes		
RWS-H**	$S_o = 0.8h$			
FI-SU***	No	No	Welded	double-sided $\frac{M_{c,Rd}}{M_{pl,a,Rd}} = 1.15$
BSF***		Bare-steel		

Note: \*The presence of composite action interaction over the protected zone. \*\*Chapter 4. \*\*\*Reference (Chaudhari et al., 2019).  $M_{c,Rd}$ = connection bending capacity.  $M_{pl,a,Rd}$ = plastic bending capacity of unperforated steel beam section.



**Table 6.2: Summary of Selected Parameters.**

1) Diameter $d_o$			2) End distance $S_o$		3) The interaction between composite action	
%	mm	Number of models	%	mm	Type	Number of models
50%	155	15 x 2	50%	155	High interaction	168
55%	171	14 x 2	55%	171	Low interaction	168
60%	186	13 x 2	60%	186	bare steel (no interaction)	168
65%	202	12 x 2	65%	202	Note: High interaction = there are bolted/welded shear studs over the web opening. Low interaction = no bolted/welded shear studs over the web opening. Without composite slab = steel RWS connection. $h$ = beam height; $80d_o$ = means the opening diameter equals to 80% of $h$ ; $80S_o$ = means the end distance equal to 80% of $h$ .	
70%	217	11 x 2	70%	217		
75%	233	10 x 2	75%	233		
80%	248	9 x 2	80%	248		
			85%	264		
			90%	279		
			95%	295		
			100%	310		
			105%	326		
			110%	341		
			115%	357		
			120%	372		

### 6.3.2 Parametric results

The main objective of this section is to examine the effects of introducing web opening in both partial- and full-strength solid webbed-beam connections. The discussion focuses on assessing the four key factors, namely i) the location and ii) the size of the web opening, iii) the capacity design ratio, and iv) the presence/absence of composite action. These factors were selected for assessment owing to their crucial impacts on ductility, energy dissipation, and equivalent viscous damping. It is worth noting that this study used the response of the right beam's connection in the double-sided joint for a fair comparison with single-sided connections.

#### 6.3.2.1 Ductility

One of the key response characteristics to examine the robustness of moment-resisting frames (MRFs) under seismic loads is the rotational ductility of the connections. The ductility needs to be present in designated structural components for safe transfer and redistribution of loads within MRFs. It is quantified as the ratio of the ultimate rotation to yield rotation ( $\theta_u/\theta_y$ ). It is worth

emphasising that the single-sided and double-sided RWS connections were designed based on equal-strength ( $M_{c,Rd}/M_{pl,a,Rd} = 1$ ) and full-strength ( $M_{c,Rd}/M_{pl,a,Rd} = 1.15$ ) connections with a solid webbed-beam, respectively.

The location of the web opening has less effect on the ductility, among other key factors. Generally, as the location of the web opening moves farther from the connection, both sagging and hogging ductility ratios decrease. This finding has been highlighted in the literature (Tsavdaridis et al., 2014; Tsavdaridis and Papadopoulos, 2016; Tsavdaridis et al., 2017; Boushehri et al., 2019), where it is shown that the effects of RWS (Vierendeel mechanism) diminish as the end distance ( $S_o$ ) increases.

The web opening size is the factor that has the most significant consequences, when considered in combination with other factors, in affecting the ductility; as shown in Figures 6.3 and 6.4. This is mainly attributed to the Tee-section depth that directly triggers the yielding of the perforated section as shown in Figure 6.5. The earlier the Tee-section yields, the higher the ductility, provided that ultimate rotations remain equal or constant among other RWS connections. This is because of the mathematical formulation of ductility ( $\theta_u/\theta_y$ ), indicating that lower yield rotation leads to higher ductility.

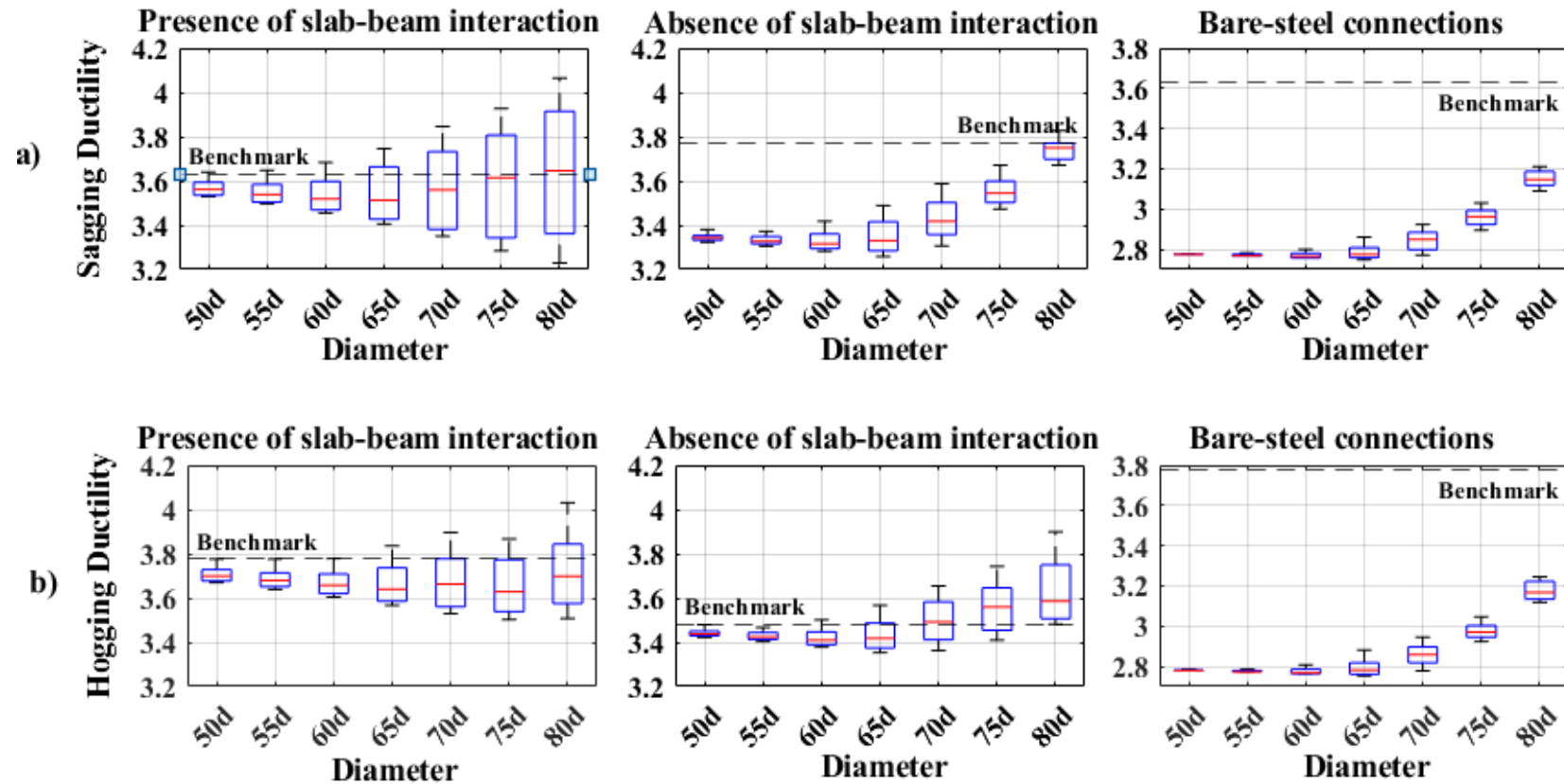


Figure 6.3: Rotation ductility of single-sided connections (based on equal-strength solid webbed-beam connection).

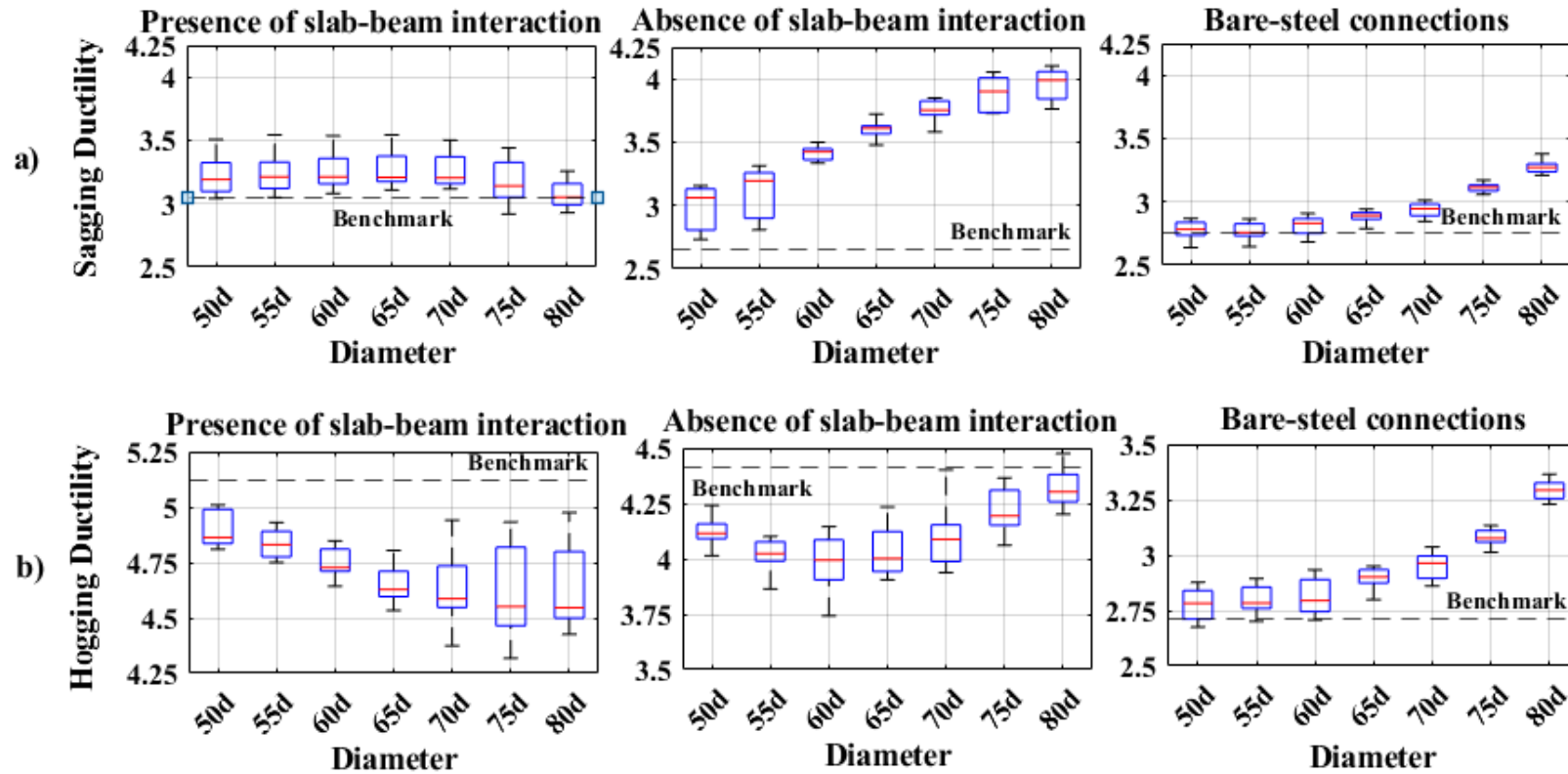
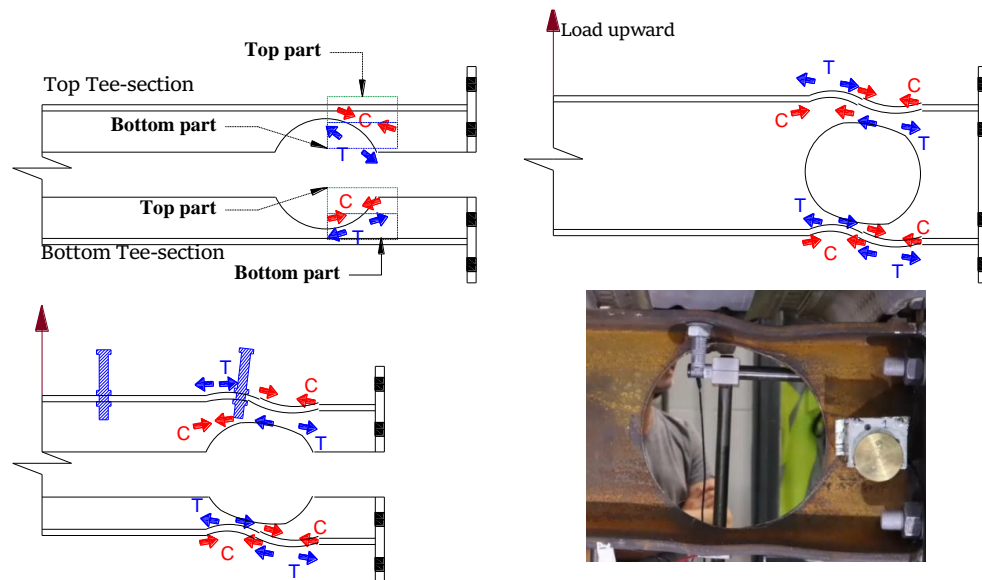


Figure 6.4: Rotation ductility of double-sided connections (based on full-strength solid webbed-beam connection).



**Figure 6.5: Illustration of the behaviour of Tee-sections.**

Figure 6.5 also demonstrates the combined effects of the web opening size with the presence or absence of composite interaction. The location of the extra row of bolts/welded shear studs also affect on the onset of yielding in the top Tee-section. The critical location of shear studs is at the centreline of the circular web opening due to the smaller Tee-section depth. Such combination effects can be seen in Figure 6.3. Although the number of numerical models using RWS connections with  $50d_o$  amounted to 15, the ductility range is narrow (i.e., the maximum and minimum values were close).

Conversely, the ductility range of RWS connections with  $80d_o$  is wider, despite the small number of numerical models that complied with SCI P355 guidance (Lawson and Hicks, 2011), as shown in Table 6.1. This was more pronounced with the presence of composite action than with those without composite interactions (Figure 6.3). This observation applies to single-sided RWS connections (equal-strength) but not to double-sided RWS connections (full-strength) due to the capacity design ratio, as shown in Figure 6.4.

Given that, the capacity design ratio could reduce the effectiveness of large web openings, especially with the presence of composite action as shown in Figure 6.4, this is mainly attributed to the fact that the RWS connections were designed based on the full-strength of the solid webbed-beam connection. For such full-strength connections, deformation primarily occurs in the beam itself, as the connection's capacity exceeds that of the connected unperforated steel beam. In other words, the steel beam becomes weaker when the web opening is

introduced, leading to an earlier yielding. Additionally, the arrangement of the joint (double-sided) and applied cyclic loads on the column tip caused early deformations of Tee-sections due to the high forces acting on the beams from the column.

The behaviour of RWS connection, whether designed based on partial- or full-strength solid webbed-beam connections, can be more accurately predicted by eliminating the composite slab-beam interaction over the protected zone, as depicted in Figures 6.3 and 6.4. This conclusion is drawn from the observation that the trends of RWS connections in this parametric investigation are similar to those of bare steel RWS connections under both sagging and hogging moments. These findings align with Chapters 3, 4 and 5, regarding the superior cyclic behaviour of RWS connections with an absence of composite action to avoid high strain demand on the beam bottom flange, as well as cracking and crushing of the concrete slab, without jeopardising the strong column-weak beam concept; following the requirements of (CEN, 2005d; ANSI/AISC 358-16, 2016).

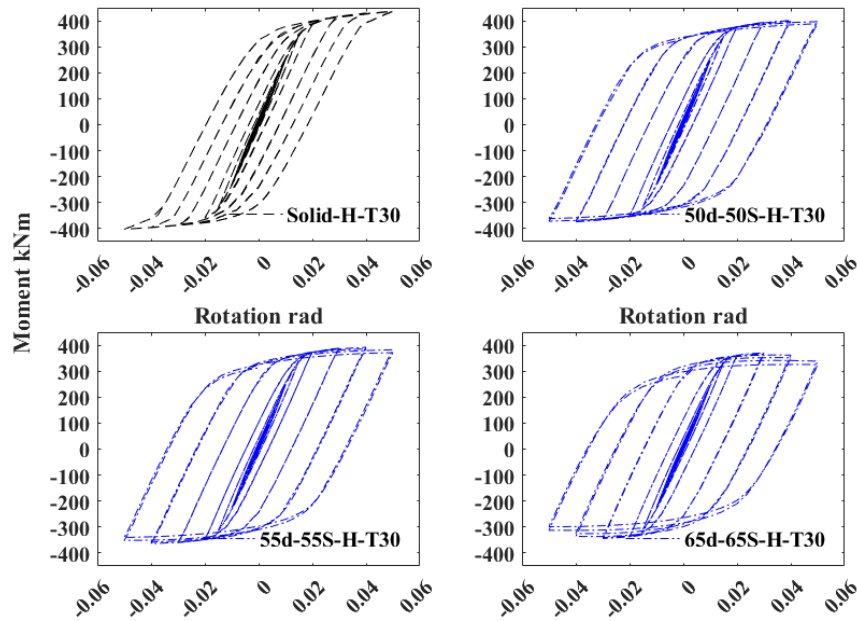
It can be concluded that, for single-sided RWS connections that are designed based on partial-strength solid webbed-beam connection, the sagging and hogging ductility marginally improves when the  $d_o/S_o$  ratio equals 1 for diameters equal to  $0.5h$  and  $0.55h$ . The improvement in ductility becomes more pronounced with web opening diameters equal to  $0.60h$  and  $0.65h$  when the  $d_o/S_o$  ratio ranges between 0.92 to 1 and 0.81 to 1, respectively. The range of  $d_o/S_o$  ratio broadens for diameter equal to  $0.70h$ ,  $0.75h$  and  $0.8h$ , and the presence of composite action over the web opening significantly influenced them. For these diameters, the ideal  $d_o/S_o$  ratios range between approximately 0.7 to 1.

For double-sided RWS connections designed based on full-strength solid webbed-beam connections, ductility alone cannot capture the overall response of the RWS connection. Energy dissipation and equivalent viscous damping must also be considered when introducing web openings into full-strength solid webbed-beam connections.

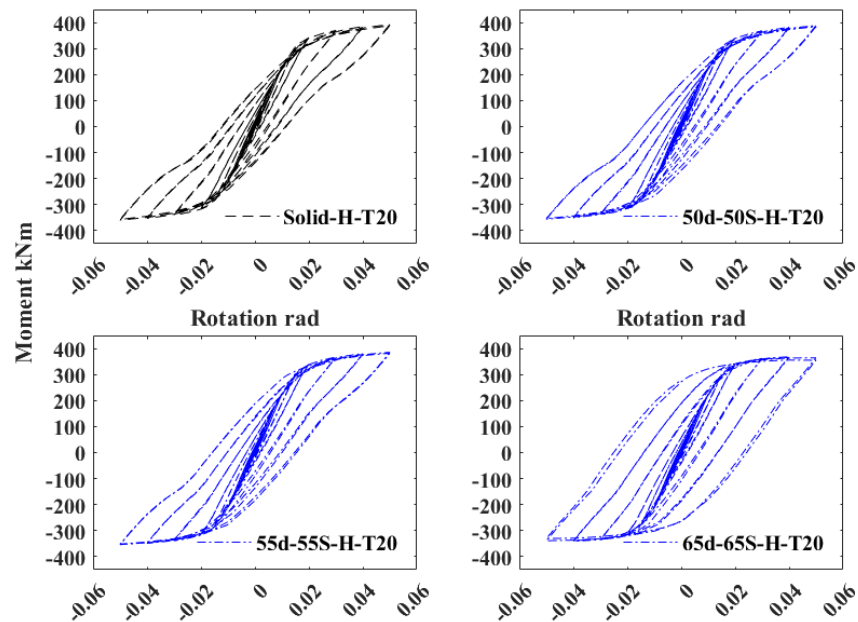
### **6.3.2.2 Energy dissipation and equivalent viscous damping**

Although ductility is an important indicator in seismic design, it alone cannot capture the overall hysteretic response of the structure. For instance, the pinching phenomenon is well-represented by the area of the hysteresis loops, which depicts the amount of plastic work dissipated in each cycle. In Chapter 5, it was observed that the RWS connections with smaller web openings could achieve higher ductility. In this case, the bending of the extended end plate acted as one of the dissipative elements, leading to a pinching mechanism and a significant reduction in the total amount of dissipated seismic energy, as shown in Figure

6.6. This was also well-captured in this parametric study, as shown in Figures 6.3b and 6.7 for single-sided connections (equal-strength). The web openings with small sizes have higher hogging ductility on average and lower dissipated energy compared to the large size of web openings. However, this is not the case for the double-sided RWS connections.



a) Thickness of end-plate = 30 mm  $\frac{M_{j,Rd}}{M_{pl,a,Rd}} = 1.06$  (full-strength connection)



b) Thickness of end-plate = 20 mm  $\frac{M_{j,Rd}}{M_{pl,a,Rd}} = 1$   
(equal/partial-strength connection)

Figure 6.6: Comparison between two different connections with high composite action in terms of capacity ratio (from Chapter 5).

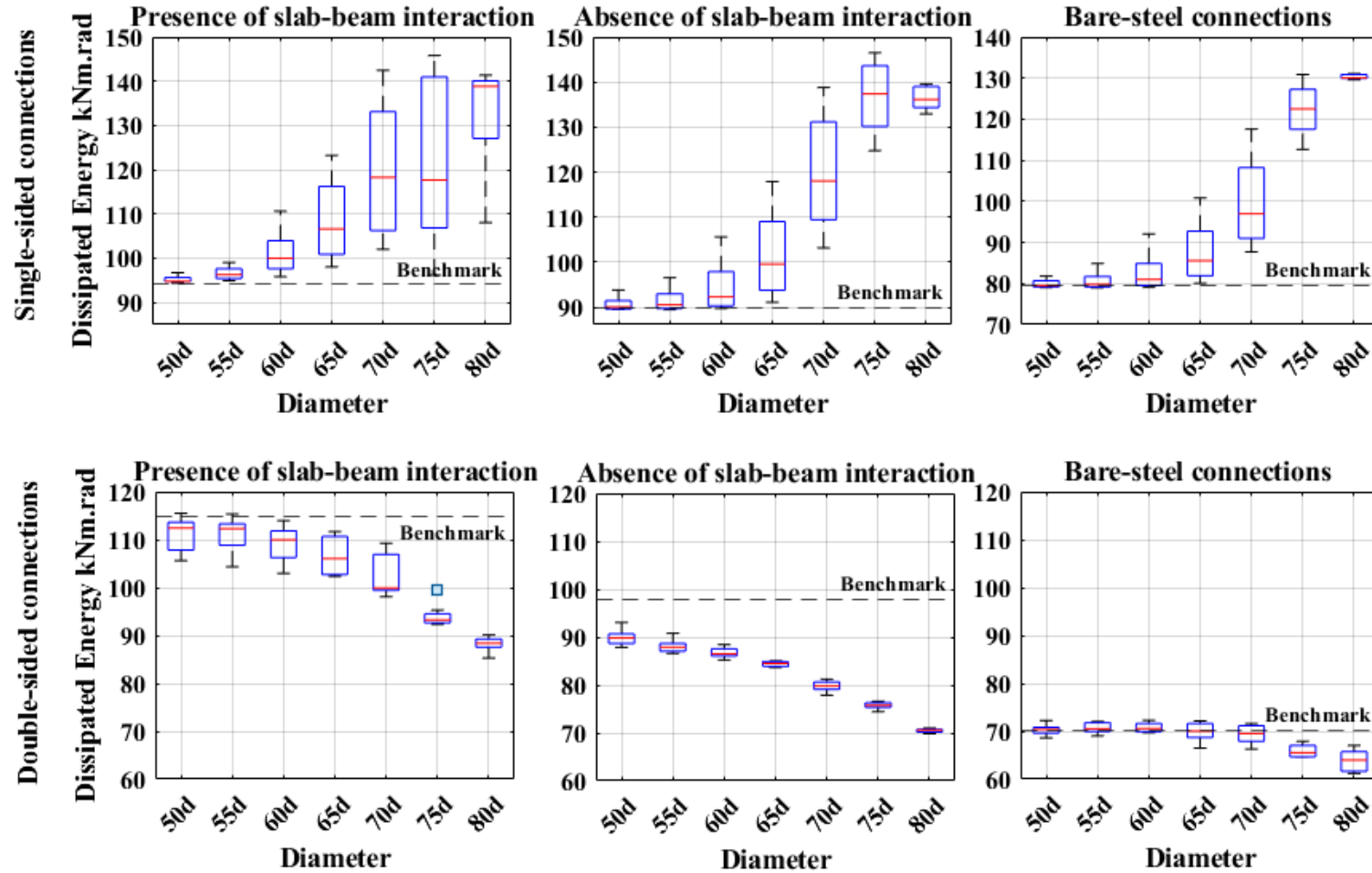


Figure 6.7: Energy dissipation.



Double-sided connections were designed based on a full-strength connection with a solid webbed beam, so they were intended to have the beam serve as the primary dissipative element. Thus, any web opening, regardless of size, would serve as a predetermined location for plasticity. For RWS connections with the presence of composite action, an increase of 15% of the connection's moment capacity led to an average difference of 21% in dissipated energy in favour of the web opening with  $50d_o$  compared with  $80d_o$ . These findings align with the findings of Shaheen et al. (2018) and those in Chapters 3, 4 and 5, which advocate for using small to medium web opening sizes when a high capacity design ratio was considered. When employing a high-capacity design ratio, it is recommended to use small to medium web opening sizes, and the opposite is when lower-capacity design ratios are employed. Overall, double-sided RWS connections with  $50d_o$  and  $55d_o$  demonstrate impressive responses, offering both superior energy dissipation and competitive ductility compared to other designs, including the stiffened BEEP (FI-SU) with a value of 109.5 kNm.rad. The findings suggest that RWS connections work more effectively when designed based on partial/equal-strength solid webbed-beam connection. This originates from a predictable hysteretic response.

Another important indicator to evaluate the energy dissipating capacity of the connections is an equivalent viscous damping ratio ( $\xi_{eq}$ ) (Parastesh et al., 2014; Shaheen, 2022). The energy dissipation is examined in terms of equivalent viscous damping and defined as:

$$\xi_{eq} = \frac{1}{2\pi} \frac{S_{ABC} + S_{CDA}}{S_{ODA} + S_{OBF}}$$

The energy is depicted by  $S_{ABC} + S_{CDA}$  is the energy dissipated at the expected rotation, as shown by the shaded region in Figure 6.8. Similarly,  $S_{ODA} + S_{OBF}$  indicates the total strain energy at the expected rotation highlighted by the area with double shading in Figure 6.8. Furthermore, points B and D represent the peak positive and negative moment capacities within a hysteresis loop, respectively. The equivalent viscous damping coefficients at 0.04rad for all models are shown in Figure 6.9. At the rotation of 0.04 rad, the magnitudes of equivalent viscous damping were generally above 30% which indicates good energy dissipation capacity and seismic response of RWS connections. These also imply that the RWS connection has not experienced brittle or sudden failures, likely maintaining its integrity, which is crucial for the stability of the structure and safety immediately after the earthquake.

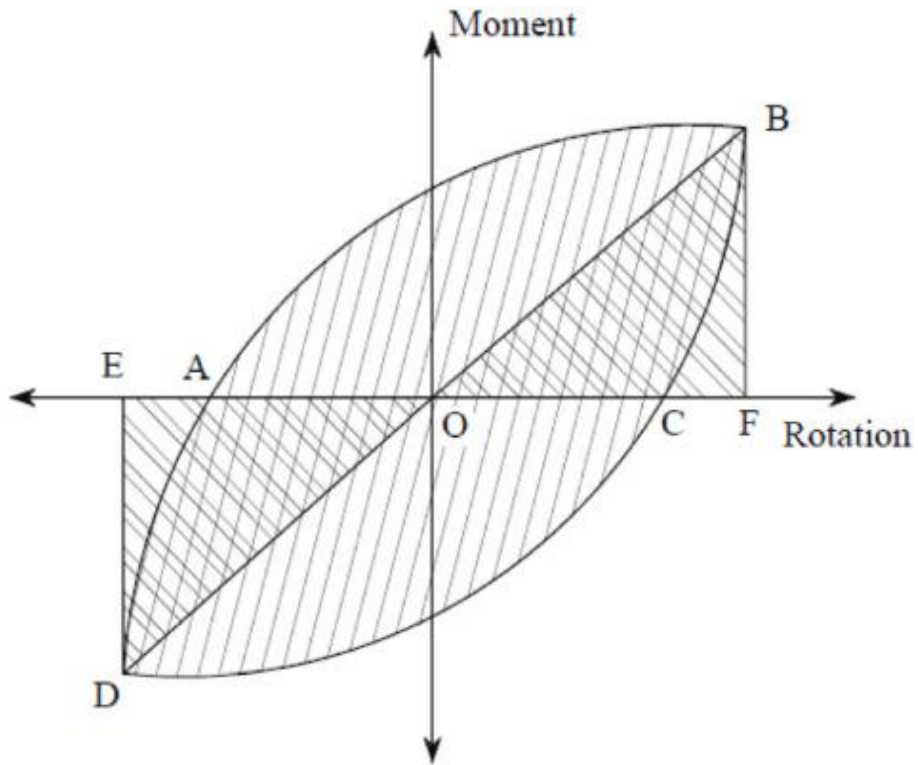
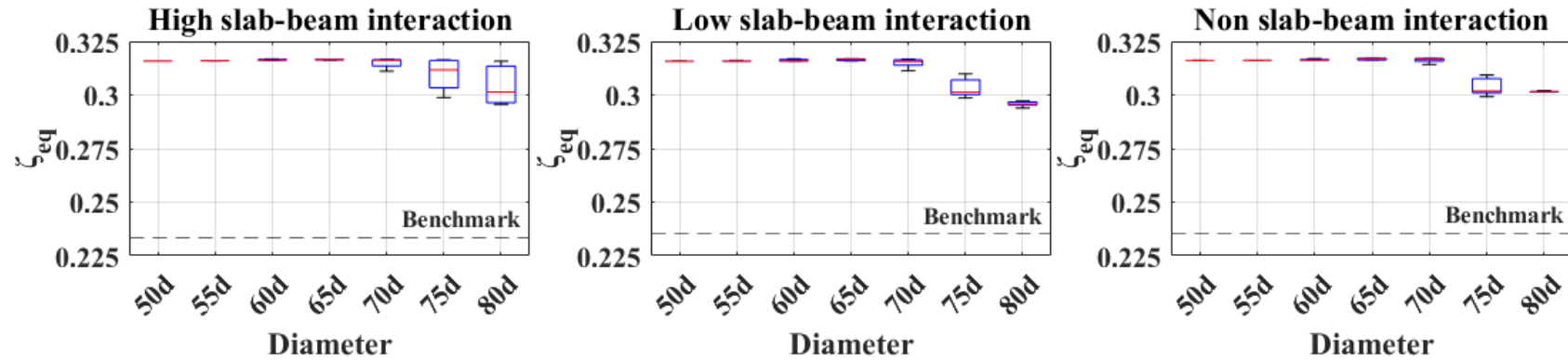
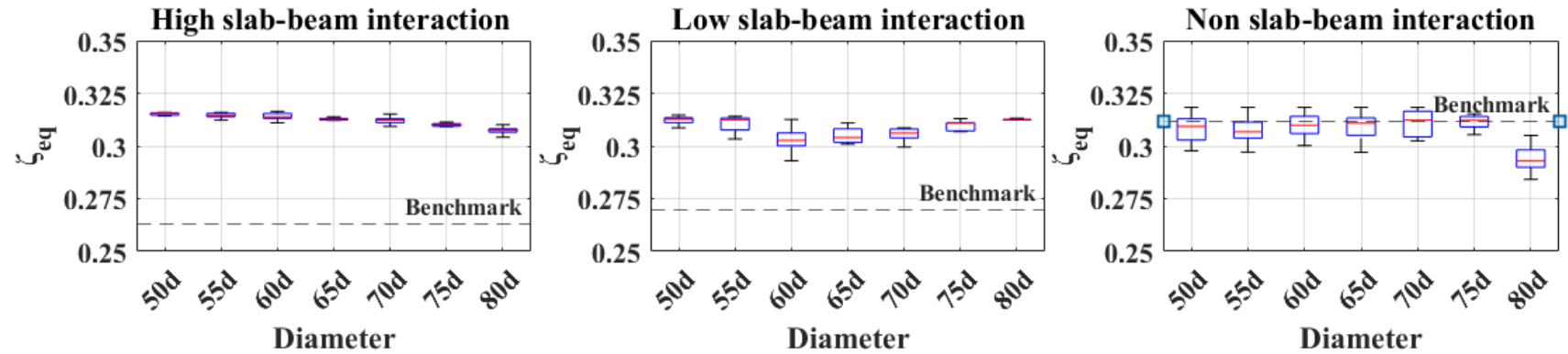


**Figure 6.8: Basis to calculate the equivalent viscous damping coefficient (Shaheen, 2022).**



a) Single-sided connections (based on equal-strength solid webbed-beam connection).



b) Double-sided connections (based on full-strength solid webbed-beam connection).

Figure 6.9: Equivalent viscous damping coefficient at 0.04 rad.

## **6.4 Capacity assessment**

### **6.4.1 RWS database assembly**

The assembled RWS connections database consists of 13 experimental and FE programs, along with the results from Chapter 3. This database covers both bare steel and composite RWS connections as well as benchmarked solid webbed-beam connections. It contains data on both welded and BEEP (3 rows and 4 rows of bolts) connections. Additionally, the database captures only a single circular web opening. In total, there are 251 specimens and FE models for 247 RWS connections, in addition to their benchmarked 14 solid webbed-beam connections counterparts. The database accounts for different types of test setups, namely, cantilever, cruciform and frame arrangements, with load and/or displacement applied at the beam or the column ends. Although this is a comprehensive RWS connections database, a few test and FE programs were excluded from the current database due to scarce test and FE details. A summary breakdown of the collected RWS database is presented in Tables 6.3 and 6.4.

**Table 6.3: Summary breakdown of the collected RWS database.**

Reference	Study	Joint	Connection	# of specimens	Slab
1- Guo et al. (2011)	FE	Frame	Welded	6	No
2- Li et al. (2011)	Test	Cantilever	Welded	3	No
3- Tsavdaridis et al. (2014)	FE	Cantilever	Welded	9	No
4- Tsavdaridis and Papadopoulos (2016)	FE	Cantilever	BEEP-3-R	1	No
5- Shin et al. (2017)	Test	Frame	WUF-B	2	No
6- Erfani and Akrami (2017)	FE	Cantilever	Welded	1	No
7- Shaheen et al. (2018)	FE	Cantilever	PN	12	Yes
8- Zhang et al. (2019)	Test	Cantilever	Welded	1	No
	FE			1	
9- Boushehri et al. (2019)	FE	Cantilever	Welded	144	No
10- Nazaralizadeh et al. (2020)	FE	Cantilever	BEEP-4-R	1	No
11- Tsavdaridis et al. (2021)	Test	Cantilever	BEEP-3-R	1	No
12- Xu et al. (2022)	Test	Cantilever	Welded	5	No
13- Chapter 3	FE	Cruciform	BEEP-4-R	45	Yes

Note: # = number. FE = Finite element analysis. Exp. experimental test. BEEP-3-R and 4-R = bolted extended end-plate with 3 rows and 4 rows, respectively. WUF-B = welded unreinforced flange-bolted web. PN = pre-Northridge.

Table 6.4: Breakdown of capacity design of the collected RWS database.

Ref. (See Table 6.3)	Connection	Column Section	Beam Section	Connection capacity	Capacity design ratio
		$M_{pl,col} = W_{pl,y,c} f_{y,c}$	$M_{pl,b} = W_{pl,y,b} f_{y,b}$	$M_{c,Rd}$ using Component method Eurocode 3-1-8	
1	Welded	H500x350x14x18	H600x250x10x14	NA	1.28
		911	710		
2	Welded	H450x300x12x16	H400x200x8x12	NA	2.15
		613	285		
3	Welded	HEB 300	HEA 240	NA	2.51
		570	227		
4	BEEP-3-R	HEB 160	IPE 300	87	0.50
		97	173		
5	WUF-B	W14X145	W12X50	NA	4.02
		1763	439		
6	Welded	HB500x200x10x16	HB414x405x18x28	NA	0.42
		735	1735		
7	PN	HB428x407x20x35	HB700x300x13x24	NA	1.38
		2051	1490		
8	Welded	HW250x250x9x14	HN300x150x6.5x9	NA	1.79
		220	123		
9	Welded	HEB 300, 450, 500, 600	IPE 330, 450, 500, 600	NA	2.32, 2.34, 2.19, 2.08
		663, 1414, 1709, 2599	285, 604, 779, 1247		
10	BEEP-4-R	HEB 200	IPE 270	95	0.82
		154	116		
11	BEEP-3-R	UC 203 x 203 x 71	UB 305 x 127 x 48	157	0.62
		284	252		
12	Welded	HW250x250x9x14	HN300x150x6.5x9	NA	1.79
		220	123		
13	BEEP-4-R	HEB 320	IPE 300	216	0.96
		765	224		
		1221	300		

Note:  $M_{pl}$  = moment capacity of bare steel solid webbed-beam section. [kNm].  $W_{pl,y}$  = plastic section modulus.  $f_y$  = yield strength. Subscript col, b and c = column, beam and connection, respectively. BEEP-3-R and 4-R = bolted extended end-plate with 3 rows and 4 rows, respectively. WUF-B = welded unreinforced flange-bolted web. PN = pre-Northridge.

#### 6.4.2 Observed trends in the collected RWS database

The collected database reveals a range of beam, column, connection types and capacity design ratios. An inconsistency in capacity design ratios was observed. The capacity design is a key requirement in controlling the plastic response of beam-to-column joints by managing the connecting components' capacities. With this objective in mind, employing the capacity design in RWS connections is critical since the reduction in shear capacity is particularly undesirable in seismic areas because it deteriorates more rapidly than its moment capacity. However, the concept of RWS connection, which relies on the Vierendeel mechanism, is only effective in areas of high shear. The Vierendeel mechanism is a shear action that requires a large opening and an ideal end distance to be triggered. Otherwise, a non-ductile failure characterised by tearing and out-of-plane buckling may ensue. Chung et al. noted that both shear failure and the Vierendeel mechanism can occur concurrently around the web opening (Chung et al., 2003; Lagaros et al., 2008). Therefore, attention should be paid not only to the size and location of the web opening, which has been the focus of previous studies in the literature but also to the capacity design ratio between the connected components. This ensures that the beam's shear capacity is not excessively compromised by incorporating RWS. To this end, a balanced contribution (capacity design) of a panel zone, end-plate and/or column flange, with the connected bare steel solid webbed-beam, is preferable in an RWS connection with a large web opening size. This promotes a Vierendeel (ductile) mechanism to become the dominant failure rather than simple shear failure at the web opening, which may cause instability after an earthquake. In the design process, the web opening size should be decreased along with the capacity design ratio increase. This is consistent with prior observations of the studies in Chapters 3, 4 and 5, regarding the importance of capacity design ratios.

Having thoroughly examined the collected RWS database, the above conclusions are verified. Figures 6.10 and 6.11 display the trends in the collected RWS database between energy dissipation, equivalent viscous damping, and ductility concerning the capacity design ratio. It can be seen that an increase in the capacity design ratio leads to a decrease in energy dissipation, equivalent viscous damping, and ductility, regardless of the connection type. Figure 6.11 depicts the decrease in sagging ductility of identical connections with an increase in web opening size with a high capacity design ratio, as employed in the study of Shaheen et al. (2018). In contrast, in Chapter 3, an increase in sagging ductility of identical connections was observed, along with a decrease in web opening size when accompanied by an equal/partial capacity design ratio. Figures 6.10 and 6.11 highlight the importance of capacity design ratios in RWS connections

compared to solid webbed-beam connections. A capacity design ratio larger than 1.5, is preferable with a solid webbed-beam connection to account for steel hardening and prevent fracture, as Elkady and Lignos (2014) suggested. This capacity design ratio does not apply to RWS connections. However, the high ductility found in RWS connections with a high capacity design ratio (larger than 1.5), can be attributed to two factors. The first one is the early yielding of Tee-sections, which leads to increased ductility. The second one is due to the exclusion of the composite slab from testing, which would have resulted in a lower ultimate rotation and, consequently, reduced ductility.



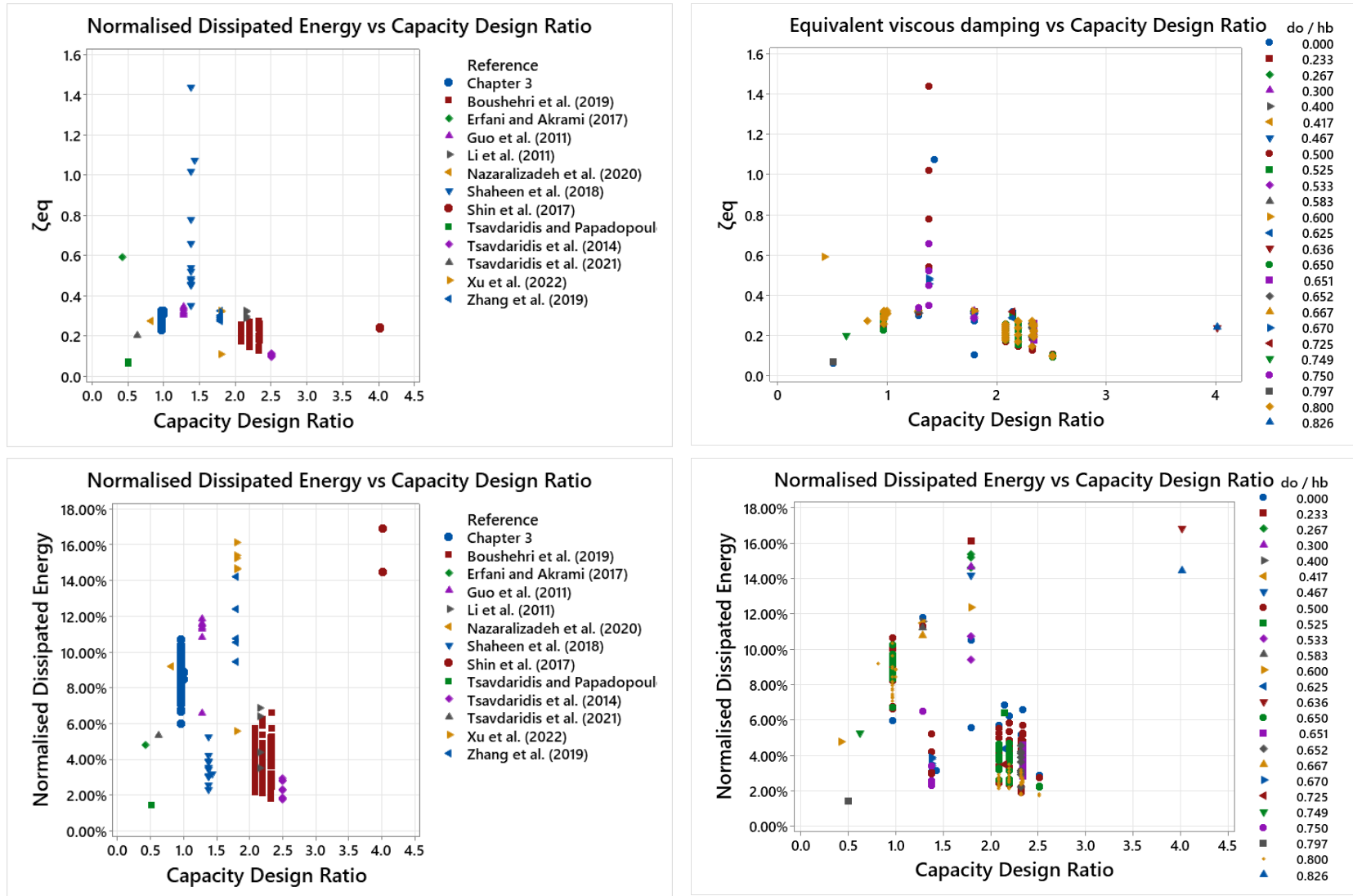


Figure 6.10: Energy dissipation and equivalent viscous damping

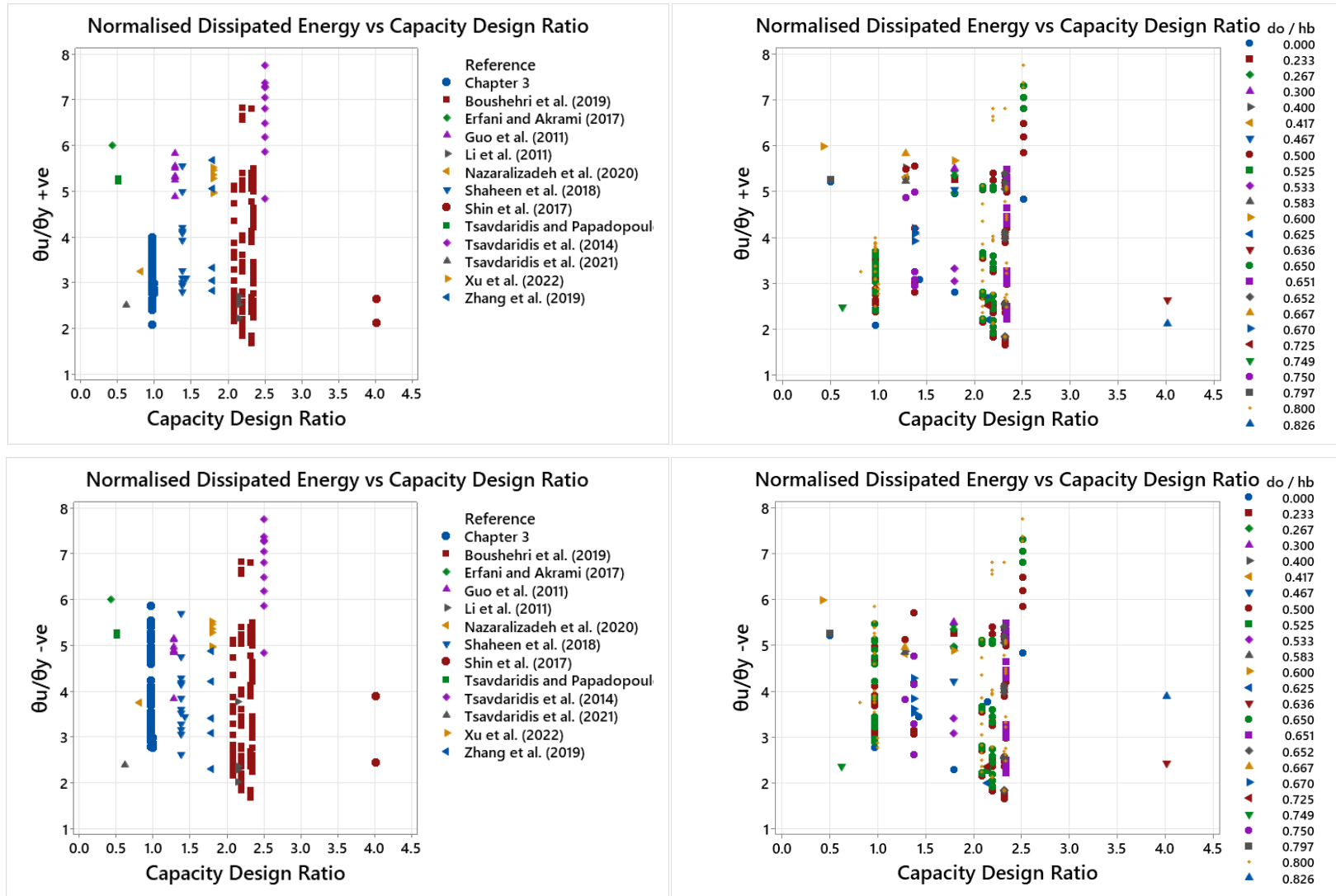


Figure 6.11: Ductility for RWS connections.

### 6.4.3 Detailing recommendations

Different design methodologies for RWS connections have been proposed in the literature (Hedayat and Celikag, 2009; Momenzadeh et al., 2017; Tsavdaridis et al., 2017; Boushehri et al., 2019; Zhang et al., 2019; Asl and Jahanian, 2020; Davarpanah et al., 2020a) based on the current design guidelines for perforated beams in both the UK and the US (Darwin, 1990; Lawson and Hicks, 2011; Fares et al., 2016) as well as on the design process for RBS connection outlined in AISC-385 (ANSI/AISC 358-16, 2016). Despite considering the strong column-weak beam concept, not all proposed design methodologies for RWS connections have addressed the capacity design ratio between the connected components. The strong column-weak beam and capacity design concepts are similar in that they aim to control how structures respond to earthquakes. Still, they approach the design objectives in different ways.

The strong column-weak beam concept is a design rule that is limited to beams and columns. It is intended to prevent column failure by ensuring that plastification forms in beams before it does in columns. This is important since the columns' failure can lead to the progressive collapse of a structure. On the other hand, capacity design is a broader principle aimed at ensuring the proportioned contribution of each component of the joint to the inelastic response of the entire joint. This discrepancy highlights a gap in current design approaches that warrants further investigation and the prequalification of RWS connections with both bolted and welded connections.

Based on the analysis of the collected RWS database and parametric numerical investigation conducted in this study, recommended details for the design of RWS connections are proposed herein. The recommendations pertain to extended end-plate connections with 4 rows of bolts. The proposed details apply to both retrofitting existing structures and designing new ones.

Regarding the retrofit of existing structures, it is noted that steel-concrete composite beams with welded shear studs present challenges. Creating a gap between the concrete slab and the column or removing welded shear studs over the protected zone, would be obstructive and costly. However, such a gap is essential to ensure that no forces are transferred to the column from the concrete slab. This minimises the possibility of slab damage and reduces the strain/stress demand on the column. Therefore, proper consideration of such force transfer mechanisms, as stated in Eurocode 8, is required when modelling the joint for retrofit purposes. Table 6.5 shows the recommended ratios of capacity design, diameter-to-depth ( $d_o/h_b$ ), and diameter-to-end distance ( $d_o/S_o$ ) for retrofitting

existing structures. The recommendations in Table 6.5 could serve as a starting point for modelling the joint for retrofitting of the existing building.

**Table 6.5: Capacity design requirements for RWS connections for retrofitting existing structures.**

Connection's strength category			
Bolted connections	Capacity design ratio		
	Full-strength	Equal-strength	Partial-strength
	$M_{c,Rd} \leq 1.3 M_{pl,b}$	$M_{c,Rd} = M_{pl,b}$	$M_{c,Rd} \geq 0.8 M_{pl,b}$
$d_o/h_b =$	0.5 – 0.67	0.7 – 0.8	
$d_o/S_o =$	1	0.7 – 1	

Where  $M_{c,Rd}$  = connection bending capacity according to the component method in Eurocode 3-1-8 (CEN, 2005b).  $M_{pl,b}$  = nominal bending capacity of bare steel solid webbed-beam section.  $d_o$  = opening diameter.  $h_b$  = steel beam depth.  $S_o$  = end distance from column/end-plate face to web opening centreline.

Specific recommendations for detailing the size and location of web openings in relation to the location of shear studs are critical for both existing and new structures. This is particularly important when composite slab-beam interaction over the protected zone is necessary or unavoidable. Ensuring this can activate the Vierendeel mechanism for small to medium web openings, which is significant due to the large depth of the Tee-section at such sizes (Figure 6.14). For large web openings, locating them between the studs is preferable to avoid a premature crack in the vicinity of the web opening.

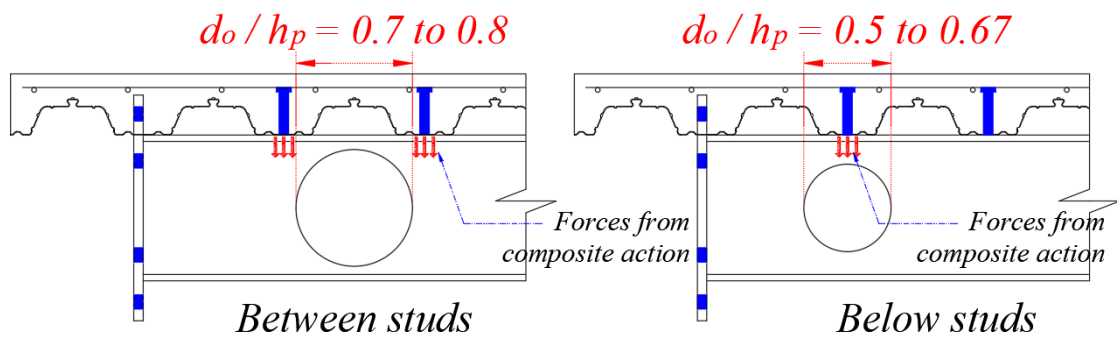


**Figure 6.12: Diameter-to-depth ratio in relation to shear studs' location.**

Although the guidance presented in SCI P355 guidance was developed for monotonic loads, it has been shown to predict the moment capacity of RWS connections under cyclic loads. It is well-known that the moment capacity of connection under cyclic loads is always lower than that under monotonic loads due to repeated loading and unloading. This repetition causes various mechanisms, such as material low cyclic fatigue, which leads to reduced capacity. This has been confirmed by the study of Tsavdaridis et al. (2017) which found that the cyclic moment and rotational capacities of the RWS connections were lower than those of their monotonic counterparts. The guidance outlined in SCI P3555 guidance is derived from the T-section approach (TSA), one that was initially introduced for composite perforated beams. The findings of this study, manifest that the SCI P355 guidance can be applied to estimate the moment capacity of RWS connections under cyclic loads.

In this study, the effective yield moment ( $M_{ye}$ ) is used to represent the connection's plastic moment capacity ( $M_{c,Rd}$ ) due to a lack of consensus on its calculation in the existing literature (Özkılıç, 2023).  $M_{c,Rd}$  was employed to assess the bending capacity of the perforated section ( $M_{o,a,Rd}$ ;  $M_{o,Rd}$ ) in both bare steel and steel-concrete composite connections according to SCI P355 guidance, respectively. Table 6.6 presents the statistical values indicating the applicability of the SCI P355 guidance in estimating RWS connections. Table 6.7 lists capacity design requirements for RWS connections for new structures. It is worth noting that these requirements follow the capacity design principles of EQUALJOINTS and EQUALJOINTS-Plus (Tartaglia, D'Aniello, Rassati, et al., 2018; Tartaglia, D'Aniello, Zimbru, et al., 2018; Tartaglia et al., 2019; Landolfo, 2022; D'Aniello et al., 2023), with the inclusion of recommendations from SCI P355 guidance.

Regarding welded connections, further investigations into the capacity design are needed. However, based on the collected RWS database, the ideal  $d_o/S_o$  ratio for the welded connection is 1 for a diameter equal to  $0.5h$  to  $0.67h$ . The capacity design ratio for the welded connection should be  $M_{pl,col} \leq 1.3 M_{pl,b}$ .

**Table 6.6: Statistical results for the collected RWS database and parametric investigations.**

		<b>Sagging</b>	<b>Hogging</b>
$M_{ye} / M_{o,Rd}$	<b>Average</b>	1.1260	-1.0170
	<b>Maximum</b>	1.6426	-0.8196
	<b>Minimum</b>	0.7445	-1.5045
	<b>Standard Deviation</b>	0.1548	0.0891
$M_{ye} / M_{o,a,Rd}$	<b>Average</b>	1.0618	-1.0582
	<b>Maximum</b>	1.2439	-0.7954
	<b>Minimum</b>	0.7933	-1.2618
	<b>Standard Deviation</b>	0.0635	0.0644

**Table 6.7: Capacity design requirements for RWS connections for new structures.**

- Full-strength:  $M_{c,Rd} \geq 1.1 \cdot \gamma_{ov} \cdot (M_{o,Rd} + V_{Ed} \cdot S_o)$
- Equal -strength:  $M_{c,Rd} \geq (M_{o,Rd} + V_{Ed} \cdot S_o)$
- Partial -strength:  $M_{c,Rd} \geq 0.8 \cdot (M_{o,Rd} + V_{Ed} \cdot S_o)$

Where  $M_{c,Rd}$  = connection bending capacity according to the component method in Eurocode 3-1-8 (CEN, 2005b). ( $M_{o,Rd}$  bending capacity of perforated composite beam section according to SCI P355 guidance.  $V_{Ed}$  is the shear force corresponding to the formation of a plastic hinge in the connected beam,  $S_o$  = is the end distance between the connection face and the centerline of web opening.  $\gamma_{ov}$  = the overstrength factor =1.25.

Diameter-to-depth ( $d_o/h_b$ ), and diameter-to-end distance ( $d_o/S_o$ ) for retrofitting existing structures are applicable to design RWS connections for new structures.

## 6.5 Summary

Capacity design is a comprehensive approach that ensures that each joint component contributes proportionally, behaving in a predictable and ductile manner as part of the entire joint. This approach has not been addressed in previous studies of RWS connections. Therefore, a comprehensive parametric numerical investigation has been performed and analysed for single-sided and double-sided steel-concrete composite connections, providing valuable insights into how the capacity design approach influences their performance. Subsequently, a database of 13 test and FE programs, including the data from Chapter 3 on RWS connections, was compiled and analysed. It contains data on both welded and bolted RWS connections with a single circular web opening. The total number of RWS specimens is 247, alongside their benchmarked counterparts, for a total of 14 solid webbed-beam connections.

Both the parametric numerical data and the collected RWS database were analysed to assess the impact of capacity design ratio on ductility, energy dissipation and equivalent viscous damping. The findings revealed that the cyclic response of RWS connections is significantly influenced by the capacity design ratio between the connected components of the joint/connection. Proper consideration of the capacity design ratio ensures that a stable inelastic mechanism is governed when the RWS connection is subjected to cyclic loads. This enhances the ductility and energy dissipation of RWS connections through a stable yielding of Tee-sections, thereby capping plasticity to non-ductile components. Moreover, the assessment of RWS connections manifests the critical effects of the location and size of web opening, in relation to shear studs' location on triggering the desirable ductile Vierendeel mechanism.

## Chapter 7

### Conclusion

#### 7.1 Overview

Steel-concrete composite moment-resisting frames (MRFs) are considered a suitable solution in earthquake-prone areas, with the expectation that structural damage would be solely confined to ductile responses, such as the yielding of connections and members. However, this perception was challenged following the extensive damage observed in steel-concrete composite MRFs during the 1994 Northridge and 1995 Kobe earthquakes. The damage was attributed to brittle tearing failures in the traditional beam-to-column connections, even in those areas that experienced only moderate earthquake ground motion. Research efforts have successfully implemented fuse approaches that divert deformation away from the column face and concentrate them within the beam. These fuse approaches can be subcategorised into strengthening or weakening of beam-to-column connections. However, the former approach often necessitates extensive work and/or a complex retrofitting process that increases construction costs and timelines. While the latter is often achieved by the well-known pre-qualified reduced beam section (RBS) connection, this raises concerns about accessibility to the top beam flange and the overall structural stability arising due to beam flange cuts. One of the most promising options based on the weakening approach is the reduced web section (RWS) connections that could improve out-of-plane stability. Such connections utilise perforations within the beam web as a means of enhancing moment capacity at the column interface, thereby alleviating the need for flange cuts or supplemental plates. Notably, the relative ease of modifying beam webs facilitates retrofitting applications compared to removing floors or modifying flanges.

Although there has been extensive research about RWS connections, their behaviour when excited by ground motion and as slabs overlay them is yet not well understood. Fortunately, the inherent response mechanism of RWS connections, which effectively function as two separate partial beams above and below the web opening (top and bottom Tee-sections), facilitates the formation of four plastic hinges encircling the web opening via the Vierendeel mechanism. This distinct mechanism bridges the challenges that pre-qualified connections (e.g., RBS connections) encounter. These challenges relate to the potential impact of composite action within the protected zone that could compromise the fundamental "strong column-weak beam" design philosophy, by introducing an asymmetric yield moment mechanism.



This thesis aims to address the extant knowledge gap regarding the behaviour of RWS connections with composite slabs by comprehensively analysing the findings of both experimental and numerical investigations conducted as part of the present research alongside relevant results/data gathered and extrapolated from the existing literature. The primary goal is to promote the widespread adoption of RWS connections in designing new buildings resistant to earthquakes and retrofitting structures not originally designed for seismic activity.

## 7.2 Summary of contributions

Before delving into the contributions, the primary objectives of this thesis encompass uncovering the phenomena governing the global behaviour of RWS connections, exploring the impact of composite action on RWS connections and the applicability of SCI P355 guidance, developing numerical models for further parametric assessments of the local cyclic behaviour of RWS connections, and compiling data from the literature to assess capacity design ratios. To fulfil these objectives, a research program that included an extensive literature review, preliminary finite element analysis (FEA), testing, parametric FEA, and the empirical study was completed.

**Objective:** *Uncover the phenomena that govern the behaviour of composite RWS connections when subjected to cyclic actions by using adaptable but detailed finite element modelling (FEM).*

### **Achieved in Chapter 3: Preliminary FEA and Chapter 5: Parametric Assessments**

FEA parametric investigation in Chapter 3, uncovered the effects of composite action on RWS connections, contributing to understanding the seismic response beyond just the size and location of the web opening. Based on the parametric investigation, the size and location of the web opening are not the only major factors that influence the seismic response of RWS connections. The capacity design principles at the component level could be utilised to make the most of the RWS connections' mechanism. Most of the RWS specimens performed well, with over 84% reaching a 6% drift level and all exceeding the minimum requirement of 4% outlined by ANSI/AISC 358-16, ANSI/AISC 341-16 and Eurocode 8. The findings support the idea that eliminating composite interaction over the protected zone helps to mitigate the inelastic demands outside the protected zone without compromising the beam's stability, even leading to a significant reduction of slab cracking. Chapter 5 furthered this objective by developing a comprehensive FE model to assess various parameters, including the presence of composite action, thereby enhancing our understanding of the local cyclic behaviour of RWS connections.

**Objective:** *Perform experimental tests to examine how composite action influences the cyclic behaviour of RWS connections, aiming to augment available data.*

#### **Achieved in Chapter 4: Experimental Investigation**

This chapter directly addressed the objective by conducting experimental tests on demountable steel-concrete composite bolted RWS connections. The tests explored the impact of web opening location and the presence of shear studs on the cyclic behaviour of RWS connections. The results confirmed the viability of RWS connections for seismic retrofitting, demonstrating their strength, ductility, and energy dissipation capabilities, thus significantly augmenting available data on RWS connections. These were achieved by generating a highly ductile Vierendeel mechanism, resulting in concentrating the high plasticity on the beam, which, in turn, leads to an increase in the deformability and ductility of the connections. All RWS connections could achieve an inter-storey drift larger than 4%, thereby complying with the performance targets, as set out by ANSI/AISC 358-16, ANSI/AISC 341-16 and Eurocode 8. The adopted capacity design framework was effective in obtaining the expected performance; namely, plastic deformations occurred in the vicinity of the web openings only. This means that a web opening effectively constrains inelastic action in the protected zone away from the joint plate and the column. Hence, providing such a web opening is a reliable course of action, that allows for full-strength connections within the strong column/connection weak beam paradigm.

**Objective:** *Conduct comprehensive parametric assessments to extend the observations on the experimental results.*

#### **Achieved in Chapter 5: Parametric Assessments**

This chapter directly achieved the objective of developing a high-fidelity FE model by examining 285 FE models. Through an in-depth analysis of RWS connections under varying conditions, it provided valuable insights into their cyclic behaviour. The results revealed that RWS connections exhibit cyclic strength degradation with medium to large web opening sizes, yet meet the seismic standards of ANSI/AISC 358-16, ANSI/AISC 341-16, and Eurocode 8. Notably, a good balance was achieved for all RWS connections, including non-composite ones. This balance involved a reduction in moment capacity of up to 19%, offset by increases in ductility and energy dissipation by up to 13% and 65%, respectively. The strength of RWS connections with bolted shear studs is more predictable than with the traditional welded shear studs, with demountable RC slabs contributing to about 5% of maximum strength. The size and location of the web opening should align with the capacity design ratio between the column,

connection, and the connected beam. The findings also highlighted the need for additional data for reliable design guidance, especially concerning the Vierendeel bending capacity. Recommendations were made regarding the optimal size and location of web openings.

**Objective:** *Compile test and FEA databases from this research and existing literature for assessing the capacity design ratio effect and the applicability of SCI P355 guidance (Lawson and Hicks, 2011), thereby promoting the use of RWS connections in MRFs in seismic areas.*

### **Achieved in Chapter 6: Capacity Design Assessment**

Chapter 6 involved a detailed analysis of the compiled test and FEA data to assess the effect of the capacity design ratio on RWS connections. This chapter significantly contributed to understanding how the capacity design approach can be effectively applied in the design of RWS connections, aligning with the guidelines of SCI P355. A gap in current design approaches demands explicitly introducing a capacity design approach when designing RWS connections. This is crucial, as evidenced by the results: a 15% increase in the connection's moment capacity led to an average 21% difference in dissipated energy, favouring the web opening with a diameter of  $50d_o$  over  $80d_o$ , in RWS connections with the presence of composite action. The results show that proper consideration of the capacity design approach in designing RWS connections ensures a stable yield mechanism is governed, resulting in the redistribution of global action and capping deformation demands on non-ductile elements. This enhances the rotational capacity and ductility of connections through the formation of the Vierendeel mechanism. This chapter presents recommendations detailing the employment of RWS connections in both existing and new structures for seismic purposes.

### 7.3 Recommendations for future research

Based on the contributions of this thesis, the following set of potential research topics is proposed for further investigation:

- The limitations of current laboratory testing facilities necessitate further investigation into the behaviour of RWS connections subjected to combined gravity and earthquake loads. This is particularly concerning due to the location of the web opening within a high shear zone, a critical region during seismic events.
- The focus of this current research was on the cyclic response of composite bolted RWS connections that consist of two components, namely extended end plate connections and the interconnected beam with web opening. Further physical tests should be conducted on the whole beam-to-column RWS joints, with and without composite slab both in double-sided and single-sided configurations. It is encouraged to follow the EQUALJOINTS' prequalification method and focus on the capacity contribution of each component both with and without composite slab. This will help to augment the database and seismically prequalified RWS connections with different connections (e.g., welded and bolted).
- Further review and assessment of available predictive models for bolted and welded connections, aimed at the development of robust guidance and numerical models and acceptance criteria for design and the promotion of the use of RWS connections in MRFs within seismic areas. The establishment of benchmarked models for seismic non-linear modelling is essential, as is setting acceptance criteria and reliably predicting the cyclic degradation effects and properties of RWS connections. These steps are crucial in assisting researchers and engineers in integrating these properties into analysis tools. This endeavour should be extended based on the developed comprehensive database of RWS connections in this thesis, and by incorporating data from future studies or any additional information not covered in this thesis due to unavailable results data from the existing literature, both experimentally and numerically. This approach ensures that the comprehensive database of RWS connections serves as a foundation for future research, allowing others to build upon and expand their knowledge in this field.
- Since the current study did not consider the contact force between a reinforced concrete slab and the connection/column. This omission was intentional, as a 25 mm gap was introduced to specifically focus on the local response of RWS connections without the column's contribution. The

purpose was to draw clear and fair conclusions regarding the presence or absence of composite action over the protected zone. Further investigation on the three force transfer mechanisms in an interior composite beam-to-column joint that was adopted in Eurocode 8 (CEN, 2005d) needs to be evaluated with a suitable web opening.

## References

- ABAQUS 2019. Abaqus User's manual, Version 6.19. *Dassault Systemes Simulia Corp., Providence, RI, USA.*
- ACI 2005. ACI T1.1-01: Acceptance criteria for moment frames based on structural testing and commentary. *ACI*. **374**, pp.1–5.
- Ahmed, I.M. and Tsavdaridis, K.D. 2022. Shear connection of prefabricated ultra-lightweight concrete slab systems (PUSSTM) *In: Structures*. Elsevier, pp.65–97.
- Akrami, V. and Erfani, S. 2015. Effect of local web buckling on the cyclic behavior of reduced web beam sections (RWBS). *Steel and Composite Structures*. **18**(3), pp.641–657.
- ANSI/AISC 341-16 2016. Seismic provisions for structural steel buildings. *Seismic provisions for structural steel buildings.*, p.60601.
- ANSI/AISC 358-16 2016. Prequalified Connections for Special and Intermediate Steel Moment Frames for Seismic Applications *In: Chicago, IL: AISC.*
- ASCE 2017. *ASCE/SEI 41-17: Seismic Evaluation and Retrofit of Existing Buildings.*
- Aschheim, M.A. 2000. Moment-resistant structure, sustainer and method of resisting episodic loads.
- Asl, M.H. and Jahanian, M. 2020. Behaviour of Steel Deep Beams in Moment Frames with Web Opening Subjected to Lateral Loading. *International Journal of Steel Structures*. **20**(5), pp.1482–1497.
- Ataei, A., Bradford, M.A. and Liu, X. 2017. Computational modelling of the moment-rotation relationship for deconstructable flush end plate beam-to-column composite joints. *Journal of Constructional Steel Research*. **129**, pp.75–92.
- Ataei, A., Bradford, M.A., Valipour, H.R. and Liu, X. 2016. Experimental study of sustainable high strength steel flush end plate beam-to-column composite joints with deconstructable bolted shear connectors. *Engineering Structures*. **123**, pp.124–140.
- Ataei, A., Zeynalian, M. and Yazdi, Y. 2019. Cyclic behaviour of bolted shear connectors in steel-concrete composite beams. *Engineering Structures*. **198**, p.109455.
- Augusto, H., da Silva, L.S., Rebelo, C. and Castro, J.M. 2017. Cyclic behaviour characterization of web panel components in bolted end-plate steel joints. *Journal of Constructional Steel Research*. **133**, pp.310–333.
- Baskar, K., Shanmugam, N.E. and Thevendran, V. 2002. Finite-element analysis of steel–concrete composite plate girder. *Journal of Structural Engineering*. **128**(9), pp.1158–1168.
- BCSA/SCI 2013. *Joints in Steel Construction: Moment-Resisting Joints to Eurocode 3.*
- Bernuzzi, C., Zandonini, R. and Zanon, P. 1996. Experimental analysis and modelling of semi-rigid steel joints under cyclic reversal loading. *Journal of Constructional Steel Research*. **38**(2), pp.95–123.

- Bi, R., Jia, L., Li, P. and Wang, Q. 2021. Multiparameter seismic behavior of castellated beam-to-column connections based on stress migration *In: Structures*. Elsevier, pp.1137–1153.
- Boushehri, K., Tsavdaridis, K.D. and Cai, G. 2019. Seismic behaviour of RWS moment connections to deep columns with European sections. *Journal of Constructional Steel Research*. **161**, pp.416–435.
- Bruneau, M.P.D.P., Uang, C.-M. and SE, R.S. 2011. *Ductile design of steel structures* Second Edi. McGraw-Hill Education.
- CEN 2011. *EN 1090-2:2008+A1:2011 – Execution of steel structures and aluminium structures*.
- CEN 2005a. *Eurocode 3: Design of steel structures-Part 1-1: General rules and rules for buildings*.
- CEN 2005b. Eurocode 3: Design of steel structures—Part 1–8: Design of joints—the European Standard EN 1993-1-8: 2005 *In: European Committee for Standardization, Brussels*.
- CEN 2005c. Eurocode 4. Design of Composite Steel and Concrete Structures. Part 1.1: General Rules and Rules for Buildings. *European Committee for Standardization, Brussels*. (1994).
- CEN 2005d. Eurocode 8: Design of structures for earthquake resistance-Part 1: General rules, seismic actions and rules for buildings. *European Committee for Standardization, Brussels*. (1998).
- CEN, E.C. for S. 2004. *Eurocode 2: design of concrete structures—part 1.1: general rules and rules for buildings*.
- Chaudhari, T. 2017. *Seismic performance evaluation of steel frame building with different composite slab configurations*. University of Canterbury.
- Chaudhari, T., MacRae, G., Bull, D., Clifton, C. and Hicks, S. 2019. Experimental behaviour of steel beam-column subassemblies with different slab configurations. *Journal of Constructional Steel Research*. **162**, p.105699.
- Chen, S.-J. and Chao, Y.C. 2001. Effect of composite action on seismic performance of steel moment connections with reduced beam sections. *Journal of Constructional Steel Research*. **57**(4), pp.417–434.
- Chiniforush, A.A., Ataei, A. and Bradford, M.A. 2021. Experimental study of deconstructable bolt shear connectors subjected to cyclic loading. *Journal of Constructional Steel Research*. **183**, p.106741.
- Chung, K.F. 2012. Recent advances in design of steel and composite beams with web openings. *Advances in Structural Engineering*. **15**(9), pp.1521–1536.
- Chung, K.F., Liu, C.H. and Ko, A.C.H. 2003. Steel beams with large web openings of various shapes and sizes: an empirical design method using a generalised moment-shear interaction curve. *Journal of Constructional Steel Research*. **59**(9), pp.1177–1200.
- Chung, K.F., Liu, T.C.H. and Ko, A.C.H. 2001. Investigation on Vierendeel mechanism in steel beams with circular web openings. *Journal of Constructional Steel Research*. **57**(5), pp.467–490.
- Civjan, S.A., Engelhardt, M.D. and Gross, J.L. 2000. Retrofit of pre-Northridge moment-resisting connections. *Journal of Structural Engineering*. **126**(4),

pp.445–452.

- Civjan, S.A., Engelhardt, M.D. and Gross, J.L. 2001. Slab effects in SMRF retrofit connection tests. *Journal of Structural Engineering*. **127**(3), pp.230–237.
- Cornelissen, H.A.W., Hordijk, D.A. and Reinhardt, H. 1986. Experimental determination of crack softening characteristics of normalweight and lightweight. *Heron*. **31**(2), pp.45–56.
- D'Alessandro, E., Brando, G. and De Matteis, G. 2018. Design charts for end-plate beam-to-column steel joints. *Proceedings of the Institution of Civil Engineers–Structures and Buildings*. **171**(6), pp.444–462.
- D'Aniello, M., Tartaglia, R., Costanzo, S. and Landolfo, R. 2017. Seismic design of extended stiffened end-plate joints in the framework of Eurocodes. *Journal of Constructional Steel Research*. **128**, pp.512–527.
- D'Aniello, M., Tartaglia, R., Landolfo, R., Jaspart, J.-P. and Demonceau, J.-F. 2023. Seismic pre-qualification tests of EC8-compliant external extended stiffened end-plate beam-to-column joints. *Engineering Structures*. **291**, p.116386.
- Darwin, D. 1990. *AISC design guide 31 Steel and Composite Beams with Web Openings*.
- Darwin, D. 2000. Design of composite beams with web openings. *Progress in structural engineering and materials*. **2**(2), pp.157–163.
- Darwin, D. and Donahey, R.C. 1988. LRFD for composite beams with unreinforced web openings. *Journal of Structural Engineering*. **114**(3), pp.535–552.
- Davarpanah, M., Ronagh, H., Memarzadeh, P. and Behnamfar, F. 2020a. Cyclic behavior of welded elliptical-shaped RWS moment frame. *Journal of Constructional Steel Research*. **175**, p.106319.
- Davarpanah, M., Ronagh, H., Memarzadeh, P. and Behnamfar, F. 2020b. Cyclic behaviour of elliptical-shaped reduced web section connection *In: Structures*. Elsevier, pp.955–973.
- Davison, B. and Owens, G.W. (eds.). 2012. *Steel Designers' Manual*. John Wiley & Sons.
- Degtyarev, V. V and Tsavdaridis, K.D. 2022. Buckling and ultimate load prediction models for perforated steel beams using machine learning algorithms. *Journal of Building Engineering*. **51**, p.104316.
- Díaz, C., Martí, P., Victoria, M. and Querin, O.M. 2011. Review on the modelling of joint behaviour in steel frames. *Journal of constructional steel research*. **67**(5), pp.741–758.
- Díaz, C., Victoria, M., Martí, P. and Querin, O.M. 2011. FE model of beam-to-column extended end-plate joints. *Journal of Constructional Steel Research*. **67**(10), pp.1578–1590.
- Díaz, C., Victoria, M., Querin, O.M. and Martí, P. 2018. FE model of three-dimensional steel beam-to-column bolted extended end-plate joint. *International Journal of Steel Structures*. **18**(3), pp.843–867.
- Ding, Z. and Elkady, A. 2023. Semirigid Bolted Endplate Moment Connections: Review and Experimental-Based Assessment of Available Predictive



Models. *Journal of Structural Engineering*. **149**(9), p.4023117.

- Dong, Y., Jia, L., Xu, F. and Li, X. 2021. Experimental study on seismic behavior of steel structure with cellular beams and composite concrete slab. *Structures*. **34**(January), pp.507–522.
- Du, H., Hu, X., Shi, D. and Fang, B. 2021. Effect of reinforcement on the strength of the web opening in steel-concrete composite beam. *Engineering Structures*. **235**(February), p.112038.
- Elflah, M., Theofanous, M. and Dirar, S. 2019. Behaviour of stainless steel beam-to-column joints-part 2: Numerical modelling and parametric study. *Journal of Constructional Steel Research*. **152**, pp.194–212.
- Elkady, A. and Lignos, D.G. 2014. Modeling of the composite action in fully restrained beam-to-column connections: implications in the seismic design and collapse capacity of steel special moment frames. *Earthquake Engineering & Structural Dynamics*. **43**(13), pp.1935–1954.
- EISabbagh, A., Sharaf, T., Nagy, S. and ElGhandour, M. 2019. Behavior of extended end-plate bolted connections subjected to monotonic and cyclic loads. *Engineering Structures*. **190**, pp.142–159.
- EQUALJOINTS 2017. European Pre-QUALified Steel JOINTS–EQUALJOINTS: Final Report-European Commission Research Programme of the Research Fund for Coal and Steel.
- Erfani, S. and Akrami, V. 2019. A Nonlinear Macro-model for Numerical Simulation of Perforated Steel Beams. *International Journal of Steel Structures*., pp.1–19.
- Erfani, S. and Akrami, V. 2017. Increasing Seismic Energy Dissipation of Steel Moment Frames Using Reduced Web Section (RWS) Connection. *Journal of Earthquake Engineering*. **21**(7), pp.1090–1112.
- Erfani, S., Akrami, V. and Mohammad-nejad, A. 2020. Lateral load resisting behavior of steel moment frames with reduced web section (RWS) beams *In: Structures*. Elsevier, pp.251–265.
- Fares, S., Coulson, J. and Dinehart, D. 2016. *AISC design guide 31 castellated and cellular beam design*.
- FEMA 350 2000. Recommended Seismic Design Criteria for New Steel Moment-Frame Buildings, FEMA 350. *Federal Emergency Management Agency, USA*. **13**.
- FEMA 355E 2000. State of the art report on past performance of steel moment frame buildings in earthquakes.” FEMA-355E.
- FEMA P440a 2009. *Effects of strength and stiffness degradation on seismic response* [Online]. Available from: [www.ATCCouncil.org](http://www.ATCCouncil.org).
- Ferreira, F.P.V., Shamass, R., Limbachiya, V., Tsavdaridis, K.D. and Martins, C.H. 2022. Lateral–torsional buckling resistance prediction model for steel cellular beams generated by Artificial Neural Networks (ANN). *Thin-Walled Structures*. **170**, p.108592.
- Gerami, M., Saberi, H., Saberi, V. and Daryan, A.S. 2011. Cyclic behavior of bolted connections with different arrangement of bolts. *Journal of Constructional Steel Research*. **67**(4), pp.690–705.

- Ghobarah, A., Osman, A. and Korol, R.M. 1990. Behaviour of extended end-plate connections under cyclic loading. *Engineering Structures*. **12**(1), pp.15–27.
- Gil, B., Goñi, R. and Bayo, E. 2013. Experimental and numerical validation of a new design for three-dimensional semi-rigid composite joints. *Engineering structures*. **48**, pp.55–69.
- Gioncu, V. 2000. Design criteria for seismic resistant steel structures *In: Seismic Resistant Steel Structures*. Springer, pp.19–99.
- Gioncu, V. and Mazzolani, F. 2013. *Seismic design of steel structures*. CRC Press.
- Girão Coelho, A., Coelho, G., Lawson, M., Lam, D. and Jie Yang 2020. *GUIDANCE ON DEMOUNTABLE COMPOSITE CONSTRUCTION SYSTEMS FOR UK PRACTICE*. Berkshire: SCI.
- Guo, B., Gu, Q. and Liu, F. 2006. Experimental behavior of stiffened and unstiffened end-plate connections under cyclic loading. *Journal of Structural Engineering*. **132**(9), pp.1352–1357.
- Guo, B., Wang, J.T., Liang, T. and Bao, Z. 2011. Study on seismic performance of a new type energy dissipation steel moment frames *In: Applied Mechanics and Materials*. Trans Tech Publ, pp.764–770.
- Guo, J., Shi, Q., Li, T. and Ma, G. 2023. Mechanical performance of hybrid high-strength steel composite cellular beam under low cyclic loading. *Journal of Constructional Steel Research*. **203**, p.107801.
- Hamburger, R.O. and Malley, J.O. 2009. Seismic design of steel special moment frames. *NIST GCR.*, pp.9–917.
- Hedayat, A.A. and Celikag, M. 2009. Post-Northridge connection with modified beam end configuration to enhance strength and ductility. *Journal of Constructional Steel Research*. **65**(7), pp.1413–1430.
- Hibbeler, R.C. 2017. *Mechanics of Materials*. Pearson Higher Ed.
- Ibarra, L.F., Medina, R.A. and Krawinkler, H. 2005. Hysteretic models that incorporate strength and stiffness deterioration. *Earthquake engineering & structural dynamics*. **34**(12), pp.1489–1511.
- ISO 6892-1 2009. 6892-1. Metallic materials-Tensile testing-Part 1: Method of test at room temperature. *International Organization for Standardization*.
- Jia, L., Li, Q., Bi, R. and Dong, Y. 2021. Behaviour of castellated beam-to-column end-plate connection under monotonic load. *Structures*. **34**(July), pp.4616–4633.
- Jisr, H.E.L. 2022. *The Role of the Composite Floor System and Framing Action in the Seismic Performance of Composite Steel Moment-Resisting Frames*. ÉCOLE POLYTECHNIQUE FÉDÉRALE DE LAUSANNE.
- Jones, S.L., Fry, G.T. and Engelhardt, M.D. 2002. Experimental evaluation of cyclically loaded reduced beam section moment connections. *Journal of Structural Engineering*. **128**(4), pp.441–451.
- Kerdal, D. and Nethercot, D.A. 1984. Failure modes for castellated beams. *Journal of Constructional Steel Research*. **4**(4), pp.295–315.
- Kim, S.-Y. and Lee, C.-H. 2017. Seismic retrofit of welded steel moment connections with highly composite floor slabs. *Journal of Constructional*

- Steel Research*. **139**, pp.62–68.
- Kim, Y.-J., Oh, S.-H. and Moon, T.-S. 2004. Seismic behavior and retrofit of steel moment connections considering slab effects. *Engineering structures*. **26**(13), pp.1993–2005.
- Korol, R.M., Ghobarah, A. and Osman, A. 1990. Extended end-plate connections under cyclic loading: Behaviour and design. *Journal of Constructional Steel Research*. **16**(4), pp.253–280.
- Lagaros, N.D., Psarras, L.D., Papadrakakis, M. and Panagiotou, G. 2008. Optimum design of steel structures with web openings. *Engineering Structures*. **30**(9), pp.2528–2537.
- Lam, D. and Fu, F. 2005. Modelling of semi-rigid composite beam-column connections with precast hollowcore slabs *In: Fourth International Conference on Advances in Steel Structures*. Elsevier, pp.787–792.
- Landolfo, R. 2022. European seismic prequalification of steel beam-to-column joints: EQUALJOINTS and EQUALJOINTS-Plus projects. *Journal of Constructional Steel Research*. **192**(March), p.107238.
- Landolfo, R., Mazzolani, F., Dubina, D. and Simões da Silva, L. 2010. Design of steel structures for buildings in seismic areas. *ECCS Eurocode Design Manuals*.
- Landolfo, R., Mazzolani, F.M., Dubina, D., da Silva, L.S. and D’Aniello, M. 2017. Design of Steel Structures for Buildings in Seismic Areas: Eurocode 8: Design of Steel Structures in Seismic Areas. General Rules and Rules for Buildings *In: ECCS*.
- Lawson, R.M. and Hicks, S.J. 2011. *Design of composite beams with large web openings*.
- Lee, C.-H., Jung, J.H., Kim, S.Y. and Kim, J.J. 2016. Investigation of Composite Slab Effect on Seismic Performance of Steel Moment Connections. *Journal of Constructional Steel Research*. **117**, pp.91–100.
- Li, B., Yang, Q. and Yang, N. 2011. An investigation on aseismic connection with opening in beam web in steel moment frames. *Advances in Structural Engineering*. **14**(3), pp.575–587.
- Lignos, D.G., Hikino, T., Matsuoka, Y. and Nakashima, M. 2013. Collapse assessment of steel moment frames based on E-Defense full-scale shake table collapse tests. *Journal of Structural Engineering*. **139**(1), pp.120–132.
- Lignos, D.G. and Krawinkler, H. 2011. Deterioration modeling of steel components in support of collapse prediction of steel moment frames under earthquake loading. *Journal of Structural Engineering*. **137**(11), pp.1291–1302.
- Lim, C., Choi, W. and Sumner, E.A. 2012. Low cycle fatigue life prediction using a four-bolt extended unstiffened end plate moment connection. *Engineering structures*. **41**, pp.373–384.
- Lin, S., Qiao, H., Wang, J., Shi, J. and Chen, Y. 2021. Anti-collapse performance of steel frames with RWS connections under a column removal scenario. *Engineering Structures*. **227**, p.111495.
- Lin, S., Xue, X., Qiao, H. and Chen, Y. 2022. Prediction model for catenary action of welded RWS connections using PVM link element. *Journal of*

- Constructional Steel Research*. **191**, p.107207.
- Liu, T.C.H. and Chung, K.F. 2003. Steel beams with large web openings of various shapes and sizes: finite element investigation. *Journal of Constructional Steel Research*. **59**(9), pp.1159–1176.
- Liu, X., Bradford, M.A. and Ataei, A. 2017. Flexural performance of innovative sustainable composite steel-concrete beams. *Engineering Structures*. **130**, pp.282–296.
- Liu, X., Bradford, M.A., Chen, Q.J. and Ban, H. 2016. Finite element modelling of steel-concrete composite beams with high-strength friction-grip bolt shear connectors. *Finite Elements in Analysis and Design*. **108**, pp.54–65.
- Mashaly, E., El-Heweity, M., Abou-Elfath, H. and Osman, M. 2011. Behavior of four-bolt extended end-plate connection subjected to lateral loading. *Alexandria Engineering Journal*. **50**(1), pp.79–90.
- Momenzadeh, S., Kazemi, M.T. and Asl, M.H. 2017. Seismic performance of reduced web section moment connections. *International Journal of Steel Structures*. **17**(2), pp.413–425.
- Morrison, M., Quayyum, S. and Hassan, T. 2017. Performance enhancement of eight bolt extended end-plate moment connections under simulated seismic loading. *Engineering Structures*. **151**, pp.444–458.
- Mou, B., Li, X., Bai, Y. and Wang, L. 2019. Shear behavior of panel zones in steel beam-to-column connections with unequal depth of outer annular stiffener. *Journal of Structural Engineering*. **145**(2), p.4018247.
- Moynihan, M.C. and Allwood, J.M. 2014. Viability and performance of demountable composite connectors. *Journal of Constructional Steel Research*. **99**, pp.47–56.
- Naughton, D.T., Tsavdaridis, K.D., Maraveas, C. and Nicolaou, A. 2017. Pushover analysis of steel seismic resistant frames with reduced web section and reduced beam section connections. *Frontiers in Built Environment*. **3**, p.59.
- Nazaralizadeh, H., Ronagh, H., Memarzadeh, P. and Behnamfar, F. 2020. Cyclic performance of bolted end-plate RWS connection with vertical-slits. *Journal of Constructional Steel Research*. **173**, p.106236.
- NZS3404:1 1997. 'Standards New Zealand, steel structures standard, Part 1.
- Özkılıç, Y.O. 2023. Cyclic and monotonic performance of unstiffened extended end-plate connections having thin end-plates and large-bolts. *Engineering Structures*. **281**, p.115794.
- Parastesh, H., Hajirasouliha, I. and Ramezani, R. 2014. A new ductile moment-resisting connection for precast concrete frames in seismic regions: An experimental investigation. *Engineering Structures*. **70**, pp.144–157.
- PATRICK, M. 2001. *Design of simply-supported composite beams with large web penetrations*.
- Qiao, H., Guo, Z. and Chen, Y. 2022. Experimental investigation of a substructure in a frame with castellated steel beams in case of a column loss. *Engineering Structures*. **255**, p.113926.
- Qiao, H., Xie, X. and Chen, Y. 2022. Improvement of progressive collapse

- resistance for a steel frame system with beam–web opening. *Engineering Structures*. **256**, p.113995.
- Qureshi, J., Lam, D. and Ye, J. 2010. Finite element modelling of shear connection behaviour in a push test using profiled sheeting. *Advances and Trends in Structural Engineering, Mechanics and Computation.*, p.167.
- Roeder, C.W. 2002. Connection performance for seismic design of steel moment frames. *Journal of Structural Engineering*. **128**(4), pp.517–525.
- Sencu, R.M., Wang, Y.C., Yang, J. and Lam, D. 2019. Performance evaluation of demountable shear connectors with collar step at ambient and elevated temperatures. *Engineering Structures*. **194**(December 2018), pp.94–105.
- Shaheen, M.A. 2022. A new idea to improve the cyclic performance of end plate beam–column connections. *Engineering Structures*. **253**, p.113759.
- Shaheen, M.A., Tsavdaridis, K.D. and Yamada, S. 2018. Comprehensive FE Study of the Hysteretic Behaviour of Steel-Concrete Composite and Non-Composite RWS Beam-to-Column Connections. *Journal of Structural Engineering*.
- Shin, M., Kim, S.-P., Halterman, A. and Aschheim, M. 2017a. Seismic toughness and failure mechanisms of reduced web-section beams: Phase 1 tests. *Engineering Structures*. **141**, pp.198–216.
- Shin, M., Kim, S.-P., Halterman, A. and Aschheim, M. 2017b. Seismic toughness and failure mechanisms of reduced web-section beams: Phase 2 tests. *Engineering Structures*. **141**, pp.607–623.
- Sofias, C.E., Kalfas, C.N. and Pachoumis, D.T. 2014. Experimental and FEM analysis of reduced beam section moment endplate connections under cyclic loading. *Engineering Structures*. **59**, pp.320–329.
- Sumner, E.A. 2003. *Unified design of extended end-plate moment connections subject to cyclic loading*. Virginia Tech.
- Sumner, E.A., Mays, T.W. and Murray, T.M. 2000a. *Cyclic testing of bolted moment end-plate connections*. Research report SAC/BD-00/21. CE/VPI-ST 00/03. Department of Civil and Environmental Engineering, Virginia Polytechnic ....
- Sumner, E.A., Mays, T.W. and Murray, T.M. 2000b. End-plate moment connections: test results and finite element method validation *In: Connections in Steel Structures IV: Steel Connections in the New Millennium: Proceedings of the Fourth International Workshop*. Citeseer, pp.22–25.
- Sumner, E.A. and Murray, T.M. 2002. Behavior of extended end-plate moment connections subject to cyclic loading. *Journal of Structural Engineering*. **128**(4), pp.501–508.
- Tabar, A.M., Alonso-Rodriguez, A. and Daniel Tsavdaridis, K. 2022. Building Retrofit with Reduced Web (RWS) and Beam (RBS) Section Limited-Ductility Connections. *Journal of Constructional Steel Research*.
- Tartaglia, R., D’Aniello, M. and Landolfo, R. 2018. The influence of rib stiffeners on the response of extended end-plate joints. *Journal of Constructional Steel Research*. **148**, pp.669–690.
- Tartaglia, R., D’Aniello, M. and Rassati, G.A. 2019. Proposal of AISC-compliant

- seismic design criteria for ductile partially-restrained end-plate bolted joints. *Journal of Constructional Steel Research*. **159**, pp.364–383.
- Tartaglia, R., D’Aniello, M., Rassati, G.A., Swanson, J.A. and Landolfo, R. 2018. Full strength extended stiffened end-plate joints: AISC vs recent European design criteria. *Engineering Structures*. **159**, pp.155–171.
- Tartaglia, R., D’Aniello, M., Zimbru, M. and Landolfo, R. 2018. Finite element simulations on the ultimate response of extended stiffened end-plate joints. *Steel and Composite Structures, An International Journal*. **27**(6), pp.727–745.
- Terracciano, G., Della Corte, G., Di Lorenzo, G. and Landolfo, R. 2018. Design tools for bolted end-plate beam-to-column joints. *Journal of Engineering*. **2018**.
- Tsavdaridis, K.D. and D’Mello, C. 2009. FE investigation of perforated sections with standard and non-standard web opening configurations and sizes *In: 6th International Conference on Advances in Steel Structures*. Hong Kong, China: Hong Kong Institute of Steel Construction.
- Tsavdaridis, K.D. and D’Mello, C. 2012. Vierendeel bending study of perforated steel beams with various novel web opening shapes through nonlinear finite-element analyses. *Journal of Structural Engineering*. **138**(10), pp.1214–1230.
- Tsavdaridis, K.D. and D’Mello, C. 2011. Web buckling study of the behaviour and strength of perforated steel beams with different novel web opening shapes. *Journal of Constructional Steel Research*. **67**(10), pp.1605–1620.
- Tsavdaridis, K.D., Faghih, F. and Nikitas, N. 2014. Assessment of perforated steel beam-to-column connections subjected to cyclic loading. *Journal of Earthquake Engineering*. **18**(8), pp.1302–1325.
- Tsavdaridis, K.D., Lau, C.K. and Alonso-Rodríguez, A. 2021. Experimental behaviour of non-seismical RWS connections with perforated beams under cyclic actions. *Journal of Constructional Steel Research*. **183**, p.106756.
- Tsavdaridis, K.D. and Papadopoulos, T. 2016. A FE parametric study of RWS beam-to-column bolted connections with cellular beams. *Journal of Constructional Steel Research*. **116**, pp.92–113.
- Tsavdaridis, K.D., Pilbin, C. and Lau, C.K. 2017. FE parametric study of RWS/WUF-B moment connections with elliptically-based beam web openings under monotonic and cyclic loading. *International Journal of Steel Structures*. **17**(2), pp.677–694.
- Uang, C.-M., Yu, Q.-S. “Kent”, Noel, S. and Gross, J. 2000. Cyclic testing of steel moment connections rehabilitated with RBS or welded haunch. *Journal of Structural Engineering*. **126**(1), pp.57–68.
- Vasdravellis, G., Valente, M. and Castiglioni, C.A. 2009. Behavior of exterior partial-strength composite beam-to-column connections: Experimental study and numerical simulations. *Journal of Constructional Steel Research*. **65**(1), pp.23–35.
- Wang, A.J. 2010. Numerical studies on the structural behaviour of composite end-plate connections. *Canadian Journal of Civil Engineering*. **37**(6), pp.907–921.

- Wang, J., Uy, B., Thai, H.-T. and Li, D. 2018. Behaviour and design of demountable beam-to-column composite bolted joints with extended end-plates. *Journal of Constructional Steel Research*. **144**, pp.221–235.
- Xu, Q., Chen, H., Li, W., Zheng, S. and Zhang, X. 2022. Experimental investigation on seismic behavior of steel welded connections considering the influence of structural forms. *Engineering Failure Analysis*. **139**, p.106499.
- Yang, F., Liu, Y., Jiang, Z. and Xin, H. 2018. Shear performance of a novel demountable steel-concrete bolted connector under static push-out tests. *Engineering Structures*. **160**(January), pp.133–146.
- Yang, Q., Li, B. and Yang, N. 2009. Aseismic behaviors of steel moment resisting frames with opening in beam web. *Journal of Constructional Steel Research*. **65**(6), pp.1323–1336.
- Zeytinci, B.M., Şahin, M., Güler, M.A. and Tsavdaridis, K.D. 2021. A practical design formulation for perforated beams with openings strengthened with ring type stiffeners subject to Vierendeel actions. *Journal of Building Engineering*. **43**(June).
- Zhang, X. and Ricles, J.M. 2006a. Experimental evaluation of reduced beam section connections to deep columns. *Journal of Structural Engineering*. **132**(3), pp.346–357.
- Zhang, X. and Ricles, J.M. 2006b. Seismic behavior of reduced beam section moment connections to deep columns. *Journal of structural engineering*. **132**(3), pp.358–367.
- Zhang, X., Ricles, J.M., Lu, L.-W. and Fisher, J.W. 2004. Development of seismic guidelines for deep-column steel moment connections.
- Zhang, X., Zheng, S. and Zhao, X. 2019. Seismic performance of steel beam-to-column moment connections with different structural forms. *Journal of Constructional Steel Research*. **158**, pp.130–142.

**Appendix A: Summary of Studies on RWS connections**



**Table A 2: Summary of Studies on RWS connections**

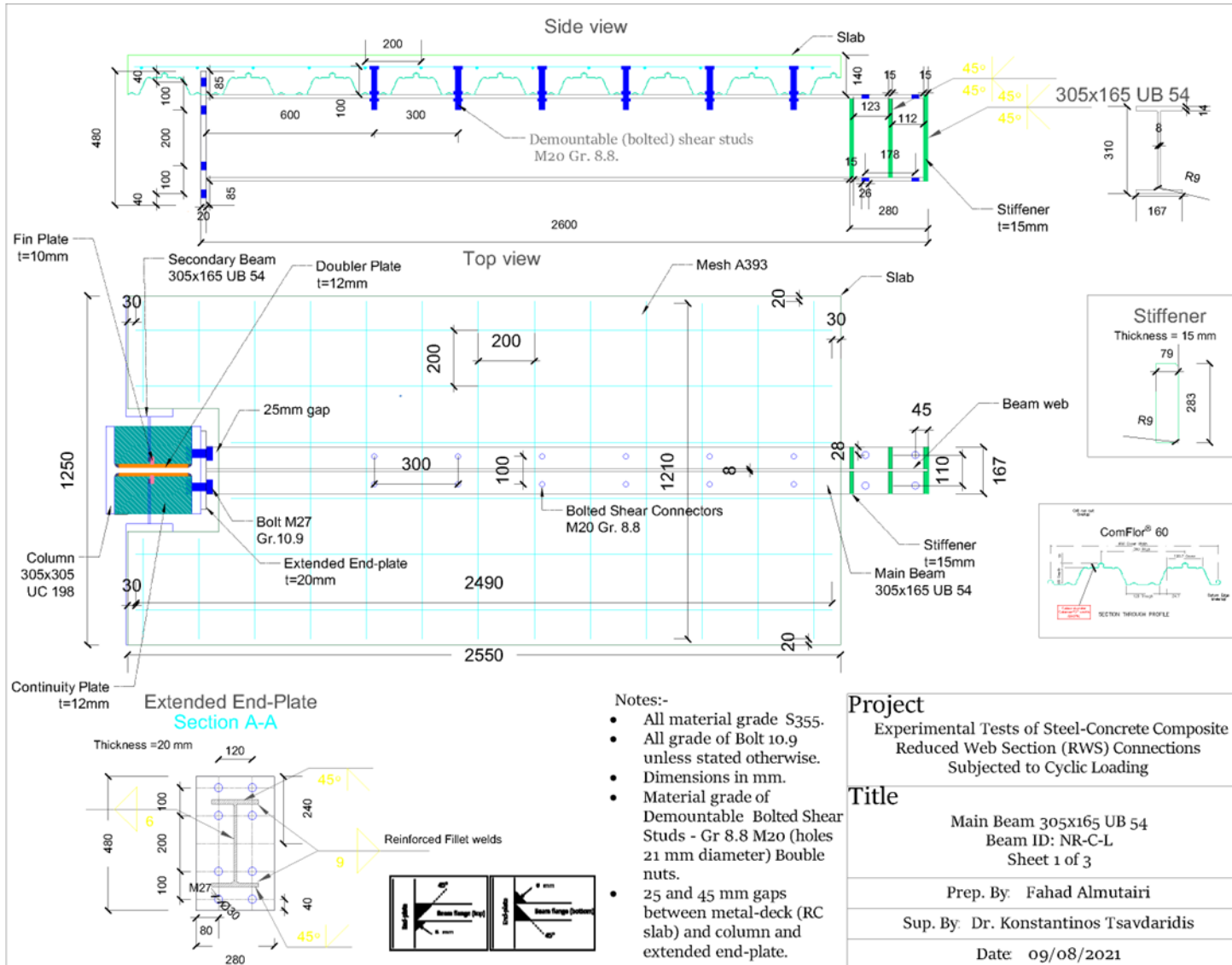
SN	Reference	Type of study	Total number of specimens	Joint configuration	Loading	Type of connection	Shape of a web opening	No. of a web opening	Composite slab	Axial force
1	(Guo et al., 2011)	FE	16	Frame	M/C	Welded	Circular	Single	No	No
2	(Li et al., 2011)	Exp.	3	Cantilever	C	Welded	Circular	Single	No	No
3	(Tsavdaridis et al., 2014)	FE	27	Cantilever	C	Welded	Circular, wide and narrow elliptical	Single	No	No
4	(Tsavdaridis and Papadopoulos, 2016)	FE	11	Cantilever	C	Bolted extended end-plate 3 rows	Circular	Single and multiple	No	No
5	(Shin et al., 2017a)	Exp.	5	Frame	C	WUF-B	Circular and other shapes	Single and multiple	No	No
6	(Shin et al., 2017b)	Exp.	5	Frame	C	WUF-B	Circular and other shapes	Single and multiple	No	No
7	(Tsavdaridis et al., 2017)	FE	54	Cantilever	M/C	WUF-B	Circular, wide and narrow elliptical	Single	No	No

SN	Reference	Type of study	Total number of specimens	Joint configuration	Loading	Type of connection	Shape of a web opening	No. of a web opening	Composite slab	Axial force
8	(Erfani and Akrami, 2017)	FE	12	Cantilever	C	Welded	Circular	Single	No	No
9	(Shaheen et al., 2018)	FE	24	Cantilever	C	Pre-Northridge	Circular	Single	Yes	No
10	(Zhang et al., 2019)	Exp. and FE	4	Cantilever	C	Welded	Circular	Single	No	Yes
11	(Boushehri et al., 2019)	FE	144	Cantilever	C	Welded	Circular	Single	No	No
12	(Nazaralizadeh et al., 2020)	Exp. and FE	14	Cantilever	C	Bolted extended end-plate 4 rows	Circular and other shapes	Single and multiple	No	No
13	(Davaranpanah et al., 2020a)	Exp. and FE	5	Cantilever	C	Welded	Elliptical	Single	No	No
14	(Davaranpanah et al., 2020b)	Exp. and FE	15	Cantilever	C	Welded	Elliptical	Single	No	No
15	(Jia et al., 2021)	Exp. and FE	226	Cantilever	M	Bolted extended end-plate 5 rows	Castellated	Multiple	No	No

SN	Reference	Type of study	Total number of specimens	Joint configuration	Loading	Type of connection	Shape of a web opening	No. of a web opening	Composite slab	Axial force
16	(Bi et al., 2021)	Exp. and FE	40	Cantilever	C	Welded	Castellated	Multiple	Yes	No
17	(Tsavdaridis et al., 2021)	Exp.	3	Cantilever	C	Bolted extended end-plate 3 rows	Circular	Single and multiple	No	No
18	(Xu et al., 2022)	Exp.	5	Cantilever	C	Welded	Circular	Single	No	No
19	(Guo et al., 2023)	Exp. and FE	5	Cantilever	C	Welded	Circular	Multiple	Yes	No

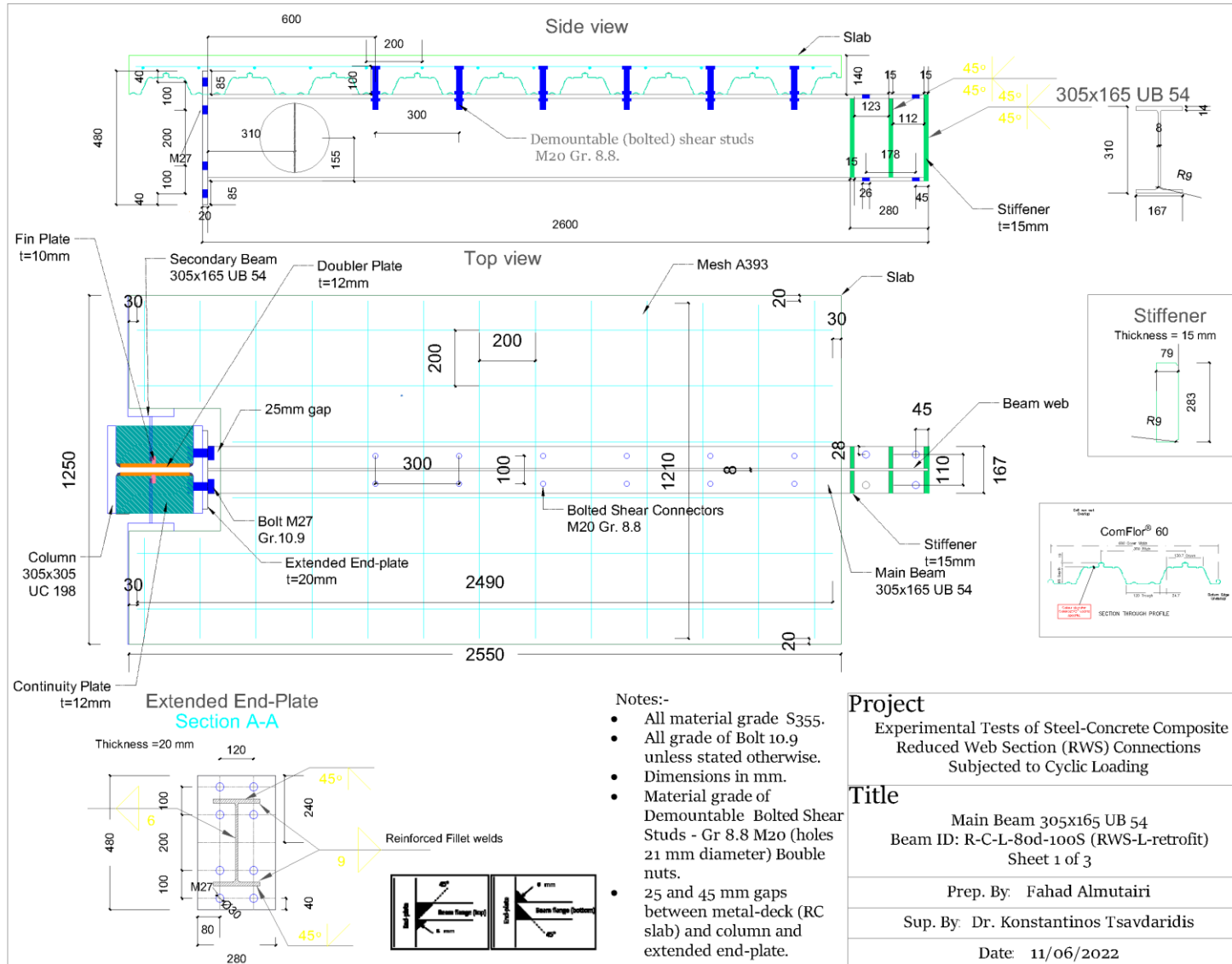
Note: SN = Serial number of the study. FE = Finite element. Exp.= experimental tests. M = monotonic. C = cyclic. WUF-B = Welded Unreinforced Flange-Bolted Web.

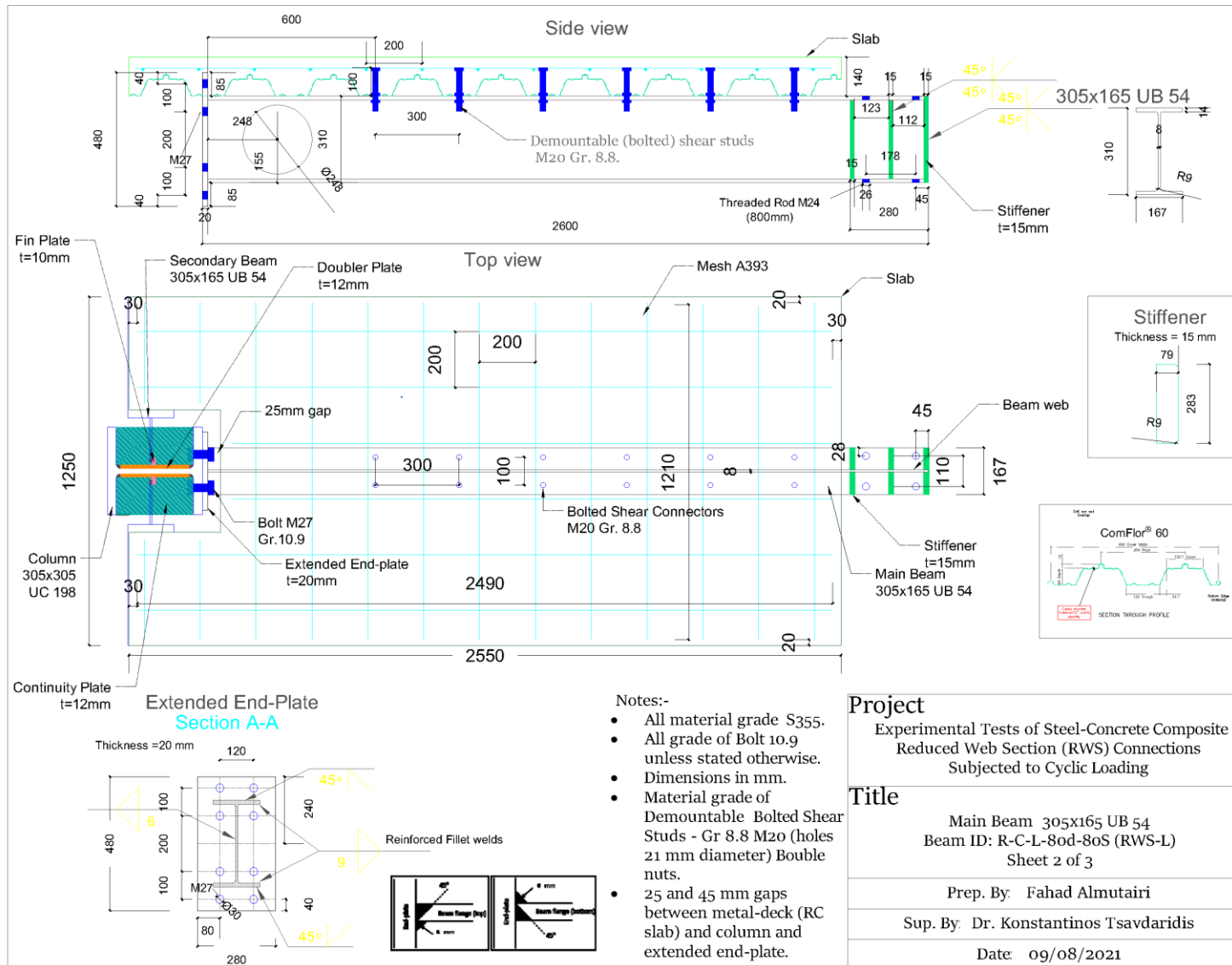
## **Appendix B: Drawings**

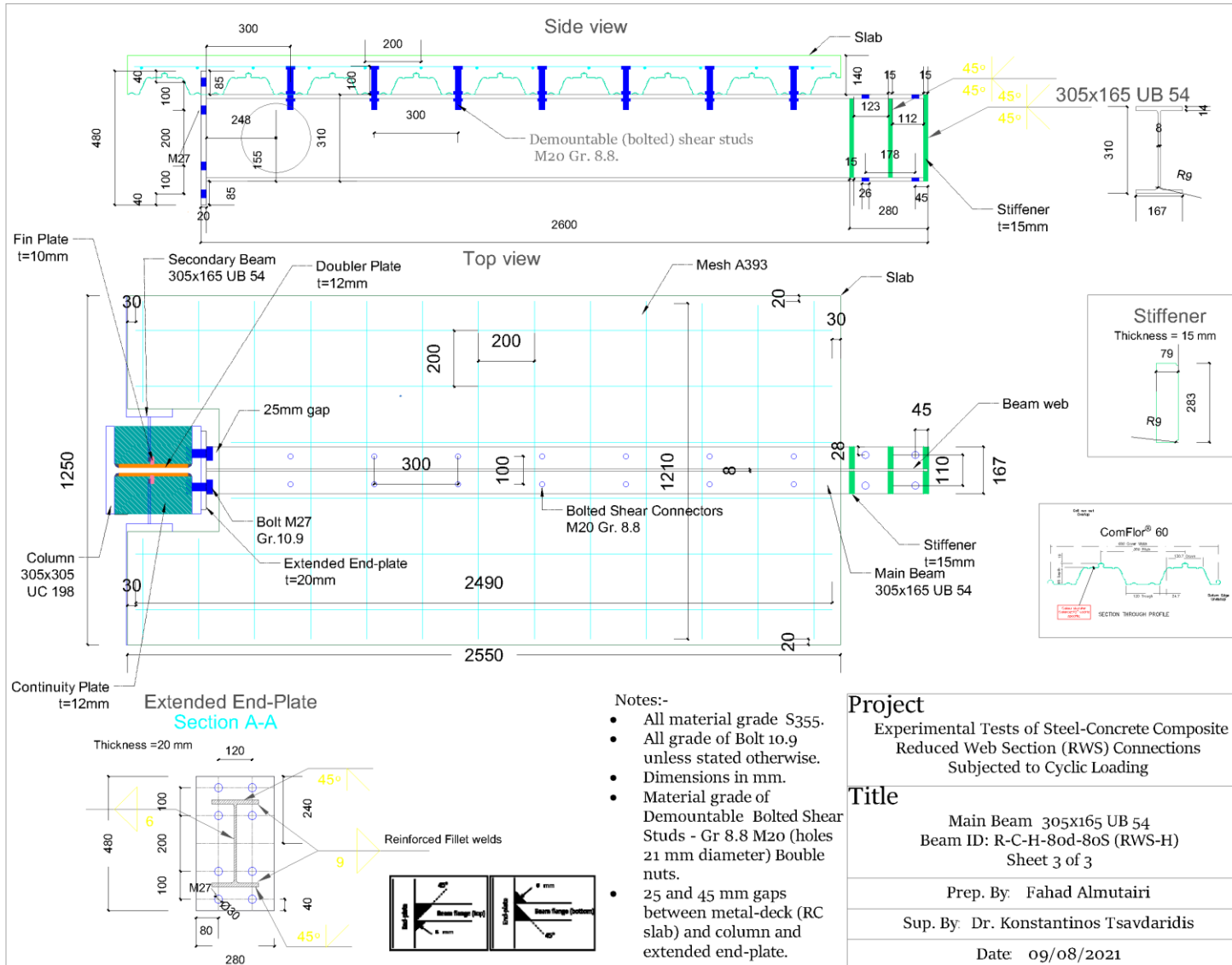


- Notes:-
- All material grade S355.
  - All grade of Bolt 10.9 unless stated otherwise.
  - Dimensions in mm.
  - Material grade of Demountable Bolted Shear Studs - Gr 8.8 M20 (holes 21 mm diameter) Bouble nuts.
  - 25 and 45 mm gaps between metal-deck (RC slab) and column and extended end-plate.

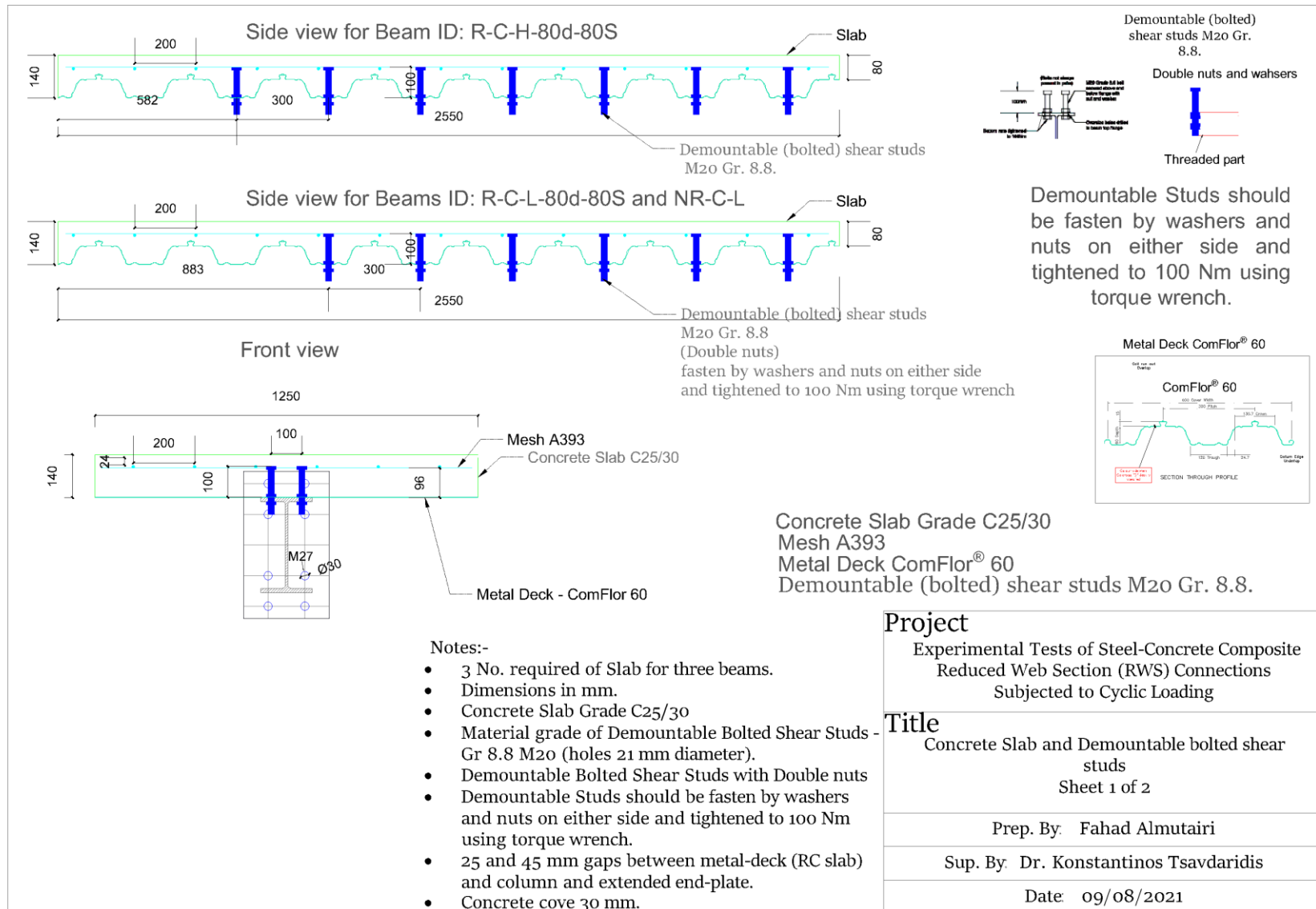
<b>Project</b>	Experimental Tests of Steel-Concrete Composite Reduced Web Section (RWS) Connections Subjected to Cyclic Loading
<b>Title</b>	Main Beam 305x165 UB 54 Beam ID: NR-C-L Sheet 1 of 3
	Prep. By: Fahad Almutairi
	Sup. By: Dr. Konstantinos Tsavdaridis
	Date: 09/08/2021

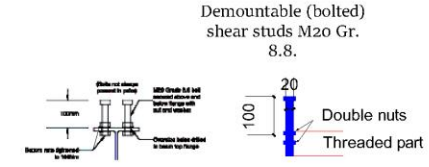
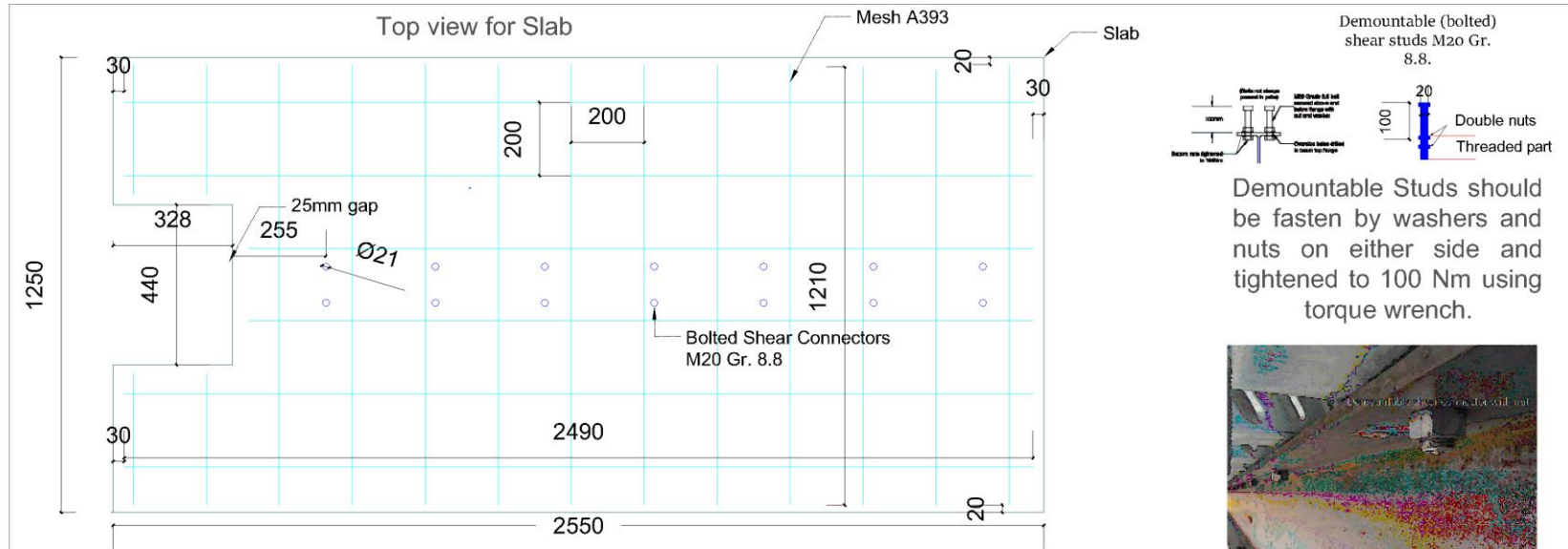




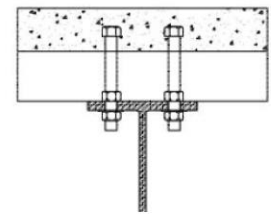
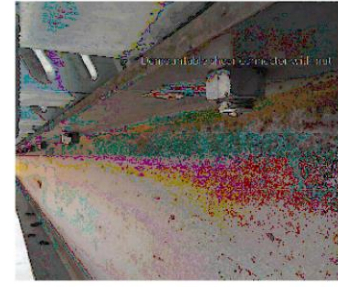








Demountable (bolted) shear studs M20 Gr. 8.8.  
 Demountable Studs should be fasten by washers and nuts on either side and tightened to 100 Nm using torque wrench.

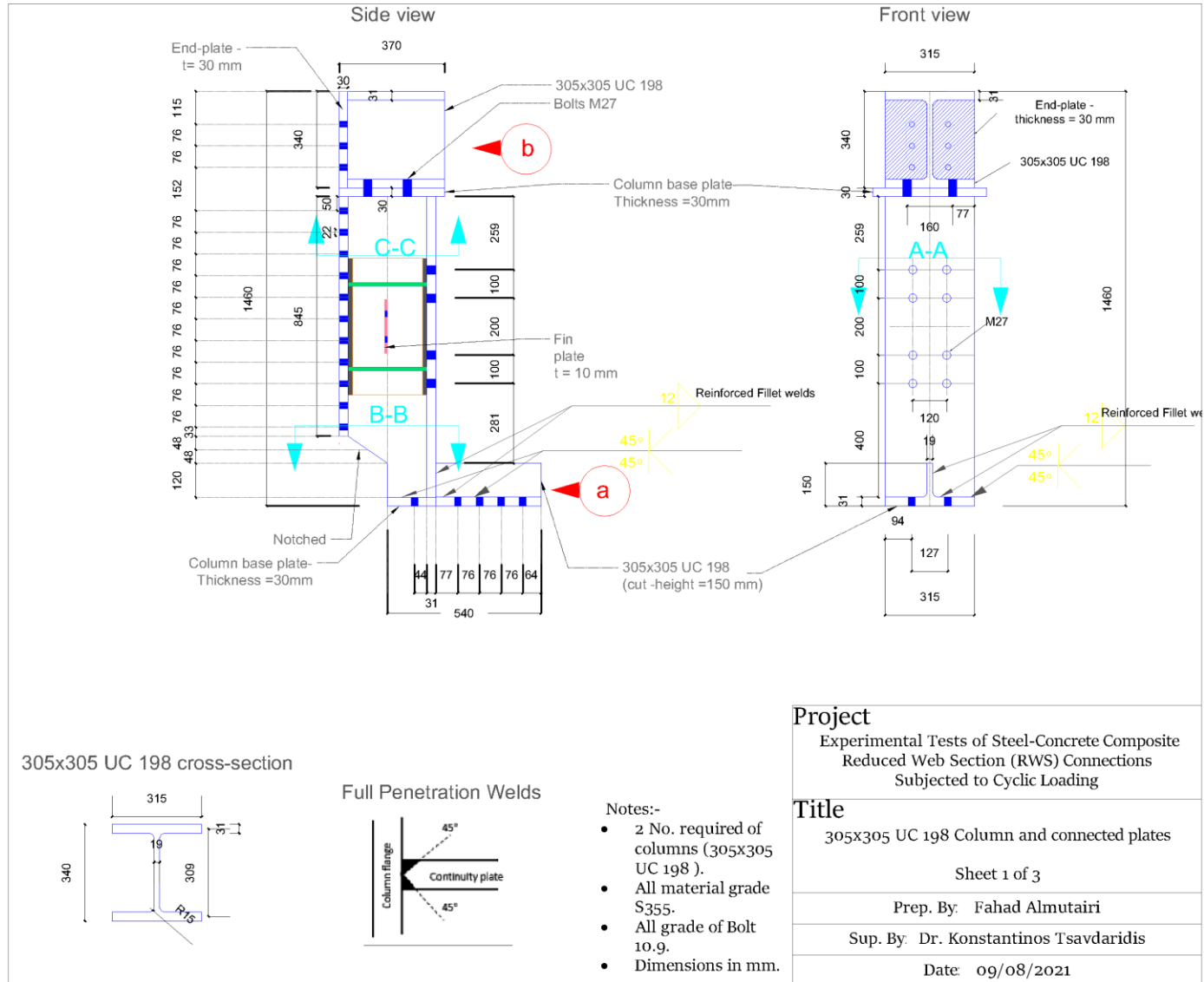


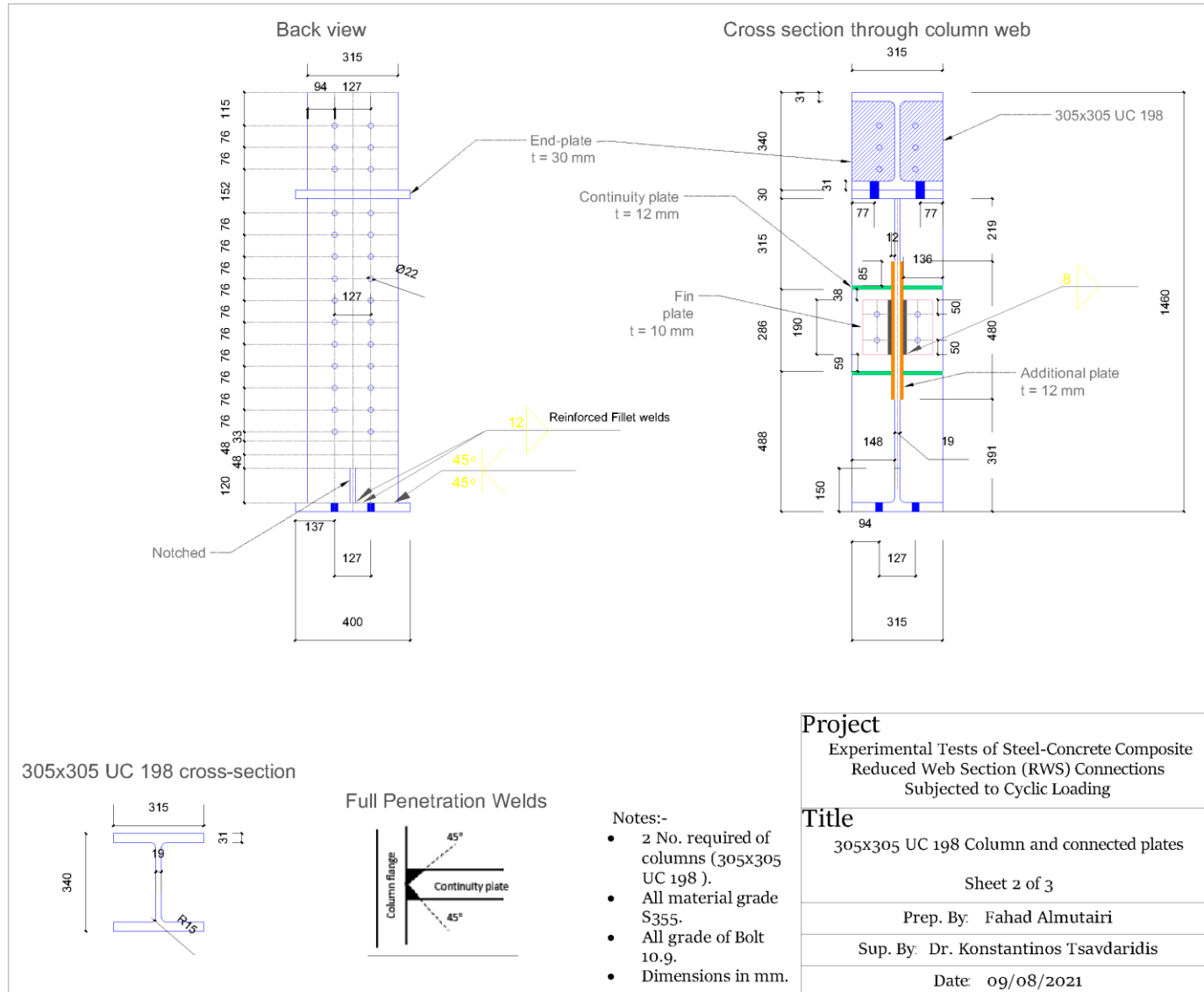
Concrete Slab Grade C25/30  
 Mesh A393  
 Metal Deck ComFlor® 60  
 Demountable (bolted) shear studs M20 Gr. 8.8.

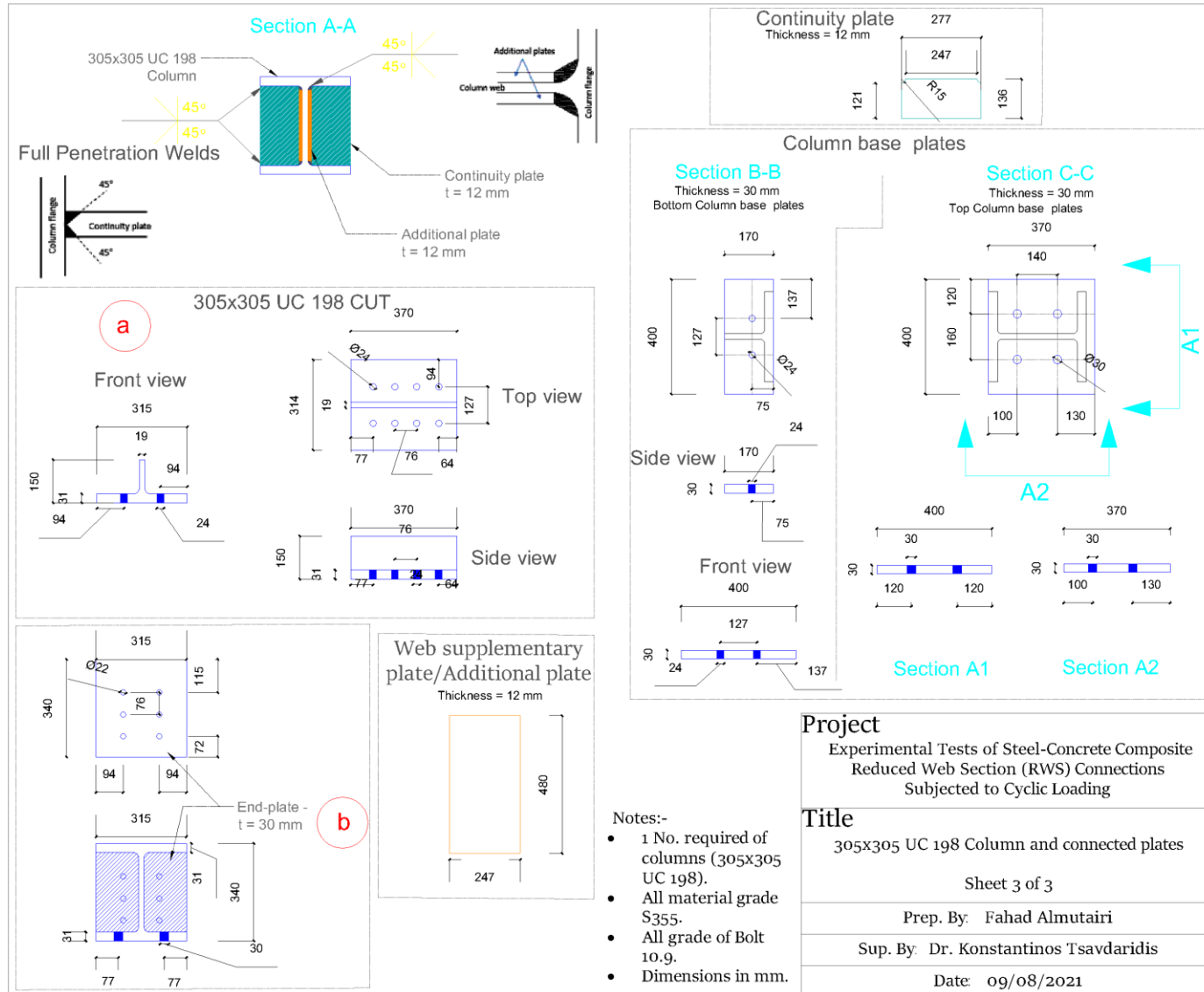


- Notes:-
- 3 No. required of Slab for three beams.
  - Dimensions in mm.
  - Concrete Slab Grade C25/30
  - Material grade of Demountable Bolted Shear Studs Gr 8.8 M20 (holes 21 mm diameter).
  - Demountable Bolted Shear Studs with Double nuts
  - Demountable Studs should be fasten by washers and nuts on either side and tightened to 100 Nm using torque wrench.
  - 25 and 45 mm gaps between metal-deck (RC slab) and column and extended end-plate.
  - Concrete cove 30 mm.

<b>Project</b>
Experimental Tests of Steel-Concrete Composite Reduced Web Section (RWS) Connections Subjected to Cyclic Loading
<b>Title</b>
Concrete Slab and Demountable bolted shear studs Sheet 2 of 2
Prep. By: Fahad Almutairi
Sup. By: Dr. Konstantinos Tsavdaridis
Date: 09/08/2021







**Project**  
 Experimental Tests of Steel-Concrete Composite  
 Reduced Web Section (RWS) Connections  
 Subjected to Cyclic Loading

**Title**  
 305x305 UC 198 Column and connected plates

Sheet 3 of 3

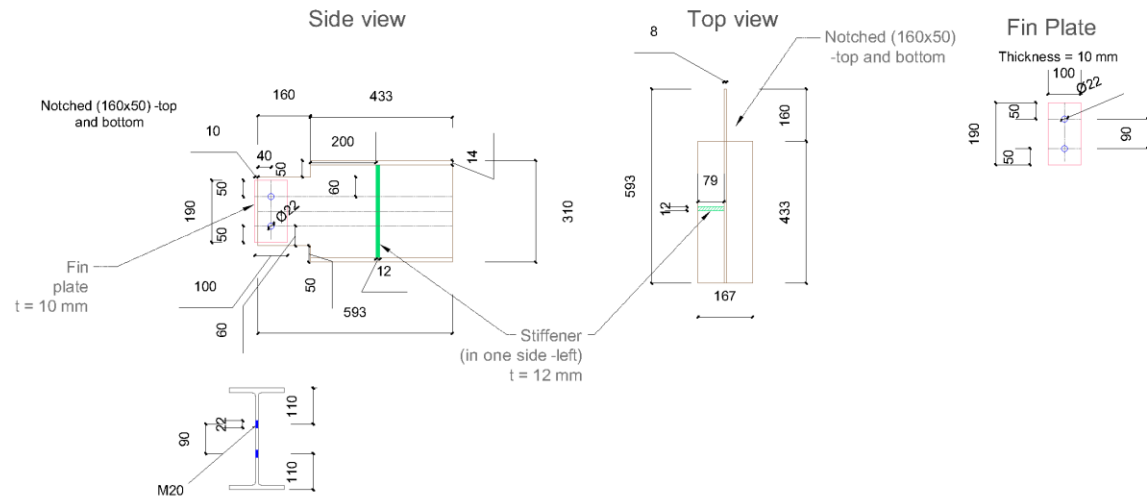
Prep. By: Fahad Almutairi

Sup. By: Dr. Konstantinos Tsavdaridis

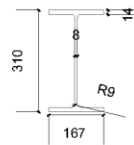
Date: 09/08/2021

- Notes:-
- 1 No. required of columns (305x305 UC 198).
  - All material grade S355.
  - All grade of Bolt 10.9.
  - Dimensions in mm.

Secondary beam 305x165 UB 54



Secondary beam 305x165 UB 54



Notes:-

- 2 No. required of Sec. Beam (305x165 UB 54).
- All material grade S355.
- All grade of Bolt 10.9.
- Dimensions in mm.

Project

Experimental Tests of Steel-Concrete Composite Reduced Web Section (RWS) Connections Subjected to Cyclic Loading

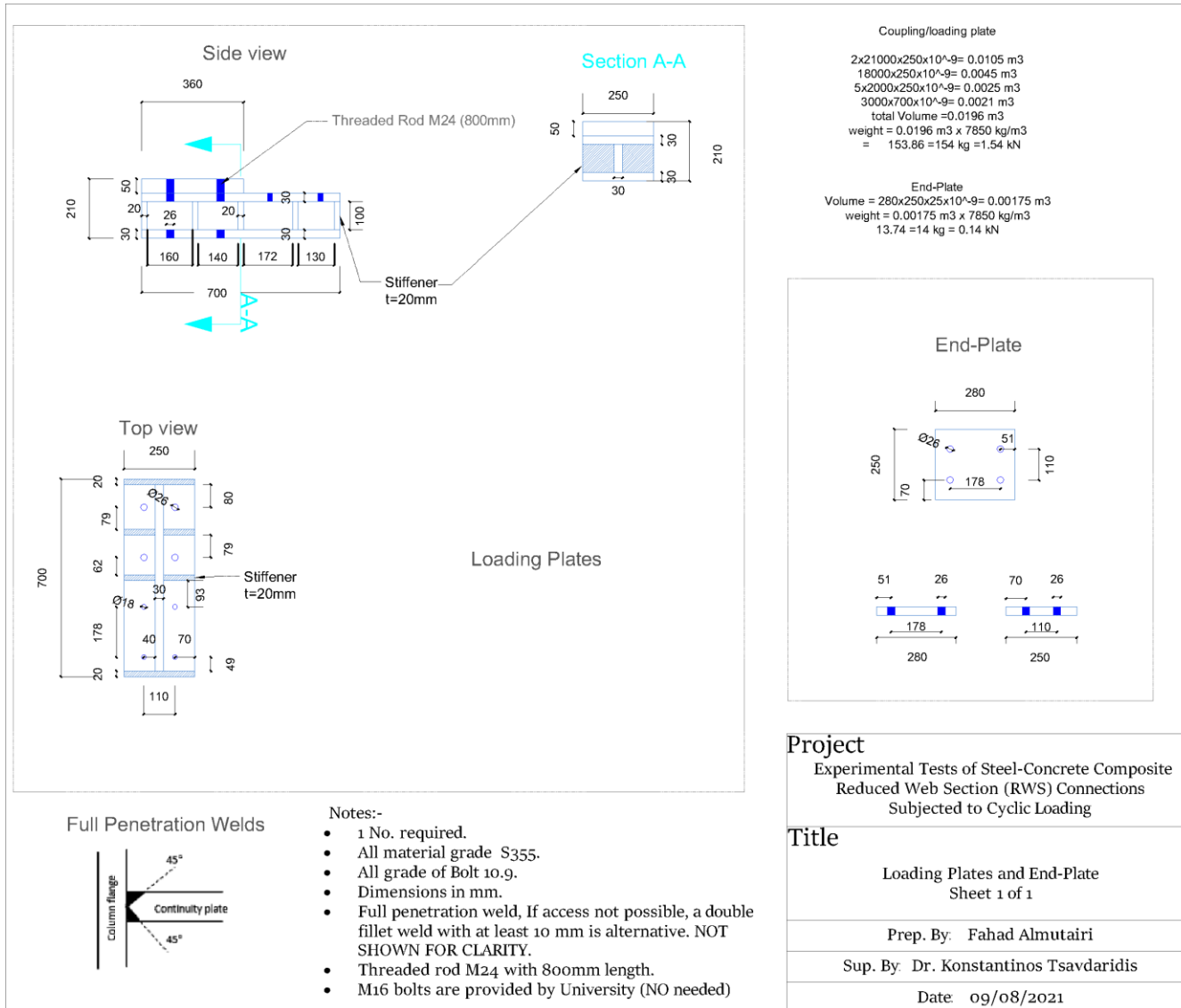
Title

Secondary Beam 305x165 UB 54  
Sheet 1 of 1

Prep. By: Fahad Almutairi

Sup. By: Dr. Konstantinos Tsavdaridis

Date: 09/08/2021



# Appendix C: Design of Extended End-Plate Connection

Project:  
Client:

1 / 15  
7/20/2021

## Design of joints

### 1 General

Project name  
Project number  
Comment

Client name  
Client address

Company  
Company address  
Designer

Calculation in accordance with CEN EN 1993-1-8

Note: In the following calculations references to the Eurocodes are given. If the relevant part of Eurocode is not specified reference is made to EN 1993-1-8.

#### 1.1 Safety factors

Safety factor	$\gamma_{M0}$	=	1
Safety factor	$\gamma_{M1}$	=	1
Safety factor	$\gamma_{M2}$	=	1.25
Safety factor	$\gamma_{M5}$	=	1
Safety factor	$\gamma_s$	=	1.15
Safety factor	$\gamma_c$	=	1.5

### 2 Joint configuration

Name:	Single sided beam-to-column joint configuration (1)
Comment:	
Configuration:	Single sided beam-to-column joint configuration
Connection type:	End plate connection (moment resistant)
Position number:	
Position name:	
Braced structure:	No
Ratio $K_b/K_c$ greater or equal 0.1:	Yes
Global design procedure:	Plastic



## 2.1 Joint 1

### 2.1.1 Joint geometry

#### 2.1.1.1 Supporting member profile

Name	UC 305 x 305 x 198, S355
Section height	$h = 339.9 \text{ mm}$
Section width	$b = 314.5 \text{ mm}$
Flange thickness	$t_f = 31.4 \text{ mm}$
Web thickness	$t_w = 19.1 \text{ mm}$
Radius	$r = 15.2 \text{ mm}$
Yield strength of flange	$f_{y,f} = 355 \text{ N/mm}^2$
Ultimate strength of flange	$f_{u,f} = 490 \text{ N/mm}^2$
Yield strength of web	$f_{y,w} = 355 \text{ N/mm}^2$
Ultimate strength of web	$f_{u,w} = 490 \text{ N/mm}^2$
Web height	$d = 246.7 \text{ mm}$
Profile area	$A = 2.524 \cdot 10^4 \text{ mm}^2$
Profile shear area	$A_{vz} = 7045 \text{ mm}^2$

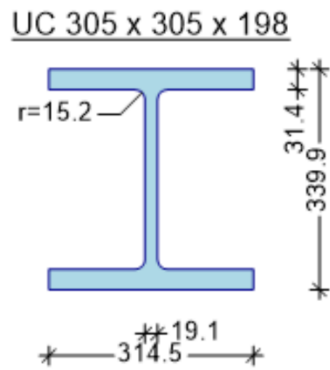


Figure 1: Supporting member profile

#### 2.1.1.2 Web plates

Web plate thickness	$t_{wp} = 12 \text{ mm}$
Web plate is placed two sided	

#### 2.1.1.3 Stiffeners

Top stiffener	Yes
Bottom stiffener	Yes
Diagonal stiffener	No
Stiffener thickness	$t_s = 12 \text{ mm}$
Stiffener width	$b_s = 135.7 \text{ mm}$

Project:  
Client:

3 / 15  
7/20/2021

Stiffener flange weld	$a_f$	= 12 mm
Stiffener web weld	$a_w$	= 12 mm
Stiffener yield stress	$f_{y,st}$	= 355 N/mm <sup>2</sup>
Stiffener ultimate strength	$f_{u,st}$	= 490 N/mm <sup>2</sup>

#### 2.1.1.4 Beam profile

Name	UB 305 x 165 x 54, S355
Section height	$h$ = 310.4 mm
Section width	$b$ = 166.9 mm
Flange thickness	$t_f$ = 13.7 mm
Web thickness	$t_w$ = 7.9 mm
Radius	$r$ = 8.9 mm
Yield strength of flange	$f_{y,f}$ = 355 N/mm <sup>2</sup>
Ultimate strength of flange	$f_{u,f}$ = 490 N/mm <sup>2</sup>
Yield strength of web	$f_{y,w}$ = 355 N/mm <sup>2</sup>
Ultimate strength of web	$f_{u,w}$ = 490 N/mm <sup>2</sup>
Web height	$d$ = 265.2 mm
Profile area	$A$ = 6877 mm <sup>2</sup>
Profile shear area	$A_{vz}$ = 2656 mm <sup>2</sup>
Beam inclination	$\alpha$ = 0°

#### UB 305 x 165 x 54

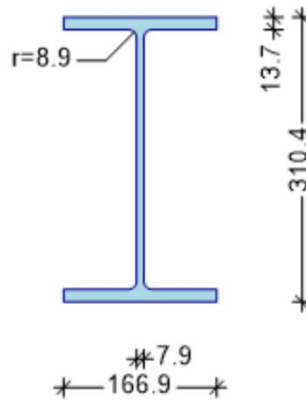


Figure 2: Beam profile

#### 2.1.1.5 End plate

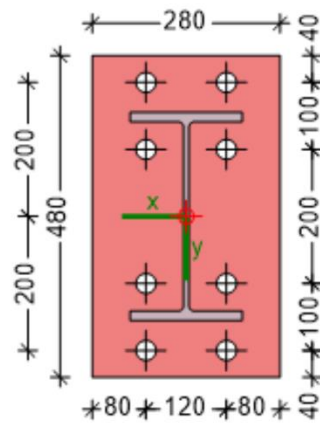
End plate height	$h$	= 480 mm
End plate width	$b$	= 280 mm
End plate thickness	$t_{cp}$	= 20 mm
Yield stress of end plate	$f_y$	= 355 N/mm <sup>2</sup>

**2.1.1.6 Bolt pattern****2.1.1.6.1 Bolt properties**

Caption	M27, 10.9
Diameter	$d = 27 \text{ mm}$
Hole diameter	$d_b = 30 \text{ mm}$
Shank area	$A_s = 459 \text{ mm}^2$
Bolt head height	$k_b = 17 \text{ mm}$
Nut height	$m_n = 23.8 \text{ mm}$
Washer thickness	$h_w = 5 \text{ mm}$
Yield strength	$f_{y0} = 900 \text{ N/mm}^2$
Ultimate strength	$f_{ub} = 1000 \text{ N/mm}^2$

**2.1.1.6.2 Bolt positions**

No. of rows	$n_1 = 4$
Pitch between bolt rows	$p_{11} = 100 \text{ mm}$
Pitch between bolt rows	$p_{12} = 200 \text{ mm}$
Pitch between bolt rows	$p_{13} = 100 \text{ mm}$
No. of columns	$n_2 = 2$
Pitch between bolt columns	$p_{21} = 120 \text{ mm}$

*Figure 3: End plate***2.1.1.7 Welds**

Flange weld size	$a_f = 9 \text{ mm}$
Web weld size	$a_w = 6 \text{ mm}$

**2.1.1.8 General**

Alternative T stub method	Yes
---------------------------	-----

## 2.1.2 Loading on joint

**Table 1:** Loads on beam (local oriented)

No.	Name	$V_{j,b1,Ed}$ [kN]	$M_{j,b1,Ed}$ [kNm]	$N_{j,b1,Ed}$ [kN]
1	Default loadcase	0	0	0

**Table 2:** Loads on beam (global oriented)

LC	Name	$V_{j,b1,Ed}$ [kN]	$M_{j,b1,Ed}$ [kNm]	$N_{j,b1,Ed}$ [kN]
1	Default loadcase	0	0	0

**Table 3:** Loads for shear (global oriented)

LC	Name	$M_{j,b2,Ed}$ [kNm]	$V_{j,c1,Ed}$ [kN]	$V_{j,c2,Ed}$ [kN]
1	Default loadcase	0	0	0

## 2.1.3 Joint properties

Remark: Member checks according to EN 1993-1-1 are not part of this calculation note.

### 2.1.3.1 Positive moment

#### 2.1.3.1.1 Components

##### 2.1.3.1.1.1 Beam flange and web in compression (1)

Section class for  $M_y$

Plastic section modulus

Elastic section modulus

Effective section modulus  
4.3(4)

Moment capacity of beam flanges

**Beam flange resistance**

**Stiffness coefficient**

Class = 1

$W_{pl,y}$  =  $8.461 \cdot 10^5$  mm<sup>3</sup>

$W_{el,y}$  =  $7.536 \cdot 10^5$  mm<sup>3</sup>

$W_{eff,y}$  =  $7.536 \cdot 10^5$  mm<sup>3</sup> EN 1993-1-5

$M_{c,Rd}$  = 300.4 kNm

$F_{Rd}$  = **1012 kN** 6.2.6.7 (6.21)

$k_T$  = +∞ m

##### 2.1.3.1.1.2 Column web in shear (Loadcase 1: Default loadcase)

WARNING: Column web in shear: web plates are ignored due to too small plate thickness

In order to take into account the effect of web stiffening plates it must be ensured that the web plates extend throughout the effective width of the web in compression and tension.

This check is not performed here.

Column web height

$d$  = 246.7 mm

Column web thickness

$t_w$  = 19.1 mm

Epsilon

$\epsilon$  = 0.8136 EN 1993-1-1 Tbl. 5.2

Check of column web slenderness  
EN 1993-1-8 6.2.6.1 (1)

$$d / t_w \leq 69\epsilon$$

Normal force in column	$N_c$	=	0 kN	
Load transformation parameter	$\beta$	=	1	5.3 (9) (5.4a/b)
Internal lever arm	$z_s$	=	289.1 mm	
Height of web panel in shear	$z$	=	289.1 mm	
Column profile shear area	$A_{vz,c}$	=	7045 mm <sup>2</sup>	EN 1993-1-1 6.2.6 (3)
Web plate width	$b_s$	=	246.7 mm	6.2.6.1
Web plate thickness	$t_{wp}$	=	12 mm	
Additional shear area by web plates	$A_{vz,wp}$	=	0 mm <sup>2</sup>	6.2.6.1 (6)

The web plate welds should be designed to resist the design forces (EN 1993-1-8, 6.2.6.1 (12)). This check is not performed here.

Shear resistance of web	$V_{wp,Rd}$	=	1300 kN	6.2.6.1 (2) (6.7)
-------------------------	-------------	---	---------	-------------------

2.1.3.1.1.3 Top/bottom stiffeners

Moment resistance of column flange	$M_{pl,fc,Rd}$	=	27.52 kNm	6.2.6.1 (4)
Moment resistance of stiffeners	$M_{pl,st,Rd}$	=	3.08 kNm	6.2.6.1 (4)
Distance of horizontal stiffeners	$d_{st}$	=	296.7 mm	
Shear resistance of stiffeners	$V_{wp,add,Rd}$	=	206.3 kN	6.2.6.1 (4) (6.8)
<b>Shear resistance</b>	$F_{Rd}$	=	<b>1506 kN</b>	
	$F_{Rd}/\beta$	=	1506 kN	
Stiffness coefficient	$k_{1,a}$	=	0.009261 m	6.3.2 (1) Tbl. 6.11
<b>Stiffness coefficient</b>	$k_1$	=	<b>0.009261 m</b>	

2.1.3.1.1.4 Column web in compression (Loadcase 1: Default loadcase)

**WARNING: Column web in compression: web plates are ignored due to too small plate thickness**

In order to take into account the effect of web stiffening plates it must be ensured that the web plates extend throughout the effective width of the web in compression and tension.

This check is not performed here.

Load transformation parameter	$\beta$	=	1	
Max. longit. compressive stress due to axial force and bending in column	$\sigma_{com,a}$	=	0 N/mm <sup>2</sup>	
Loaded length	$L_0$	=	79.16 mm	
Total column shear area	$A_{vz,tot}$	=	7045 mm <sup>2</sup>	
Column profile web height	$d_{w,c}$	=	246.7 mm	
Effective width	$b_{eff,c,wc}$	=	312.2 mm	6.2.6.2(1) (6.10-6.12)
Effective web thickness	$t_{w,eff,c}$	=	19.1 mm	6.2.6.3(8)
Plate slenderness	$\lambda_p$	=	0.5567	6.2.6.2(1) (6.13c)
Reduction factor for plate buckling	$\rho$	=	1	6.2.6.2(1)
Factor	$\omega_1$	=	0.7196	6.2.6.2 Tbl. 6.3
Factor	$\omega_2$	=	0.4601	6.2.6.2 Tbl. 6.3
Reduction factor for interaction with shear	$\omega$	=	0.7196	6.2.6.2 Tbl. 6.3
Reduction factor for compression in column	$k_{wc,a}$	=	1	6.2.6.2(2)
Crushing resistance of web	$F_{a,c,wc,cr,Rd}$	=	1523 kN	6.2.6.2(1) (6.9)
Buckling resistance of Web	$F_{a,c,wc,bu,Rd}$	=	1523 kN	6.2.6.2(1) (6.9)

Project:  
Client:

7 / 15  
7/20/2021

#### 2.1.3.1.1.4.1 Requirements for stiffeners

Stiffener width	$b_{st}$	=	135.7 mm
Stiffener thickness	$t_{st}$	=	12 mm
Stiffener yield stress	$f_{y,st}$	=	355 N/mm <sup>2</sup>
Stiffener weld size	$a_{w,st}$	=	12 mm
Beam width	$b_b$	=	0 mm
Beam yield stress	$f_{y,b}$	=	355 N/mm <sup>2</sup>
Beam flange thickness	$t_{f,b}$	=	0 mm
Stiffener class 3 check			$(b_{st} - \sqrt{(2) \cdot a_w}) / t_{st} \leq 14 \cdot \sqrt{(235 / f_{y,st})}$

Stiffener yield stress check  
ENV 1993-1-1 J.3.5.2 / J.3.3.2

$$f_{y,st} \geq f_{y,b}$$

Stiffener thickness check  
ENV 1993-1-1 J.3.5.2 / J.3.3.2

$$t_{st} \geq t_{f,b}$$

Stiffener width check

$$b_{st} \geq (b_b - t_{w,c}) / 2$$

#### Resistance

Web thickness	$t_w$	=	+∞ kN
Web height	$d_{w,c}$	=	19.1 mm
Effective width	$b_{eff,c}$	=	246.7 mm
Stiffness of column web A.2.2.2)	$k_{w,c}$	=	312.2 mm 6.2.6.2(1) (6.10-6.12)
		=	0.01692 m Tbl. 6.11 (EN1994-1-1)

#### Stiffness coefficient

$$k_2 = +\infty \text{ m}$$

#### 2.1.3.1.1.5 Bolts in tension

Shear area of bolt	$A_s$	=	459 mm <sup>2</sup>
Factor	$k_2$	=	0.9 3.6.1 Tbl. 3.4
Tension resistance (per bolt)	$F_{t,Rd}$	=	330.5 kN 3.6.1 Tbl. 3.4
Bolt elongation length	$L_b$	=	76.8 mm
Stiffness per bolt row	$k_{10}$	=	0.009563 m

#### 2.1.3.1.1.6 Bolt row 1:

##### 2.1.3.1.1.6.1 Column flange in bending

Effective length in mode 1	$L_{eff,1}$	=	240.6 mm
Effective length in mode 2	$L_{eff,2}$	=	315.8 mm
Edge distance	$n$	=	47.86 mm EN1993-1-8 Tbl. 6.2
Design tension resistance of t-stub in mode 1	$F_{T,1,Rd}$	=	2975 kN EN1993-1-8 Tbl. 6.2
Design tension resistance of t-stub in mode 2	$F_{T,2,Rd}$	=	1009 kN EN1993-1-8 Tbl. 6.2
Design tension resistance of t-stub in mode 3	$F_{T,3,Rd}$	=	661 kN EN1993-1-8 Tbl. 6.2
Resistance	$F_{Rd}$	=	661 kN 6.2.4 Tbl. 6.2
Stiffness coefficient	$k_4$	=	0.1194 m 6.3.2 Tbl. 6.11

##### 2.1.3.1.1.6.2 Column web in tension (Loadcase 1: Default loadcase)

WARNING: Column web in tension: web plates are ignored due to too small plate thickness

In order to take into account the effect of web stiffening plates it must be ensured that the web plates extend throughout the effective width of the web in compression and tension.

This check is not performed here.

Effective width	$b_{\text{eff},t,wc}$	=	315.8 mm	6.2.6.3 (2/3)
Column profile shear area	$A_{vz,c}$	=	7045 mm <sup>2</sup>	6.2.6 (3)
Total column shear area	$A_{vz,tot}$	=	7045 mm <sup>2</sup>	
Factor	$\omega_1$	=	0.7156	6.2.6 Tbl. 6.3
Factor	$\omega_2$	=	0.4559	6.2.6 Tbl. 6.3
Reduction factor for shear interaction	$\omega$	=	0.7156	6.2.6 Tbl. 6.3
Tension resistance of web	$F_{a,t,wc,Rd}$	=	1532 kN	6.2.6.3 (1) (6.15)
<b>Resistance</b>	$F_{Rd}$	=	<b>1532 kN</b>	
<b>Stiffness coefficient</b>	$k_3$	=	<b>0.01304 m</b>	<b>6.3.2 Tbl. 6.11</b>

#### 2.1.3.1.1.6.3 End plate in bending

Effective length in mode 1	$L_{\text{eff},1}$	=	140 mm	
Effective length in mode 2	$L_{\text{eff},2}$	=	140 mm	
Edge distance	$n$	=	40 mm	EN1993-1-8 Tbl. 6.2
Design tension resistance of t-stub in mode 1	$F_{T,1,Rd}$	=	820 kN	EN1993-1-8 Tbl. 6.2
Design tension resistance of t-stub in mode 2	$F_{T,2,Rd}$	=	487.5 kN	EN1993-1-8 Tbl. 6.2
Design tension resistance of t-stub in mode 3	$F_{T,3,Rd}$	=	661 kN	EN1993-1-8 Tbl. 6.2
<b>Resistance</b>	$F_{Rd}$	=	<b>487.5 kN</b>	<b>6.2.4 Tbl. 6.2</b>
<b>Stiffness coefficient</b>	$k_5$	=	<b>0.0243 m</b>	<b>6.3.2 Tbl. 6.11</b>

#### 2.1.3.1.1.7 Bolt row 2:

##### 2.1.3.1.1.7.1 Column flange in bending

Effective length in mode 1	$L_{\text{eff},1}$	=	240.6 mm	
Effective length in mode 2	$L_{\text{eff},2}$	=	319 mm	
Edge distance	$n$	=	47.86 mm	EN1993-1-8 Tbl. 6.2
Design tension resistance of t-stub in mode 1	$F_{T,1,Rd}$	=	2975 kN	EN1993-1-8 Tbl. 6.2
Design tension resistance of t-stub in mode 2	$F_{T,2,Rd}$	=	1015 kN	EN1993-1-8 Tbl. 6.2
Design tension resistance of t-stub in mode 3	$F_{T,3,Rd}$	=	661 kN	EN1993-1-8 Tbl. 6.2
<b>Resistance</b>	$F_{Rd}$	=	<b>661 kN</b>	<b>6.2.4 Tbl. 6.2</b>
<b>Stiffness coefficient</b>	$k_4$	=	<b>0.1194 m</b>	<b>6.3.2 Tbl. 6.11</b>

##### 2.1.3.1.1.7.2 Column web in tension (Loadcase 1: Default loadcase)

**WARNING:** Column web in tension: web plates are ignored due to too small plate thickness

In order to take into account the effect of web stiffening plates it must be ensured that the web plates extend throughout the effective width of the web in compression and tension.

This check is not performed here.

Effective width	$b_{\text{eff},t,wc}$	=	319 mm	6.2.6.3 (2/3)
Column profile shear area	$A_{vz,c}$	=	7045 mm <sup>2</sup>	6.2.6 (3)
Total column shear area	$A_{vz,tot}$	=	7045 mm <sup>2</sup>	
Factor	$\omega_1$	=	0.7121	6.2.6 Tbl. 6.3
Factor	$\omega_2$	=	0.4523	6.2.6 Tbl. 6.3
Reduction factor for shear interaction	$\omega$	=	0.7121	6.2.6 Tbl. 6.3
Tension resistance of web	$F_{a,t,wc,Rd}$	=	1540 kN	6.2.6.3 (1) (6.15)

Project:  
Client:

9 / 15  
7/20/2021

<b>Resistance</b>	$F_{Rd}$	=	<b>1540 kN</b>	
<b>Stiffness coefficient</b>	$k_s$	=	<b>0.01304 m</b>	<b>6.3.2 Tbl. 6.11</b>
<b>2.1.3.1.1.7.3 End plate in bending</b>				
Effective length in mode 1	$L_{eff,1}$	=	309.5 mm	
Effective length in mode 2	$L_{eff,2}$	=	375.6 mm	
Edge distance	$n$	=	61.58 mm	EN1993-1-8 Tbl. 6.2
Design tension resistance of t-stub in mode 1	$F_{T,1,Rd}$	=	1114 kN	EN1993-1-8 Tbl. 6.2
Design tension resistance of t-stub in mode 2	$F_{T,2,Rd}$	=	607.8 kN	EN1993-1-8 Tbl. 6.2
Design tension resistance of t-stub in mode 3	$F_{T,3,Rd}$	=	661 kN	EN1993-1-8 Tbl. 6.2
<b>Resistance</b>	$F_{Rd}$	=	<b>607.8 kN</b>	<b>6.2.4 Tbl. 6.2</b>
<b>Stiffness coefficient</b>	$k_s$	=	<b>0.01864 m</b>	<b>6.3.2 Tbl. 6.11</b>

**2.1.3.1.1.7.4 Beam web in tension**

<b>Resistance</b>	$F_{Rd}$	=	<b>1053 kN</b>	<b>6.2.6.8</b>
-------------------	----------	---	----------------	----------------

**2.1.3.1.1.8 Bolt row 3:**

**2.1.3.1.1.8.1 Column flange in bending**

Effective length in mode 1	$L_{eff,1}$	=	240.6 mm	
Effective length in mode 2	$L_{eff,2}$	=	319 mm	
Edge distance	$n$	=	47.86 mm	EN1993-1-8 Tbl. 6.2
Design tension resistance of t-stub in mode 1	$F_{T,1,Rd}$	=	2975 kN	EN1993-1-8 Tbl. 6.2
Design tension resistance of t-stub in mode 2	$F_{T,2,Rd}$	=	1015 kN	EN1993-1-8 Tbl. 6.2
Design tension resistance of t-stub in mode 3	$F_{T,3,Rd}$	=	661 kN	EN1993-1-8 Tbl. 6.2
<b>Resistance</b>	$F_{Rd}$	=	<b>661 kN</b>	<b>6.2.4 Tbl. 6.2</b>
<b>Stiffness coefficient</b>	$k_4$	=	<b>0.1194 m</b>	<b>6.3.2 Tbl. 6.11</b>

**2.1.3.1.1.8.2 Column flange in bending / Group 2 to 3**

Effective length in mode 1	$L_{eff,1}$	=	563.2 mm	
Effective length in mode 2	$L_{eff,2}$	=	563.2 mm	
Edge distance	$n$	=	47.86 mm	EN1993-1-8 Tbl. 6.2
Design tension resistance of t-stub in mode 1	$F_{T,1,Rd}$	=	6965 kN	EN1993-1-8 Tbl. 6.2
Design tension resistance of t-stub in mode 2	$F_{T,2,Rd}$	=	1878 kN	EN1993-1-8 Tbl. 6.2
Design tension resistance of t-stub in mode 3	$F_{T,3,Rd}$	=	1322 kN	EN1993-1-8 Tbl. 6.2

**2.1.3.1.1.8.3 Column web in tension (Loadcase 1: Default loadcase)**

**WARNING: Column web in tension: web plates are ignored due to too small plate thickness**

In order to take into account the effect of web stiffening plates it must be ensured that the web plates extend throughout the effective width of the web in compression and tension.  
This check is not performed here.

Effective width	$b_{eff,1,wc}$	=	319 mm	6.2.6.3 (2/3)
Column profile shear area	$A_{vz,c}$	=	7045 mm <sup>2</sup>	6.2.6 (3)
Total column shear area	$A_{vz,tot}$	=	7045 mm <sup>2</sup>	
Factor	$\omega_1$	=	0.7121	6.2.6 Tbl. 6.3
Factor	$\omega_2$	=	0.4523	6.2.6 Tbl. 6.3
Reduction factor for shear interaction	$\omega$	=	0.7121	6.2.6 Tbl. 6.3
Tension resistance of web	$F_{a,1,wc,Rd}$	=	1540 kN	6.2.6.3 (1) (6.15)
<b>Resistance</b>	$F_{Rd}$	=	<b>1540 kN</b>	



Project:  
Client:

10 / 15  
7/20/2021

**Stiffness coefficient**  $k_s = 0.01304 \text{ m}$  6.3.2 Tbl. 6.11

2.1.3.1.1.8.4 Column web in tension (Loadcase 1: Default loadcase) / Group 2 to 3

**WARNING:** Column web in tension: web plates are ignored due to too small plate thickness

In order to take into account the effect of web stiffening plates it must be ensured that the web plates extend throughout the effective width of the web in compression and tension.

This check is not performed here.

Effective width	$b_{\text{eff},\text{Lwc}}$	= 563.2 mm	6.2.6.3 (2/3)
Column profile shear area	$A_{\text{vz,c}}$	= 7045 mm <sup>2</sup>	6.2.6 (3)
Total column shear area	$A_{\text{vz,tot}}$	= 7045 mm <sup>2</sup>	
Factor	$\omega_1$	= 0.4981	6.2.6 Tbl. 6.3
Factor	$\omega_2$	= 0.276	6.2.6 Tbl. 6.3
Reduction factor for shear interaction	$\omega$	= 0.4981	6.2.6 Tbl. 6.3
Tension resistance of web	$F_{\text{a},\text{Lwc,Rd}}$	= 1902 kN	6.2.6.3 (1) (6.15)
<b>Resistance</b>	$F_{\text{Rd}}$	= 1902 kN	

2.1.3.1.1.8.5 End plate in bending

Effective length in mode 1	$L_{\text{eff},1}$	= 309.5 mm	
Effective length in mode 2	$L_{\text{eff},2}$	= 375.6 mm	
Edge distance	$n$	= 61.58 mm	EN1993-1-8 Tbl. 6.2
Design tension resistance of t-stub in mode 1	$F_{\text{T},1,\text{Rd}}$	= 1114 kN	EN1993-1-8 Tbl. 6.2
Design tension resistance of t-stub in mode 2	$F_{\text{T},2,\text{Rd}}$	= 607.8 kN	EN1993-1-8 Tbl. 6.2
Design tension resistance of t-stub in mode 3	$F_{\text{T},3,\text{Rd}}$	= 661 kN	EN1993-1-8 Tbl. 6.2
<b>Resistance</b>	$F_{\text{Rd}}$	= 607.8 kN	6.2.4 Tbl. 6.2
<b>Stiffness coefficient</b>	$k_s$	= 0.01864 m	6.3.2 Tbl. 6.11

2.1.3.1.1.8.6 End plate in bending / Group 2 to 3

Effective length in mode 1	$L_{\text{eff},1}$	= 654.1 mm	
Effective length in mode 2	$L_{\text{eff},2}$	= 654.1 mm	
Edge distance	$n$	= 61.58 mm	EN1993-1-8 Tbl. 6.2
Design tension resistance of t-stub in mode 1	$F_{\text{T},1,\text{Rd}}$	= 2355 kN	EN1993-1-8 Tbl. 6.2
Design tension resistance of t-stub in mode 2	$F_{\text{T},2,\text{Rd}}$	= 1153 kN	EN1993-1-8 Tbl. 6.2
Design tension resistance of t-stub in mode 3	$F_{\text{T},3,\text{Rd}}$	= 1322 kN	EN1993-1-8 Tbl. 6.2
<b>Resistance</b>	$F_{\text{Rd}}$	= 1153 kN	

2.1.3.1.1.8.7 Beam web in tension

**Resistance**  $F_{\text{Rd}} = 1053 \text{ kN}$  6.2.6.8

2.1.3.1.1.8.8 Beam web in tension / Group 2 to 3

**Resistance**  $F_{\text{Rd}} = 1834 \text{ kN}$  6.2.6.8

**2.1.3.1.2 Moment resistance / stiffness****2.1.3.1.2.1 Loadcase 1 (Default loadcase)****Table 4:** Component assembly for hogging moment

Global	Beam flange in compression	$F_{BFC,Rd}$	1012 kN	$k_7$	$+\infty$ mm
	Column web in shear	$F_{CWS,Rd}$	1506 kN	$k_1$	9.261 mm
	Column web in compression	$F_{CWC,Rd}$	$+\infty$ kN	$k_2$	$+\infty$ mm
	Compression resistance	$F_{c,Rd}$	1012 kN		
Bolts	Bolts in tension	$F_{t,Rd}$	330.5 kN	$k_{10}$	9.563 mm
Bolt row 1	End plate in bending	$F_{EPB,1,Rd}$	487.5 kN	$k_5$	24.3 mm
	Column web in tension	$F_{CWT,1,Rd}$	1532 kN	$k_3$	13.04 mm
	Column flange in bending	$F_{CFB,1,Rd}$	661 kN	$k_4$	119.4 mm
	Effective tension resistance	$F_{t1,Rd}$	487.5 kN		
	Lever arm	$h_1$	348.4 mm		
Bolt row 2	End plate in bending	$F_{EPB,2,Rd}$	607.8 kN	$k_5$	18.64 mm
	Beam web in tension	$F_{BWT,2,Rd}$	1053 kN	$k_8$	$+\infty$ mm
	Column web in tension	$F_{CWT,2,Rd}$	1540 kN	$k_3$	13.04 mm
	Column flange in bending	$F_{CFB,2,Rd}$	661 kN	$k_4$	119.4 mm
	Effective tension resistance	$F_{t2,Rd}$	524.8 kN		
	Lever arm	$h_2$	248.4 mm		
Bolt row 3	End plate in bending	$F_{EPB,3,Rd}$	607.8 kN	$k_5$	18.64 mm
	Beam web in tension	$F_{BWT,3,Rd}$	1053 kN	$k_8$	$+\infty$ mm
	Column web in tension	$F_{CWT,3,Rd}$	1540 kN	$k_3$	13.04 mm
	Column flange in bending	$F_{CFB,3,Rd}$	661 kN	$k_4$	119.4 mm
	Effective tension resistance	$F_{t3,Rd}$	0 kN		
	Lever arm	$h_3$	48.35 mm		

The effective tension resistance considers reduction due to bolt group effects, global components and possible lack of ductility (see EN 1993-1-8, 6.2.7.2 (5)-(9)).

**Plastic moment resistance**

$$M_{pl,Rd} = 300.2 \text{ kNm}$$

**Elastic moment resistance**

$$M_{el,Rd} = 200.1 \text{ kNm}$$

**Initial rotational stiffness**

$$S_{j,ini} = 8.204 \cdot 10^4 \text{ kNm/rad}$$

**Rotational stiffness**

$$S_{j,ini} / \eta = 4.102 \cdot 10^4 \text{ kNm/rad}$$

**2.1.3.2 Shear****2.1.3.2.1 Shear components****2.1.3.2.1.1 Bolts in shear (Loadcase 1: Default loadcase)**

Factor

$$\alpha_v = 0.6 \quad 3.6.1 \text{ Tbl. 3.4}$$

Shear resistance per shear plane

$$F_{v,Rd} = 274.8 \text{ kN} \quad 3.6.1 \text{ Tbl. 3.4}$$

Shear resistance of bolt row 1

$$F_{v,1,Rd} = 157 \text{ kN}$$

Project:  
Client:

12 / 15  
7/20/2021

Shear resistance of bolt row 2	$F_{v,2,Rd}$	=	157 kN
Shear resistance of bolt row 3	$F_{v,3,Rd}$	=	549.7 kN
Shear resistance of bolt row 4	$F_{v,4,Rd}$	=	549.7 kN

#### 2.1.3.2.1.2 End plate in bearing

##### 2.1.3.2.1.2.1 Bolt row 1:

Factor	$\alpha_d$	=	0.4444	3.6.1 Tbl. 3.4
Factor	$\alpha_b$	=	0.4444	3.6.1 Tbl. 3.4
Factor	$k_1$	=	2.5	3.6.1 Tbl. 3.4
Bearing resistance	$F_{b,Rd}$	=	235.2 kN	3.6.1 Tbl. 3.4
Resistance	$F_{b,Rd}$	=	470.4 kN	

##### 2.1.3.2.1.2.2 Bolt row 2:

Factor	$\alpha_d$	=	0.8611	3.6.1 Tbl. 3.4
Factor	$\alpha_b$	=	0.8611	3.6.1 Tbl. 3.4
Factor	$k_1$	=	2.5	3.6.1 Tbl. 3.4
Bearing resistance	$F_{b,Rd}$	=	455.7 kN	3.6.1 Tbl. 3.4
Resistance	$F_{b,Rd}$	=	911.4 kN	

##### 2.1.3.2.1.2.3 Bolt row 3:

Factor	$\alpha_d$	=	1.972	3.6.1 Tbl. 3.4
Factor	$\alpha_b$	=	1	3.6.1 Tbl. 3.4
Factor	$k_1$	=	2.5	3.6.1 Tbl. 3.4
Bearing resistance	$F_{b,Rd}$	=	529.2 kN	3.6.1 Tbl. 3.4
Resistance	$F_{b,Rd}$	=	1058 kN	

##### 2.1.3.2.1.2.4 Bolt row 4:

Factor	$\alpha_d$	=	0.8611	3.6.1 Tbl. 3.4
Factor	$\alpha_b$	=	0.8611	3.6.1 Tbl. 3.4
Factor	$k_1$	=	2.5	3.6.1 Tbl. 3.4
Bearing resistance	$F_{b,Rd}$	=	455.7 kN	3.6.1 Tbl. 3.4
Resistance	$F_{b,Rd}$	=	911.4 kN	

#### 2.1.3.2.1.3 Column flange in bearing

##### 2.1.3.2.1.3.1 Bolt row 1:

Factor	$\alpha_d$	=	$+\infty$	3.6.1 Tbl. 3.4
Factor	$\alpha_b$	=	1	3.6.1 Tbl. 3.4
Factor	$k_1$	=	2.5	3.6.1 Tbl. 3.4
Bearing resistance	$F_{b,Rd}$	=	830.8 kN	3.6.1 Tbl. 3.4
Resistance	$F_{b,Rd}$	=	1662 kN	

##### 2.1.3.2.1.3.2 Bolt row 2:

Factor	$\alpha_d$	=	0.8611	3.6.1 Tbl. 3.4
Factor	$\alpha_b$	=	0.8611	3.6.1 Tbl. 3.4
Factor	$k_1$	=	2.5	3.6.1 Tbl. 3.4
Bearing resistance	$F_{b,Rd}$	=	715.4 kN	3.6.1 Tbl. 3.4
Resistance	$F_{b,Rd}$	=	1431 kN	

Project:  
Client:

13 / 15  
7/20/2021

#### 2.1.3.2.1.3.3 Bolt row 3:

Factor	$\alpha_d$	= 1.972	3.6.1 Tbl. 3.4
Factor	$\alpha_b$	= 1	3.6.1 Tbl. 3.4
Factor	$k_1$	= 2.5	3.6.1 Tbl. 3.4
Bearing resistance	$F_{b,Rd}$	= 830.8 kN	3.6.1 Tbl. 3.4
Resistance	$F_{b,Rd}$	= 1662 kN	

#### 2.1.3.2.1.3.4 Bolt row 4:

Factor	$\alpha_d$	= 0.8611	3.6.1 Tbl. 3.4
Factor	$\alpha_b$	= 0.8611	3.6.1 Tbl. 3.4
Factor	$k_1$	= 2.5	3.6.1 Tbl. 3.4
Bearing resistance	$F_{b,Rd}$	= 715.4 kN	3.6.1 Tbl. 3.4
Resistance	$F_{b,Rd}$	= 1431 kN	

#### 2.1.3.2.1.4 End plate in block tearing

Net area in tension	$A_{nt,1}$	= 1800 mm <sup>2</sup>	3.10.2 (2)
Net area in shear	$A_{nv,1}$	= 1000 mm <sup>2</sup>	3.10.2 (2)
Resistance of shape 1	$V_{eff,Rd,1}$	= 910.6 kN	3.10.2 (2) (3.9/3.10)
Net area in tension	$A_{nt,2}$	= 2600 mm <sup>2</sup>	3.10.2 (2)
Net area in shear	$A_{nv,2}$	= 1000 mm <sup>2</sup>	3.10.2 (2)
Resistance of shape 2	$V_{eff,Rd,2}$	= 1224 kN	3.10.2 (2) (3.9/3.10)
Net area in tension	$A_{nt,3}$	= 4400 mm <sup>2</sup>	3.10.2 (2)
Net area in shear	$A_{nv,3}$	= 0 mm <sup>2</sup>	3.10.2 (2)
Resistance of shape 3	$V_{eff,Rd,3}$	= 1725 kN	3.10.2 (2) (3.9/3.10)

#### 2.1.3.2.1.5 Beam web in shear

Shear area	$A_v$	= 2656 mm <sup>2</sup>	
Resistance (6.18)	$V_{Rd,7}$	= 272.2 kN	EN 1993-1-1 6.2.6 (2)

(Remark: resistance is limited to 50% of the shear resistance of the beam {0} to avoid reduction of moment due to interaction with shear.)

#### 2.1.3.2.1.6 Web weld in shear

Weld size	$a_w$	= 6 mm	
Length of web weld	$L_w$	= 530.4 mm	
Resistance	$V_{Rd,weld}$	= 800.3 kN	4.5.3.2

#### 2.1.3.2.2 Shear downwards

**Table 5:** Component assembly for shear downwards(LC 1)

Bolt row 1	$V_{Rd,1}$	157 kN
Bolt row 2	$V_{Rd,2}$	157 kN
Bolt row 3	$V_{Rd,3}$	549.7 kN
Bolt row 4	$V_{Rd,4}$	549.7 kN
Total	$V_{Rd,1-4}$	1413 kN
Beam web in shear	$V_{Rd,BWS}$	272.2 kN
Web weld in shear	$V_{Rd,weld}$	800.3 kN

Project:  
Client:

14 / 15  
7/20/2021

Resistance  $V_{Rd} = 272.2 \text{ kN}$

## 2.1.4 Joint checks

### 2.1.4.1 Resistance checks

**Table 6:** Moment check

LC	Name	$M_{j,Ed}$ [kN]	$M_{j,Rd}$ [kN]	Utilization factor	Design check
1	Default loadcase	0	300.2	0	OK

**Table 7:** Shear check

LC	Name	$V_{j,Ed}$ [kN]	$V_{j,Rd}$ [kN]	Utilization factor	Design check
1	Default loadcase	0	272.2	0	OK

**Table 8:** Column web panel in shear

LC	Name	$V_{wp,Ed}$ [kN]	z [mm]	$V_{wp,Rd}$ [kN]	Utilization factor	Design check
1	Default loadcase	0	289.1	1506	0	OK

### 2.1.4.2 Further checks

**Table 9:** Welds of beam 1

LC	Name	$a_r$	$a_{r,req}$	Design check	$a_w$	$a_{w,req}$	Design check
1	Default loadcase	9 mm	7.896 mm	OK	6 mm	4.553 mm	OK

## 2.1.5 Classification

### 2.1.5.1 Stiffness classification

Factor  $k_b = 25$  EN1993-1-8 5.2.2.5  
 Span of beam  $L_b = 3.1 \text{ m}$   
 Stiffness boundary for rigid joints  
 EN1993-1-8 5.2.2.5  $S_{j,lim1} = 1.981 \cdot 10^5 \text{ kNm/rad}$   
 Stiffness boundary for pinned joints  
 5.2.2.5  $S_{j,lim2} = 3962 \text{ kNm/rad}$  EN1993-1-8

**Table 10:** Stiffness classification

LC	Name	Initial rotational stiffness $S_{j,ini}$	Classification
1	Default loadcase	$8.204 \cdot 10^4 \text{ kNm/rad}$	Semi-rigid

### 2.1.5.2 Strength classification

Relevant moment  $M_{relevant} = 300.4 \text{ kNm}$  EN1993-1-8 5.2.3.3

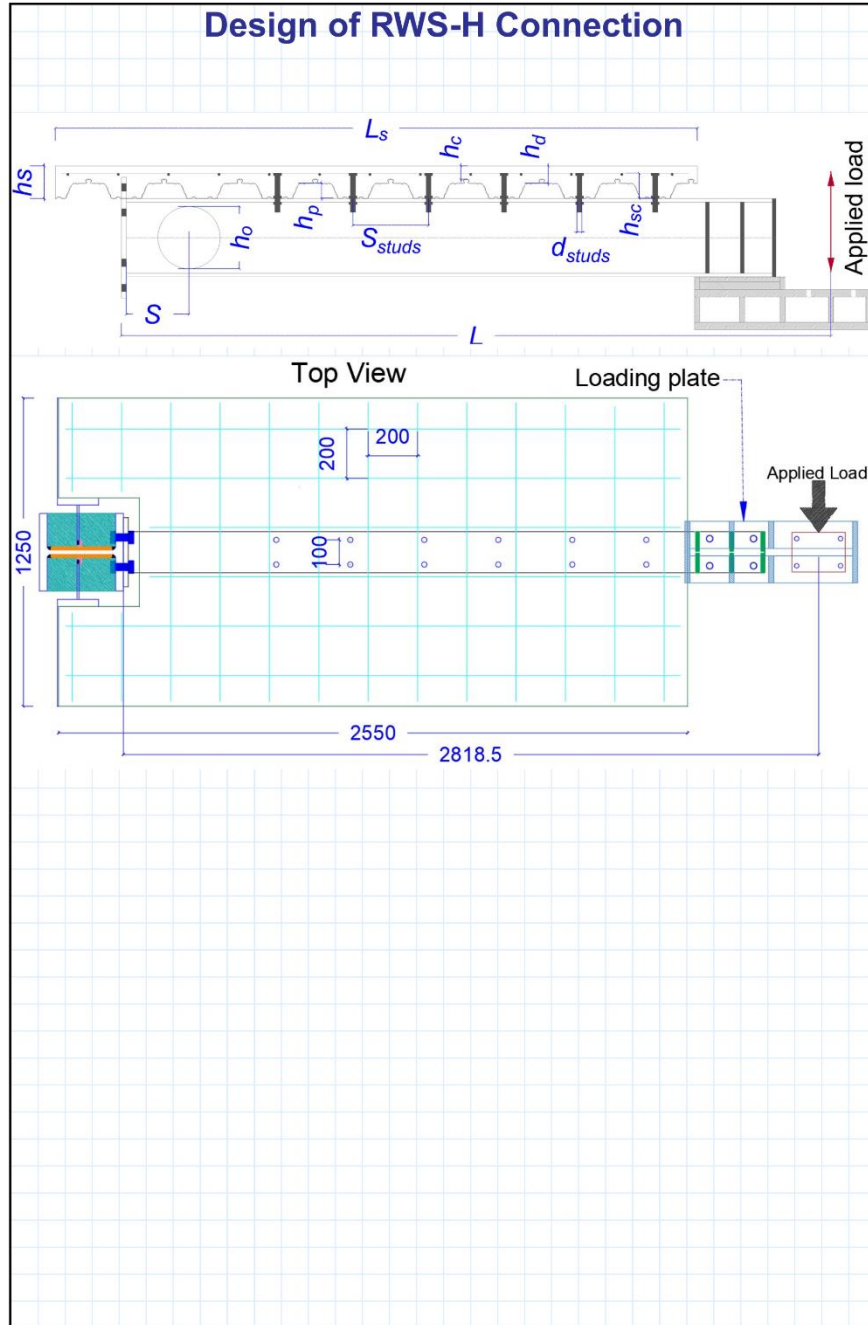
**Table 11:** Strength classification

LC	Name	Moment resistance $M_{i,Rd}$	Classification
1	Default loadcase	300.2 kNm	Partial-strength

### 3 References

- [1] EN 1993-1-1:2005 Eurocode 3: Design of steel structures, Part 1-1: General rules and rules for buildings
- [2] EN 1993-1-8:2005 Eurocode 3: Design of steel structures, Part 1-8: Design of joints
- [3] EN 1994-1-1:2004 Eurocode 4: Design of composite steel and concrete structures, Part 1-1: General rules and rules for buildings
- [4] Connections with four bolts per horizontal row - Application of Eurocode 3, Eurosteel 2011 6th International conference on Steel and Composite Structures, Budapest, Hungary
- [5] European Recommendations for the Design of Simple Joints in Steel Structures - Eurocode 3, Part 1-8, ECCS Technical Committee 10 - Structural connections, ECCS Publication No. 126, 2009
- [6] Steel and composite building frames: sway response under conventional loading and development of membrane effects in beams further to an exceptional action, Jean-Francois Demonceau, PhD thesis, Liège University, Belgium, 2008

## Appendix D: Design of RWS Connections



## 1. Dimensions and properties (Inputs)

### 1.1. General dimensions

Beam span	$L := 5000 \text{ mm}$
Beam span to loading point	$L_a := 2818.5 \text{ mm}$
Beam spacing	$b := 3000 \text{ mm}$
Slab depth	$h_s := 140 \text{ mm}$
Slab span	$L_s := 5000 \text{ mm}$
Effective slab width	$b_{eff} := (L) \div 4 = 1.25 \text{ m}$

• **Profiled Metal Deck - Tata Steel ComFlor60**

Profile weight	$m_d := 0.1 \frac{\text{kN}}{\text{m}^2}$
Deck depth	$h_p := 60 \text{ mm}$
Slab depth above profile	$h_c := 65 \text{ mm}$
Overall height of sheeting profile	$h_d := 75 \text{ mm}$
Deck thickness	$t := 0.9 \text{ mm}$
Average trough width	$b_{o,deck} := 145 \cdot \text{mm}$
Yield strength	$f_{y,decking} := 350 \frac{\text{N}}{\text{mm}^2}$

• **Bolted Shear Studs M20 Gr.8.8**

Connector effective diameter	$d_{studs} := 17.7 \text{ mm}$
Height of shear connectors	$h_{sc} := 100 \text{ mm}$
Longitudinal spacing of studs	$S_{studs} := 300 \text{ mm}$
Transverse spacing of studs:	
$b_0 := 100 \text{ mm}$	
width for end-post	$S_e := 186 \text{ mm}$
# of stud in one rib	$n_r := 2$
Tensile stress area of the bolt	$A_{studs} := 245 \text{ mm}^2$
Ultimate strength	$f_{u,studs} := 800 \frac{\text{N}}{\text{mm}^2}$

• **Mesh A393 to BS 4483**

Weight	$m_m := 0.06 \frac{\text{kN}}{\text{m}^2}$	$A_{st} := 393 \text{ mm}^2$
--------	--	------------------------------

### 1.2. Section properties of the beam

• **Beam size 457 x 191 UB 74 kg/m UB:**

Depth	$h := 310.4 \text{ mm}$	Second moment of area	$I_y := 11700 \cdot 10^4 \cdot \text{mm}^4$
Breadth	$b_f := 166.9 \text{ mm}$	Elastic section modulus	$W_{el,y} := 754000 \text{ mm}^3$
Flange thickness	$t_f := 13.7 \text{ mm}$	Plastic section modulus	$W_{pl,y} := 846000 \text{ mm}^3$
Web thickness	$t_w := 7.9 \text{ mm}$	Shear area	$A_v := 2659 \text{ mm}^2$
Root radius	$r := 8.9 \text{ mm}$		
Clear depth of web	$d_w := 265.2 \text{ mm}$		
Cross-sectional area	$A_a := 6880 \cdot \text{mm}^2$	Weight	$m_{beam} := \frac{0.54 \cdot \frac{\text{kN}}{\text{m}}}{b} = 0.18 \frac{\text{kN}}{\text{m}^2}$

### 1.3. Material properties

Steel grade S355

$f_{y,beam} := 355 \frac{\text{N}}{\text{mm}^2}$	$E_{beam} := 210 \frac{\text{N}}{\text{mm}^2}$
--	--

Concrete grade C25/30

$f_{ck} := 25 \frac{\text{N}}{\text{mm}^2}$	$E_{cm} := 31 \frac{\text{N}}{\text{mm}^2}$
---	---

### 1.4. Partial factors

$\gamma_v := 1.25$	$\gamma_c := 1.5$
$\gamma_{m2} := 1.25$	$\gamma_{m0} := 1$
$\xi_{material} := 0.925$	

Vertical shear resistance

$$V_{pl.a.Rd} := \frac{A_v \cdot \left( \frac{f_{y,beam}}{\sqrt{3}} \right)}{\gamma_{m0}} = 544.987 \text{ kN}$$



### 1.5. Dimensions and properties of web opening:

- Diameter of opening  $h_o := h \cdot 0.8 = 248.32 \text{ mm}$
- Edge-to-edge spacing  $S_o := 0 \text{ mm}$
- Equivalent rectangular opening length  $l_e := 0.45 \cdot h_o = 111.744 \text{ mm}$
- End distance to web opening centreline  $S := 0.8 \cdot h = 248.32 \text{ mm}$
- Height of equivalent rectangular opening  $h_{e,o} := 0.9 \cdot h_o = 223.488 \text{ mm}$
- Effective length of opening  $l_{o,eff} := 0.7 \cdot h_o = 173.824 \text{ mm}$

- Area of each of the two Tees (neglecting radius, using in Tensile resistance of bottom Tee)

$$A_{T,e.o} := \frac{(A_a - h_{e,o} \cdot t_w)}{2} = 2557.222 \text{ mm}^2$$

- Area of each of the two Tees (the full height of the circular opening, neglecting radius - using in shear resistance and perforated composite beam section)

$$A_T := \frac{(A_a - h_o \cdot t_w)}{2} = 2459.136 \text{ mm}^2$$

- Shear Area

$$A_{v,T} := A_T - b_f \cdot t_f + (2 \cdot r + t_w) \cdot 0.5 \cdot t_f = 348.651 \text{ mm}^2$$

- Depth of Tees  $h_T := \frac{(h - h_{e,o})}{2} = 43.456 \text{ mm}$

- Depth of web of Tees  $h_{w,T} := h_T - t_f = 29.756 \text{ mm}$

- Depth of centroid of Tee from flange

$$z_{el} := \frac{\left( b_f \cdot \left( \frac{t_f^2}{2} \right) \right) + \left( t_f + \left( \frac{h_{w,T}}{2} \right) \right) \cdot h_{w,T} \cdot t_w}{A_T} = 9.1 \text{ mm}$$

- Effective depth between centroid of Tees

$$h_{eff} := h - 2 \cdot z_{el} = 292.2 \text{ mm}$$

- The cross sectional area of the flange is

$$A_f := t_f \cdot b_f = 2286.53 \text{ mm}^2$$

- The cross sectional area of web of the Tee is

$$A_{w,T} := h_{w,T} \cdot t_w = 235.072 \text{ mm}^2$$

- The depth of the plastic neutral axis of the Tee from the outer surface of the flange is given by:

$$z_{pl} := \frac{A_f + A_{w,T}}{2 \cdot b_f} = 7.554 \text{ mm}$$

- Plastic bending resistance of steel section at the web opening

$$M_{a,Rd.o} := \left( \frac{f_{y,beam}}{\gamma_{m0}} \right) \cdot \left( W_{pl,y} - \frac{h_o^2 \cdot t_w}{4} \right) = 257.1 \text{ kN} \cdot \text{m}$$

## 2. Actions

### 2.1. Construction stage

• **Permanent action:** ← Output

Self weight of beam  $g_{beam,1} := m_{beam} = 0.18 \frac{kN}{m^2}$

Self weight of decking  $g_{decking,1} := m_d = 0.1 \frac{kN}{m^2}$

Self weight of mesh  $g_{mesh,1} := m_m = 0.06 \frac{kN}{m^2}$

**Total permanent actions**

$$g_{k,1} := g_{beam,1} + g_{decking,1} + g_{mesh,1} = 0.34 \frac{kN}{m^2}$$

• **Variable action:** ← Input

Weight of wet concrete

$$q_{concrete,1} := 25 \frac{kN}{m^3} \cdot 0.097 \cdot \frac{m^2}{m} = 2.425 \frac{kN}{m^2}$$

Construction load

$$q_{construction,1} := 0.75 \frac{kN}{m^2}$$

**Total variable actions**

$$q_{k,1} := q_{concrete,1} + q_{construction,1} = 3.2 \frac{kN}{m^2}$$

### 2.2. Composite stage

• **Permanent action:** ← Output

Self weight of beam  $g_{beam} := m_{beam} = 0.18 \frac{kN}{m^2}$

Self weight of decking  $g_{decking} := m_d = 0.1 \frac{kN}{m^2}$

Self weight of mesh  $g_{mesh} := m_m = 0.06 \frac{kN}{m^2}$

Self weight of Slab

$$q_{slab} := 24 \frac{kN}{m^3} \cdot 0.097 \cdot \frac{m^2}{m} = 2.33 \frac{kN}{m^2}$$

Finishes, services etc.  $q_{finishes} := 1.3 \frac{kN}{m^2}$

**Total permanent actions**

$$g_k := g_{beam} + g_{decking} + g_{mesh} + q_{slab} + q_{finishes} = 4 \frac{kN}{m^2}$$

• **Variable action:** ← Input

**Imposed load**

$$q_k := 5.0 \cdot \frac{kN}{m^2}$$

### 2.3. Partial factors for actions

$$\gamma_G := 1.35 \quad \gamma_Q := 1.5 \quad \xi_{actions} := 0.925$$

### 2.4. Design values of combined actions [Outputs]

• **Construction stage**

$$W_1 := \gamma_G \cdot g_{k,1} + \gamma_Q \cdot q_{k,1} = 5.222 \frac{kN}{m^2}$$

• **Composite stage**

$$W := \xi_{actions} \cdot \gamma_G \cdot g_k + \gamma_Q \cdot q_k = 12.455 \frac{kN}{m^2}$$

### 2.5. Design bending moments and shear forces [Outputs]

• **Construction stage**

Maximum shear force

$$V_{Ed,1} := W_1 \cdot b \cdot \frac{L}{2} = 39.2 \text{ kN}$$

Maximum moment (mid-span)

$$M_{Ed,1} := W_1 \cdot b \cdot \frac{L^2}{8} = 49 \text{ m} \cdot \text{kN}$$

• **Composite stage**

Maximum shear force

$$V_{Ed} := W \cdot b \cdot \frac{L}{2} = 93.4 \text{ kN}$$

Maximum moment (mid-span)

$$M_{Ed} := W \cdot b \cdot \frac{L^2}{8} = 117 \text{ m} \cdot \text{kN}$$

### 3. Shear connection

#### 3.1. Shear connector resistance

4-1-1/  
§6.6.3.1(1)  
Eq.(6.18) Shear resistance of a headed stud connector ( $P_{Rd}$ ) is the smaller of:

$$(1) P_{Rd,1} := 0.8 \cdot f_{u, studs} \cdot \frac{\left(\pi \cdot \frac{d_{studs}^2}{4}\right)}{\gamma_v} = 125.981 \text{ kN}$$

or

4-1-1/  
§6.6.3.1  
(1)  
Eq.(6.21)  $\frac{h_{sc}}{d_{studs}} = 5.65$  if  $\frac{h_{sc}}{d_{studs}} > 4 = 1$  Therefore  $\alpha := 1$  Input  
(Note: 1 means it is true and 0 means not true)

4-1-1/  
§6.6.3.1(1)  
Eq.(6.19)  $(2) P_{Rd,2} := 0.29 \cdot \alpha \cdot d_{studs}^2 \cdot \frac{\left(\sqrt{f_{ck} \cdot E_{cm} \cdot 1000}\right)}{\gamma_v} = 63.986 \text{ kN}$

Therefore, the shear resistance of a shear connector in a solid slab is

$$P_{Rd,min} := \min(P_{Rd,1}, P_{Rd,2}) = 63.986 \text{ kN}$$

- Reduction factor due to decking profile – decking ribs transverse to the supporting beams:

The number of stud in one rib at a beam intersection (no greater than 2)

$$n_r = 2$$

Average trough width  $b_{o,deck} = 145 \text{ mm}$

4-1-1  
§6.6.4.2(1)  
Eq.(6.23)

$$k_{t,1} := \left(\frac{0.7}{\sqrt{n_r}}\right) \cdot \left(\frac{b_{o,deck}}{h_p}\right) \cdot \left(\frac{h_{sc}}{h_p} - 1\right) = 0.797$$

SCI P428  
Eq. (3.12)

However, the upper limit for  $k_t$  is 0.6 when  $n_r = 2$ , and sheet thickness  $\leq 1.0 \text{ mm}$ . Therefore,  $k_t := 0.6$  and the shear resistance of a single shear connector, when placed in pairs per decking rib, is:

BS EN  
1994-1-1  
Table 6.2  
SCI P428  
Eq.(3.11)

$$P_{Rd} := P_{Rd,min} \cdot k_t = 38.392 \text{ kN}$$

However, The shear connectors are non-ductile but satisfy the requirement of a slip capacity of 6 mm. Therefore, use  $P_{Rd,eff} := P_{Rd} \cdot k_{flex}$  for plastic design for uniform spacing  $k_{flex} := 0.8$

SCI P428 Eq.(3.11)

$$P_{Rd,eff} := P_{Rd} \cdot k_{flex} = 30.713 \text{ kN}$$

#### 3.2. Number of shear connectors

$$n_r = 2$$

$$n_{row,Low} := 6$$

$$n_{row,high} := 7$$

$$n_{sc,Low} := n_r \cdot n_{row,Low} = 12$$

$$n_{sc,high} := n_r \cdot n_{row,high} = 14$$


From face of column to the end of web opening

$$n_{sc,o,Low} := 0$$


$$n_{sc,o,high} := 2$$

### 4. Bending resistance at mid-span (composite stage)

#### Solid webbed section (without opening)



#### 4.1. Resistances of sections



- Effective width of compression flange at mid-span, ignoring spacing of studs  $b_{eff} = 1.25 \text{ m}$
- Compressive resistance of slab  

$$N_{c.s.Rd} := \frac{0.85 \cdot f_{ck} \cdot b_{eff} \cdot h_c}{\gamma_c} = 1151.042 \text{ kN}$$
- Tensile resistance of steel section  

$$N_{a.Rd} := \frac{A_a \cdot f_{y,beam}}{\gamma_{m0}} = 2442.4 \text{ kN}$$

Since  $N_{a.Rd} > N_{c.s.Rd} = 1$  the PNA lies in the **steel section**

**(Note: 1 means it is true and 0 means not true)**

- Tensile resistance of steel flange:  

$$N_{f.Rd} := \frac{b_f \cdot t_f \cdot f_{y,beam}}{\gamma_{m0}} = 811.718 \text{ kN}$$
- Tensile resistance of steel web  

$$N_{w.Rd} := N_{a.Rd} - (2 \cdot N_{f.Rd}) = 818.964 \text{ kN}$$

Since  $N_{a.Rd} > N_{c.s.Rd} = 1$  and  $N_{w.Rd} < N_{c.s.Rd} = 1$  the PNA lies in the **steel Flange**


**(Note: 1 means it is true and 0 means not true)**

#### 4.2. Degree of shear connection

$N_{c,max,high} := n_{sc,high} \cdot P_{Rd,eff} = 430 \text{ kN}$

The degree of shear connection at mid-span is

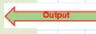
$$\eta_{high} := \frac{N_{c,max,high}}{N_{c.s.Rd}} = 0.37$$




#### 4.3. Bending resistance for full shear connection

- Bending resistance of steel section  $M_{pl,a.Rd} := W_{pl,y} \cdot \frac{f_{y,beam}}{\gamma_{m0}} = 300 \text{ kN} \cdot \text{m}$
- Bending resistance of composite solid webbed section

Taking moments about the top flange (neglecting the contribution from the part of the top flange that is in compression)  $M_{pl,Rd,1} := N_{c.s.Rd} \cdot \left( \frac{h_c}{2} + h_p \right) + N_{a.Rd} \cdot \frac{h}{2} = 485.5 \text{ kN} \cdot \text{m}$





**Using Stress-Block Method:**

**P.N.A. Lies in the Steel flange**

$N_{pl,a} > N_{cf}$  Therefore neutral axis lies in the steel beam  
 $N_{pl,a} > N_{cf} \geq N_{av}$  Therefore neutral axis lies in the flange

Neutral axis depth:  $x = \frac{N_{pl,a} - N_{cf}}{2b f_y}$

Take moments about the base of the bottom flange of the steel beam:

$$M_{pl,Rd} = (N_{cf} \times (h + h_p + \frac{h_s - h_p}{2})) - (((h - 2t_f) \times t_w) \times f_y \times \frac{h}{2}) - (t_f \times b \times f_y) \times \frac{t_f}{2} + (x \times b \times f_y) \times (h - \frac{x}{2}) - (((t_f - x) \times f_y \times b) \times (h - x - \frac{t_f - x}{2}))$$

Since  $N_{a,Rd} > N_{c.s.Rd}$  and  $N_{w,Rd} < N_{c.s.Rd}$  the PNA lies in the steel Flange

PNA depth  $z := \frac{(N_{a,Rd} - N_{c.s.Rd})}{(2 \cdot b_f \cdot f_{y,beam})} = 10.9 \text{ mm}$

Take moments about the base of the bottom flange of the steel beam:

$$M_1 := N_{c.s.Rd} \cdot \left( h + h_p + \frac{h_s - h_p}{2} \right) = 472 \text{ kN} \cdot \text{m}$$

$$M_2 := \left( ((h - 2 \cdot t_f) \cdot t_w) \cdot f_{y,beam} \cdot \frac{h}{2} \right) = 123 \text{ kN} \cdot \text{m}$$

$$M_3 := \left( (t_f \cdot b_f \cdot f_{y,beam}) \cdot \frac{t_f}{2} \right) = 6 \text{ kN} \cdot \text{m}$$

$$M_4 := \left( (z \cdot b_f \cdot f_{y,beam}) \cdot \left( h - \frac{z}{2} \right) \right) = 197 \text{ kN} \cdot \text{m}$$

$$M_5 := \left( ((t_f - z) \cdot (f_{y,beam} \cdot b_f)) \cdot \left( h - z - \frac{t_f - z}{2} \right) \right) = 49 \text{ kN} \cdot \text{m}$$

$M_{pl,Rd,2} := M_1 - M_2 - M_3 + M_4 - M_5 = 491 \text{ kN} \cdot \text{m}$

**4.4. Bending resistance for partial shear connection**

Use linear interpolation:

For partial shear connection, the bending resistance of the composite section is obtained by interpolation between that of the steel section and that of the composite section with full shear connection.

$$M_{Rd,high} := M_{pl,a,Rd} + 0.4 \cdot (M_{pl,Rd,1} - M_{pl,a,Rd}) = 374.4 \text{ kN} \cdot \text{m}$$

$$M_{Ed} = 116.766 \text{ kN} \cdot \text{m}$$

Since  $M_{Rd,high} \geq M_{Ed} = 1$  the design bending resistance at mid-span is satisfactory.  
 (Note: 1 means it is true and 0 means not true)

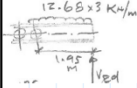
### 5. Design of beam at circular opening (composite stage)

#### 5.1. Design effects

Bending moment at the centreline of opening ( $x_{0.4} := S = 248.32 \text{ mm}$ ) is:

$$W = 12.46 \frac{\text{kN}}{\text{m}^2} \quad \text{---} \quad b = 3 \text{ m} \quad \text{---} \quad V_{Ed} = 93 \text{ kN}$$

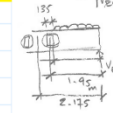
$$M_{Ed.o} := V_{Ed} \cdot x_{0.4} - W \cdot b \cdot \frac{x_{0.4}^2}{2} = 22 \text{ kN} \cdot \text{m}$$



Shear force at edge of equivalent opening

4 (at  $x_{0.4} - \frac{l_c}{2} = 0.192 \text{ m}$ ) is:

$$V_{Ed.o} := V_{Ed} - W \cdot b \cdot \left( x_{0.4} - \frac{l_c}{2} \right) = 86.2 \text{ kN}$$



#### 5.2. Section classification

The top flange is Class 2, due to its attachment to the slab (shear connectors in mid-outstand at 300 mm spacing along the beam).

Classification of web outstand of the top Tee in Vierendeel bending (ignoring axial compression): For the web to be Class 2, independent of its depth:

$$l_{o,eff} \leq 32 \cdot \epsilon \cdot t_w \quad \text{---} \quad l_{o,eff} = 173.824 \text{ mm} \quad \text{Where} \quad \epsilon := \sqrt{\frac{235 \cdot N}{f_{y,beam} \cdot \text{mm}^2}} = 0.814$$

Therefore  $32 \cdot \epsilon \cdot t_w = 205.7 \text{ mm}$  then  $32 \cdot \epsilon \cdot t_w > l_{o,eff} = 1$

(Note: 1 means it is true and 0 means not true)

Table 3.2  
page 39  
P355

The Tee is Class 2 in Vierendeel bending. The bottom Tee is thus also Class 2, irrespective of the tension force in the Tee (which would improve the classification).

#### 5.3. Bending resistance at centreline of circular opening

##### Resistances of section at the opening

P355  
Eq.  
(5)

• Tensile resistance of bottom Tee (The axial resistance of the Top Tee)

$$N_{b,T,Rd} := \frac{A_{T,e.o} \cdot f_{y,beam}}{\gamma_{m0}} = 908 \text{ kN}$$

• The compressive resistance of the effective width of slab at the opening  
Neglecting  $b_0 = 100 \text{ mm}$ , the effective width is given by

$$L_e = 2.819 \text{ m} \quad \text{---} \quad x_{0.4} = 248.32 \text{ mm} \quad \text{---} \quad b_{eff.o} := \left( 3 \cdot \frac{L}{16} \right) + \frac{x_{0.4}}{4} = 1000 \text{ mm}$$

P355  
Eq.  
(6)

$$N_{c,Rd} := \min \left( 0.85 \cdot \frac{f_{ck}}{\gamma_c} \cdot b_{eff.o} \cdot h_c \right) \cdot (n_{sc.o,high} \cdot P_{Rd,eff})$$

$$N_{c,Rd.o1} := \left( 0.85 \cdot \frac{f_{ck}}{\gamma_c} \cdot b_{eff.o} \cdot h_c \right) = 920 \text{ kN} \quad \text{---or---}$$

$$N_{c,Rd.o,high,2} := n_{sc.o,high} \cdot P_{Rd,eff} = 61 \text{ kN} \quad \text{No shear studs above web opening}$$

$$\text{Thus } N_{c,Rd.o,high} := \min(N_{c,Rd.o1}, N_{c,Rd.o,high,2}) = 61 \text{ kN}$$

P355  
Eq.  
(9)

• Plastic bending resistance of composite at the web opening

$$M_{c,Rd.o,high} := (N_{b,T,Rd} \cdot h_{eff}) + (N_{c,Rd.o,high} \cdot (z_{el} + h_s - 0.5 \cdot h_c)) = 272 \text{ kN} \cdot \text{m}$$

This bending resistance is adequate at opening

$$M_{c,Rd.o,high} > M_{Ed.o} = 1$$

(Note: 1 means it is true and 0 means not true)

$$(n_{sc.o,high} \cdot P_{Rd,e})$$

$$(N_{c,Rd.o1} \cdot (z_e$$

For the consideration of coexistent global bending, Vierendeel bending and shear at opening, the design tension force in the bottom Tee is required.

For Case 2, the value of  $N_{bT.Ed}$  is given by the following (unless this exceeds  $N_{c.Rd.o}$ , see Section 3.2.2)

$$N_{bT.Ed} := \frac{M_{Ed.o}}{(h_{eff} + z_{el} + h_s - 0.5 \cdot h_c)} = 53.924 \text{ kN}$$

$$N_{bT.Ed} > N_{c.Rd.o.high} = 0$$

(Note: 1 means it is true and 0 means not true)

thus NO need to use Eq. (10) to determine the force in the bottom Tee for high composite

P355  
Eq. (8)

#### 5.4. Shear resistance of perforated composite beam section

I have to solve it as there is a problem in units

The design shear resistance is the sum of the resistances of the top and bottom Tees and the concrete slab:  $V_{Rd.o} := V_{b.T.Rd} + V_{t.T.Rd} + V_{c.Rd}$

1. Plastic shear resistance of a Tee section is given by:

$$V_{pl.Rd.o} = V_{t.T.Rd} = V_{b.T.Rd}$$

3-1-1/  
§6.2.6

$$V_{pl.Rd.o} := \frac{A_{v.T} \cdot \frac{f_{y.beam}}{\sqrt{3}}}{\gamma_{m0}} = 71.5 \text{ kN}$$

P355  
Eq. (12)

1. Shear resistance of the concrete slab at an opening

$$V_{c.Rd} := \left[ C_{Rd.o} \cdot k \cdot (100 \rho_1 \cdot f_{ck})^{\frac{1}{3}} + k_1 \cdot \sigma_{cp} \right] \cdot b_w \cdot h_c$$

(13)

With a minimum value of:

$$V_{c.Rd.min} := [v_{min} + k_1 \cdot \sigma_{cp}] \cdot b_w \cdot h_c$$

2-1-1/  
Table  
NA.1  
(§6.2.2  
(1))

$h_{s,eff} := 0.75 \cdot h_s = 105 \text{ mm}$   
**Effective width of the slab**  
 $b_w := b_f + 2 \cdot h_{s,eff} = 376.9 \text{ mm}$

2-1-1/  
§6.2.2  
(1))

$C_{Rd,c} := \frac{0.18}{\gamma_c} = 0.12 \quad k_1 := 0.15$   
 $d := h_c = 65 \text{ mm}$

$k := 1 + \sqrt{\frac{200 \cdot \text{mm}}{d}} = 2.754 \text{ but } k \leq 2 = 0$

(Note: 1 means it is true and 0 means not true)

therefore  $k_{limit} := 2$  (I have changed the  $k$  to  $k_{limit}$  as it is greater than limit)

$\rho_1 := A_{st} \div (1000 \cdot \text{mm} \cdot d) = 0.006$   
 $\rho_1 \leq 0.02 = 1$   
 (Note: 1 means it is true and 0 means not true)

$b_{eff,o} = 999.6 \text{ mm}$

The value of the first term in the expression for  $V_{c,Rd}$

$$y := \left( \frac{(100 \cdot \rho_1 \cdot f_{ck})^{\frac{1}{3}} \cdot C_{Rd,c} \cdot k_{limit}}{\frac{\text{kg}}{\text{m}^3 \cdot \text{s}^3}} \right) \cdot 10^{-2} \cdot \frac{\text{N}}{\text{mm}^2} = 0.593 \frac{\text{N}}{\text{mm}^2}$$

I have to solve it like this as there is a problem in the units and I need the results in N/mm2

The value of the first term in the expression for the minimum value,  $v_{min}$  is:

2-1-1/  
Table  
NA.1  
(§6.2.2(1))

$$v_{min} := \left( \frac{0.035 \cdot (k_{limit}^{\frac{3}{2}}) \cdot (\sqrt{f_{ck}})}{\frac{\text{m}^2 \cdot \text{s}}{\text{kg}^{\frac{1}{2}}}} \right) \cdot 10^3 = 0.495 \frac{\text{N}}{\text{mm}^2}$$

I have to solve it like this as there is a problem in the units and I need the results in N/mm2

So, use  $y = 0.59 \frac{\text{N}}{\text{mm}^2}$

From above, assuming no compression in the top Tee, the force in the slab at the opening equals the force in the bottom Tee  $N_{bT,Ed} = 53.924 \text{ kN}$

$\sigma_{cp} := (N_{bT,Ed}) \div (b_{eff,o} \cdot h_c) = 0.83 \frac{\text{N}}{\text{mm}^2}$   
 $k_1 \cdot \sigma_{cp} = 0.124 \frac{\text{N}}{\text{mm}^2}$

Total shear strength of concrete is:  
 $V_{c,Rd} := (y + k_1 \cdot \sigma_{cp}) \cdot b_w \cdot h_c = 17.6 \text{ kN}$

Hence, Shear resistance of perforated composite beam section because  $V_{pl,Rd,o} = V_{b,T,Rd} = V_{l,T,Rd}$   
 $V_{Rd,o} := 2 \cdot V_{pl,Rd,o} + V_{c,Rd} = 160.5 \text{ kN}$

$V_{Rd,o} > V_{Ed} = 1$  it is safe  
 $V_{Ed} = 93.413 \text{ kN}$   
 (Note: 1 means it is true and 0 means not true)



**5.5. Bending resistance of Tees (Vierendeel bending resistance)**

Vierendeel bending resistance at web opening for steel section  $M_{V.T.Rd} := M_{V.t.T.Rd} + M_{V.b.T.Rd}$

Vierendeel bending resistance at web opening for composite section  $M_{V.c.Rd}$

Initial assumption of distribution of shear force

Since the shear force in each Tee  $V_{T.Ed} := \frac{V_{Ed.o}}{2} = 43.111 \text{ kN}$

$V_{T.Ed} < V_{pl.Rd} = ?$  it is safe

(Note: 1 means it is true and 0 means not true)

Then, the web thickness does not need to be reduced when determining plastic bending resistance and axial resistance. If the shear force in the bottom Tee is limited by Vierendeel bending resistance across the Tee, the shear forces may need to be redistributed.

- Plastic bending resistance of an unstiffened Tee, in the absence of axial force and high shear  $M_{V.T.Rd}$

For a Class 1 and 2 cross section, the plastic bending resistance of an unstiffened Tee  $M_{V.T.Rd} = M_{t.T.Rd} = M_{b.T.Rd}$ , in the absence of axial force and high shear.

Hence: Vierendeel bending resistance at web opening for steel section

P355 Eq. (19)  $M_{V.t.T.Rd} := \left( \frac{A_{w.T} \cdot f_{y.beam}}{\gamma_{m0}} \cdot (0.5 \cdot h_{w.T} + t_f - z_{pl}) \right) + \left( \frac{A_f \cdot f_{y.beam}}{\gamma_{m0}} \cdot \left( 0.5 \cdot t_f - z_{pl} + \frac{z_{pl}^2}{t_f} \right) \right) = 4.6 \text{ kN}\cdot\text{m}$

- The plastic bending resistance of the bottom Tee is reduced for axial tension, as follows:

P355 Eq. (26)  $M_{V.b.T.Rd} := M_{V.t.T.Rd} \cdot \left( 1 - \left( \frac{N_{b.T.Ed}}{N_{b.T.Rd}} \right)^2 \right) = 4.5 \text{ kN}\cdot\text{m}$

The plastic resistance of the top Tee is not reduced for axial force and thus:  $M_{V.t.T.Rd} = 4.6 \text{ kN}\cdot\text{m}$

- Vierendeel bending resistance at web opening for composite section  $M_{V.c.Rd}$

The compression force developed in the slab due to composite action over the opening  $\Delta N_{c.Rd}$

the number of shear studs above the web opening  $n_{sc.o} := 2$

$\Delta N_{c.Rd} := n_{sc.o} \cdot P_{Rd,eff} = 61.4 \text{ kN}$

For unstiffened openings, reduction factor due to the length of the openings  $k_o$  is given by  $k_o := 1 - \frac{l_{o,eff}}{(25 \cdot h_T)} = 0.84$

where  $z_i := t_f = 13.7 \text{ mm}$

Vierendeel bending resistance due to local composite action is given by:  $M_{V.c.Rd} := \Delta N_{c.Rd} \cdot (h_s + z_i - 0.5 \cdot h_c) \cdot k_o = 6.3 \text{ kN}\cdot\text{m}$

**5.6. Verification of resistance to Vierendeel bending**

The criterion for adequacy of Vierendeel resistance is:

P355 Eq. (14)  $M_{V.Rd,high} := 2 \cdot M_{V.t.T.Rd} + 2 \cdot M_{V.b.T.Rd} + M_{V.c.Rd} = 24.477 \text{ kN}\cdot\text{m}$  (with composite slab)  $V_{Ed.o} \cdot l_e = 9.635 \text{ kN}\cdot\text{m}$

$M_{V.Rd,high} \geq V_{Ed.o} \cdot l_e = 1$  it is safe

### Plastic analysis of composite beams with partial shear connection according to SCI-P428

$$N_{c,f} := \min(N_{c.s.Rd}, N_{a.Rd}) = (1.151 \cdot 10^3) \text{ kN}$$

$$\eta_{high.p428} := \frac{k_{flex} \cdot P_{Rd} \cdot \eta_{sc.high}}{N_{c,f}} = 0.374$$

is the design value of the plastic resistance of the clear depth of the steel web to normal force

$$N_{pl.d} := f_{y,beam} \cdot d_w \cdot t_w = 743.753 \text{ kN}$$

$$z_{pl1} := \frac{h}{2} + h_c + h_p - \frac{\eta_{high.p428} \cdot N_{c.s.Rd}}{N_{pl.d}} \cdot \frac{d_w}{2} = 203.5 \text{ mm}$$

$$\eta_{high.p428} \cdot N_{c,f} < N_{w.Rd} = 1$$

(Note: 1 means it is true and 0 means not true)

**Then**

**Case 1: plastic neutral axis within the web**

$$x1 := M_{pl.a.Rd} = 300.33 \text{ kN} \cdot \text{m}$$

$$x2 := \eta_{high.p428} \cdot N_{c,f} \cdot \left( \frac{h}{2} + h_c + h_p \right) = 120.482 \text{ kN} \cdot \text{m}$$

$$x3 := \left( \eta_{high.p428} \cdot N_{c,f} \right)^2 \cdot \left( \frac{h_c}{2 \cdot N_{c.s.Rd}} + \frac{d_w}{4 \cdot f_{y,beam} \cdot d_w \cdot t_w} \right) = 21.702 \text{ kN} \cdot \text{m}$$

$$M_{pl,\eta.Rd} := x1 + x2 - x3 = 399.1 \text{ kN} \cdot \text{m}$$

## 6. Results Summary

### • Resistances

Compressive resistance of slab

$$N_{c.s.Rd} = 1151 \text{ kN}$$

Tensile resistance of steel section

$$N_{a.Rd} = 2442.4 \text{ kN}$$

Vertical shear resistance

$$V_{pl.o.Rd} = 545 \text{ kN}$$

Bending resistance of steel section

$$M_{pl.a.Rd} = 300 \text{ kN}\cdot\text{m}$$

Bending resistance of composite solid webbed section

$$M_{pl.Rd.1} = 485.5 \text{ kN}\cdot\text{m} \text{ (neglecting the contribution from the part of the top flange that is in compression)}$$

$$M_{pl.Rd.2} = 491.1 \text{ kN}\cdot\text{m} \text{ (using stress block method)}$$

Bending resistance for partial connections

$$M_{Rd.high} = 374.4 \text{ kN}\cdot\text{m}$$

Tensile resistance of bottom Tee (The axial resistance of the Top Tee)

$$N_{b.T.Rd} = 907.8 \text{ kN}$$

The compressive resistance of the effective width of slab at the opening

$$N_{c.Rd.o.high} = 61.427 \text{ kN}$$

Plastic bending resistance of steel section at the web opening

$$M_{a.Rd.o} = 257.1 \text{ kN}\cdot\text{m}$$

Plastic bending resistance of composite section at the web opening

$$M_{c.Rd.o.high} = 272.4 \text{ kN}\cdot\text{m}$$

Total shear strength of concrete is:

$$V_{c.Rd} = 17.6 \text{ kN}$$

Shear resistance of perforated beam section

$$V_{Rd.o.steel} := 2 \cdot V_{pl.Rd.o} = 142.9 \text{ kN}$$

Shear resistance of perforated composite beam section

$$V_{Rd.o} = 160.5 \text{ kN}$$

Vierendeel bending resistance perforated composite beam section

$$M_{V.Rd.steel} := 2 \cdot M_{V.l.T.Rd} + 2 \cdot M_{V.b.T.Rd} = 18.2 \text{ kN}\cdot\text{m}$$

Vierendeel bending resistance perforated composite beam section

$$M_{V.Rd.high} = 24.5 \text{ kN}\cdot\text{m}$$

Plastic analysis of composite solid webbed beams with partial shear connection according to SCI-P428

$$M_{pl,q.Rd} = 399.11 \text{ kN}\cdot\text{m}$$

### • Design values

Maximum shear force

$$V_{Ed} = 93.41 \text{ kN}$$

Maximum moment (mid-span)

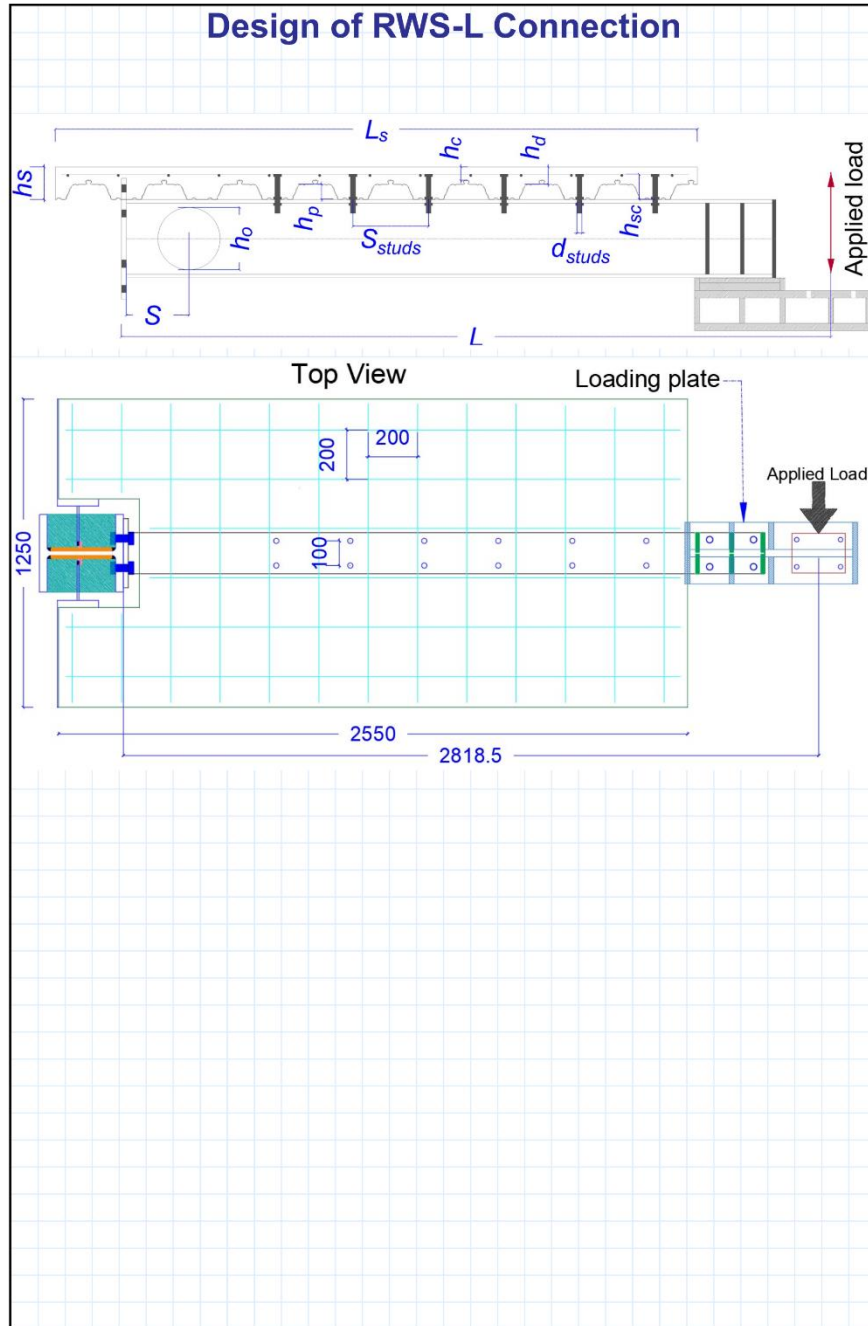
$$M_{Ed} = 116.77 \text{ kN}\cdot\text{m}$$

Shear force at edge of equivalent opening

$$V_{Ed.o} = 86.22 \text{ kN}$$

Bending moment at the centreline of opening

$$M_{Ed.o} = 22.04 \text{ kN}\cdot\text{m}$$



## 1. Dimensions and properties (Inputs)

### 1.1. General dimensions

Beam span	$L := 5000 \text{ mm}$
Beam span to loading point	$L_a := 2818.5 \text{ mm}$
Beam spacing	$b := 3000 \text{ mm}$
Slab depth	$h_s := 140 \text{ mm}$
Slab span	$L_s := 5000 \text{ mm}$
Effective slab width	$b_{eff} := (L) \div 4 = 1.25 \text{ m}$

• **Profiled Metal Deck - Tata Steel ComFlor60**

Profile weight	$m_d := 0.1 \frac{\text{kN}}{\text{m}^2}$
Deck depth	$h_p := 60 \text{ mm}$
Slab depth above profile	$h_c := 65 \text{ mm}$
Overall height of sheeting profile	$h_d := 75 \text{ mm}$
Deck thickness	$t := 0.9 \text{ mm}$
Average trough width	$b_{o,deck} := 145 \cdot \text{mm}$
Yield strength	$f_{y,decking} := 350 \frac{\text{N}}{\text{mm}^2}$

• **Bolted Shear Studs M20 Gr.8.8**

Connector effective diameter	$d_{studs} := 17.7 \text{ mm}$
Height of shear connectors	$h_{sc} := 100 \text{ mm}$
Longitudinal spacing of studs	$S_{studs} := 300 \text{ mm}$
Transverse spacing of studs:	$b_0 := 100 \text{ mm}$
width for end-post	$S_e := 186 \text{ mm}$
# of stud in one rib	$n_r := 2$
Tensile stress area of the bolt	$A_{studs} := 245 \text{ mm}^2$
Ultimate strength	$f_{u,studs} := 800 \frac{\text{N}}{\text{mm}^2}$

• **Mesh A393 to BS 4483**

Weight	$m_m := 0.06 \frac{\text{kN}}{\text{m}^2} \quad A_{st} := 393 \text{ mm}^2$
--------	---

### 1.2. Section properties of the beam

• **Beam size 457 x 191 UB 74 kg/m UB:**

Depth	$h := 310.4 \text{ mm}$	Second moment of area	$I_y := 11700 \cdot 10^4 \cdot \text{mm}^4$
Breadth	$b_f := 166.9 \text{ mm}$	Elastic section modulus	$W_{el,y} := 754000 \text{ mm}^3$
Flange thickness	$t_f := 13.7 \text{ mm}$	Plastic section modulus	$W_{pl,y} := 846000 \text{ mm}^3$
Web thickness	$t_w := 7.9 \text{ mm}$	Shear area	$A_v := 2659 \text{ mm}^2$
Root radius	$r := 8.9 \text{ mm}$		
Clear depth of web	$d_w := 265.2 \text{ mm}$		
Cross-sectional area	$A_a := 6880 \cdot \text{mm}^2$	Weight	$m_{beam} := \frac{0.54 \cdot \frac{\text{kN}}{\text{m}}}{b} = 0.18 \frac{\text{kN}}{\text{m}^2}$

### 1.3. Material properties

Steel grade S355

$f_{y,beam} := 355 \frac{\text{N}}{\text{mm}^2}$	$E_{beam} := 210 \frac{\text{N}}{\text{mm}^2}$
--	--

Concrete grade C25/30

$f_{ck} := 25 \frac{\text{N}}{\text{mm}^2}$	$E_{cm} := 31 \frac{\text{N}}{\text{mm}^2}$
---	---

### 1.4. Partial factors

$\gamma_v := 1.25$	$\gamma_c := 1.5$
$\gamma_{m2} := 1.25$	$\gamma_{m0} := 1$
$\xi_{material} := 0.925$	

Vertical shear resistance

$$V_{pl,a,Rd} := \frac{A_v \cdot \left( \frac{f_{y,beam}}{\sqrt{3}} \right)}{\gamma_{m0}} = 544.987 \text{ kN}$$

### 1.5. Dimensions and properties of web opening:

- Diameter of opening  $h_o := h \cdot 0.8 = 248.32 \text{ mm}$
- Edge-to-edge spacing  $S_o := 0 \text{ mm}$
- Equivalent rectangular opening length  $l_e := 0.45 \cdot h_o = 111.744 \text{ mm}$
- End distance to web opening centreline  $S := 0.8 \cdot h = 248.32 \text{ mm}$
- Height of equivalent rectangular opening  $h_{e,o} := 0.9 \cdot h_o = 223.488 \text{ mm}$
- Effective length of opening  $l_{o,eff} := 0.7 \cdot h_o = 173.824 \text{ mm}$

- Area of each of the two Tees (neglecting radius, using in Tensile resistance of bottom Tee)

$$A_{T,e.o} := \frac{(A_a - h_{e,o} \cdot t_w)}{2} = 2557.222 \text{ mm}^2$$

- Area of each of the two Tees (the full height of the circular opening, neglecting radius - using in shear resistance and perforated composite beam section)

$$A_T := \frac{(A_a - h_o \cdot t_w)}{2} = 2459.136 \text{ mm}^2$$

- Shear Area

$$A_{v,T} := A_T - b_f \cdot t_f + (2 \cdot r + t_w) \cdot 0.5 \cdot t_f = 348.651 \text{ mm}^2$$

- Depth of Tees  $h_T := \frac{(h - h_{e,o})}{2} = 43.456 \text{ mm}$

- Depth of web of Tees  $h_{w,T} := h_T - t_f = 29.756 \text{ mm}$

- Depth of centroid of Tee from flange

$$z_{el} := \frac{\left( b_f \cdot \left( \frac{t_f^2}{2} \right) \right) + \left( t_f + \left( \frac{h_{w,T}}{2} \right) \right) \cdot h_{w,T} \cdot t_w}{A_T} = 9.1 \text{ mm}$$

- Effective depth between centroid of Tees

$$h_{eff} := h - 2 \cdot z_{el} = 292.2 \text{ mm}$$

- The cross sectional area of the flange is

$$A_f := t_f \cdot b_f = 2286.53 \text{ mm}^2$$

- The cross sectional area of web of the Tee is

$$A_{w,T} := h_{w,T} \cdot t_w = 235.072 \text{ mm}^2$$

- The depth of the plastic neutral axis of the Tee from the outer surface of the flange is given by:

$$z_{pl} := \frac{A_f + A_{w,T}}{2 \cdot b_f} = 7.554 \text{ mm}$$

- Plastic bending resistance of steel section at the web opening

$$M_{a,Rd.o} := \left( \frac{f_{y,beam}}{\gamma_{m0}} \right) \cdot \left( W_{pl,y} - \frac{h_o^2 \cdot t_w}{4} \right) = 257.1 \text{ kN} \cdot \text{m}$$

## 2. Actions

### 2.1. Construction stage

• **Permanent action:** ← Output

Self weight of beam  $g_{beam,1} := m_{beam} = 0.18 \frac{kN}{m^2}$

Self weight of decking  $g_{decking,1} := m_d = 0.1 \frac{kN}{m^2}$

Self weight of mesh  $g_{mesh,1} := m_m = 0.06 \frac{kN}{m^2}$

**Total permanent actions**

$$g_{k,1} := g_{beam,1} + g_{decking,1} + g_{mesh,1} = 0.34 \frac{kN}{m^2}$$

• **Variable action:** ← Input

Weight of wet concrete

$$q_{concrete,1} := 25 \frac{kN}{m^3} \cdot 0.097 \cdot \frac{m^2}{m} = 2.425 \frac{kN}{m^2}$$

Construction load

$$q_{construction,1} := 0.75 \frac{kN}{m^2}$$

**Total variable actions**

$$q_{k,1} := q_{concrete,1} + q_{construction,1} = 3.2 \frac{kN}{m^2}$$

### 2.2. Composite stage

• **Permanent action:** ← Output

Self weight of beam  $g_{beam} := m_{beam} = 0.18 \frac{kN}{m^2}$

Self weight of decking  $g_{decking} := m_d = 0.1 \frac{kN}{m^2}$

Self weight of mesh  $g_{mesh} := m_m = 0.06 \frac{kN}{m^2}$

Self weight of Slab

$$q_{slab} := 24 \frac{kN}{m^3} \cdot 0.097 \cdot \frac{m^2}{m} = 2.33 \frac{kN}{m^2}$$

Finishes, services etc.

$$q_{finishes} := 1.3 \frac{kN}{m^2}$$

**Total permanent actions**

$$g_k := g_{beam} + g_{decking} + g_{mesh} + q_{slab} + q_{finishes} = 4 \frac{kN}{m^2}$$

• **Variable action:** ← Input

**Imposed load**

$$q_k := 5.0 \cdot \frac{kN}{m^2}$$

### 2.3. Partial factors for actions

$$\gamma_G := 1.35 \quad \gamma_Q := 1.5 \quad \xi_{actions} := 0.925$$

### 2.4. Design values of combined actions [Outputs]

• **Construction stage**

$$W_1 := \gamma_G \cdot g_{k,1} + \gamma_Q \cdot q_{k,1} = 5.222 \frac{kN}{m^2}$$

• **Composite stage**

$$W := \xi_{actions} \cdot \gamma_G \cdot g_k + \gamma_Q \cdot q_k = 12.455 \frac{kN}{m^2}$$

### 2.5. Design bending moments and shear forces [Outputs]

• **Construction stage**

Maximum shear force

$$V_{Ed,1} := W_1 \cdot b \cdot \frac{L}{2} = 39.2 \text{ kN}$$

Maximum moment (mid-span)

$$M_{Ed,1} := W_1 \cdot b \cdot \frac{L^2}{8} = 49 \text{ m} \cdot \text{kN}$$

• **Composite stage**

Maximum shear force

$$V_{Ed} := W \cdot b \cdot \frac{L}{2} = 93.4 \text{ kN}$$

Maximum moment (mid-span)

$$M_{Ed} := W \cdot b \cdot \frac{L^2}{8} = 117 \text{ m} \cdot \text{kN}$$

### 3. Shear connection

#### 3.1. Shear connector resistance

Shear resistance of a headed stud connector ( $P_{Rd}$ ) is the smaller of:

4-1-1/  
§6.6.3.1(1)  
Eq.(6.18)

$$(1) P_{Rd,1} := 0.8 \cdot f_{u, studs} \cdot \frac{\left(\pi \cdot \frac{d_{studs}^2}{4}\right)}{\gamma_v} = 125.981 \text{ kN}$$

or

4-1-1/  
§6.6.3.1  
(1)  
Eq.(6.21)

$$\frac{h_{sc}}{d_{studs}} = 5.65 \text{ if } \frac{h_{sc}}{d_{studs}} > 4 = 1 \text{ Therefore } \alpha := 1 \text{ Input}$$

(Note: 1 means it is true and 0 means not true)

4-1-1/  
§6.6.3.1(1)  
Eq.(6.19)

$$(2) P_{Rd,2} := 0.29 \cdot \alpha \cdot d_{studs}^2 \cdot \frac{\left(\sqrt{f_{ck} \cdot E_{cm} \cdot 1000}\right)}{\gamma_v} = 63.986 \text{ kN}$$

Therefore, the shear resistance of a shear connector in a solid slab is

$$P_{Rd,min} := \min(P_{Rd,1}, P_{Rd,2}) = 63.986 \text{ kN}$$

- Reduction factor due to decking profile – decking ribs transverse to the supporting beams:

The number of stud in one rib at a beam intersection (no greater than 2)

$$n_r = 2$$

Average trough width  $b_{o,deck} = 145 \text{ mm}$

4-1-1  
§6.6.4.2(1)  
Eq.(6.23)

$$k_{t,1} := \left(\frac{0.7}{\sqrt{n_r}}\right) \cdot \left(\frac{b_{o,deck}}{h_p}\right) \cdot \left(\frac{h_{sc}}{h_p} - 1\right) = 0.797$$

SCI P428  
Eq. (3.12)

However, the upper limit for  $k_t$  is 0.6 when  $n_r = 2$ , and sheet thickness  $\leq 1.0 \text{ mm}$ .

Therefore,  $k_t := 0.6$  and the shear resistance of a single shear connector, when placed in pairs per decking rib, is:

BS EN  
1994-1-1  
Table 6.2  
SCI P428  
Eq.(3.11)

$$P_{Rd} := P_{Rd,min} \cdot k_t = 38.392 \text{ kN}$$

However, The shear connectors are non-ductile but satisfy the requirement of a slip capacity of 6 mm. Therefore, use  $P_{Rd,eff} := P_{Rd} \cdot k_{flex}$  for plastic design for uniform spacing  $k_{flex} := 0.8$

SCI P428 Eq.(3.11)

$$P_{Rd,eff} := P_{Rd} \cdot k_{flex} = 30.713 \text{ kN}$$

#### 3.2. Number of shear connectors

$$n_r = 2$$

$$n_{row,Low} := 6$$

$$n_{row,high} := 7$$

$$n_{sc,Low} := n_r \cdot n_{row,Low} = 12$$

$$n_{sc,high} := n_r \cdot n_{row,high} = 14$$

From face of column to the end of web opening

$$n_{sc,o,Low} := 0$$

$$n_{sc,o,high} := 2$$



### 4. Bending resistance at mid-span (composite stage)

#### Solid webbed section (without opening)

#### 4.1. Resistances of sections

- Effective width of compression flange at mid-span, ignoring spacing of studs  $b_{eff} = 1.25 \text{ m}$
- Compressive resistance of slab**  

$$N_{c.s.Rd} := \frac{0.85 \cdot f_{ck} \cdot b_{eff} \cdot h_c}{\gamma_c} = 1151.042 \text{ kN}$$
- Tensile resistance of steel section**  

$$N_{a.Rd} := \frac{A_a \cdot f_{y,beam}}{\gamma_{m0}} = 2442.4 \text{ kN}$$

Since  $N_{a.Rd} > N_{c.s.Rd} = 1$  the PNA lies in the **steel section**

(Note: 1 means it is true and 0 means not true)

- Tensile resistance of steel flange:**  

$$N_{f.Rd} := \frac{b_f \cdot t_f \cdot f_{y,beam}}{\gamma_{m0}} = 811.718 \text{ kN}$$
- Tensile resistance of steel web**  

$$N_{w.Rd} := N_{a.Rd} - (2 \cdot N_{f.Rd}) = 818.964 \text{ kN}$$

Since  $N_{a.Rd} > N_{c.s.Rd} = 1$  and  $N_{w.Rd} < N_{c.s.Rd} = 1$  the PNA lies in the **steel Flange**

(Note: 1 means it is true and 0 means not true)

#### 4.2. Degree of shear connection

$N_{c,max,Low} := n_{sc,Low} \cdot P_{Rd,eff} = 368.6 \text{ kN}$

The degree of shear connection at mid-span is

$$\eta_{Low} := \frac{N_{c,max,Low}}{N_{c.s.Rd}} = 0.32$$

#### 4.3. Bending resistance for full shear connection

- Bending resistance of steel section**  $M_{pl,a.Rd} := W_{pl,y} \cdot \frac{f_{y,beam}}{\gamma_{m0}} = 300 \text{ kN} \cdot \text{m}$
- Bending resistance of composite solid webbed section**

Taking moments about the top flange (neglecting the contribution from the part of the top flange that is in compression)  $M_{pl,Rd,1} := N_{c.s.Rd} \cdot \left( \frac{h_c}{2} + h_p \right) + N_{a.Rd} \cdot \frac{h}{2} = 485.5 \text{ kN} \cdot \text{m}$

**Using Stress-Block Method:**

**P.N.A. Lies in the Steel flange**

$N_{pl,a} > N_{cf}$  Therefore neutral axis lies in the steel beam  
 $N_{pl,a} > N_{cf} \geq N_{av}$  Therefore neutral axis lies in the flange

Neutral axis depth:  $x = \frac{N_{pl,a} - N_{cf}}{2b f_y}$

Take moments about the base of the bottom flange of the steel beam:

$$M_{pl,Rd} = (N_{cf} \times (h + h_p + \frac{h_s - h_p}{2})) - (((h - 2t_f) \times t_w) \times f_y \times \frac{h}{2}) - (t_f \times b \times f_y) \times \frac{t_f}{2} + (x \times b \times f_y) \times (h - \frac{x}{2}) - (((t_f - x) \times t_f \times b) \times (h - x - \frac{t_f - x}{2}))$$

Since  $N_{a,Rd} > N_{c.s.Rd}$  and  $N_{w,Rd} < N_{c.s.Rd}$  the PNA lies in the steel Flange

PNA depth  $z := \frac{(N_{a,Rd} - N_{c.s.Rd})}{(2 \cdot b_f \cdot f_{y,beam})} = 10.9 \text{ mm}$

Take moments about the base of the bottom flange of the steel beam:

$$M_1 := N_{c.s.Rd} \cdot \left( h + h_p + \frac{h_s - h_p}{2} \right) = 472 \text{ kN} \cdot \text{m}$$

$$M_2 := \left( ((h - 2 \cdot t_f) \cdot t_w) \cdot f_{y,beam} \cdot \frac{h}{2} \right) = 123 \text{ kN} \cdot \text{m}$$

$$M_3 := \left( (t_f \cdot b_f \cdot f_{y,beam}) \cdot \frac{t_f}{2} \right) = 6 \text{ kN} \cdot \text{m}$$

$$M_4 := \left( (z \cdot b_f \cdot f_{y,beam}) \cdot \left( h - \frac{z}{2} \right) \right) = 197 \text{ kN} \cdot \text{m}$$

$$M_5 := \left( ((t_f - z) \cdot (f_{y,beam} \cdot b_f)) \cdot \left( h - z - \frac{t_f - z}{2} \right) \right) = 49 \text{ kN} \cdot \text{m}$$

$M_{pl,Rd,2} := M_1 - M_2 - M_3 + M_4 - M_5 = 491 \text{ kN} \cdot \text{m}$

**4.4. Bending resistance for partial shear connection**

Use linear interpolation:

For partial shear connection, the bending resistance of the composite section is obtained by interpolation between that of the steel section and that of the composite section with full shear connection.

$M_{Rd,high} := M_{pl,a,Rd} + 0.4 \cdot (M_{pl,Rd,1} - M_{pl,a,Rd}) = 374.4 \text{ kN} \cdot \text{m}$

$M_{Ed} = 116.766 \text{ kN} \cdot \text{m}$

Since  $M_{Rd,high} \geq M_{Ed} = 1$  the design bending resistance at mid-span is satisfactory.  
 (Note: 1 means it is true and 0 means not true)

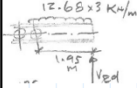
### 5. Design of beam at circular opening (composite stage)

#### 5.1. Design effects

Bending moment at the centreline of opening ( $x_{0.4} := S = 248.32 \text{ mm}$ ) is:

$$W = 12.46 \frac{\text{kN}}{\text{m}^2} \quad \text{---} \quad b = 3 \text{ m} \quad \text{---} \quad V_{Ed} = 93 \text{ kN}$$

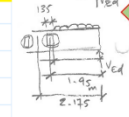
$$M_{Ed.o} := V_{Ed} \cdot x_{0.4} - W \cdot b \cdot \frac{x_{0.4}^2}{2} = 22 \text{ kN} \cdot \text{m}$$



Shear force at edge of equivalent opening

4 (at  $x_{0.4} - \frac{l_c}{2} = 0.192 \text{ m}$ ) is:

$$V_{Ed.o} := V_{Ed} - W \cdot b \cdot \left( x_{0.4} - \frac{l_c}{2} \right) = 86.2 \text{ kN}$$



#### 5.2. Section classification

The top flange is Class 2, due to its attachment to the slab (shear connectors in mid-outstand at 300 mm spacing along the beam).

Classification of web outstand of the top Tee in Vierendeel bending (ignoring axial compression): For the web to be Class 2, independent of its depth:

$$l_{o,eff} \leq 32 \cdot \epsilon \cdot t_w \quad \text{---} \quad l_{o,eff} = 173.824 \text{ mm} \quad \text{Where} \quad \epsilon := \sqrt{\frac{235 \cdot N}{f_{y,beam} \cdot \text{mm}^2}} = 0.814$$

Therefore  $32 \cdot \epsilon \cdot t_w = 205.7 \text{ mm}$  then  $32 \cdot \epsilon \cdot t_w > l_{o,eff} = 1$

(Note: 1 means it is true and 0 means not true)

Table 3.2  
page 39  
P355

The Tee is Class 2 in Vierendeel bending. The bottom Tee is thus also Class 2, irrespective of the tension force in the Tee (which would improve the classification).

#### 5.3. Bending resistance at centreline of circular opening

##### Resistances of section at the opening

P355  
Eq.  
(5)

• Tensile resistance of bottom Tee (The axial resistance of the Top Tee)

$$N_{b,T,Rd} := \frac{A_{T,e.o} \cdot f_{y,beam}}{\gamma_{m0}} = 908 \text{ kN}$$

• The compressive resistance of the effective width of slab at the opening  
Neglecting  $b_0 = 100 \text{ mm}$ , the effective width is given by

$$L_e = 2.819 \text{ m} \quad \text{---} \quad x_{0.4} = 248.32 \text{ mm} \quad \text{---} \quad b_{eff.o} := \left( 3 \cdot \frac{L}{16} \right) + \frac{x_{0.4}}{4} = 1000 \text{ mm}$$

P355  
Eq.  
(6)

$$N_{c,Rd} := \min \left( 0.85 \cdot \frac{f_{ck}}{\gamma_c} \cdot b_{eff.o} \cdot h_c \right) \cdot (n_{sc.o,Low} \cdot P_{Rd,eff})$$

$$N_{c,Rd.o1} := \left( 0.85 \cdot \frac{f_{ck}}{\gamma_c} \cdot b_{eff.o} \cdot h_c \right) = 920 \text{ kN} \quad \text{---or---}$$

$$N_{c,Rd.o,Low.2} := n_{sc.o,Low} \cdot P_{Rd,eff} = 0 \text{ kN} \quad \text{No shear studs above web opening}$$

$$\text{Thus } N_{c,Rd.o,Low} := \min(N_{c,Rd.o1}, N_{c,Rd.o,Low.2}) = 0 \text{ kN}$$

P355  
Eq.  
(9)

• Plastic bending resistance of composite at the web opening

$$M_{c,Rd.o,Low} := (N_{b,T,Rd} \cdot h_{eff}) + (N_{c,Rd.o,Low} \cdot (z_{el} + h_s - 0.5 \cdot h_c)) = 265 \text{ kN} \cdot \text{m}$$

This bending resistance is adequate at opening

$$M_{c,Rd.o,Low} > M_{Ed.o} = 1$$

(Note: 1 means it is true and 0 means not true)

For the consideration of coexistent global bending, Vierendeel bending and shear at opening, the design tension force in the bottom Tee is required.

For Case 2, the value of  $N_{bT.Ed}$  is given by the following (unless this exceeds  $N_{c.Rd.o}$ , see Section 3.2.2)

$$N_{bT.Ed} := \frac{M_{Ed.o}}{(h_{eff} + z_{el} + h_s - 0.5 \cdot h_c)} = 53.924 \text{ kN}$$

$$N_{bT.Ed} > N_{c.Rd.o} = 0$$

(Note: 1 means it is true and 0 means not true)

thus NO need to use Eq. (10) to determine the force in the bottom Tee for Low composite. Note I didn't use  $N_{c.Rd.o.Lov.2} = 0 \text{ kN}$  because it is 0

P355  
Eq. (8)

#### 5.4. Shear resistance of perforated composite beam section

I have to solve it as there is a problem in units

The design shear resistance is the sum of the resistances of the top and bottom Tees and the concrete slab:  $V_{Rd.o} := V_{b.T.Rd} + V_{t.T.Rd} + V_{c.Rd}$

1. Plastic shear resistance of a Tee section is given by:

$$V_{pl.Rd.o} = V_{t.T.Rd} = V_{b.T.Rd}$$

3-1-1/  
§6.2.6

$$V_{pl.Rd.o} := \frac{A_{v.T} \cdot \frac{f_{y.beam}}{\sqrt{3}}}{\gamma_{m0}} = 71.5 \text{ kN}$$

P355  
Eq. (12)

1. Shear resistance of the concrete slab at an opening

$$V_{c.Rd} := \left[ C_{Rd.o} \cdot k \cdot (100 \rho_1 \cdot f_{ck})^{\frac{1}{3}} + k_1 \cdot \sigma_{cp} \right] \cdot b_w \cdot h_c$$

(13)


With a minimum value of:

$$V_{c.Rd.min} := [v_{min} + k_1 \cdot \sigma_{cp}] \cdot b_w \cdot h_c$$


$h_{s,eff} := 0.75 \cdot h_s = 105 \text{ mm}$   
**Effective width of the slab**  
 $b_w := b_f + 2 \cdot h_{s,eff} = 376.9 \text{ mm}$

2-1-1/  
 Table  
 NA.1  
 (§6.2.2  
 (1))
  $C_{Rd,c} := \frac{0.18}{\gamma_c} = 0.12 \quad k_1 := 0.15$   
 $d := h_c = 65 \text{ mm}$

2-1-1/  
 §6.2.2  
 (1)
  $k := 1 + \sqrt{\frac{200 \cdot \text{mm}}{d}} = 2.754 \text{ but } k \leq 2 = 0$

(Note: 1 means it is true and 0 means not true)
 

therefore  $k_{limit} := 2$  (I have changed the  $k$  to  $k_{limit}$  as it is greater than limit)
   
 $\rho_1 := A_{sl} \div (1000 \cdot \text{mm} \cdot d) = 0.006$   
 $\rho_1 \leq 0.02 = 1$

(Note: 1 means it is true and 0 means not true)
 

$b_{eff,o} = 999.6 \text{ mm}$

The value of the first term in the expression for  $V_{c,Rd}$

$$y := \left( \frac{(100 \cdot \rho_1 \cdot f_{ck})^{\frac{1}{3}} \cdot C_{Rd,c} \cdot k_{limit}}{\frac{\text{kg}}{\text{m}^3 \cdot \text{s}^3}} \right) \cdot 10^{-2} \cdot \frac{\text{N}}{\text{mm}^2} = 0.593 \frac{\text{N}}{\text{mm}^2}$$

I have to solve it like this as there is a problem in the units and I need the results in N/mm<sup>2</sup>

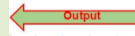
The value of the first term in the expression for the minimum value,  $v_{min}$  is:
   
 2-1-1/  
 Table  
 NA.1  
 (§6.2.2  
 (1))
 
$$v_{min} := \left( \frac{0.035 \cdot \left(k_{limit}^{\frac{3}{2}}\right) \cdot (\sqrt{f_{ck}})}{\frac{\text{m}^2 \cdot \text{s}}{\text{kg}^{\frac{1}{2}}}} \right) \cdot 10^3 = 0.495 \frac{\text{N}}{\text{mm}^2}$$

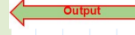
I have to solve it like this as there is a problem in the units and I need the results in N/mm<sup>2</sup>

So, use  $y = 0.59 \frac{\text{N}}{\text{mm}^2}$


From above, assuming no compression in the top Tee, the force in the slab at the opening equals the force in the bottom Tee  $N_{bT,Ed} = 53.924 \text{ kN}$

$\sigma_{cp} := (N_{bT,Ed}) \div (b_{eff,o} \cdot h_c) = 0.83 \frac{\text{N}}{\text{mm}^2}$   
 $k_1 \cdot \sigma_{cp} = 0.124 \frac{\text{N}}{\text{mm}^2}$

Total shear strength of concrete is:  
 $V_{c,Rd} := (y + k_1 \cdot \sigma_{cp}) \cdot b_w \cdot h_c = 17.6 \text{ kN}$ 


Hence, Shear resistance of perforated composite beam section because  $V_{pl,Rd,o} = V_{bT,Rd} = V_{lT,Rd}$ 


$V_{Rd,o} := 2 \cdot V_{pl,Rd,o} + V_{c,Rd} = 160.5 \text{ kN}$

$V_{Rd,o} > V_{Ed} = 1$  it is safe  
 $V_{Ed} = 93.413 \text{ kN}$ 


(Note: 1 means it is true and 0 means not true)

**5.5. Bending resistance of Tees (Vierendeel bending resistance)**

Vierendeel bending resistance at web opening for steel section  $M_{V.T.Rd} := M_{V.t.T.Rd} + M_{V.b.T.Rd}$

Vierendeel bending resistance at web opening for composite section  $M_{V.c.Rd}$

Initial assumption of distribution of shear force

Since the shear force in each Tee  $V_{T.Ed} := \frac{V_{Ed.o}}{2} = 43.111 \text{ kN}$

$V_{T.Ed} < V_{pl.Rd} = ?$  it is safe

(Note: 1 means it is true and 0 means not true)

Then, the web thickness does not need to be reduced when determining plastic bending resistance and axial resistance. If the shear force in the bottom Tee is limited by Vierendeel bending resistance across the Tee, the shear forces may need to be redistributed.

- Plastic bending resistance of an unstiffened Tee, in the absence of axial force and high shear  $M_{V.T.Rd}$

For a Class 1 and 2 cross section, the plastic bending resistance of an unstiffened Tee  $M_{V.T.Rd} = M_{t.T.Rd} = M_{b.T.Rd}$ , in the absence of axial force and high shear.

Hence: Vierendeel bending resistance at web opening for steel section

P355 Eq. (19)  $M_{V.t.T.Rd} := \left( \frac{A_{w.T} \cdot f_{y.beam}}{\gamma_{m0}} \right) \cdot (0.5 \cdot h_{w.T} + t_f - z_{pl}) + \left( \frac{A_f \cdot f_{y.beam}}{\gamma_{m0}} \right) \cdot \left( 0.5 \cdot t_f - z_{pl} + \frac{z_{pl}^2}{t_f} \right) = 4.6 \text{ kN}\cdot\text{m}$

- The plastic bending resistance of the bottom Tee is reduced for axial tension, as follows:

P355 Eq. (26)  $M_{V.b.T.Rd} := M_{V.t.T.Rd} \cdot \left( 1 - \left( \frac{N_{b.T.Ed}}{N_{b.T.Rd}} \right)^2 \right) = 4.5 \text{ kN}\cdot\text{m}$

The plastic resistance of the top Tee is not reduced for axial force and thus:  $M_{V.t.T.Rd} = 4.6 \text{ kN}\cdot\text{m}$

- Vierendeel bending resistance at web opening for composite section  $M_{V.c.Rd}$

The compression force developed in the slab due to composite action over the opening  $\Delta N_{c.Rd}$

the number of shear studs above the web opening  $n_{sc.o} := 0$

$\Delta N_{c.Rd} := n_{sc.o} \cdot P_{Rd,eff} = 0 \text{ kN}$

P355 Eq. (25) For unstiffened openings, reduction factor due to the length of the openings  $k_o$  is given by  $k_o := 1 - \frac{l_{o,eff}}{(25 \cdot h_T)} = 0.84$

where  $z_i := t_f = 13.7 \text{ mm}$

P355 Eq. (24) Vierendeel bending resistance due to local composite action is given by:  $M_{V.c.Rd} := \Delta N_{c.Rd} \cdot (h_s + z_i - 0.5 \cdot h_c) \cdot k_o = 0 \text{ kN}\cdot\text{m}$

**5.6. Verification of resistance to Vierendeel bending**

The criterion for adequacy of Vierendeel bending resistance is:

P355 Eq. (14)  $M_{V.Rd,high} := 2 \cdot M_{V.t.T.Rd} + 2 \cdot M_{V.b.T.Rd} + M_{V.c.Rd} = 18.224 \text{ kN}\cdot\text{m}$  (with composite slab)  $V_{Ed.o} \cdot l_e = 9.635 \text{ kN}\cdot\text{m}$

$M_{V.Rd,high} \geq V_{Ed.o} \cdot l_e = 1$  it is safe

### Plastic analysis of composite beams with partial shear connection according to SCI-P428

$$N_{c,f} := \min(N_{c.s.Rd}, N_{a.Rd}) = (1.151 \cdot 10^3) \text{ kN}$$

$$\eta_{high.p428} := \frac{k_{flex} \cdot P_{Rd} \cdot \eta_{sc.high}}{N_{c,f}} = 0.374$$

is the design value of the plastic resistance of the clear depth of the steel web to normal force

$$N_{pl.d} := f_{y,beam} \cdot d_w \cdot t_w = 743.753 \text{ kN}$$

$$z_{pl1} := \frac{h}{2} + h_c + h_p - \frac{\eta_{high.p428} \cdot N_{c.s.Rd}}{N_{pl.d}} \cdot \frac{d_w}{2} = 203.5 \text{ mm}$$

$$\eta_{high.p428} \cdot N_{c,f} < N_{w.Rd} = 1$$

(Note: 1 means it is true and 0 means not true)

**Then**

**Case 1: plastic neutral axis within the web**

$$x1 := M_{pl.a.Rd} = 300.33 \text{ kN} \cdot \text{m}$$

$$x2 := \eta_{high.p428} \cdot N_{c,f} \cdot \left( \frac{h}{2} + h_c + h_p \right) = 120.482 \text{ kN} \cdot \text{m}$$

$$x3 := \left( \eta_{high.p428} \cdot N_{c,f} \right)^2 \cdot \left( \frac{h_c}{2 \cdot N_{c.s.Rd}} + \frac{d_w}{4 \cdot f_{y,beam} \cdot d_w \cdot t_w} \right) = 21.702 \text{ kN} \cdot \text{m}$$

$$M_{pl,\eta.Rd} := x1 + x2 - x3 = 399.1 \text{ kN} \cdot \text{m}$$

## 6. Results Summary

### • Resistances

Compressive resistance of slab

$$N_{c.s.Rd} = 1151 \text{ kN}$$

Tensile resistance of steel section

$$N_{a.Rd} = 2442.4 \text{ kN}$$

Vertical shear resistance

$$V_{pl.o.Rd} = 545 \text{ kN}$$

Bending resistance of steel section

$$M_{pl.a.Rd} = 300 \text{ kN}\cdot\text{m}$$

Bending resistance of composite solid webbed section

$$M_{pl.Rd.1} = 485.5 \text{ kN}\cdot\text{m} \text{ (neglecting the contribution from the part of the top flange that in compression)}$$

$$M_{pl.Rd.2} = 491.1 \text{ kN}\cdot\text{m} \text{ (using stress block method)}$$

Bending resistance for partial connections

$$M_{Rd.high} = 374.4 \text{ kN}\cdot\text{m}$$

Tensile resistance of bottom Tee (The axial resistance of the Top Tee)

$$N_{b.T.Rd} = 907.8 \text{ kN}$$

The compressive resistance of the effective width of slab at the opening

$$N_{c.Rd.o.Low} = 0 \text{ kN}$$

Plastic bending resistance of steel section at the web opening

$$M_{a.Rd.o} = 257.1 \text{ kN}\cdot\text{m}$$

Plastic bending resistance of composite section at the web opening

$$M_{c.Rd.o.Low} = 265.3 \text{ kN}\cdot\text{m}$$

Total shear strength of concrete is:

$$V_{c.Rd} = 17.6 \text{ kN}$$

Shear resistance of perforated beam section

$$V_{Rd.o.steel} := 2 \cdot V_{pl.Rd.o} = 142.9 \text{ kN}$$

Shear resistance of perforated composite beam section

$$V_{Rd.o} = 160.5 \text{ kN}$$

Vierendeel bending resistance perforated composite beam section

$$M_{V.Rd.steel} := 2 \cdot M_{V.l.T.Rd} + 2 \cdot M_{V.b.T.Rd} = 18.2 \text{ kN}\cdot\text{m}$$

Vierendeel bending resistance perforated composite beam section

$$M_{V.Rd.high} = 18.2 \text{ kN}\cdot\text{m}$$

Plastic analysis of composite solid webbed beams with partial shear connection according to SCI-P428

$$M_{pl,q.Rd} = 399.11 \text{ kN}\cdot\text{m}$$

### • Design values

Maximum shear force

$$V_{Ed} = 93.41 \text{ kN}$$

Maximum moment (mid-span)

$$M_{Ed} = 116.77 \text{ kN}\cdot\text{m}$$

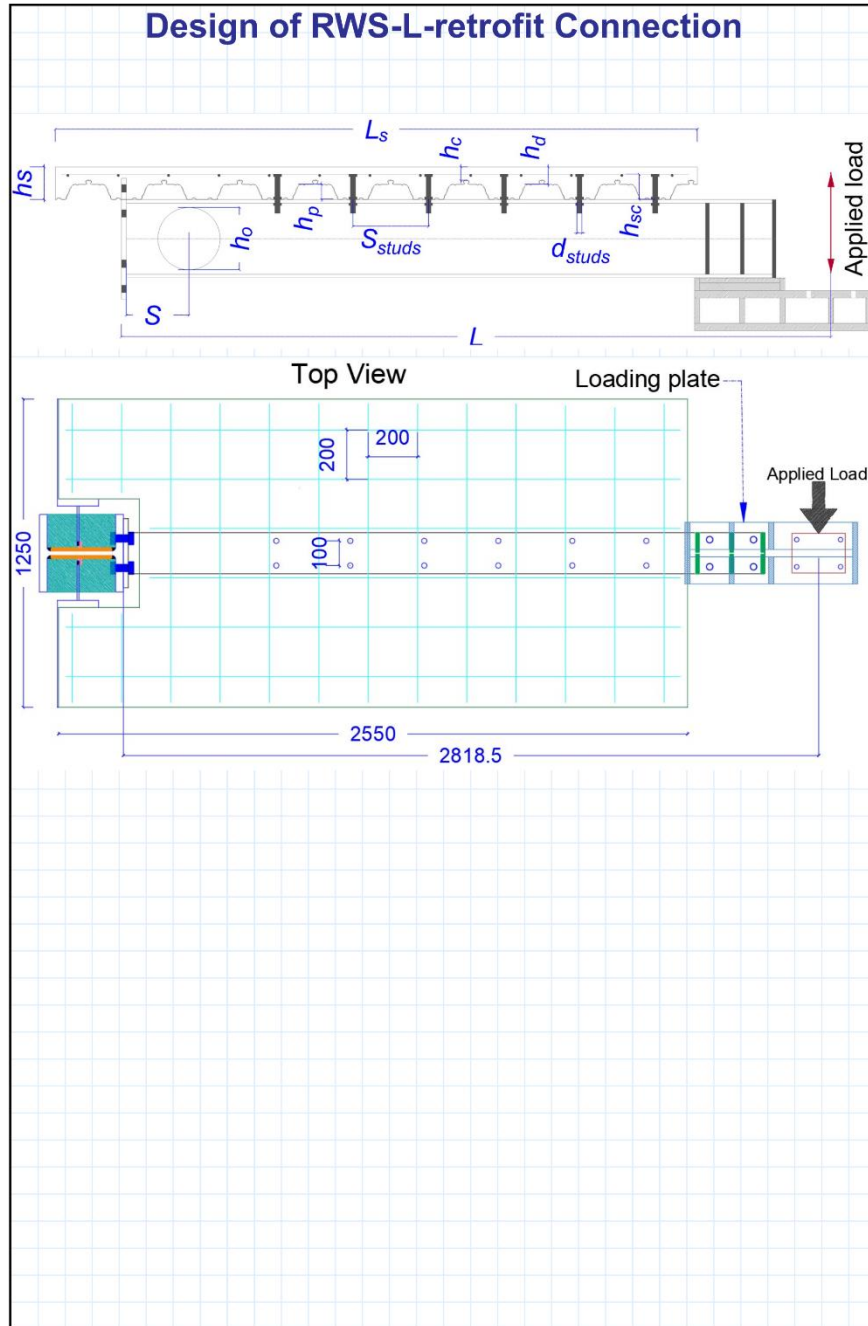
Shear force at edge of equivalent opening

$$V_{Ed.o} = 86.22 \text{ kN}$$

Bending moment at the centreline of opening

$$M_{Ed.o} = 22.04 \text{ kN}\cdot\text{m}$$





## 1. Dimensions and properties (Inputs)

### 1.1. General dimensions

Beam span	$L := 5000 \text{ mm}$
Beam span to loading point	$L_a := 2818.5 \text{ mm}$
Beam spacing	$b := 3000 \text{ mm}$
Slab depth	$h_s := 140 \text{ mm}$
Slab span	$L_s := 5000 \text{ mm}$
Effective slab width	$b_{eff} := (L) \div 4 = 1.25 \text{ m}$

• **Profiled Metal Deck - Tata Steel ComFlor60**

Profile weight	$m_d := 0.1 \frac{\text{kN}}{\text{m}^2}$
Deck depth	$h_p := 60 \text{ mm}$
Slab depth above profile	$h_c := 65 \text{ mm}$
Overall height of sheeting profile	$h_d := 75 \text{ mm}$
Deck thickness	$t := 0.9 \text{ mm}$
Average trough width	$b_{o,deck} := 145 \cdot \text{mm}$
Yield strength	$f_{y,decking} := 350 \frac{\text{N}}{\text{mm}^2}$

• **Bolted Shear Studs M20 Gr.8.8**

Connector effective diameter	$d_{studs} := 17.7 \text{ mm}$
Height of shear connectors	$h_{sc} := 100 \text{ mm}$
Longitudinal spacing of studs	$S_{studs} := 300 \text{ mm}$
Transverse spacing of studs:	$b_0 := 100 \text{ mm}$
width for end-post	$S_e := 186 \text{ mm}$
# of stud in one rib	$n_r := 2$
Tensile stress area of the bolt	$A_{studs} := 245 \text{ mm}^2$
Ultimate strength	$f_{u,studs} := 800 \frac{\text{N}}{\text{mm}^2}$

• **Mesh A393 to BS 4483**

Weight	$m_m := 0.06 \frac{\text{kN}}{\text{m}^2} \quad A_{st} := 393 \text{ mm}^2$
--------	---

### 1.2. Section properties of the beam

• **Beam size 457 x 191 UB 74 kg/m UB:**

Depth	$h := 310.4 \text{ mm}$	Second moment of area	$I_y := 11700 \cdot 10^4 \cdot \text{mm}^4$
Breadth	$b_f := 166.9 \text{ mm}$	Elastic section modulus	$W_{el,y} := 754000 \text{ mm}^3$
Flange thickness	$t_f := 13.7 \text{ mm}$	Plastic section modulus	$W_{pl,y} := 846000 \text{ mm}^3$
Web thickness	$t_w := 7.9 \text{ mm}$	Shear area	$A_v := 2659 \text{ mm}^2$
Root radius	$r := 8.9 \text{ mm}$		
Clear depth of web	$d_w := 265.2 \text{ mm}$		
Cross-sectional area	$A_a := 6880 \cdot \text{mm}^2$	Weight	$m_{beam} := \frac{0.54 \cdot \frac{\text{kN}}{\text{m}}}{b} = 0.18 \frac{\text{kN}}{\text{m}^2}$

### 1.3. Material properties

Steel grade S355

$f_{y,beam} := 355 \frac{\text{N}}{\text{mm}^2}$	$E_{beam} := 210 \frac{\text{N}}{\text{mm}^2}$
--	--

Concrete grade C25/30

$f_{ck} := 25 \frac{\text{N}}{\text{mm}^2}$	$E_{cm} := 31 \frac{\text{N}}{\text{mm}^2}$
---	---

### 1.4. Partial factors

$\gamma_v := 1.25$	$\gamma_c := 1.5$
$\gamma_{m2} := 1.25$	$\gamma_{m0} := 1$
$\xi_{material} := 0.925$	

Vertical shear resistance

$$V_{pl.a,Rd} := \frac{A_v \cdot \left( \frac{f_{y,beam}}{\sqrt{3}} \right)}{\gamma_{m0}} = 544.987 \text{ kN}$$

### 1.5. Dimensions and properties of web opening:

- Diameter of opening  $h_o := h \cdot 0.8 = 248.32 \text{ mm}$
- Edge-to-edge spacing  $S_o := 0 \text{ mm}$
- Equivalent rectangular opening length  $l_e := 0.45 \cdot h_o = 111.744 \text{ mm}$
- End distance to web opening centreline  $S := 1 \cdot h = 310.4 \text{ mm}$
- Height of equivalent rectangular opening  $h_{e.o} := 0.9 \cdot h_o = 223.488 \text{ mm}$
- Effective length of opening  $l_{o,eff} := 0.7 \cdot h_o = 173.824 \text{ mm}$

- Area of each of the two Tees (neglecting radius, using in Tensile resistance of bottom Tee)

$$A_{T,e.o} := \frac{(A_a - h_{e.o} \cdot t_w)}{2} = 2557.222 \text{ mm}^2$$

- Area of each of the two Tees (the full height of the circular opening, neglecting radius - using in shear resistance and perforated composite beam section)

$$A_T := \frac{(A_a - h_o \cdot t_w)}{2} = 2459.136 \text{ mm}^2$$

- Shear Area

$$A_{v,T} := A_T - b_f \cdot t_f + (2 \cdot r + t_w) \cdot 0.5 \cdot t_f = 348.651 \text{ mm}^2$$

- Depth of Tees  $h_T := \frac{(h - h_{e.o})}{2} = 43.456 \text{ mm}$

- Depth of web of Tees  $h_{w,T} := h_T - t_f = 29.756 \text{ mm}$

- Depth of centroid of Tee from flange

$$z_{el} := \frac{\left( b_f \cdot \left( \frac{t_f^2}{2} \right) + \left( t_f + \left( \frac{h_{w,T}}{2} \right) \right) \cdot h_{w,T} \cdot t_w \right)}{A_T} = 9.1 \text{ mm}$$

- Effective depth between centroid of Tees

$$h_{eff} := h - 2 \cdot z_{el} = 292.2 \text{ mm}$$

- The cross sectional area of the flange is

$$A_f := t_f \cdot b_f = 2286.53 \text{ mm}^2$$

- The cross sectional area of web of the Tee is

$$A_{w,T} := h_{w,T} \cdot t_w = 235.072 \text{ mm}^2$$

- The depth of the plastic neutral axis of the Tee from the outer surface of the flange is given by:

$$z_{pl} := \frac{A_f + A_{w,T}}{2 \cdot b_f} = 7.554 \text{ mm}$$

- Plastic bending resistance of steel section at the web opening

$$M_{a,Rd.o} := \left( \frac{f_{y,beam}}{\gamma_{m0}} \right) \cdot \left( W_{pl,y} - \frac{h_o^2 \cdot t_w}{4} \right) = 257.1 \text{ kN} \cdot \text{m}$$

## 2. Actions

### 2.1. Construction stage

• **Permanent action:** ← Output

Self weight of beam  $g_{beam,1} := m_{beam} = 0.18 \frac{kN}{m^2}$

Self weight of decking  $g_{decking,1} := m_d = 0.1 \frac{kN}{m^2}$

Self weight of mesh  $g_{mesh,1} := m_m = 0.06 \frac{kN}{m^2}$

**Total permanent actions**

$$g_{k,1} := g_{beam,1} + g_{decking,1} + g_{mesh,1} = 0.34 \frac{kN}{m^2}$$

• **Variable action:** ← Input

Weight of wet concrete

$$q_{concrete,1} := 25 \frac{kN}{m^3} \cdot 0.097 \cdot \frac{m^2}{m} = 2.425 \frac{kN}{m^2}$$

Construction load

$$q_{construction,1} := 0.75 \frac{kN}{m^2}$$

**Total variable actions**

$$q_{k,1} := q_{concrete,1} + q_{construction,1} = 3.2 \frac{kN}{m^2}$$

### 2.2. Composite stage

• **Permanent action:** ← Output

Self weight of beam  $g_{beam} := m_{beam} = 0.18 \frac{kN}{m^2}$

Self weight of decking  $g_{decking} := m_d = 0.1 \frac{kN}{m^2}$

Self weight of mesh  $g_{mesh} := m_m = 0.06 \frac{kN}{m^2}$

Self weight of Slab

$$q_{slab} := 24 \frac{kN}{m^3} \cdot 0.097 \cdot \frac{m^2}{m} = 2.33 \frac{kN}{m^2}$$

Finishes, services etc.

$$q_{finishes} := 1.3 \frac{kN}{m^2}$$

**Total permanent actions**

$$g_k := g_{beam} + g_{decking} + g_{mesh} + q_{slab} + q_{finishes} = 4 \frac{kN}{m^2}$$

• **Variable action:** ← Input

**Imposed load**

$$q_k := 5.0 \cdot \frac{kN}{m^2}$$

### 2.3. Partial factors for actions

$$\gamma_G := 1.35 \quad \gamma_Q := 1.5 \quad \xi_{actions} := 0.925$$

### 2.4. Design values of combined actions [Outputs]

• **Construction stage**

$$W_1 := \gamma_G \cdot g_{k,1} + \gamma_Q \cdot q_{k,1} = 5.222 \frac{kN}{m^2}$$

• **Composite stage**

$$W := \xi_{actions} \cdot \gamma_G \cdot g_k + \gamma_Q \cdot q_k = 12.455 \frac{kN}{m^2}$$

### 2.5. Design bending moments and shear forces [Outputs]

• **Construction stage**

Maximum shear force

$$V_{Ed,1} := W_1 \cdot b \cdot \frac{L}{2} = 39.2 \text{ kN}$$

Maximum moment (mid-span)

$$M_{Ed,1} := W_1 \cdot b \cdot \frac{L^2}{8} = 49 \text{ m} \cdot \text{kN}$$

• **Composite stage**

Maximum shear force

$$V_{Ed} := W \cdot b \cdot \frac{L}{2} = 93.4 \text{ kN}$$

Maximum moment (mid-span)

$$M_{Ed} := W \cdot b \cdot \frac{L^2}{8} = 117 \text{ m} \cdot \text{kN}$$

### 3. Shear connection

#### 3.1. Shear connector resistance

4-1-1/  
§6.6.3.1(1)  
Eq.(6.18)

Shear resistance of a headed stud connector ( $P_{Rd}$ ) is the smaller of:

$$(1) P_{Rd,1} := 0.8 \cdot f_{u, studs} \cdot \frac{\left(\pi \cdot \frac{d_{studs}^2}{4}\right)}{\gamma_v} = 125.981 \text{ kN}$$

or

4-1-1/  
§6.6.3.1  
(1)  
Eq.(6.21)

$$\frac{h_{sc}}{d_{studs}} = 5.65 \text{ if } \frac{h_{sc}}{d_{studs}} > 4 = 1 \text{ Therefore } \alpha := 1 \text{ Input}$$

(Note: 1 means it is true and 0 means not true)

4-1-1/  
§6.6.3.1(1)  
Eq.(6.19)

$$(2) P_{Rd,2} := 0.29 \cdot \alpha \cdot d_{studs}^2 \cdot \frac{\left(\sqrt{f_{ck} \cdot E_{cm} \cdot 1000}\right)}{\gamma_v} = 63.986 \text{ kN}$$

Therefore, the shear resistance of a shear connector in a solid slab is

$$P_{Rd,min} := \min(P_{Rd,1}, P_{Rd,2}) = 63.986 \text{ kN}$$

- Reduction factor due to decking profile – decking ribs transverse to the supporting beams:

The number of stud in one rib at a beam intersection (no greater than 2)

$$n_r = 2$$

Average trough width  $b_{o,deck} = 145 \text{ mm}$

4-1-1  
§6.6.4.2(1)  
Eq.(6.23)

$$k_{t,1} := \left(\frac{0.7}{\sqrt{n_r}}\right) \cdot \left(\frac{b_{o,deck}}{h_p}\right) \cdot \left(\frac{h_{sc}}{h_p} - 1\right) = 0.797$$

SCI P428  
Eq. (3.12)

However, the upper limit for  $k_t$  is 0.6 when  $n_r = 2$ , and sheet thickness  $\leq 1.0 \text{ mm}$ . Therefore,  $k_t := 0.6$  and the shear resistance of a single shear connector, when placed in pairs per decking rib, is:

BS EN  
1994-1-1  
Table 6.2  
SCI P428  
Eq.(3.11)

$$P_{Rd} := P_{Rd,min} \cdot k_t = 38.392 \text{ kN}$$

However, The shear connectors are non-ductile but satisfy the requirement of a slip capacity of 6 mm. Therefore, use  $P_{Rd,eff} := P_{Rd} \cdot k_{flex}$  for plastic design for uniform spacing  $k_{flex} := 0.8$

SCI P428 Eq.(3.11)

$$P_{Rd,eff} := P_{Rd} \cdot k_{flex} = 30.713 \text{ kN}$$

#### 3.2. Number of shear connectors

$$n_r = 2$$

$$n_{row,Low} := 6$$

$$n_{row,high} := 7$$

$$n_{sc,Low} := n_r \cdot n_{row,Low} = 12$$

$$n_{sc,high} := n_r \cdot n_{row,high} = 14$$

From face of column to the end of web opening

$$n_{sc,o,Low} := 0$$

$$n_{sc,o,high} := 2$$

### 4. Bending resistance at mid-span (composite stage)

#### Solid webbed section (without opening)

#### 4.1. Resistances of sections

- Effective width of compression flange at mid-span, ignoring spacing of studs  $b_{eff} = 1.25 \text{ m}$
- Compressive resistance of slab**  

$$N_{c.s.Rd} := \frac{0.85 \cdot f_{ck} \cdot b_{eff} \cdot h_c}{\gamma_c} = 1151.042 \text{ kN}$$
- Tensile resistance of steel section**  

$$N_{a.Rd} := \frac{A_a \cdot f_{y,beam}}{\gamma_{m0}} = 2442.4 \text{ kN}$$

Since  $N_{a.Rd} > N_{c.s.Rd} = 1$  the PNA lies in the **steel section**

(Note: 1 means it is true and 0 means not true)

- Tensile resistance of steel flange:**  

$$N_{f.Rd} := \frac{b_f \cdot t_f \cdot f_{y,beam}}{\gamma_{m0}} = 811.718 \text{ kN}$$
- Tensile resistance of steel web**  

$$N_{w.Rd} := N_{a.Rd} - (2 \cdot N_{f.Rd}) = 818.964 \text{ kN}$$

Since  $N_{a.Rd} > N_{c.s.Rd} = 1$  and  $N_{w.Rd} < N_{c.s.Rd} = 1$  the PNA lies in the **steel Flange**

(Note: 1 means it is true and 0 means not true)

---

#### 4.2. Degree of shear connection

$N_{c,max,Low} := n_{sc,Low} \cdot P_{Rd,eff} = 368.6 \text{ kN}$

The degree of shear connection at mid-span is

$\eta_{Low} := \frac{N_{c,max,Low}}{N_{c.s.Rd}} = 0.32$

---

#### 4.3. Bending resistance for full shear connection

- Bending resistance of steel section**  $M_{pl,a.Rd} := W_{pl,y} \cdot \frac{f_{y,beam}}{\gamma_{m0}} = 300 \text{ kN} \cdot \text{m}$
- Bending resistance of composite solid webbed section**

Taking moments about the top flange (neglecting the contribution from the part of the top flange that is in compression)  $M_{pl,Rd,1} := N_{c.s.Rd} \cdot \left( \frac{h_c}{2} + h_p \right) + N_{a.Rd} \cdot \frac{h}{2} = 485.5 \text{ kN} \cdot \text{m}$

**Using Stress-Block Method:**

**P.N.A. Lies in the Steel flange**

$N_{pl,a} > N_{cf}$  Therefore neutral axis lies in the steel beam  
 $N_{pl,a} > N_{cf} \geq N_{av}$  Therefore neutral axis lies in the flange

Neutral axis depth:  $x = \frac{N_{pl,a} - N_{cf}}{2b f_y}$

Take moments about the base of the bottom flange of the steel beam:

$$M_{pl,Rd} = (N_{cf} \times (h + h_p + \frac{h_s - h_p}{2})) - (((h - 2t_f) \times t_w) \times f_y \times \frac{h}{2}) - (t_f \times b \times f_y) \times \frac{t_f}{2} + (x \times b \times f_y) \times (h - \frac{x}{2}) - (((t_f - x) \times f_y \times b) \times (h - x - \frac{t_f - x}{2}))$$

Since  $N_{a,Rd} > N_{c.s.Rd}$  and  $N_{w,Rd} < N_{c.s.Rd}$  the PNA lies in the steel Flange

PNA depth  $z := \frac{(N_{a,Rd} - N_{c.s.Rd})}{(2 \cdot b_f \cdot f_{y,beam})} = 10.9 \text{ mm}$

Take moments about the base of the bottom flange of the steel beam:

$$M_1 := N_{c.s.Rd} \cdot \left( h + h_p + \frac{h_s - h_p}{2} \right) = 472 \text{ kN} \cdot \text{m}$$

$$M_2 := \left( ((h - 2 \cdot t_f) \cdot t_w) \cdot f_{y,beam} \cdot \frac{h}{2} \right) = 123 \text{ kN} \cdot \text{m}$$

$$M_3 := \left( (t_f \cdot b_f \cdot f_{y,beam}) \cdot \frac{t_f}{2} \right) = 6 \text{ kN} \cdot \text{m}$$

$$M_4 := \left( (z \cdot b_f \cdot f_{y,beam}) \cdot \left( h - \frac{z}{2} \right) \right) = 197 \text{ kN} \cdot \text{m}$$

$$M_5 := \left( ((t_f - z) \cdot (f_{y,beam} \cdot b_f)) \cdot \left( h - z - \frac{t_f - z}{2} \right) \right) = 49 \text{ kN} \cdot \text{m}$$

$M_{pl,Rd,2} := M_1 - M_2 - M_3 + M_4 - M_5 = 491 \text{ kN} \cdot \text{m}$

**4.4. Bending resistance for partial shear connection**

Use linear interpolation:

For partial shear connection, the bending resistance of the composite section is obtained by interpolation between that of the steel section and that of the composite section with full shear connection.

$M_{Rd,high} := M_{pl,a,Rd} + 0.4 \cdot (M_{pl,Rd,1} - M_{pl,a,Rd}) = 374.4 \text{ kN} \cdot \text{m}$

$M_{Ed} = 116.766 \text{ kN} \cdot \text{m}$

Since  $M_{Rd,high} \geq M_{Ed} = 1$  the design bending resistance at mid-span is satisfactory.  
 (Note: 1 means it is true and 0 means not true)

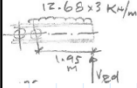
## 5. Design of beam at circular opening (composite stage)

### 5.1. Design effects

Bending moment at the centreline of opening ( $x_{0.4} := S = 310.4 \text{ mm}$ ) is:

$$W = 12.46 \frac{\text{kN}}{\text{m}^2} \quad \text{--- } b = 3 \text{ m} \quad \text{--- } V_{Ed} = 93 \text{ kN}$$

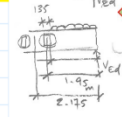
$$M_{Ed.o} := V_{Ed} \cdot x_{0.4} - W \cdot b \cdot \frac{x_{0.4}^2}{2} = 27.2 \text{ kN} \dots$$



Shear force at edge of equivalent opening

4 (at  $x_{0.4} - \frac{l_c}{2} = 0.255 \text{ m}$ ) is:

$$V_{Ed.o} := V_{Ed} - W \cdot b \cdot \left( x_{0.4} - \frac{l_c}{2} \right) = 83.9 \text{ kN}$$



### 5.2. Section classification

The top flange is Class 2, due to its attachment to the slab (shear connectors in mid-outstand at 300 mm spacing along the beam).

Classification of web outstand of the top Tee in Vierendeel bending (ignoring axial compression): For the web to be Class 2, independent of its depth:

$$l_{o,eff} \leq 32 \cdot \epsilon \cdot t_w \quad \text{--- } l_{o,eff} = 173.824 \text{ mm} \quad \text{Where } \epsilon := \sqrt{\frac{235 \cdot N}{f_{y,beam} \cdot \text{mm}^2}} = 0.814$$

Therefore  $32 \cdot \epsilon \cdot t_w = 205.7 \text{ mm}$  then  $32 \cdot \epsilon \cdot t_w > l_{o,eff} = 1$

(Note: 1 means it is true and 0 means not true)

Table 3.2  
page 39  
P355

The Tee is Class 2 in Vierendeel bending. The bottom Tee is thus also Class 2, irrespective of the tension force in the Tee (which would improve the classification).

### 5.3. Bending resistance at centreline of circular opening

#### Resistances of section at the opening

P355  
Eq.  
(5)

• Tensile resistance of bottom Tee (The axial resistance of the Top Tee)

$$N_{b,T,Rd} := \frac{A_{T,e.o} \cdot f_{y,beam}}{\gamma_{m0}} = 908 \text{ kN}$$

• The compressive resistance of the effective width of slab at the opening  
Neglecting  $b_0 = 100 \text{ mm}$ , the effective width is given by

$$L_e = 2.819 \text{ m} \quad \text{--- } x_{0.4} = 310.4 \text{ mm} \quad \text{--- } b_{eff,o} := \left( 3 \cdot \frac{L}{16} \right) + \frac{x_{0.4}}{4} = (1 \cdot 10^3) \text{ mm}$$

P355  
Eq.  
(6)

$$N_{c,Rd} := \min \left( 0.85 \cdot \frac{f_{ck}}{\gamma_c} \cdot b_{eff,o} \cdot h_c \right) \cdot (n_{sc,o,Low} \cdot P_{Rd,eff})$$

$$N_{c,Rd,o1} := \left( 0.85 \cdot \frac{f_{ck}}{\gamma_c} \cdot b_{eff,o} \cdot h_c \right) = 935 \text{ kN} \quad \text{---or---}$$

$$N_{c,Rd,o,Low,2} := n_{sc,o,Low} \cdot P_{Rd,eff} = 0 \text{ kN} \quad \text{No shear studs above web opening}$$

$$\text{Thus } N_{c,Rd,o,Low} := \min(N_{c,Rd,o1}, N_{c,Rd,o,Low,2}) = 0 \text{ kN}$$

P355  
Eq.  
(9)

• Plastic bending resistance of composite at the web opening

$$M_{c,Rd,o,Low} := (N_{b,T,Rd} \cdot h_{eff}) + (N_{c,Rd,o,Low} \cdot (z_{el} + h_s - 0.5 \cdot h_c)) = 265 \text{ kN} \cdot \text{m}$$

This bending resistance is adequate at opening

$$M_{c,Rd,o,Low} > M_{Ed,o} = 1$$

(Note: 1 means it is true and 0 means not true)



For the consideration of coexistent global bending, Vierendeel bending and shear at opening, the design tension force in the bottom Tee is required.

For Case 2, the value of  $N_{bT.Ed}$  is given by the following (unless this exceeds  $N_{c.Rd.o}$ , see Section 3.2.2)

$$N_{bT.Ed} := \frac{M_{Ed.o}}{(h_{eff} + z_{el} + h_s - 0.5 \cdot h_c)} = 66.525 \text{ kN}$$

$$N_{bT.Ed} > N_{c.Rd.o} = 0$$

(Note: 1 means it is true and 0 means not true)

thus NO need to use Eq. (10) to determine the force in the bottom Tee for Low composite. Note I didn't use  $N_{c.Rd.o.Lov.2} = 0 \text{ kN}$  because it is 0

P355  
Eq. (8)



### 5.4. Shear resistance of perforated composite beam section

I have to solve it as there is a problem in units

The design shear resistance is the sum of the resistances of the top and bottom Tees and the concrete slab:  $V_{Rd.o} := V_{b.T.Rd} + V_{t.T.Rd} + V_{c.Rd}$

1. Plastic shear resistance of a Tee section is given by:

$$V_{pl.Rd.o} = V_{t.T.Rd} = V_{b.T.Rd}$$

3-1-1/  
§6.2.6

$$V_{pl.Rd.o} := \frac{A_{v.T} \cdot \frac{f_{y.beam}}{\sqrt{3}}}{\gamma_{m0}} = 71.5 \text{ kN}$$

P355  
Eq. (12)

1. Shear resistance of the concrete slab at an opening

$$V_{c.Rd} := \left[ C_{Rd.o} \cdot k \cdot (100 \rho_1 \cdot f_{ck})^{\frac{1}{3}} + k_1 \cdot \sigma_{cp} \right] \cdot b_w \cdot h_c$$

P355  
Eq. (13)

With a minimum value of:

$$V_{c.Rd.min} := [v_{min} + k_1 \cdot \sigma_{cp}] \cdot b_w \cdot h_c$$

2-1-1/  
Table  
NA.1  
(§6.2.2  
(1))

$h_{s,eff} := 0.75 \cdot h_s = 105 \text{ mm}$   
**Effective width of the slab**  
 $b_w := b_f + 2 \cdot h_{s,eff} = 376.9 \text{ mm}$

2-1-1/  
§6.2.2  
(1))

$C_{Rd,c} := \frac{0.18}{\gamma_c} = 0.12 \quad k_1 := 0.15$   
 $d := h_c = 65 \text{ mm}$

$k := 1 + \sqrt{\frac{200 \cdot \text{mm}}{d}} = 2.754 \text{ but } k \leq 2 = 0$

(Note: 1 means it is true and 0 means not true)

therefore  $k_{limit} := 2$  (I have changed the  $k$  to  $k_{limit}$  as it is greater than limit)

$\rho_1 := A_{st} \div (1000 \cdot \text{mm} \cdot d) = 0.006$   
 $\rho_1 \leq 0.02 = 1$   
 (Note: 1 means it is true and 0 means not true)

$b_{eff,o} = 1015.1 \text{ mm}$

The value of the first term in the expression for  $V_{c,Rd}$

$$y := \left( \frac{(100 \cdot \rho_1 \cdot f_{ck})^{\frac{1}{3}} \cdot C_{Rd,c} \cdot k_{limit}}{\frac{\text{kg}}{\text{m}^3 \cdot \text{s}^3}} \right) \cdot 10^{-2} \cdot \frac{\text{N}}{\text{mm}^2} = 0.593 \frac{\text{N}}{\text{mm}^2}$$

I have to solve it like this as there is a problem in the units and I need the results in N/mm2

The value of the first term in the expression for the minimum value,  $v_{min}$  is:

2-1-1/  
Table  
NA.1  
(§6.2.2  
(1))

$$v_{min} := \left( \frac{0.035 \cdot (k_{limit}^{\frac{3}{2}}) \cdot (\sqrt{f_{ck}})}{\frac{\text{m}^2 \cdot \text{s}}{\text{kg}^{\frac{1}{2}}}} \right) \cdot 10^3 = 0.495 \frac{\text{N}}{\text{mm}^2}$$

I have to solve it like this as there is a problem in the units and I need the results in N/mm2

So, use  $y = 0.59 \frac{\text{N}}{\text{mm}^2}$

From above, assuming no compression in the top Tee, the force in the slab at the opening equals the force in the bottom Tee  $N_{bT,Ed} = 66.525 \text{ kN}$

$$\sigma_{cp} := (N_{bT,Ed}) \div (b_{eff,o} \cdot h_c) = 1.01 \frac{\text{N}}{\text{mm}^2}$$

$$k_1 \cdot \sigma_{cp} = 0.151 \frac{\text{N}}{\text{mm}^2}$$

Total shear strength of concrete is:  
 $V_{c,Rd} := (y + k_1 \cdot \sigma_{cp}) \cdot b_w \cdot h_c = 18.2 \text{ kN}$

Hence, Shear resistance of perforated composite beam section because  $V_{pl,Rd,o} = V_{b,T,Rd} = V_{l,T,Rd}$

$$V_{Rd,o} := 2 \cdot V_{pl,Rd,o} + V_{c,Rd} = 161.2 \text{ kN}$$

$V_{Rd,o} > V_{Ed} = 1$  it is safe  
 $V_{Ed} = 93.413 \text{ kN}$   
 (Note: 1 means it is true and 0 means not true)

**5.5. Bending resistance of Tees (Vierendeel bending resistance)**

Vierendeel bending resistance at web opening for steel section  $M_{V.T.Rd} := M_{V.t.T.Rd} + M_{V.b.T.Rd}$

Vierendeel bending resistance at web opening for composite section  $M_{V.c.Rd}$

Initial assumption of distribution of shear force

Since the shear force in each Tee  $V_{T.Ed} := \frac{V_{Ed.o}}{2} = 41.951 \text{ kN}$

$V_{T.Ed} < V_{pl.Rd} = ?$  it is safe

(Note: 1 means it is true and 0 means not true)

Then, the web thickness does not need to be reduced when determining plastic bending resistance and axial resistance. If the shear force in the bottom Tee is limited by Vierendeel bending resistance across the Tee, the shear forces may need to be redistributed.

- Plastic bending resistance of an unstiffened Tee, in the absence of axial force and high shear  $M_{V.T.Rd}$

For a Class 1 and 2 cross section, the plastic bending resistance of an unstiffened Tee  $M_{V.T.Rd} = M_{t.T.Rd} = M_{b.T.Rd}$ , in the absence of axial force and high shear.

Hence: Vierendeel bending resistance at web opening for steel section

P355 Eq. (19)  $M_{V.t.T.Rd} := \left( \frac{A_{w.T} \cdot f_{y.beam}}{\gamma_{m0}} \cdot (0.5 \cdot h_{w.T} + t_f - z_{pl}) \right) + \left( \frac{A_f \cdot f_{y.beam}}{\gamma_{m0}} \cdot \left( 0.5 \cdot t_f - z_{pl} + \frac{z_{pl}^2}{t_f} \right) \right) = 4.6 \text{ kN}\cdot\text{m}$

- The plastic bending resistance of the bottom Tee is reduced for axial tension, as follows:

P355 Eq. (26)  $M_{V.b.T.Rd} := M_{V.t.T.Rd} \cdot \left( 1 - \left( \frac{N_{bT.Ed}}{N_{b.T.Rd}} \right)^2 \right) = 4.5 \text{ kN}\cdot\text{m}$

The plastic resistance of the top Tee is not reduced for axial force and thus:  $M_{V.t.T.Rd} = 4.6 \text{ kN}\cdot\text{m}$

- Vierendeel bending resistance at web opening for composite section  $M_{V.c.Rd}$

The compression force developed in the slab due to composite action over the opening  $\Delta N_{c.Rd}$

the number of shear studs above the web opening  $n_{sc.o} := 0$

$\Delta N_{c.Rd} := n_{sc.o} \cdot P_{Rd,eff} = 0 \text{ kN}$

P355 Eq. (25) For unstiffened openings, reduction factor due to the length of the openings  $k_o$  is given by  $k_o := 1 - \frac{l_{o,eff}}{(25 \cdot h_T)} = 0.84$

where  $z_i := t_f = 13.7 \text{ mm}$

P355 Eq. (24) Vierendeel bending resistance due to local composite action is given by:  $M_{V.c.Rd} := \Delta N_{c.Rd} \cdot (h_s + z_i - 0.5 \cdot h_c) \cdot k_o = 0 \text{ kN}\cdot\text{m}$

**5.6. Verification of resistance to Vierendeel bending**

The criterion for adequacy of Vierendeel bending resistance is:

P355 Eq. (14)  $M_{V.Rd,high} := 2 \cdot M_{V.t.T.Rd} + 2 \cdot M_{V.b.T.Rd} + M_{V.c.Rd} = 18.207 \text{ kN}\cdot\text{m}$  (with composite slab)  $V_{Ed.o} \cdot l_e = 9.376 \text{ kN}\cdot\text{m}$

$M_{V.Rd,high} \geq V_{Ed.o} \cdot l_e = 1$  it is safe

### Plastic analysis of composite beams with partial shear connection according to SCI-P428

$$N_{c,f} := \min(N_{c.s.Rd}, N_{a.Rd}) = (1.151 \cdot 10^3) \text{ kN}$$

$$\eta_{high.p428} := \frac{k_{flex} \cdot P_{Rd} \cdot \eta_{sc.high}}{N_{c,f}} = 0.374$$

is the design value of the plastic resistance of the clear depth of the steel web to normal force

$$N_{pl.d} := f_{y,beam} \cdot d_w \cdot t_w = 743.753 \text{ kN}$$

$$z_{pl1} := \frac{h}{2} + h_c + h_p - \frac{\eta_{high.p428} \cdot N_{c.s.Rd}}{N_{pl.d}} \cdot \frac{d_w}{2} = 203.5 \text{ mm}$$

$$\eta_{high.p428} \cdot N_{c,f} < N_{w.Rd} = 1$$

(Note: 1 means it is true and 0 means not true)

**Then**

**Case 1: plastic neutral axis within the web**

$$x1 := M_{pl.a.Rd} = 300.33 \text{ kN} \cdot \text{m}$$

$$x2 := \eta_{high.p428} \cdot N_{c,f} \cdot \left( \frac{h}{2} + h_c + h_p \right) = 120.482 \text{ kN} \cdot \text{m}$$

$$x3 := \left( \eta_{high.p428} \cdot N_{c,f} \right)^2 \cdot \left( \frac{h_c}{2 \cdot N_{c.s.Rd}} + \frac{d_w}{4 \cdot f_{y,beam} \cdot d_w \cdot t_w} \right) = 21.702 \text{ kN} \cdot \text{m}$$

$$M_{pl,\eta.Rd} := x1 + x2 - x3 = 399.1 \text{ kN} \cdot \text{m}$$

## 6. Results Summary

### • Resistances

Compressive resistance of slab

$$N_{c.s.Rd} = 1151 \text{ kN}$$

Tensile resistance of steel section

$$N_{a.Rd} = 2442.4 \text{ kN}$$

Vertical shear resistance

$$V_{pl.o.Rd} = 545 \text{ kN}$$

Bending resistance of steel section

$$M_{pl.a.Rd} = 300 \text{ kN}\cdot\text{m}$$

Bending resistance of composite solid webbed section

$$M_{pl.Rd.1} = 485.5 \text{ kN}\cdot\text{m} \text{ (neglecting the contribution from the part of the top flange that in compression)}$$

$$M_{pl.Rd.2} = 491.1 \text{ kN}\cdot\text{m} \text{ (using stress block method)}$$

Bending resistance for partial connections

$$M_{Rd.high} = 374.4 \text{ kN}\cdot\text{m}$$

Tensile resistance of bottom Tee (The axial resistance of the Top Tee)

$$N_{b.T.Rd} = 907.8 \text{ kN}$$

The compressive resistance of the effective width of slab at the opening

$$N_{c.Rd.o.Low} = 0 \text{ kN}$$

Plastic bending resistance of steel section at the web opening

$$M_{a.Rd.o} = 257.1 \text{ kN}\cdot\text{m}$$

Plastic bending resistance of composite section at the web opening

$$M_{c.Rd.o.Low} = 265.3 \text{ kN}\cdot\text{m}$$

Total shear strength of concrete is:

$$V_{c.Rd} = 18.2 \text{ kN}$$

Shear resistance of perforated beam section

$$V_{Rd.o.steel} := 2 \cdot V_{pl.Rd.o} = 142.9 \text{ kN}$$

Shear resistance of perforated composite beam section

$$V_{Rd.o} = 161.2 \text{ kN}$$

Vierendeel bending resistance perforated composite beam section

$$M_{V.Rd.steel} := 2 \cdot M_{V.l.T.Rd} + 2 \cdot M_{V.b.T.Rd} = 18.2 \text{ kN}\cdot\text{m}$$

Vierendeel bending resistance perforated composite beam section

$$M_{V.Rd.high} = 18.2 \text{ kN}\cdot\text{m}$$

Plastic analysis of composite solid webbed beams with partial shear connection according to SCI-P428

$$M_{pl,q.Rd} = 399.11 \text{ kN}\cdot\text{m}$$

### • Design values

Maximum shear force

$$V_{Ed} = 93.41 \text{ kN}$$

Maximum moment (mid-span)

$$M_{Ed} = 116.77 \text{ kN}\cdot\text{m}$$

Shear force at edge of equivalent opening

$$V_{Ed.o} = 83.9 \text{ kN}$$

Bending moment at the centreline of opening

$$M_{Ed.o} = 27.2 \text{ kN}\cdot\text{m}$$